Groundwater-atmosphere Interactions as Environmental Drivers of Water Cycle, Energy, and Greenhouse Gas Fluxes in West Africa

OUSSOU, ENAGNON FRANCIS,

B.sc. (Hydrology), PM (GIS&RS), M.sc. (Hydrology)

MCS/20/7728

A Thesis of the Doctoral Research Programme of the West Africa Climate Systems, under the West African Science Service Center on Climate Change and Adapted Land Use, in the Department of Meteorology and Climate Science, submitted to the School of Postgraduate Studies in partial fulfillment of the requirements for the award of the degree of Doctor of Philosophy in Meteorology and Climate Science of the Federal University of Technology, Akure, Nigeria.

August 2025

DECLARATION

I hereby declare that this Thesis was written by me and is a correct record of my own research work. It has not been presented in any previous application for any degree of this or any University. All citations and sources are clearly acknowledged by means of references.

Candidate's Name: OUSSOU, Enagnon Francis,

Signature:……..…

Date:……..

CERTIFICATION

We certify that this Dissertation entitled "Groundwater-atmosphere Interactions as Environmental Drivers of Water Cycle, Energy, and Greenhouse Gas Fluxes in West Africa" is the outcome of the research carried out by OUSSOU, Enagnon Francis under the WASCAL DRP-WACS in the Department of Meteorology and Climate Science of the Federal University of Technology, Akure.

Prof. Y.A. Asiwaju-Bello
(Major Supervisor)

……..……..
Signature Date

Department Applied Geology,
Federal University of Technology,
Akure, Nigeria

Prof. Harald Kunstmann
(Co-Supervisor)

……..……..
Signature Date

Institute for Meteorology and Climate Research, Karlsruhe Institute of Technology, Atmospheric Environmental Research (IMK-IFU);
Garmisch-Partenkirchen, Germany

Prof. Nicaise Yalo
(Co-Supervisor)

……..……..
Signature Date

Laboratoire d'Hydrologie Appliquée,
Institut National de l'Eau (INE),
Université d'Abomey-Calavi,
Cotonou, Benin.

Prof. Balogun Ifeoluwa Adebola
(Director)

……..……..
Signature Date

Doctoral Research Program West African Climate Systems,
West African Science Service Center on Climate Change and Adapted Land Use (DRP-WACS WASCAL),
Federal University of Technology,
Akure, Nigeria

ACRONYMS

AMMA-CATCH: African Monsoon Multidisciplinary Analysis - Coupling the Tropical Atmosphere and the Hydrological Cycle

BEXP: Soil pore size distribution index

CZO: Critical Zone Observatory

DKSAT: Saturated hydraulics conductivity

DTB: Depth-to-bedrock

EBF: Evergreen Broadleaf Forest in MODIS-IGBP land cover

EBF-VC: SBG afforestation with Evergreen Broadleaf Forest and the dynamic vegetation scheme off.

EBF-VD: SBG afforestation with Evergreen Broadleaf Forest and the dynamic vegetation scheme on.

ET: Evapotranspiration

ESMs: Earth System Models

ESA-CCI: European Space Agency Climate Change Initiative Soil Moisture

ERA5-Land: European Centre for Medium-range Weather Forecast Reanalysis product version 5 Land

GGW: Great Green Wall initiative

GliM: Global lithological database

IPCC: Intergovernmental Panel on Climate Change

ITD: Inter-tropical Discontinuity

K: subsurface permeability

KGE: Kling–Gupta efficiency

LSM: Land Surface Models

LW: Outgoing longwave radiation

LH: Latent heat

MMF: Miguez-Macho & Fan groundwater parameterization scheme

MODIS: Moderate Resolution Imaging Spectroradiometer

NSE: Nash–Sutcliffe model efficiency coefficient

PF-CLM: Parflow-Common Land Model

REF: Current land use scenario

REFKDT: Surface runoff parameter

RF: Surface runoff

RN: Net radiation

SAV: Savanna in MODIS-IGBP land cover

SAV-VC: SBG afforestation with Savanna and the dynamic vegetation scheme off.

SAV-VD: SBG afforestation with Savanna and the dynamic vegetation scheme on.

SBG: Shrubland, bare soil, and grassland (SBG) in MODIS-IGBP land cover

SDG: Sustainable Development Goal

SH: Sensible heat

SM: Soil moisture

SSP: Shared Socioeconomic Pathways

STATSGO: State Soil Geographic Database

TOPMODEL: TOPModel runoff scheme

TRI: Topography Roughness Index

UGRF: Underground runoff

WA: West Africa

WFPS: Water Filled Pore Space

WRF: Weather Research and Forecasting

WRF-Hydro: The hydrological model of Weather Research and Forecasting

WS: Woody Savanna in MODIS-IGBP land cover

WS-VC: SBG afforestation with Woody Savanna and the dynamic vegetation scheme off.

WS-VD: SBG afforestation with Woody Savanna and the dynamic vegetation scheme on.

ZWT: Water table depth

ABSTRACT

Reducing discrepancies in the simulation of water and energy fluxes remains a key challenge in accurately representing surface water flux processes, particularly in regions with limited observational data. This study evaluates the sensitivity of the WRF-Hydro model to three parameterization schemes - Free Drainage (FD), TOPMODEL, and MMF - over West Africa. The results show that MMF outperforms the other schemes in representing surface water flux variables, especially in topographic convergence zones, where soil moisture and evapotranspiration in riverbeds increase by 20% with respect to FD. At the catchment scale, soil moisture, evapotranspiration, and groundwater storage are well simulated, with correlation coefficients reaching 0.9. In addition, model calibration for the Donga River gives reliable performance with KGE value up to 0.74.

The shrubland, bare soil, and grassland (SBG) in MODIS-IGBP land cover is substituted by the Evergreen Broadleaf Forest (EBF), Savanna (SAV), and Woody Savanna (WS) to mimic the the Great Green Wall (GGW) initiative. At basin scale, the seasonal cycle and inter-annual variability are well captured as there is a strong linear relationship between the observed and simulated values with correlation coefficients from 0.9 to 0.97. The KGE values reaches respectively 0.72, 0.71, and 0.72 in Oueme, Sissili, and Faga catchments. Compared to the current land use (REF) scenario, EBF-VC and WS-VC experiments decrease the mean soil moisture (SM) by 0.2 and 0.1 mm, while the SAV-VC increases it by 0.8 mm in drier conditions in Faga. However, the scenarios reveal a decrease of mean SM by 0.5, 0.6, and 0.1 mm for EBF-VC, SAV-VC, and WS-VC in higher precipitation areas (Oueme). Remarkably, the average ET is increased whatever the climatic condition except for SAV-VC in Sissili where a negative effect is recorded. For instance, EBF-VC, SAV-VC, and WS-VC increases the average ET by 0.25, 0.08, 0.07 mm d^{-1} in Faga. EBF-VC, SAV-VC and WS-VC experiments reduce streamflow respectively by 24%, 18%, and 21% in Donga and 31%, 26%, and 28% in Oueme.

The change in the surface fluxes (e.g., LH, SH, GH, RN, ET) and subsurface dynamics (e.g., water table depth) in response to the variation of the lineaments permeability (K) is evaluated with three experiments namely High, Moderate, and Low K (see section 3.4.2.5). Remarkably, the most significant change in the diurnal cycle of the energy fluxes occurred around noon. Compared to the reference simulation (without lineament), High and Moderate K experiments decrease the outgoing longwave (LW) by -2% and -1% in the dry season. Higher permeability in

the fractures results in a decrease of the outgoing longwave radiation. An increase of 1.1 and 1.5 W m^{-2} of sensible heat is associated with Moderate K and Low K experiments from March to May. The energy balance closure increases significantly by 36.9 and 25.4% for Moderate K and High K experiments from September to November (SON). The average groundwater storage (GWS) of the basin increases with High K and Moderate K experiments by 355.8 and 326.8 million m^3.

The climate projections of five Global Circulation Models (GCMs) namely GFDL-ESM4, HadGEM3-GC31-LL, IPSL-CM6A-LR, MIROC6, and NorESM2-MM under two different Shared Socioeconomic Pathways (SSP1-2.6, SSP5-8.5) are used to assess the subsurface dynamics' sensitivity to extreme warming scenarios. Under SSP1-2.6, 3 out the 5 GCMs show an increase of groundwater storage (GWS) by 0.45 to 30.39 million m^3 in Donga basin. All the GCMs indicate a decrease of mean surface water storage (SWS) under SSP5-8.5 projection except GFDL-ESM4. According to NorESM2-MM, IPSL-CM6A-LR, MIROC6, and HadGEM3-GC31-LL projections, a decrease of surface water storage (SWS) will occur whatever the warming level by the end of the century.

Changes in land use and land management significantly affect the global emissions budget, influencing the climate through biogeochemical processes. This study provides the assessment of soil greenhouse gas GHG emissions in the Sudanian savanna region of West Africa using a chamber-based experimental setup. Our results reveal significant variation in methane (CH_4) fluxes across the sites. However, nitrous oxide (N_2O) fluxes did not vary significantly, likely due to uniformly low nitrogen input across all systems. The highest seasonal CH_4 emissions were recorded in the rainfed rice field (0.69 ± 0.17 and 0.82 ± 0.22 kg C ha^{-1} $season^{-1}$, on average), while the forest reserve acted as a net CH_4 sink (−0.019 ± 0.20 and −0.42 ± 0.13 kg C ha^{-1} $season^{-1}$). In contrast, soils across all sites, both managed and natural, were sources of N_2O, with fluxes ranging from 0.01 kg N ha^{-1} $season^{-1}$ in the forest reserve to 0.16 kg N ha^{-1} $season^{-1}$ in the rice field. This study also analyzed the environmental drivers of GHG fluxes and found that CH_4 variability was significantly influenced by soil water content and soil temperature (partial R^2 between 0.21 and 0.42). No significant relationship was observed between these variables and N_2O emissions. These results highlight that changes in land cover and land management in the Sudanian can substantially increase CH_4 emissions, while their impact on N_2O fluxes is marginal.

DEDICATION

To God be the glory, all praises and adoration to our Lord Jesus-Christ for the great things He has done and to whom this research work is dedicated.

The work is dedicated to my dear and loving parents for their sacrifices over me and for sowing seeds of hope for a better future. The promised land you worked for is at sight. Particularly, the research work is dedicated to my late mother, AGBOFIA HOUNSA Colette whose unwavering love will forever dwell with me and my father, OUSSOU Sossou Christophe for his support.

The work is also dedicated to my maternal and paternal grand-parents for their unrewarded sacrifices especially my recently late grand-mother HOUNSA Christine a.k.a Adounkponon. The Lord God is good and knows how to reward the unrewardable.

To all the children in my local communities in Nigeria and Benin, this work is dedicated to you all to serve as an example to follow and a proof of what we can achieve despite our common upbringings.

ACKNOWLEDGEMENT

My genuine thanks to God the Almighty Father, who loves me so much and provides the necessary means every day for the fulfillment of this work.

I thankfully acknowledge the German Ministry of Education and Research (BMBF) for fully funding my PhD study through the West African Science Service Center on Climate Change and Adapted Land Use (WASCAL).

I sincerely thank Prof. Daouda Kone, the Director of Capacity Building WASCAL Headquarters and his staff in Accra, Ghana. My thanks to Prof. Balogun Ifeoluwa Adebowale, the new Director, and Prof. Debo Adeyewa Z., the former Director of WASCAL-GRP-WACS of the Federal University of Technology Akure (FUTA), and the staff, namely Prof. Ayo Oluleye, the Scientific Coordinator, and new Deputy Director, Prof. Ademola Akinbobola, for providing the needed administrative and moral support throughout the research period.

I hereby thank my main supervisor, Prof. Asiwaju-Bello Yinusa A., for guiding and supporting this work until the end. My sincere thanks to my German co-supervisor Prof. Harald Kunstmann and his staff at the University of Augsburg and KIT Campus Alpin for providing their research platform in Ghana and Germany for this work.

I thank Dr. Jan-Geert Bliefernicht and Dr. Souleymane Sy, my German advisors, and the staff for their support and assistance with my research work.

My gratitude to my co-supervisor, Prof. Nicaise Yalo, for his support throughout the research period.

I also thank the WASCAL Team in Bolgatanga for hosting during the two-year research measurements. My thanks go to all the people who participated directly or indirectly to the field work especially the families that agreed to host me in Bolga.

I thank Dr. Thomas Rummler, my co-advisor, who provided the needed support to run the model WRF-Hydro on the High-Performance Computer of KIT, required to achieve the objectives of this work.

I'm grateful to Dr. Benjamin Fersch for his unwavering assistance and support for the models' setup and running on the HPC for this work.

My sincere thanks to the research team at KIT Laboratory for helping with the samples analysis namely Ralf Kiese, Anja Schäffler-Schmidt, and Ricky. M. Mwanake.

I thank my friends and colleagues, Dragan Petrovic, Maximillan Graf, Manuel Rauch, Aissatou Ndiaye, and Windmanagda J. Sawadogo for their support during my research stay at the University of Augsburg.

My sincere thanks to the Deutscher Akademischer Austauschdienst (DAAD) Stiftung for providing a short-term research grant to further my research work. My thanks to Stefanie Lohmann, Alexander Thym, and Jessica Schüller for offering the administrative support needed for my research trip.

My Thanks to Samuel Guug, Michael Ayamba, and Kwesi D. Ochard, the WASCAL team in Bolgatanga coordinating the Vea/Sissili basin, for hosting my fieldwork.

I would also like to thank the WASCAL administration for providing the necessary support for my research trip, specifically Selasi Weto, Garvary F. Akoto, and Jessica Aubin.

I also thank Prof. Julien Adounkpè, the Director of WASCAL GRP Climate Change and Water Resources at the University of Abomey-Calavi, and his team namely Dr. Jean Hounkpè and Dr. Félicien Badou, for their valuable support at the beginning of this research journey.

My thanks to the team of the WASCAL CONCERT project for offering their platform to support my research work. I would like to mention Prof. Leonard K. Amekudzi, Ines Spangenberg, Rainer Steinbrecher, Frank Neidl, Christiana F. Olusegun, Emmanuel Quansah, Alex Frempong, and Patrick Davies.

My thanks also to Dr. Mayeul Quenum and Dr. Gildas Guidigan for their various support and encouragement during the research period.

I’m grateful to the House Church of God, the Deeper Christian Life Ministry PG and Staff, for their prayer, support, and love in so many ways. The Lord Jesus rewards your loving kindness. I would like to mention Pastor Afolabi C. Akinmoladun and Pastor Mayaki Adeolu.

My thanks to my WASCAL-GRP-WACS colleagues and friends of Batch 5 for the loving and supportive environment we offered each other till the end of the program. I would like to name Nadège, Robert, John, Ifeoluwa, Yeo, Sita, Diarra, Maïga, Yamoula, and Cissé.

My sincere thanks to my entire family and loved ones for their support, patience, and encouragement during this research work. I would like to name Alphonse, Ruth, Yôyô Arnaud, Marcelin, Elisabeth, Friday, Modoukpè, Raymond, Loth, Hubert, and others.

TABLE OF CONTENTS

Declaration ii
Certification iii
Acronyms iv
Abstract vi
Dedication viii
Acknowledgments ix
Table of Contents xii
List of Tables xvi
List of Figures xviii
Chapter One 1
Introduction 1
1.1 Background 1
1.2 Problem statement and research question 8
1.3 Aim and Objectives 11
1.4 Innovation 11
1.5 Structure of the thesis 12
Chapter Two 13
Literature Review 13
2.1 Definition of some concepts 13
2.1.1 Water cycle 13
2.1.2 Energy fluxes 15
2.1.3 Earth System Modeling 17
2.1.4 Climate Change Impacts on Groundwater 19
2.2 Groundwater-Atmosphere interactions 19
2.3 Improving subsurface parameterization for Groundwater-Atmosphere modeling 21
2.4 Coupling Groundwater-Atmosphere for higher accuracy in modeling 24
2.5 Linking GW-controlled land cover change to water, energy, and greenhouse gas fluxes 25
2.6 GW-Atmosphere modeling and observation data challenges 26
2.7 Representing subsurface boundaries for GW-Atmosphere modeling 28
2.8 Greenhouse gas emissions under Groundwater-Atmosphere modeling 31
2.9 Current state of observational data availability for Groundwater-Atmosphere models validation in West Africa 38
Chapter Three 43
Materials and Methods 43
3.1 Sensitivity of water fluxes to subsurface flow parameterization schemes: A groundwater-enhanced WRF-Hydro modeling study 43
3.1.1 Study area 43
3.1.2 Dataset 46
3.1.2.1 On-site observations 46
3.1.2.2 ERA5-Land Reanalysis 46

3.1.2.3 Remote Sensing products 47
a. GLEAM dataset 47
b. ESA-CCI Soil Moisture 47
3.1.3 Methods 48
3.1.3.1 Description of the hydrological model WRF-Hydro 48
3.1.3.2 Experiments setup overview 49
3.1.3.3 Default Option or Free drainage parameterization 51
3.1.3.4 MMF runoff scheme 52
3.1.3.5 TOPMODEL runoff scheme 53
3.1.3.6 Performance measures 56
3.2 Impact of Idealized afforestation on water budget and energy fluxes 57
3.2.1 Model description and Experiment setup 57
3.2.2 Simulated afforestation scenarios 57
3.3 Improving the depth-to-bedrock for groundwater-to-atmosphere modeling 63
3.3.1 Study area 63
3.3.2 Data collect 65
3.3.2.1 Field depth-to-bedrock measurements 65
3.3.2.2 Digital Elevation Model 65
3.3.2.3 Global depth-to-bedrock maps 66
3.3.3 Methods 67
3.3.3.1 Aquifers thickness estimate 67
3.3.3.2 Test case 70
3.4 Evaluation of Fractured Aquifers' influence on water and energy fluxes 74
3.4.1 Study area 74
3.4.2 Methodology 75
3.4.2.1 ParFlow-CLM model approach 75
3.4.2.2 Eddy Covariance Fluxes 78
3.4.2.3 Fractured aquifers descriptions 80
3.4.2.4 Model setup and domain description 82
3.4.2.5 Simulated scenarios 85
3.4.2.6 Evaluation approach 88
3.5 Impact of Climate projections on groundwater recharge, levels, surface water storge 90
3.5.1 Climate scenarios 90
3.6 Soil N_2O and CH_4 emissions in contrasting land use of the Sudanian savanna 92
3.6.1 Study region and sites description 92
3.6.2 Procedures of the field GHG measurement 94
3.6.2.1 Experimental design 94
3.6.2.2 Chamber sampling and analysis 96
3.6.2.3 Soil moisture and temperature measurements 97
3.6.2.4 Soil sampling and analysis 97
3.6.2.5 Statistical Analysis 100
3.7 Sensitivity of soil N_2O, CH_4, and CO_2 fluxes to water table dynamics 102

3.7.1 Model descriptions 102
3.7.2 Joint UK Land Environment Simulator 102
3.7.3 JULES-Microbe model setup 103
Chapter Four **105**
Results and Discussion **105**
4.1 Sensitivity of water fluxes to subsurface flow parameterization schemes in West Africa: A groundwater-enhanced WRF-Hydro modeling study 105
4.1.1 Model calibration 105
4.1.2 Models' performance 117
4.1.2.1 Performance in simulating soil moisture 117
4.1.2.2 Performance in simulating actual evapotranspiration 125
4.1.2.3 Performance in simulating energy fluxes 131
4.1.2.4 Performance in simulating groundwater storage 135
4.1.3 Sensitivity of water fluxes to the parameterization schemes 139
4.1.3.1 Soil moisture response 139
4.1.3.2 Evapotranspiration response 142
4.1.3.3 Impact on streamflow 144
4.2 Contrasting effects of Idealized Afforestation on water budget and energy fluxes: a WRF-Hydro modeling study over West Africa 149
4.2.1 Model validation 149
4.2.1.1 Soil moisture 149
4.2.1.2 Evapotranspiration 153
4.2.1.3 Streamflow 157
4.2.1.4 Latent heat and sensible heat 161
4.2.2 Patterns of water and energy fluxes under the idealized afforestation 165
4.2.2.1 Evapotranspiration and soil moisture response to different idealized afforestation 165
4.2.2.2 Water table and underground runoff responses to different idealized afforestation 167
4.2.2.3 Energy fluxes response to different idealized afforestation 170
4.2.3. Evaluation of the afforestation impact on the subbasins' water budget 173
4.3 Improving the depth-to-bedrock maps for groundwater-to-atmosphere modeling in Africa 177
4.3.1 Field DTB analysis and spatial statistics 177
4.3.2 PF-CLM Model performance evaluation 185
4.3.2.1 Simulated energy fluxes evaluation 185
4.3.2.2 Simulated evaporation analysis 189
4.3.2.3 Computed DTB maps and 2D profiles 193
4.4 Evaluation of Fractured Aquifers' influence on water and energy fluxes 206
4.4.1 Model validation 206
4.4.2 Sensitivity of energy balance to fractures' permeability 209
4.4.3 Sensitivity of water fluxes 215
4.4.4 Sensitivity of water table depth 218
4.4.5 Sensitivity of terrestrial water storage 220

4.5 Impact of Climate projections on groundwater recharge, levels, surface water storge 223
4.5.1 Climate impact on groundwater recharge 223
4.5.2 Climate impact on surface water storage 227
4.5.3 Climate impact on groundwater levels 222
4.6 Soil N_2O and CH_4 emissions in contrasting land use of the Sudanian savanna (West Africa) 230
4.6.1 CH_4 flux 230
4.6.2 N_2O flux 234
4.6.3 Soil moisture 237
4.6.4 Evaluation of environmental drivers of the fluxes 239
Chapter Five **247**
5.0 Conclusion and Recommendations 247
5.1 Limitation of the study 250
5.2 Contribution to knowledge 251
References **253**

LIST OF TABLES

Table		Page
3.1:	Model setup description of WRF-Hydro and Noah-MP	50
3.2:	Idealized afforestation scenarios implemented in this study	62
3.3:	A summary of tested formulas and functions for the DTB estimation in this study.	69
3.4:	Tested scenarios with corresponding permeability values and description.	87
3.5:	Time periods of Global warming in the GCMs under SSP1-2.6 and SSP5-8.5	91
3.6:	Descriptions of the investigated sites: altitude, annual precipitation (AP), mean annual air temperature (MAT), soil organic carbon (SOC), soil nitrogen (Ntot), soil carbon to nitrogen ratio (C/N), N fertilization rate (Nr), bulk density (BD), texture (%), and soil types. The parameters refer to soil depth from 0 to 50 cm. The values are derived from Eddy Covariance measurements and reanalysis products (*) because of missing data. Further details about the sites are provided in Quansah et al. (2015), Bliefernicht et al. (2018), and Berger et al. (2019).	99
3.7	Descriptive statistics of the seasonal N_2O and CH_4 fluxes, soil temperature (T_{soil}), water filled pore space (WFPS) of the four sites for the two years. The values are in kg C/N ha^{-1} $season^{-1}$ and the monthly averages are reported in µg C m^{-2} h^{-1} (see Table S1). The period of the season considered for the seasonal mean computation is from June to October.	101
3.8	Tested scenarios for the evaluation of the impact water table change on greenhouse gas fluxes.	104
4.1a	Channel parameters per stream order	112
4.1b	Model calibration metrics	113
4.2	Evaluation metrics of the observation versus simulated soil moisture from the reference scenario.	150
4.3	Evaluation metrics of the observation versus simulated ET from the reference scenario.	154
4.4	Evaluation metrics of the observation versus simulated streamflow from the reference scenario.	158
4.5	Metrics of LH and SH versus FLUXCOM-RS product	162

4.6	Descriptive statistics of DTB based on geological lineaments, depressions, and rivers' network	179
4.7	Descriptive statistics of DTB based on rock types.	184
4.8	PF-CLM Model performance metrics for the energy fluxes	190
4.9	Difference in the energy components between the experiments and the reference simulation	210
4.10	Difference in the water fluxes between the experiments and the reference simulation	217
4.11	Difference in the groundwater storage and surface water storage between the experiments and the reference simulation	222
4.12	Description of the difference in GWS projections compared to the historical period (1850-2014).	226
4.13	Description of the difference in SWS projections compared to the historical period (1850-2014).	228
4.14	Stepwise multiple linear regression between in situ fluxes (CH_4 and N_2O), soil water content (% WFPS), and soil temperature (°C) for each land use.	246

LIST OF FIGURES

Figure		Page
1.1	Current and projected effects of global warming on biodiversity, food production, mortality and morbidity (IPCC, 2022).	2
1.2	Soil column of the Noah-MP LSM with MMF groundwater parameterization and WRF-Hydro routing extensions (Rummler et *al.* 2022).	7
2.1	Water Cycle (Image credit: Dennis Cain/NWS)	14
2.2	Global mean energy budget. From Wild et al. (2015, 2019) in Forster et al. (2021).	15
2.3	a) Progress of the development of Earth system models over last one-hundred year (Pan et al., 2025). b) Soil column of the Noah-MP LSM with MMF groundwater parameterization and WRF-Hydro routing extensions (Rummler et al. 2022).	18
2.4	Different approaches to groundwater simulation employed in continental to global scale models (Condon et al., 2021).	23
2.5	Conceptual model of watershed subsurface boundaries and examples of maximum depth-to-bedrock. (Right) Maximum depth-to-bedrock for most groundwater and integrated hydrologic models, Critical Zone Observatory (CZO) models and observations, and Land Surface Models (LMS) depending on groundwater travel time and salinity (see Condon et al., 2020).	30
2.6	Conceptual schematic of CH_4, N_2O, and CO_2 fluxes in wetlands under N deposition, potential warming, and plant community composition (see Luan et al., 2019).	33
2.7	Methane (CH_4) cycle response to different hydrological scenarios in wetlands (see Cui et al., 2024).	37
3.1	Study area represented by the digital elevation model of HydroShed (Lehner et al., 2008; Left; elevation is indicated in meters) and land cover maps of MODIS (Friedl et al., 2010; Right) with countries limits (black), catchments (red), river gauges (blue triangle), and the river network (light blue). Four basins are represented (Faga, Sissili, Oueme, and Donga).	45
3.2	Description of the idealized afforestation undertaken for the region	59

3.3	(a) The topography of the continent is mapped using the HydroSHED Digital Elevation Model (DEM). The DEM shows the distribution of elevation over the continent, and (b) the geological units are from the Global Lithological Map (GliM) produced by Hartmann & Moosdorf, (2012). The study area shapefile is used to extract the mapped geological layer. The Metamorphic unit (basement rock) covers more than 27% of the continent.	64
3.4	Digital elevation model (e), Depth to bedrock (f), MODIS land cover (c), FAO Soil types (b), basement hard rock (a), and topography of part of West Africa with a black box indicating the Nazinga reserve and an arrow to identify the study area (d).	73
3.5	Lineament map of Donga basin (a), and vertical profiles of a typical hardrock aquifer (b and c) modified from Lachassagne et al. (2011) and MacDonald et al. (2005) in Adeotan et al. (2025).	81
3.6	Digital elevation model (e), Depth to bedrock (f), MODIS land cover (c), FAO Soil types (b), basement hard rock (a), and topography of part of West Africa with a black box indicating the Nalohou and an arrow to identify the study area (d).	84
3.7	Study region and the four monitoring sites Kayoro “cropland”, Gorigo “grassland”, Janga “rice fields” and Mole Park “forest reserve”	93
3.8	Chamber-based greenhouse gas sampling plots; closed (middle) and opened for soil moisture and temperature measurements (left and right) in a rice field at Janga, Upper-East Ghana	95
4.1	Infiltration rate map computed using soil hydrologic group, slope, and land cover (shown on the right side) for the REFKDT regionalization. The different color in the soil hydrologic group map indicates the classes (A, B, C, and D).	107
4.2	Topography Roughness Index (TRI) map used for the regionalized surface roughness scaling factor OVROUGHRTFAC. The dark blue indicates high roughness values.	109
4.3a	Model calibration steps and corresponding metrics. The black and grey bars indicate respectively the KGE and NSE scores. The abbreviations are described above in section 4.4. See Figure S11 for further detail.	115

4.3b	Model calibration steps and corresponding simulations. The grey line indicates the observation.	116
4.4	Comparison of the basin averaged soil moisture of ESA CCI SM versus simulated SM. The scatter plots and metrics of FD, TOMODEL, and MMF are in red, blue, and green.	119
4.5	Error metrics for the domain level validation of MMF (b) soil moisture against ESA CCI soil moisture (a) with the bias (c) R (d), KGE (e), and NSE (f). The colour ramp is similar for R and KGE. Lower NSE are indicated in fading red and higher performance in fading blue. The blank areas correspond to no value in the ESA CCI product. The magenta polygons are basins. The horizontal resolution of the simulations is resampled to the ESA CCI data decreasing the subplots resolution to 0.25˚.	122
4.6	Simulated soil moisture from FD (dot line red), TOPMODEL (dash blue), MMF (dot line green) plotted against the EC sites' recorded soil moisture in the top soil layer (black dot). The stations located in the Savanna (Kayoro, Sumbrungu, Nazinga, Nalohou, and Belefoungou) and Sahel zones (Wankama Nord and Sud). The red dots on the map locate the flux monitoring sites, the black line is the countries limit (not inferring legal borders) and the image below is the HydroSHED digital elevation model of the domain.	124
4.7	Comparison of the basin-averaged GLEAM ET versus simulated ET. The scatter plots and metrics of FD, TOMODEL, and MMF are in red, blue, and green	126
4.8	Error metrics for the domain level comparison of MMF (b) ET against GLEAM ET (a) with the bias (c) R (d), KGE (e), and NSE (f). The colour ramp is similar for R and KGE. Lower NSE is indicated in fading red and higher performance in fading blue. The horizontal resolution of the simulations is resampled to the GLEAM data.	129
4.9	Simulated ET from FD (red), TOPMODEL (dash blue), MMF (dot line green) plotted against three computed ET using Penman (black dot), FAO-56 (red square), and Priestley-Taylor (magenta diamond) at the EC flux monitoring sites. The stations located in the Savanna (Kayoro, Sumbrungu, Nazinga, Nalohou, and Belefoungou) and Sahel zones (Wankama Nord and Sud). The	131

	red dots on the map locate the flux monitoring sites, the black line is the countries limit (not inferring legal borders) and the image below is the HydroSHED digital elevation model of the domain.	
4.10	Comparison of the averaged diurnal cycle (1st to 3rd January 2013) of the simulated energy fluxes from FD, TOPMODEL, and MMF with field measurement at site level (reading from the left). The three upper sites have all the components namely latent heat (red), sensible heat (blue), ground heat (black), and net radiation (yellow). In the vertical axis, the energy fluxes are in W m^{-2} and the horizontal axis is in hourly time step. Each line indicates the sites.	134
4.11	Comparison of the basin-averaged GLDAS ΔGWS versus simulated ΔGWS. The scatter plots and metrics of FD, TOMODEL, and MMF are in red, blue, and green	136
4.12	Error metrics for the domain level comparison of MMF (b) GWS against GLDAS ΔGWS (a) with the bias (c) R (d), KGE (e), and NSE (f). The colour ramp is similar for R and KGE. Lower NSE is indicated in fading red and higher performance in fading blue. The horizontal resolution of the simulations is resampled to the GLDAS ΔGWS model grid.	138
4.13	Computed relative and absolute soil moisture differences (units: m^3 m^{-3}) between the TOPMODEL and FD (upper); MMF and FD (lower). The difference is negative towards the red patches showing the ET decrease under a particular scheme. The blue patches indicate an increase in ET. Countries located within the domain are delimited with a black line. The blue patch in the north-west is a bias caused by temporary wetlands of the Niger river.	141
4.14	Computed relative and absolute differences of ET between the TOPMODEL and FD (upper); MMF and FD (lower). The difference is negative towards the red patches showing the ET decrease under a particular scheme. The blue patches indicate increase in ET. Countries located within the domain are delimited with black lines.	143
4.15	Simulated daily streamflow with FD (red), TOPMODEL (blue), and MMF (green), observation, and precipitation plotted on the secondary axis (upper)	145

	at Donga (a) and Bonou (b) stations. The corresponding metrics (e.g. KGE, R) of the simulations are displayed.	
4.16	Seasonal cycle of SM under the idealized afforestation experiments and the reference scenario (REF). The graph of relative difference is added to the supplementary figures.	152
4.17	Seasonal cycle of ET under the idealized afforestation experiments and the reference scenario (REF). The graph of relative difference is added to the supplementary figures.	156
4.18	Computed relative and absolute differences of soil moisture between the TOPMODEL and FD (upper); MMF and FD (lower). The difference is negative towards the red patches showing the ET decrease under a particular scheme. The blue patches indicate an increase in ET. Countries located within the domain are delimited with a black line.	160
4.19	Seasonal cycle of sensible heat (SH) and latent heat (LH) under the idealized afforestation experiments and the reference scenario (REF). The graph of relative difference is added to the supplementary figures.	164
4.20	Calculated absolute differences of ET between the idealized afforestation experiments and REF (upper) and of ΔSM (lower). The gradient of red and blue patches shows decreasing and increasing ET/ΔSM towards high impact areas. Countries located within the domain are delimited with black line and basins with magenta line. The graph of relative difference is added to the supplementary figures (Fig. S5)	166
4.21	Calculated absolute differences of underground runoff (UGRF) between the idealized afforestation experiments and REF (upper) and of water table depth (ΔZWT; lower). The gradient of red and blue patches shows decreasing and increasing UGRF/ΔZWT towards high impact areas. Countries located within the domain are delimited with black line and basins with magenta line. The graph of relative difference is added to the supplementary figures (Fig. S6)	169
4.22	Calculated absolute differences of latent heat (ΔLH; upper), sensible heat (ΔSH; middle), ground heat (ΔGH; lower) between the idealized afforestation experiments and REF (upper). The gradient of red and blue patches shows decreasing and increasing LH/SH/GH towards high impact areas. Countries	172

	located within the domain are delimited with black line and basins with magenta line. The graph of relative difference is added to the supplementary figures (Fig. S7)	
4.23a	Monthly water budget under the idealized afforestation experiments and current land use in Oueme. Highlight of the seasonal variation of ET (upper left), soil moisture storage (lower left), surface runoff (RF; upper right), and underground runoff (UGRF; lower right) covering the simulation period from 2012 to 2015. All the components are in mm. Similar figure for Sissili and Faga are added to the supplementary documents.	175
4.23b	Groundwater table change in response to the afforestation experiment in Faga, Sissili, and Oueme basins.	176
4.24	Zonal statistic (a) of DTB in relation with geological lineaments, depressions, and Rivers' network	178
4.25	Zonal statistic of DTB in relation to (a) geological and (b) soil units. The dashed green line, red, blue, and purple lines represent the maximum of DTB estimated or suggested by past authors. The two dark green lines are the 75th and 25th percentile of the field depth-to-bedrock. This figure is a complementary of the figure 4.24. The numbers on the abscise indicate the geological unit (c) and soil unit (b). The soil and geological units are described respectively in Volkoff and Willaime (1976) and OBEMINES (1989).	182
4.26	Simulated and observed energy fluxes comparison (a - d) with the black dot indicating the observations, and dotted red/blue/yellow/green lines the PF-CLM simulated fluxes. At the bottom are the spatial distribution of the temporal averages with color ramp ranging from lower values in dark red to highest values in dark green.	186
4.27	Scatter plots of the simulated energy fluxes against the observed values. The dashed blue line is the 1:1 line which indicates a perfect agreement between the values.	188
4.28	Total evapotranspiration (a), Soil evapotranspiration (b), Vegetation evapotranspiration displayed with the computed actual evapotranspiration using the Priestley-Taylor (square magenta), Penman (black dot), and FAO-	192

	56 (red dot) approaches (c). The spatial distribution of the corresponding temporal averages (d-f).	
4.29	Violin plot of DTB based on GliM geological units using the three selected approaches (ev: Evaporites, mt: Metamorphics, pa: Acid plutonic rocks, pb: Basic plutonic rocks, pi: Intermediate plutonic rocks, sc: Carbonate sedimentary rocks, sm: Mixed sedimentary rocks, ss: Siliciclastic sedimentary rocks, su: Unconsolidated sediments, va: Acid volcanic rocks, vb: Basic volcanic rocks, vi: Intermediate volcanic rocks, and wb: Water Bodies)	194
4.30	Computed DTB occurrence likelihood (a), DTB maps using Eq. 3.31 (d), 3.36 (b) and 3.46 (c); blanked areas are low to very low probability of DTB occurrence.	196
4.31	DTB maps from previous studies (a-b) and the suggested maps from this study for the Congo basin.	198
4.32a	DTB maps from previous studies (a-b) and the suggested maps from this study for the Niger basin.	200
4.32b	DTB maps from previous studies (a-b) and the suggested maps from this study for the Oueme basin.	200
4.33	Comparison of the 2D profiles in Congo (a), Niger (b), and Oueme (c) basins; red for DTB using Eq. 3.31, magenta for DTB using Eq. 3.36, blue for DTB using Eq. 3.46, black for altitude (Z), and green ligne for Shangguan et *al.* (2017) DTB map. The profiles in orange are extracted respectively from Opala to Masi-Maniba, Tudun Iya to Lokoja, and Parakou to Dassa.	202
4.34	Scatter plots of simulated outgoing longwave radiation versus observed for DJF, MAM, JJA, and SON periods under High, moderate and low permeability (High K, Moderate K, and Low K) of geological lineaments in Donga basin.	208
4.35	Diurnal cycle of the energy balance components under the geological lineament permeability experiments.	210
4.36	Potential change in the energy balance closure under the lineament permeability experiments.	214
4.37	Diurnal cycle of the total evapotranspiration, transpiration, and soil infiltration under the geological lineament permeability experiments.	216

4.38	Sensitivity of water table depth to the lineament permeability experiments.	219
4.39	Potential change in the groundwater storage and surface water storage under the lineament permeability experiments (High, Moderate, and Low K).	221
4.40	Groundwater storage projections under SSP1-2.6 and SSP5.8.5 scenarios for Donga basin.	224
4.41	Surface water storage projections under SSP1-2.6 and SSP5.8.5 scenarios for Donga basin	228
4.42	Groundwater table projections under SSP1-2.6 and SSP5.8.5 scenarios for Donga basin	229
4.43	Weekly boxplot time series of in situ CH_4 flux for 2023 (light blue) and 2024 (yellow). Each boxplot is made of fluxes from 5 sub-trial points (chambers). From top to bottom are the forest reserve, grassland, cropland, and rice fields. The number of the sampling week is in x-axis.	233
4.44	Weekly boxplot time series of in situ N_2O flux for 2023 (light blue) and 2024 (yellow). Each boxplot is made of fluxes from 5 sub-trial points (chambers). From top to bottom are the forest reserve, grassland, cropland, and rice fields.	236
4.45	Manually measured soil volumetric water content of the four sites for the two years. The soil moisture data were not fully collected noticeably at the forest site.	238
4.46	CH_4 response to soil moisture change (% WFPS) and temperature classified into three categories for 2023 and 2025. Linear regression is displayed in red if the relationship is significant with corresponding r value.	241
4.47	N_2O response to soil moisture change (% WFPS) and temperature classified into three categories for 2023 and 2025. Linear regression is displayed in red if the relationship is significant, with the corresponding r value.	243

Chapter One

Introduction

1.1 Background

Today and future fundamental challenges in West Africa (WA) point to the climate crisis and meeting urgent development needs. One of the Sustainable Development Goal (SDG) characteristics is to minimize greenhouse gases release, reduce global warming and preserve natural resources. According to the State of the Climate report of 2019, most of the climate indicators are signalling the critical unfolding threat to the planet's water resources (Blunden and Arndt, 2020). Groundwater-atmosphere related environmental features are severely pressured by climate change and anthropogenic influences. The groundwater depletion, soil degradation and deforestation are flagrant consequences affecting West Africa. Further, transboundary basins authorities in West Africa like Niger River Basin Authority are confronted with data collect irregularity, poor data collect infrastructure and coverage.

It is a global endeavour to preserve the planet, bring down disaster risks, end poverty, and achieve peace and prosperity through the implementation of the 2030 Sustainable Development Goals (SDGs), the Paris agreement, Sendai Framework and the Agenda 2063 (UNFCCC, 2015; UNISDR, 2015; United Nations General Assembly, 2015; AU, 2015). In Africa, among emerged main facts from the Assessment Report 6 (AR6), climate change is reducing food and exacerbating water insecurity, contributing to land degradation, loss of biodiversity (SR1.5, SRCCL, SROCC) and increased deaths related to airborne and waterborne diseases. In addition, under a global warming increase from 1.5℃ to 2℃, West African countries (low and middle-income countries) will witness the largest reductions in economic growth and a further move to 3℃ will make worse the burden of the exposed and vulnerable population (IPCC, 2018c). The adaptative capacity and mitigation options are more than ever required through the sustainable use of natural resources, climate resilience principles implementation, and socio-environmental change scenarios application in decision-making (IPBES, 2018; Shukla *et al.*, 2019). In rapidly growing African cities, these measures for instance can be in form of improvements to early warning systems and access to information about groundwater and surface water drought, recharge and depletion states under climate change and intensive groundwater pumping.

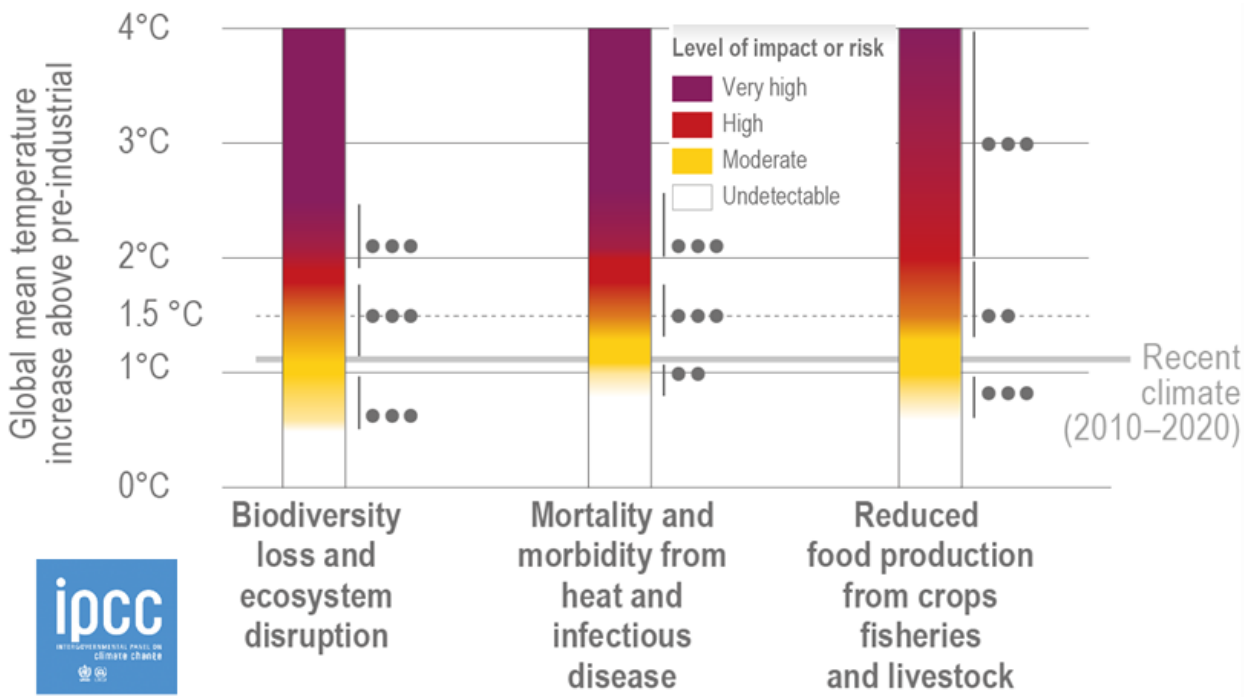

Figure 1.1: Current and projected effects of global warming on biodiversity, food production, mortality and morbidity (IPCC, 2022).

By 2050, the global water-scarce urban population under the business-as-usual scenario (SSP2&RCP4.5) of climate change will reach in average 2.065 billion (He et *al*., 2021). West Africa rapid population growth and its derivative influences on Land Cover Land Use (LULC) and water resources through urban and agricultural water use increase the magnitude of the climate change effects. The year 2050 is projected to witness more than half of global population growth living within the sub-Saharan region (UN, 2019) and water use is forecast to dramatically increase (Wada & Bierkens, 2014). Before the industrial revolution, most groundwater systems were in balance between recharge and discharge, and natural groundwater quality was generally excellent. But increased pressures have been put on groundwater from population growth, agricultural intensification, urbanisation/industrialisation and climate change. In response to these challenges, the global community is expected by 2030 to achieve cheap, universal and equitable access to safe and affordable drinking water for all (SDG 6.1). The focus is also set to provide adequate access and equitable sanitation and hygiene in the vulnerable regions. The two SDGs achievement and evaluation in WA is daunting not only because of insufficient funds but also limited spatial and temporal data offering necessary knowledge about the groundwater to atmosphere systems. The groundwater management first challenge is data availability and Conventional information systems (point data networks) are costly to maintain and is time-spatially limited. There is an unprecedented need for alternative ways to increase groundwater to atmosphere information in WA and groundwater assessment, modelling and reliable understanding require accurate hydrogeological measurements. Since the 1950s, the human-induced climate change is likely the main driver of the frequency and intensity of heavy precipitation events and other water cycle perturbation. Intensification of agricultural and ecological droughts under Human-induced climate change is evidenced in WA due, for example, to evapotranspiration increase. It is even more challenging as observations are sparse at the continental scale and climate models offer coarse spatial resolution and over-simplify the subsurface features. Though many hydrologic models have been developed to assess various water cycle component, the interactions from groundwater to atmosphere under human water use is not well developed in WA. The global community SDGs achievement requires developing innovative scientific tools in WA and the coupled terrestrial systems modelling are indeed an effective way to reach the target.

West Africa's rapid population growth and its impacts on water resources and land cover (e.g., urban and agricultural water use) increase the magnitude of the climate change effects

(Foley, 2011; Bavel, 2013; Bliefernicht et *al.*, 2018; Sy & Quesada 2020; Potapov et *al.*, 2022). The year 2050 is projected to witness more than half of global population growth living within the sub-Saharan region (UN, 2019), and groundwater use is predicted to increase dramatically in this region (Wada & Bierkens, 2014). Moreover, the Intergovernmental Panel on Climate Change (IPCC) reports projected critical state of water availability for the domain (Niang et *al.* 2014) and noticeable uncertainties for instance in runoff projections (Roudier et *al.*, 2014). The resulting uncertainty in flood and drought prediction will tamper with the mitigation and adaptation actions (Hounkpè et *al.*, 2022; Ogunjo et *al.*, 2023). Therefore, continual efforts for improving the representation of the land surface processes are required for flood and drought prediction modeling systems.

To reduce the uncertainties in water and energy fluxes simulation, it is generally suggested that both the representation of subsurface and land surface components should be improved (Lahmers et *al.*, 2019). For instance, the feedback effect of soil moisture on precipitation through regional precipitation recycling is well documented as proof of the land surface interaction with the atmosphere (Hsu et *al.*, 2017; Wei & Dirmeyer, 2019). The global circulation models employed to evaluate the soil moisture potential impact on large-scale atmospheric circulation confirmed the need to adapt the model structure to better capture the dominant climatic and hydrological conditions (Berg et *al.*, 2017). At regional scale, the interactions between land and atmosphere can be captured in finer detail with the Weather Research and Forecasting – Hydro model (WRF-Hydro) modeling system, as demonstrated by evaluation studies using the precipitation (e.g., Arnault et *al.*, 2021; Quenum et *al.*, 2022), runoff (e.g. Arnault et *al.*, 2016; Naabil et *al.*, 2017), and soil moisture (Zhang et *al.*, 2024) in data-scarce areas. The integration of lateral terrestrial water flow to enhance the WRF-Hydro code in past studies (e.g. Zhang et *al.*, 2019) resulted in increased soil evaporation and soil moisture which directly affected the simulated water balance. For instance, the application of a tagging procedure using WRF-Hydro to track moisture in the water cycle showed that the consideration of lateral terrestrial water flow slightly increases the regional precipitation recycling (Arnault et *al.*, 2019; Zhang et *al.*, 2019). These findings demonstrated that the endeavor to represent in detail the hydrological processes at the local scale can alter the model precision.

The land surface representation in land surface models (LSMs) and its interactions with the atmosphere is widely explored and reported but pertaining to its responses and connections with the lower part of the Earth system (e.g., subsurface), noticeable progress is required

especially in data-scarce areas. Despite the advance in the atmospheric and land surface models coupling for water and energy fluxes simulation, the lower boundary description and implementation are roughly detailed with arguable assumptions and foreseen biases in the models' results. In a prolonged dry season, water fluxes from groundwater sustain the soil moisture and the evapotranspiration (ET) in a limited solar radiation area of Danube's River basin (Rummler et *al.*, 2022). Although the contribution of subsurface water fluxes to surface water availability in this particular area is relatively low (<2%), this contribution may increase drastically in a water limited area such as the West African Sub-Saharan region. The West African climate characteristics have been evidenced in terms of energy balance (Quansah et *al.*, 2017; Wanner et *al.*, 2022, 2024), water budget (Schuol et *al.*, 2008; Galle et *al.*, 2015), groundwater potential (Oussou et *al.*, 2022) and various energy and water-related variables, but the question regarding how the change of the subsurface dynamics at large scale influence the fluxes at the land surface and in the soil is yet to be thoroughly investigated.

It is demonstrated in an energy-limited area that streamflow simulation using an improved hydrological model Weather Research and Forecasting – Hydro model (WRF-Hydro) with a 2D groundwater scheme performs better compared to a simplified subsurface and free drainage scheme (Rummler et *al.*, 2022). This evidence evaluation is fairly required for the present study area because of the peculiar usefulness of the improved scheme to provide further accuracy in the water and energy simulation. The interactions between water, and energy components are better highlighted with detailed descriptions of the lower boundary and the development of more effective tools (Fan et *al.*, 2007; Miguez-Macho et *al.*, 2007; Miguez-Macho et *al.*, 2008; Fan & Miguez-Macho, 2010; Niu et *al.*, 2011; Miguez-Macho & Fan, 2012; Barlage et *al.*, 2015, 2021; Martinez et *al.*, 2016). Two-way feedbacks between soil moisture and groundwater table are demonstrated in some cases (Ajami et *al.*, 2011; Atchley & Maxwell, 2011; Condon & Maxwell, 2014; Furusho-Percot et *al.*, 2019). The advantages offered by these LSM improvements are critically needed to diminish the discrepancies associated with understanding and closing the water and energy budget in data-scarce areas.

There is a handful of approaches available to further improve groundwater processes in climate and hydrological models (Sulis et *al.*, 2017, 2018) varying from computationally less expensive and column-based (1D) approaches (Niu et *al.*, 2011) to distributed lateral flow integration (medium complexity, Miguez-Macho & Fan, 2012) and variably saturated groundwater models (3D) such as Parflow (Condon & Maxwell, 2019). The model configuration

adopted in each of these studies is defined by the level of complexity, the resolution (spatial and temporal), and the coverage (global, regional, and local). While a 3D representation of the Earth system is computationally achievable and efficient at a local scale to solve a particular hydrological problem, a one-dimensional model can offer timely results for a larger scale. Notwithstanding that argument, the improved LSMs increase the accuracy of the simulation of the soil moisture (Wagner et *al.*, 2016; Forrester & Maxwell, 2020), evapotranspiration (Koirala et *al.*, 2014; Martinez et *al.*, 2016), and runoff (Batelis et *al.*, 2020; Rummler et *al.*, 2022). The above-cited studies justify the attempt to achieve reliable accuracy in groundwater dynamics representation with a dedicated land surface hydrological model such as WRF-Hydro.

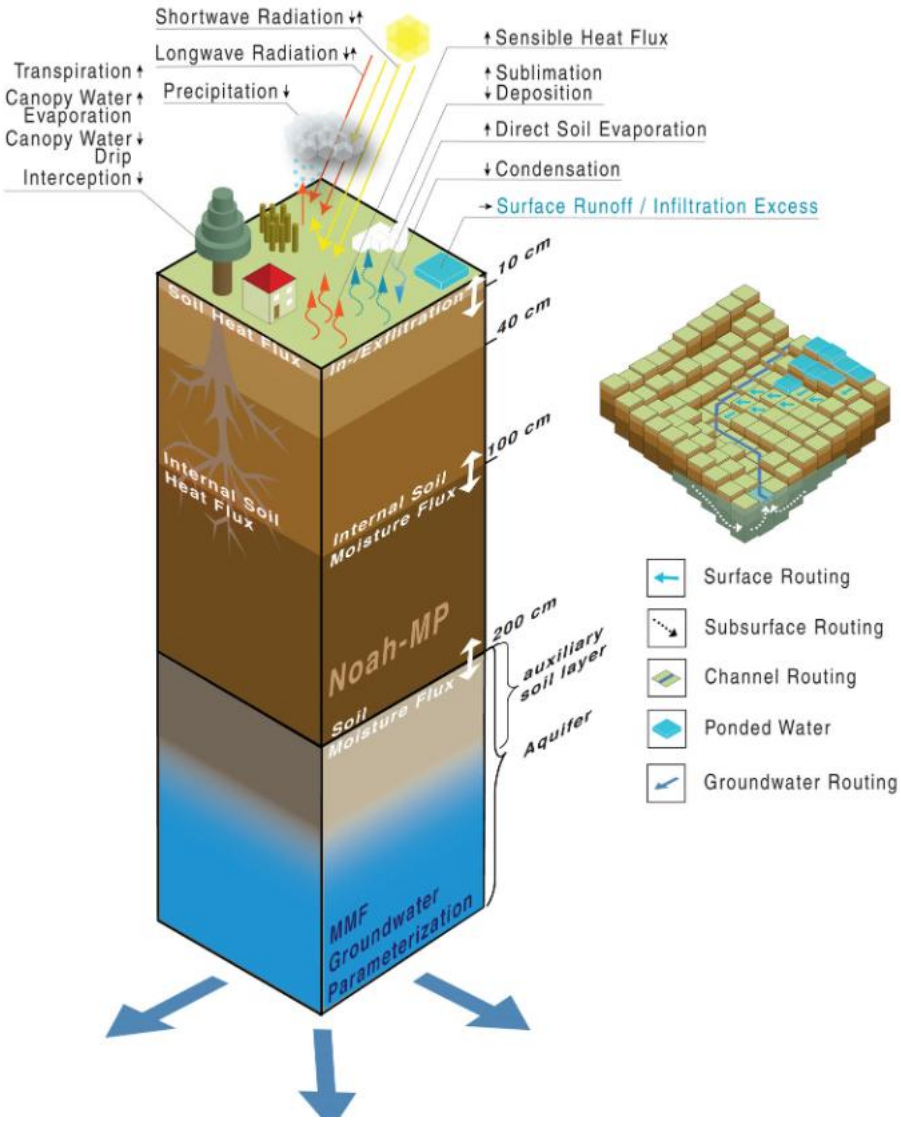

Figure 1.2: Soil column of the Noah-MP LSM with MMF groundwater parameterization and WRF-Hydro routing extensions (Rummler et *al.* 2022).

1.2 Problem statement and research question

The land surface of the Earth system is widely recognized as an intermediary interface connecting subsurface and atmospheric processes through the exchange and storage of water, energy, and carbon fluxes. Supported by extensive field measurements, Land Surface Models (LSMs) provide a confident representation of natural phenomena and anthropogenic impacts at the Earth's surface, influencing global climate policy decisions over recent decades. Despite these hurdles, substantial progress has been made in elevating awareness of climate change, backed by two key pieces of evidence. First, Sellers et al. (2007) demonstrated that plant biophysical responses to increased CO2 can have a significant impact on the global climate. Second, Cox et al. (2000) showed that the coupling of climate and carbon cycles has accelerated global warming rates. Additionally, the interconnected questions that LSMs aim to address—such as groundwater properties representation, feedbacks with the unsaturated zone and atmosphere, responses to intensive pumping, and climate change effects—further complicate these challenges (Fisher & Koven, 2020). While advancements in computational power and the availability of new datasets have enhanced LSM spatial resolution (Wood et al., 2011), epistemic uncertainties and unresolved heterogeneity continue to influence model outputs. Furthermore, the task of accurately capturing subsurface processes and linking them to surface dynamics, climate change evidence, carbon fluxes, and human activities (e.g., water supply and agriculture) remains both critical and complex for sustainable resource management.

Groundwater (GW) systems, together with surface reservoirs and flow controls, regulate and redistribute water resources between highly wet and water-scarce areas in a seasonal pattern. This buffering function helps mitigate the impacts of climate change and human activities by maintaining relatively stable outflows from land water storage. However, studies by Genereux et *al.* (2013) and Ma et *al.* (2014) connected fluctuations in groundwater levels to ecosystem shifts between carbon sinks and sources. Reliable evaluations of groundwater quantity and travel time responses to climate forcing under changing conditions have been reported (Jing et *al.*, 2020). These findings underscore the necessity for intensified research, especially in Western Australia, to understand how persistent groundwater level declines influence the carbon cycle and local warming through changes in groundwater-dependent ecosystems. Prediction of groundwater level variations has improved through training hydrosphere variables (e.g., soil moisture, vegetation water content, rainfall) and atmospheric predictors (e.g., humidity, atmospheric boundary layer, ENSO, AMO) using machine learning and deep learning techniques, revealing

significant results (Koster & Walker, 2015; Oussou et *al.*, 2022). Although subsurface flows tend to be relatively stable, exchanges between groundwater and the atmosphere (G2A) are non-negligible (Condon et *al.*, 2021), with feedback effects—sometimes delayed—impacting both water and energy components (Maxwell & Kollet, 2008; Erler et *al.*, 2019; Sorensen et *al.*, 2021). In addition, the link between climatic variability and bidirectional feedbacks and groundwater responses remains a significant research question (Jing et *al.*, 2020). Improved documentation and assessment of these dynamics would enhance understanding of groundwater system sensitivity to land surface processes.

It is arguably accepted that the main recharge process for groundwater replenishment in the West African region is diffuse recharge through which the rainfall and/or surface water reservoirs move slowly downward in form of moisture fluxes. The change in these fluxes influences the groundwater reservoirs and can be arguably related to the prevailing climatic condition at a given time and in response to climate change (Li et *al.*, 2021). For large scale groundwater system assessment in WA, although the increase in potential recharge under future climate conditions is evidenced (Cook et *al.*, 2022) at a relatively low horizontal resolution (25 km), it still requires thorough evaluation of climate change and anthropogenic impacts using different global climate models and LSMs. For instance, regional initiatives such as the Great Green Wall (GGW, Smiatek & Kunstmann, 2023) and the extreme climate events are significant scenarios to test for improved understanding of diffuse recharge and informed decision making. The diffuse recharge is the infiltration directly to the unconfined/semi-confined groundwater system which is in contact with the planetary boundary layer. As the rainfall is for the land surface processes, it is a primary factor in the subsurface fluxes and defines the groundwater sustainability and potential.

Both the weather and climate at local and regional scale are sensible systems where extreme events (e.g. flood and drought) can drive the subsurface-land-atmosphere interactions. Sustaining agriculture, water supply and living condition in dry areas demand thorough evaluation and prediction of the components of the terrestrial hydrology and their links with energy and carbon fluxes. For instance, the latent heat of vaporization connects the water and energy budgets and defines the evapotranspiration (ET) which contributes to the rainfall for more than 60% (Wei et *al.*, 2017). Berger et *al.* (2019) demonstrated in contrasting ecosystems of a semi-arid savanna (WA) that rain events can trigger carbon sink or release based on the land use characteristics. The land surface transpiration related to the vegetation represents close to 80% of

the total evaporation (Schlesinger & Jasechko, 2014). Regarding the water and energy cycle exchanges, the combined effects of the vegetation dynamics on the land-atmosphere feedback are significant (Suni et *al.*, 2015). With the reported changes in the temperature and extreme events, the evapotranspiration is prominently limited by water availability (Hosseini et *al.*, 2022) while plants carbon sink/release is mainly driven by the combined energy and water rates in the ecosystem (Zhang et *al.*, 2021). Major fluxes two-way exchange between the land surface and the atmosphere are better captured with the coupled hydroclimatic models' validation with field measurements and remote sensing products.

The simulation of groundwater-soil moisture-atmosphere fluxes exchange in the sub-Saharan climatic condition is a relevant scientific question that has not been extensively documented to enrich the scientific debate on climate change. Many models coupling (ex, ARPS, WRF-WRF Hydro, PARFLOW-CLM-COSMO, PARFLOW-WRF) are undertaken to relate the boundary layer development to surface-subsurface processes (Sulis et *al.*, 2017), assess spatial and temporal latent heat connections with lateral surface and sub-surface flow in a three dimensions condition (Rahman et *al.,* 2015. Shrestha et *al.*, 2014), evaluate soil moisture sensitivity and lateral flow influence in maintaining the surface process and boundary layer (Reed et *al.*, 2007) and the relationship of soil moisture dynamics with sub-surface lateral flow (Zhao et *al.*, 2021).

Based on the aforementioned evidence, this study attempts to answer the following research question:

i) Does the parameterization of subsurface flow dynamics control the energy fluxes and water cycle in data-scarce areas like West Africa (WA)?

ii) Do idealized afforestation experiments modify the patterns of water and energy cycles, especially in the Sahel region, improve the water restoration for ecosystem sustainability, and reduce the land warming effects?

iii) Will climate projections (e.g., Temperature and Precipitation) under the Shared Socioeconomic Pathways (SSP1-2.6, SSP5-8.5) affect turbulent fluxes and subsurface dynamics at the local scale?

iv) Does water table dynamics offset the seasonal variability of the greenhouse gas emissions (e.g., CH_4, N_2O, CO_2) in contrasting land use types under the Sudanian climatic conditions, and what are the primary environmental drivers regulating CH_4 and N_2O fluxes across these systems?

1.3 Aim and Specific Objectives

The aim of this study is to ascertain the groundwater-atmosphere interactions and controls on water, energy, and greenhouse gas fluxes over West Africa.

The specific objectives are to:

1. evaluate land surface water and energy fluxes responses to subsurface parameterizations;
2. determine the effects of vegetation dynamic schemes and land use changes on the water and energy fluxes;
3. assess the sensitivity of the surface turbulent fluxes to different warming scenarios; and
4. evaluate the effects of hydrological parameterizations on N_2O, CH_4, and CO_2 fluxes in a coupled system.

1.4 Innovation

This study evaluates the potential of the WRF-Hydro model in representing subsurface processes (e.g., water table) over West Africa, as the previous deployment of the model in the region did not focus on this particular aspect. It assesses the model calibration using regionalized parameterization (e.g., REFKDT, OVROUGHRTFAC) and ascertains its performance multi-source dataset. Different idealized afforestation experiments are undertaken to evaluate for the first time their impacts on water table depth, storage, and subsurface flow in the Sahel.

Moreover, an underground boundary dataset (Depth-to-bedrock) is produced for the continent and validated using the integrated hydrological model Parflow-CLM. The signal of the geological lineaments (e.g., fractures) in the fluxes at the land surface is evaluated for the first time at the local scale. The effect of Climate projections under SSP1-2.6 and SSP5-8.5 on

subsurface dynamics of the Donga basin is assessed. The spatial and temporal dynamics of major greenhouse gas fluxes to water table dynamics are assessed using the JULES-Microbe model.

1.5 Structure of the thesis

The structure of this thesis is partitioned into five chapters. The general introduction and statement of problem include the overview of the research question tackled in this study (Chapter One). The aim and objectives, and innovation achieved are displayed in the same chapter. In Chapter Two, the current state-of-art of the literature on the topic is presented succinctly with a review of relevant thematics like Groundwater-Atmosphere modeling, model parameterization and coupling, and water, energy, and greenhouse fluxes. This is followed by the description of the methodology, data collect, and study domain presented as Chapter Three. Chapter Four covers the results/findings obtained in this thesis with the discussions. In Chapter Five, the conclusion and limitations of the study are provided with the perspectives and foreseeable research questions as follow up.

Chapter Two

Literature Review

2.1 Definition of some concepts

2.1.1 Water cycle

The movement of water within the Earth's systems follows a complex path, linking land, atmosphere, and ocean through processes such as precipitation, evaporation, condensation, infiltration, and others. The continuous circulation of water in its various forms (e.g., liquid, solid, and gas) sustains life on Earth, whether animal or vegetal. Water droplets fall on the ground through rain and snow, evaporate into water vapor, which condenses to form clouds in the atmosphere. Water is transported by wind in its gaseous phase, flows on the land surface as runoff, goes into the ground as infiltration, and provisions underground reservoirs as groundwater. Stored in soils and biomass, water is labeled green water, sustaining plant and microbial activities. Blue water is readily available, underground or surface water found in rivers, lakes, and groundwater system, mainly exploited for human activities like agriculture and drinking water supply.

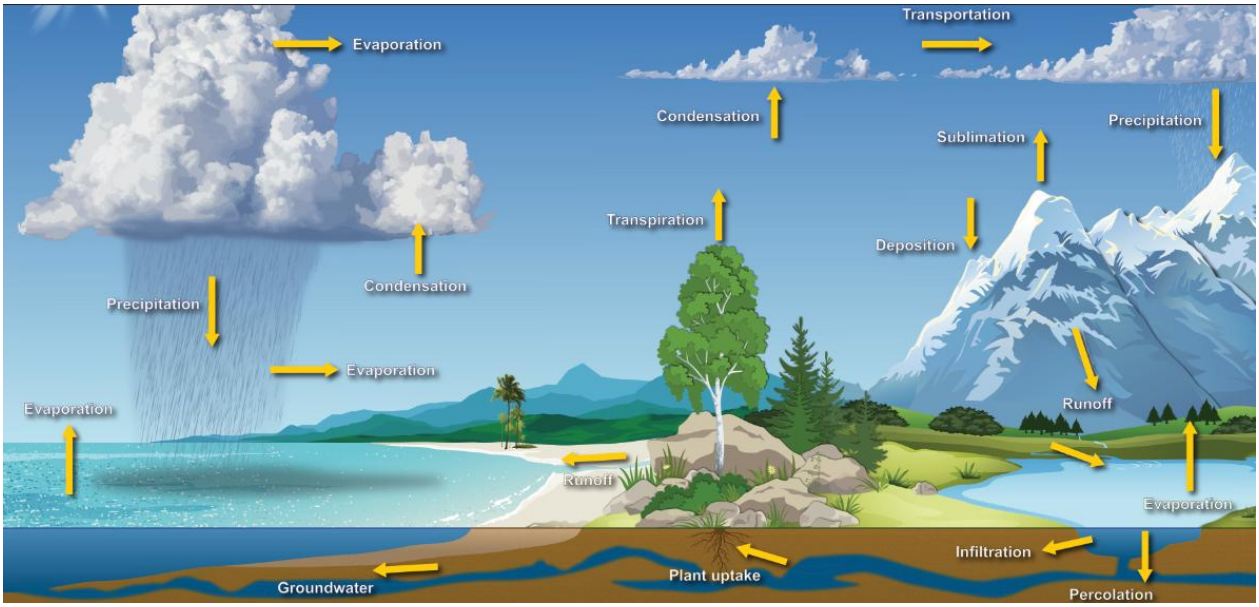

Figure 2.1: Water Cycle (Image credit: Dennis Cain/NWS)

2.1.2 Energy fluxes

The incoming shortwave and longwave radiation heat the Earth's surface, which reflects part of the energy and emits the absorbed radiation in longer wavelengths (e.g., infrared). The net radiation from the land-atmosphere interaction is partitioned into three components (Fig. 2.2). As the primary determinant of surface climate, the latent heat, sensible heat, and ground heat define the energy balance in the boundary layer in response to energy gained from the solar radiation. The magnitude of the energy balance components changes according to soil water availability and incoming solar radiation, which in turn depend on the geographical location. Both diurnal and annual cycles of solar radiation are reflected in the energy partitioning throughout the day and year. The relationships between the turbulent fluxes (latent and sensible heat), surface temperature, and net radiation are demonstrated in the Penman-Monteith equation (Forster et *al.*, 2021). The exchange of heat, also known as convection, occurs with the wind directions: eastward (zonal) and northward (meridional). Major energy movement at the top of the atmosphere (TOA) controls the energy budget of the climate system. Recent studies highlighted the Earth's energy imbalance as a result of anthropogenic actions on the global mean TOA radiation budget (Schuckmann et *al.*, 2016). The disruption of the TOA energy budget in terms of the change in the magnitude of the incoming and outgoing radiation is a major factor affecting the state of the global climate.

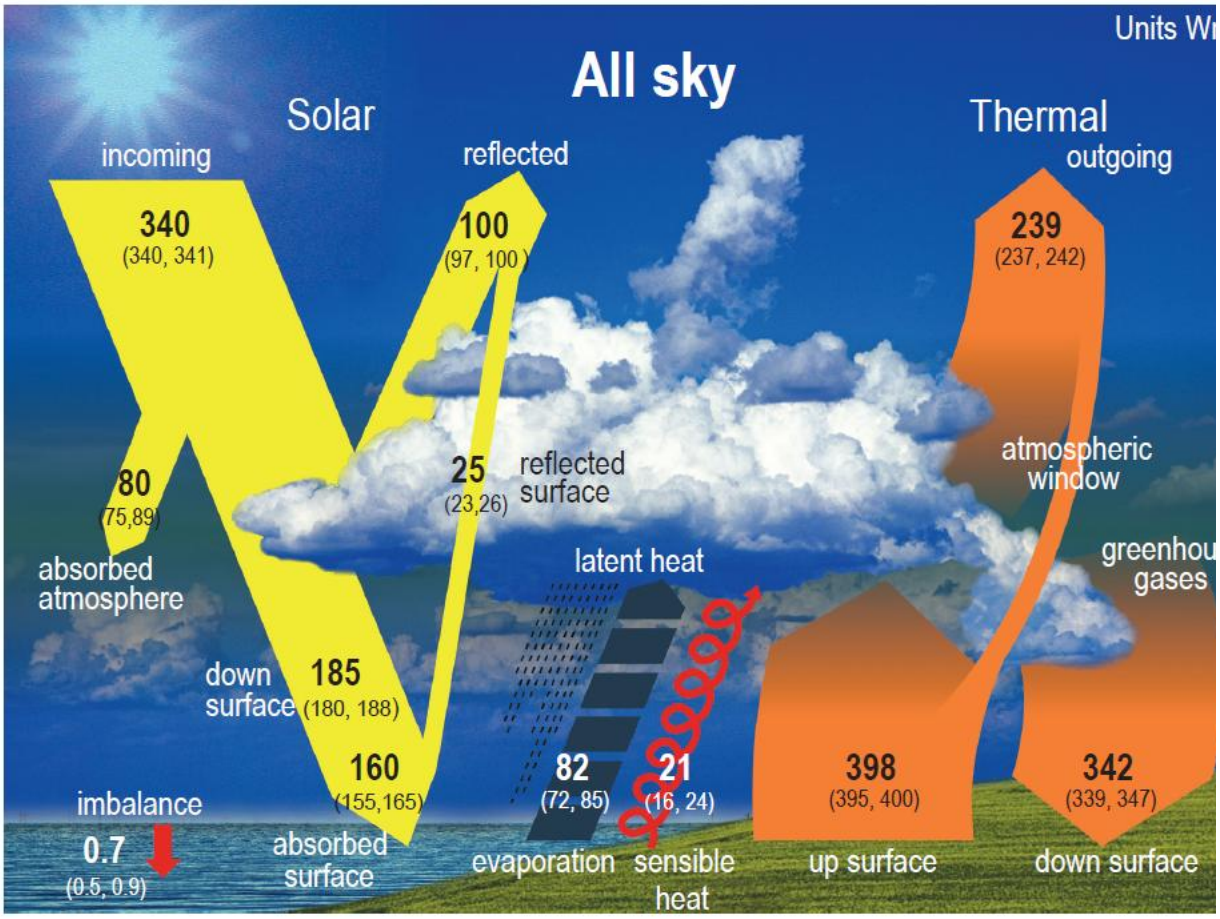

Figure 2.2: Global mean energy budget. From Wild et *al.* (2015, 2019) in Forster et *al.* (2021).

2.1.3 Earth System Modeling

The dynamic processes of the Earth System are numerically simulated and predicted to ascertain past, present, and future behaviors in the atmosphere, land, ocean, and ice using Earth System models (ESMs, Fig. 2.3). The models represent quantitative and discrete descriptions of geophysical fluid dynamic processes executed with high-performance computers to understand the climatic and environmental systems (e.g., hydrosphere, atmosphere, biosphere, lithosphere, cryosphere, and anthroposphere). The physical processes are estimated using parameterization schemes by approximation of reality with empirics, heuristics, phenomenological laws, and closing assumptions (Pan et *al.*, 2025). Models are developed to solve fluid dynamics in sub-systems in standalone mode and coupled to address peculiar scientific questions in terms of long-term and immediate state and trend in the Earth system. Numerical solvers are improved to reduce oversimplification of subsystems like groundwater in ESMs and produce accurate replica of the Earth system (Li et *al.*, 2023). Nevertheless, the caveat is higher complexity in models' resolution can lead to unforeseen discrepancies due to poor parameter tuning or coupling. Beyond the skills of Global Climate Models (GCMs), pertinent elements of the Earth System is better captured with detailed mathematical approximations of fluid dynamics in the components. Whether present or future climate system is illustrated with these models to assess climate change effects in Earth spheres. The analysis of the interactions between the simulated processes adds an invaluable advantage in understanding the causality effects and feedbacks between the Earth's components. Many studies have evidenced the undeniable role of ESMs in improving human understanding and decision-making, like raising awareness on current global warming, drought, and flood (Zhou et *al.*, 2022, Steffen et *al.*, 2020; Kawamiya et *al.*,2020).

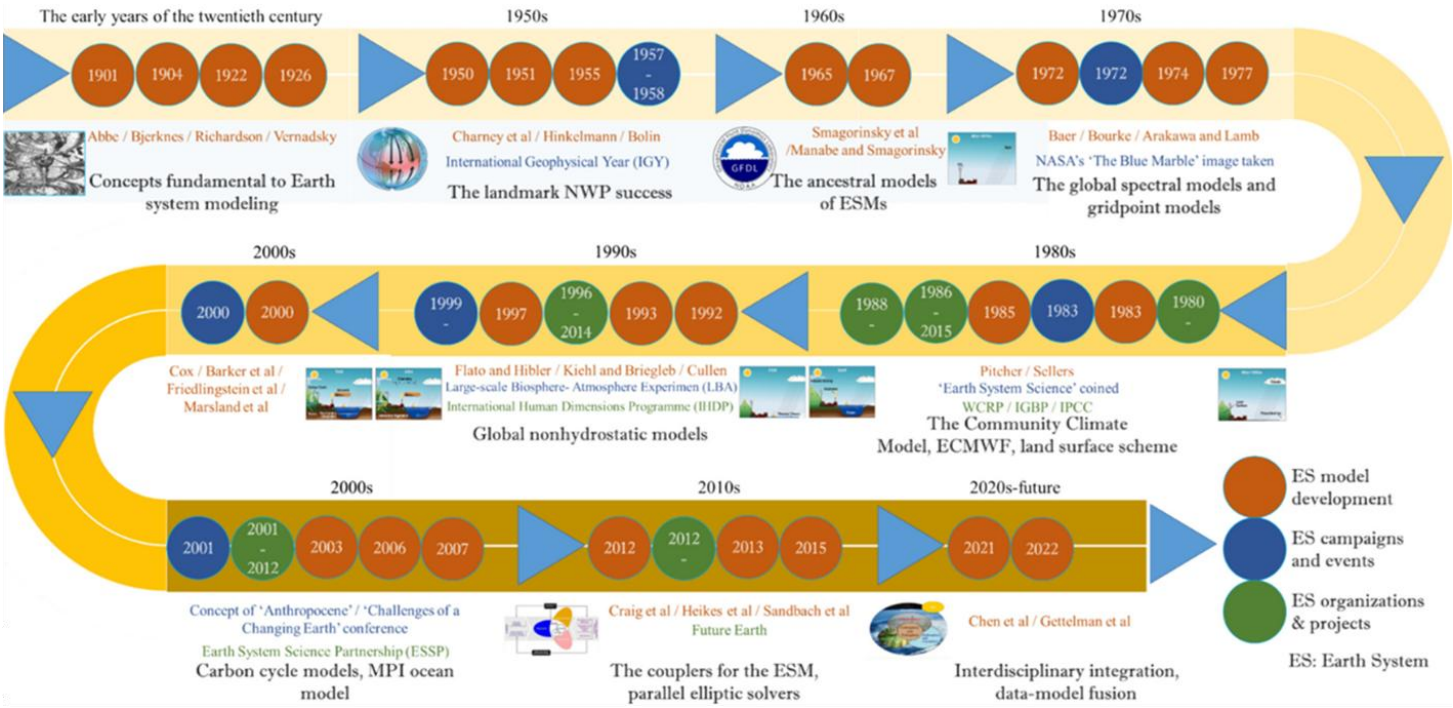

Figure 2.3: Progress of the development of Earth system models over last one-hundred year (Pan et *al.*, 2025).

2.1.4 Climate Change Impacts on Groundwater

The increase in water demand in response to population rise has triggered groundwater depletion in highly populated areas. However recent studies have evidenced the persistent dry-down in groundwater recharge and levels (Liesch and Wunsch, 2019; Wunsch et *al.*, 2022) under climate change. The variation of precipitation and temperature in a changing climatic condition has altered land-atmosphere interactions, groundwater flows, quality and discharge (Alam et *al.*, 2019). According to IPCC report on groundwater (IPCC, 2007), the knowledge of recharge is yet to be thoroughly enriched. The potential impact of climate change on groundwater still has a long way to clarify the potential changes in groundwater-surface water interactions that might occur. Nevertheless, some mitigated evidences are provided on the scientific question. For instance, groundwater recharge is projected to decrease significantly by more than 70% in south-west Africa, along Mediterranean Sea (southern rim), and north-eastern Brazil under four climate scenarios between 2050s and the historical period of 1961-1990 (Döll and Flörke, 2005; IPCC, 2007). In contrary, an increase of more than 30% is projected for the western USA, the Sahel, Siberia, northern China, and the Near East. Using JULES model with recharge estimated as soil drainage from a 3 m deep soil column, Cook et *al.* (2022) projected an increase of groundwater recharge by 1 to 20% of the rainfall in response to RCP8.5 by year 2100 with areas like eastern Sahel and northern Ghana reaching 2-fold compared the reference (2000). Further, increased evapotranspiration under global warming is likely to enhance saltwater intrusion into coastal groundwater systems and sea-level rise by just 0.1 m can reduce freshwater lens by 8m (Bobba et *al.*, 2000).

2.2 Groundwater-Atmosphere interactions

The land surface in the Earth system plays a well-documented intermediary role, facilitating the exchange and storage of water, energy, and greenhouse gases between subsurface and atmospheric processes. Supported by field observations, land surface models (LSMs) have become reliable tools for simulating both natural processes and human-induced changes at the Earth's surface. These models have significantly influenced global climate change policies over recent decades. LSMs have been widely used to assess Earth system states and fluxes at both global and regional scales. However, as highlighted by Fisher and Koven (2020), they continue to face three primary challenges: managing the complexity of processes, representing spatial

heterogeneity, and understanding dynamic parameters. Despite these limitations, LSMs have contributed greatly to raising global awareness of climate change, supported by two key findings: (1) that plant biophysical responses to elevated CO_2 can substantially affect global climate (Sellers et al., 2007), and (2) that coupling between climate and the carbon cycle accelerates global warming (Cox et al., 2000).

The interconnected nature of the questions that LSMs aim to address adds to their complexity (Fisher & Koven, 2020). This is especially true when incorporating groundwater (GW) dynamics. GW systems involve diverse physical and chemical properties, interactions with the unsaturated zone and atmosphere, responses to intensive groundwater extraction, and sensitivity to climate change, all of which expand the scope and complexity of LSMs. Although advancements in computational power and new datasets offer opportunities to improve the spatial resolution of LSMs (Wood et al., 2011), unresolved epistemic uncertainties and subsurface heterogeneity continue to limit model accuracy. Capturing subsurface processes and linking them to surface dynamics, climate change indicators, carbon fluxes, and socioeconomic factors (such as agriculture and water supply) remains a formidable but essential task for sustainable and forward-looking resource management. The demand for integrated global groundwater representation in Earth system models is growing, yet the specific GW properties to be included and the methods of their integration remain poorly defined due to the intrinsic complexity of groundwater systems. GW properties are generally categorized into hydrodynamic, chemical, and isotopic groups.

However, estimating groundwater storage (GWS) and fluxes from space—at scales ranging from tens to thousands of meters—has long been hampered by coarse spatial and temporal resolution, data uncertainty, and a lack of field-based validation, making satellite-derived GWS unreliable for critical decision-making. This issue is especially problematic in densely populated and rapidly developing regions, where the demand for accurate, up-to-date observations is urgent. Continued failure to meet these expectations could significantly compromise decision-making by stakeholders in the water sector. Moreover, the term "groundwater storage" (GWS) as used in remote sensing often oversimplifies the geometry and hydrodynamic behavior of groundwater systems—particularly those at greater depths. As noted by Miguez-Macho and Fan (2012), this oversimplification fails to capture the horizontal and vertical flows in layered aquifer systems, and their feedbacks with land surface processes.

2.3 Improving subsurface parameterization for Groundwater-Atmosphere modeling

The Earth systems' fluxes beneath the land surface represented by lateral flows are what characterize subsurface dynamics, and the simulation of these processes using bucket-type models encounters failure. Jing *et al*. (2018) summarized some of the limitations, mentioning the inseparable errors in GW storage and head estimation, thus in their feedbacks on land surface processes. Not only that, these issues are attributed to the layered groundwater systems' heterogeneity oversimplification and the absence of any possibility to account for solute transport and retention (Benettin *et al*., 2017; Van Meter *et al*., 2017) which consequently hinder the improvement of understanding about climate change impacts on groundwater resources. As the Earth's subsurface complexity relies upon mainly its heterogeneity (3D varying quantity and quality) and types of sources and sinks, partial differential equations (PDE) models have been developed since decades to capture and solve both the steady and transcient states of underground flows. One basic principle about the PDE-based models is that computations are defined by the spatial gradients of the primary variable. A summary overview of these codes starting from early 2000 indicates models such as ParFlow (Maxwell & Miller, 2005; Maxwell & Kollet, 2008), tRIBS (Ivanov *et al*., 2004) InHM (VanderKwaak & Loague, 2001), OpenGeoSys (Kolditz *et al*., 2012), CAST3M (Weill *et al*., 2009), PIHM (Qu & Duffy, 2007; Kumar *et al*., 2009), CATHY (Camporese *et al*., 2010), HydroGeoSphere (Hwang *et al*., 2014), MODHMS (Panday & Huyakorn, 2004; Phi *et al*., 2013), GEOtop (Rigon *et al*., 2006), IRENE (Spanoudaki *et al*., 2009), and PAWS (Shen & Phanikumar, 2010) in Jing *et al*., (2018). Nevertheless, groundwater simulation methods are grouped into variably saturated flow models (e.g. Parflow), saturated flow models (e.g. MODFLOW), steady state models, and Quasi-3D models (e.g. LSM and ESM). The unsaturated zone near surface flows are vital for species reproduction at the surface (e.g. Root water uptake) and food production (e.g. Soil humidity and nutrients) however their simulation accuracy using PDE-based models is reported to be less reliable (Paniconi & Putti, 2015). The attempts to resolve this issue, improve both spatial and temporal resolution, and lower outputs uncertainties are what in fact have resulted into the models' complexity and higher computational time. Though, it is arguably accepted that groundwater flow modelling should consider some key factors at stake for good results namely capture the 3D flow whatever the scale and resolution, account properly for land surface and overland flow processes, represent and connect shallow and deep groundwater systems, and the withdrawal for human activities. Recent studies have agreed on the undeniable need to bring together models' specific capabilities whether to simulate

saturated groundwater flow, water flow in the unsaturated zone, near surface quick flow, and overland flow in a coupled way across scales at the surface water-groundwater interface (e.g. Parflow-CLM, GSFLOW, PCR-GLOBWB-MOD, CP v1.0, and mHM-OGS). An impeding scientific question is to elucidate the available coupled models' regional suitability or skillfulness in areas like the Sub-Saharan region. In addition, how can they be integrated in water resources management at the local scale and how useful are they in decision making?

Adding to the global efforts to implement more realistic hydrological models, de Graaf *et al*. (2020) argued that GW systems representation at a larger-scale should be evaluated based on how well groundwater systems' properties are captured. The achievement of this target is even urgent and will be beneficial because of the multiple advantages displayed by GW resources ranging from sustaining the land surface processes (e.g. River flow, evapotranspiration, wetlands) (Maxwell & Condon, 2016; de Graaf *et al*., 2019) to soothing the global warming effects on the water budget (Schaller & Fan, 2009), and providing a reliable water quality. The reconciliation of the aforementioned desire (Gleeson *et al*., 2014) with the demand of higher spatial resolution is not without repercussion on the computational time. Nevertheless, the accurate simulation of key groundwater systems' properties namely the hydraulic head, lateral flow, and storage change is at stake for informed GW management and planning, and large-scale hydrogeological assessment (Krakauer *et al*., 2014). Recent works have recognized the gridded data GLHYMPS (Gleeson *et al*., 2014) as the most reliable for large-scale groundwater systems permeability (de Graaf *et al*., 2020) however concerns have been raised about inconsistencies in low permeability values of sedimentary basins (de Graaf *et al*., 2019; Reinecke *et al*., 2019) but this is out of this study's scope.

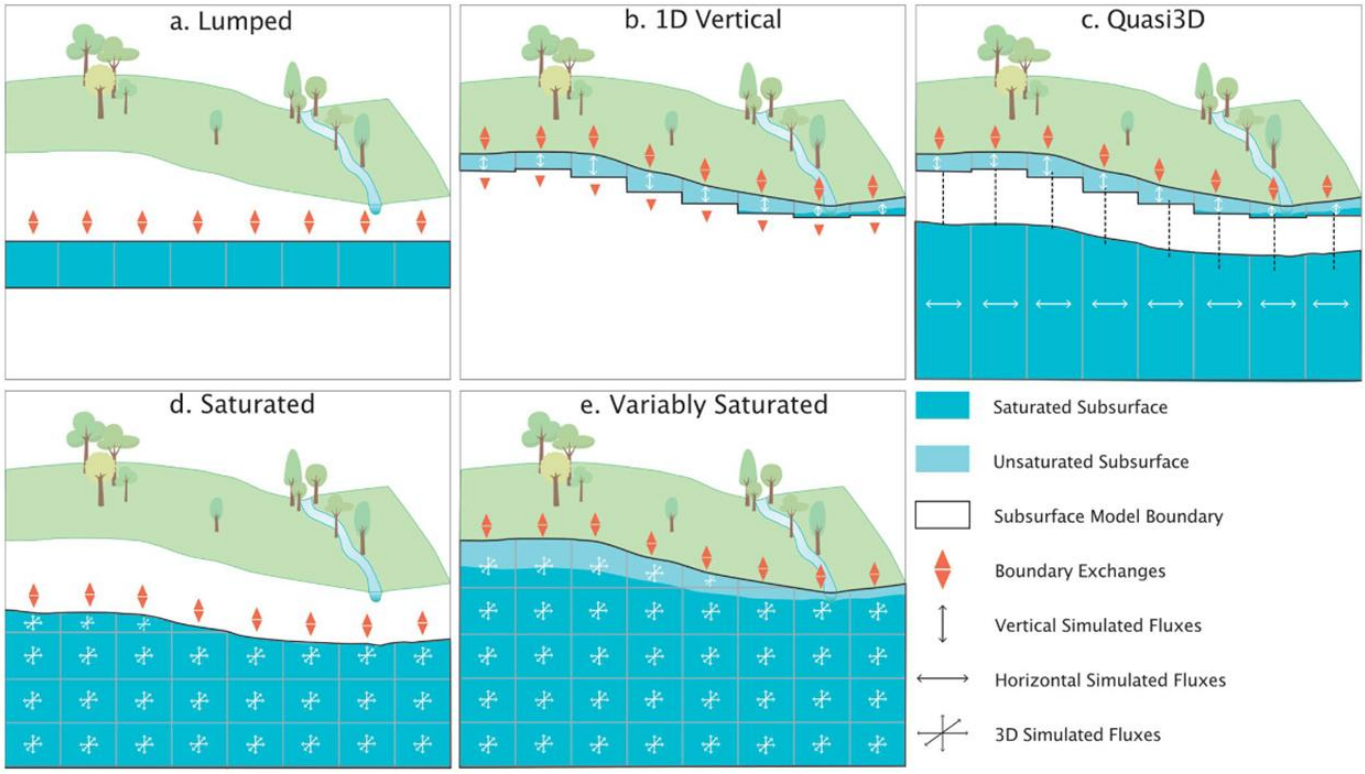

Figure 2.4: Comparison of Groundwater Simulation Methods in Continental and Global Models (Condon et *al.*, 2021).

2.4 Coupling Groundwater-Atmosphere for higher accuracy in modeling

In recent years, the long-time overlooked and hardly imaginable term "groundwater-to-atmosphere climatology" has been brought to the scientific community's attention and simulated over Europe (Kollet et *al.*, 2018) with very significant outcomes, breaching the long-time barrier between groundwater and Atmosphere experts and bolstering climate forecasts. Many works undertaken over WA attempted to relate various subsurface features to the atmospheric dynamics (Taylor *et al*., 2009), but the urgency to provide a spatially and temporally uniform assessment is more than ever felt, especially under the ever-growing water need in highly populated areas and climate change. Bloshl *et al*. (2019) laid down 23 unsolved questions in hydrology, and Condon *et al*. (2021) seven critical groundwater-related which serve as background to the following: (i) which properties representation is relevant for human water demand satisfaction and sustainability? (ii) How can they be implemented accurately in a global/continental/regional model? (iii) How to fatten the nationally standardized hydrogeological data collection frontiers for a uniform and widely accepted GW model? (iv) Depending on the primary and secondary porosity intermittence which separate hard-rock GW flow from sedimentary and karstic terrains, how do we capture natural hydrogeological frontiers complexity avoiding the pitfall of just reducing the spatial resolution? (v) How do we bring together the historical need for accuracy in Hydrology and global/continental/regional models relatively coarse resolution issue? A successful global/continental/regional hydrogeological model parameterization is the first main required achievement and is for great interest. This involves making sure that according to the geological structure and properties the 3 types of system namely low-permeability (low-K), high-permeability (K) and sedimentary systems are well represented. (vi) In low-K and high-K, how passive and active Remote Sensing fractures/lineaments mapping can improve the hydrogeological model parameterization? (vii) how remotely sensed land subsidence or displacement in response to intensive groundwater systems' pumping can be represented or add to the hydrogeological model parameterization? A comparative analysis is required and a well-documented and accepted coupled models should be retained before the development of the suggested Global Groundwater Platform (Condon *et al*., 2021) (viii) Which coupled models for accurate and effective subsurface storage and fluxes simulation through Groundwater-Atmosphere modelling?

The climate variability in form of CO_2 concentration in the atmosphere is reported to be irreversibly influenced and its annual flux quantification and related equivalent emission to the

atmosphere is arguably matched between sources and sinks (Liu & Dreybrodt, 2015). One of the most important and well explored effects of climate change since decades is the alteration in the land to atmosphere components of the regional hydrologic cycle and the feedbacks on GHG (eg. carbon release). However, the subsurface storage loss whether caused by the storage change seasonality or human induced removal is proved and labelled in recent years as a long time overlooked and significant source of atmospheric carbon dioxide (Wood & Hyndman, 2017) with an estimated global groundwater depletion from two sources of 145 km3/yr (Konikow, 2011) and 189 km3/yr (Wada, 2016) corresponding to emitted carbon dioxide of 9.7 and 13.5 MMT. The storage anomaly when it dwells persistently in the negative quadrant, induces a net flux of released CO_2, which is reported to be greater than at least seven of the 23 major sources identified by the United States Environmental Protection Agency (US EPA). Further, the groundwater discharge to the land surface into lakes, rivers, wetlands, etc, releases high concentrations of bicarbonate (HCO_3^-), which in contact of the ambient temperature releases CO_2 due to the re-equilibrium of CO_2 (Wood & Hyndman, 2017). Many studies on groundwater quality in West Africa have proved (Houéménou et *al.*, 2020) the relatively significant concentration of bicarbonate (HCO_3^-) depending on the type of groundwater systems but its contribution to carbon release is yet to be constrained using both in situ and satellite-based measurements. In fact, the satellite products offer a unique possibility to evaluate at large scale groundwater depletion induced carbon release at a relatively higher resolution.

2.5 Linking GW-controlled land cover change to water, energy, and greenhouse gas fluxes

Human-induced LULCC influence on the land surface processes is inevitable and the part it plays in intensifying climate change drivers is widely reported (Sy et *al.*, 2017). As one of the COP 21 (Paris agreement) targets demands carbon dioxide removal (CDR) in form of biomass sinks improvement with carbon capture and storage (BECCS), it is agreed that a positive influence on LULCC can be beneficial in lowering global warming (mitigation) and improving livelihood (adaptation). Groundwater controlled or dependent ecosystems contribute to LULCC especially in shallow water level aquifers conditions like the WA fractured groundwater systems (Freycon *et al*., 2015; Pierret *et al*., 2016; Oussou *et al*., 2022) but the potential of CO2 removal of this particular type of vegetation received until now less attention. Also, LULCC impacts exemplify by the biogeochemical effects (CO_2, N_2O, and CH_4) respond to the two-sided whether

natural or human-induced afforestation or deforestation (Carlson *et al*., 2016; Jia *et al*., 2019; Friedlingstein *et al*., 2020). Although the human influence on LULCC is well-documented, the GWL or storage change contribution in accelerating or decelerating these biogeochemical processes (e.g. Carbon cycle) deserves further attention and assessment. Prongatz *et al*., (2021) discussed and improved understanding about LULCC versus climate effects but acknowledged the need to expand the LULCC studies to sub-continental scales (e.g. WA) and relate them to the UN-SDGs. Thus, the LULCC versus SDG6 which is the water component of the SDGs and how it drives the water cycle remains a challenge to explore for water supply security in the ever-growing global warming concern. (i) How does a persistent drawdown of GWL or storage in GW controlled or dependent ecosystems drive biogeochemical processes in occurrence carbon cycle? (ii) How the seasonality of GW-controlled land cover change can be used to improve carbon removal from atmosphere? (iii) What land use management practices are adapted in GW controlled ecosystems for sound global warming mitigation? Although Gasser *et al*. (2020), Houghton & Nassikas (2017), and Tian *et al*. (2020) argued that anthropogenic greenhouse gases emissions and removals are attributed to LULCC basing their affirmation on bookkeeping models, the proportion of the human-induced GWL drawdown is yet to be counted. They have been a diligent endeavour toward improving bio-geophysical and biogeochemical properties and processes simulation using Dynamic Global Vegetation Models (DGVMs). As far as the LULCC influence on the atmospheric feedbacks is concerned, the state-of-art has shown that DGVMs improved in robustness and completeness from the coupled Land-Use and Climate, IDentification of robust impacts (LUCID) project to future LULCC scenarios simulation through the coupled LUCID-CMIP5 (Brovkin *et al*., 2013; Boysen *et al*., 2014) and recently recommended as part of CMIP6 in form of a dedicated Land Use Model Intercomparison Project (LUMIP) (Pongratz et *al.*, 2021). These Earth components integration orientated and accuracy minded efforts provided further evidences about the anthropogenic LULCC effects on carbon release but still need to be extended to the subsurface models. In a case of persistent human-induced GWL drawdown, soil moisture and groundwater drought, the carbon cycle response and its contribution to atmospheric feedbacks might be a clue for better LULCC effects understanding and subsequent decision-making.

2.6 GW-Atmosphere modeling and observation data challenges

There is a recent argument that GW modelling at different scales though serving specific purposes, offers complementary benefits for understanding the Earth System and its' feedbacks (Gleeson et *al.*, 2021). The attempts to capture and explain local scale GW systems behaviour with large scale GW models have remained a daunting target where successful representation is less imaginable due to their separate purposes. Moreover, the expectation that local measurements will match large-scale GW models' outputs even with high spatial resolution is arguably overblown and the performance criteria is very often subjective. Because of that, three ways of GW models' evaluation namely observation-based, model-based, and expert-based are suggested by Gleeson et *al.* (2021) but in limited GW data areas such as WA archiving this detailed analysis though required encounters several challenges. The in-situ GW observations are sparsely distributed, not well-monitored, filled with gaps, and the policy of monitoring wells siting changes from country to country. Although some countries might have regular monitoring platforms, others are undermined by the high proportion of private household GW pumping which offers no record of the fluctuations. The model-based approach is more applicable in the study area but the persistent disagreements in the outputs due to models' specificity and complexity makes it less reliable for decision making. The expert-based evaluation assumes that the field knowledge is well-developed; otherwise, the evaluation is error-prone because of GW systems variability. The regional-scale GW modeling has been preferred for decades and this is partly due to the specificity of its local management, humanly assumed spatial extent based on countries limits, and surface basin extent which are recently challenged because of the undeniable need to study the GW systems as whole introducing the term ‘’Transboundary Aquifer Systems ‘’ (IGRAC, 2021).

Adding to the well-established regional-scale GW modeling, the reaction of the GW components of the Earth System to global change and anthropogenic influences require a genuine attention to understand these vital resources from different perspective. The yearly (multiyear) seasonality in GWL in a given region cannot be assumed to be totally disconnected from the large-scale hydrological cycle, teleconnections, and feedbacks. More, large-scale GW modeling is an indirect approach to tackle the long-time GW data scarcity in developing areas like WA. Gleeson et *al.* (2021) argued the urgent need to achieve that by covering GW issues at local, regional, and global scale. The influence of GW Systems on climate through energy, water, and carbon distribution is extensively assessed but limited literature has taken into account this study area.

The longtime challenge to bridge large and regional scale GW modeling for comparison and validation purpose is argued to be no more considered as a panacea for successful GW resources representation. Instead, the two types of models' complementary based on their strengths and weaknesses appear as an envisage-able option to improve understanding, regulate water resources management, and efficiently handle the climate change crisis. Likewise, this is an urgent requirement for poorly gauged areas and a way to have a globally uniform GW related dataset at higher resolution. In the context of open science, the GW features complexity and the difficulty to accurately capture them in GHMs and LSMs hinder the reliability of available global data and their acceptance by the overall hydrologic community. This is reflected in the existing GHMs and LSMs as the simulation of GW storage, hydraulic head, baseflow, streamflow and runoff (Fan et *al.*, 2007), capillary rise, recharge, drains to a river (Müller Schmied et *al.*, 2014), surface water and groundwater two-way exchange (Döll et *al.*, 2016) is influenced by the models' conceptualization, the assumptions and simplifications, and the computation limits. Despite the existing interrogations on these models' success, the difference in their characteristics for example lateral extent, spatial resolution, models' parameterization is what opens a way to a wider possibility to duplicate at a large-scale the ongoing scientific debate at regional to local scale on GW resources with likely less details. The progress in the LSMs coupling and the methods that defines it can be a bridge not only between the numerical models but also from one layer of discussion to another; that is, switching the analysis from scale to scale, building connections between similar GW properties, and enhancing errors evaluation using the three aforementioned validation practices (observation-, model-, and expert-based). This might require the implementation of opensource and standalone tools orientated mainly towards this critical question.

2.7 Representing subsurface boundaries for GW-Atmosphere modeling

The spatial distribution of subsurface boundaries, particularly bedrock occurrence, serves as a critical lower limit for simulating land surface processes such as water, energy, and greenhouse gas fluxes (Fan et *al.*, 2013). Although recent efforts have sought to incorporate depth to bedrock (DTB) into Land Surface Models (LSMs)—transitioning from the use of constant depth values over large areas to the production of global DTB maps (Pelletier et *al.*, 2016; Shangguan et *al.*, 2017; Hengl et *al.*, 2017)—there remains a need for substantial improvements

in both accuracy and representation. Significantly, the existing global DTB datasets have been developed using borehole data from all continents, with the exception of Africa. Nevertheless, these datasets are widely used in African-focused studies, despite the data gap. There is a consensus in the literature that the minimum DTB value is 0 meters in locations where bedrock is exposed at the surface. However, the maximum DTB values, typically found beneath stream channels (de Graaf et *al.*, 2015), vary considerably across different studies (Pelletier et *al.*, 2016; Hengl et *al.*, 2017; Shangguan et *al.*, 2017; Zamrsky et *al.*, 2018). This inconsistency poses a particular challenge in hard-rock terrains, where accumulated eroded material in riverbeds results in greater DTB thickness. The spatial extent and depth of this sedimentation are shaped by a combination of geological, hydrological, and climatic factors, complicating the task of accurately estimating DTB. Because DTB is often modeled based on the probability or likelihood of thick sediment deposition, identifying maximum DTB values, especially in riverbeds, remains problematic and is still a matter of debate. Field measurements from hard-rock regions further illustrate this uncertainty, with some DTB outliers exceeding the double the suggested maximum limits (Shangguan et *al.*, 2017). For example, Lachassagne et *al.* (2021) proposed a maximum DTB of 100 meters, while estimates for Africa vary widely—50 m (Pelletier et *al.,* 2016), 237 m (Shangguan et *al.*, 2017), and 2 m (Hengl et *al.*, 2017). Although the maximum DTB suggested in Pelletier et *al.* (2016) and Lachassagne et *al.* (2021) for the Earth system modeling, the practice of assigning a constant DTB across large geological units is likely an oversimplification and may lead to inaccurate model outputs in heterogeneous terrains.

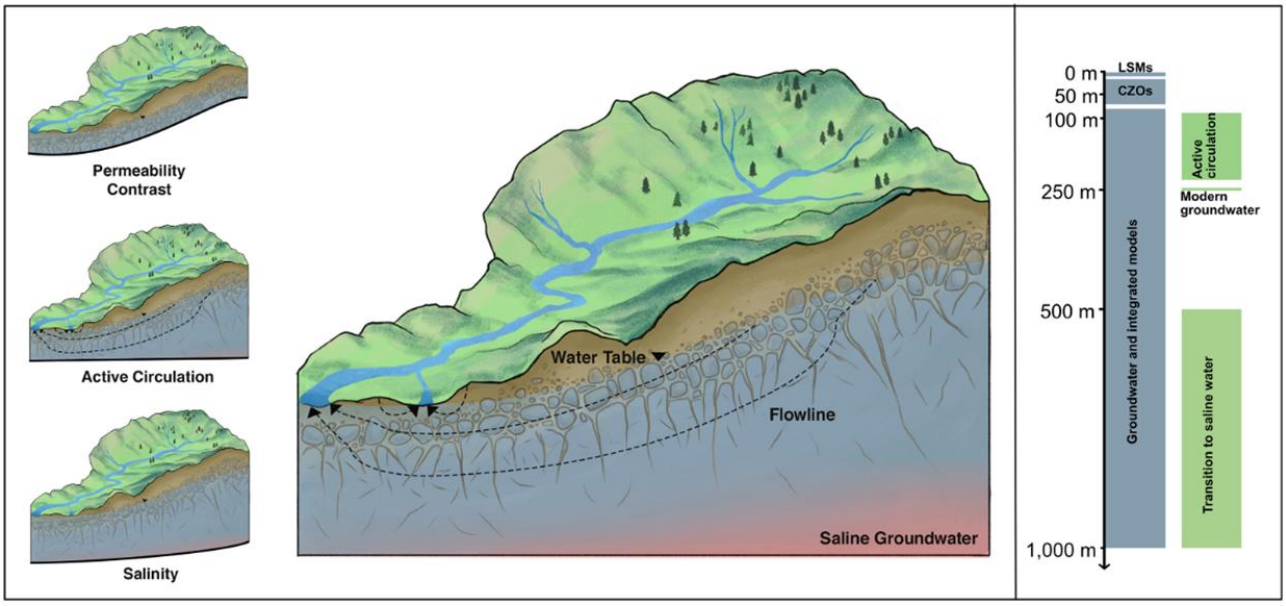

Figure 2.5: Conceptual model of watershed subsurface boundaries and examples of maximum depth-to-bedrock. (Right) Maximum depth-to-bedrock for most groundwater and integrated hydrologic models, Critical Zone Observatory (CZO) models and observations, and Land Surface Models (LSM) depending on groundwater travel time and salinity (see Condon et *al.*, 2020).

The seasonal dynamics of groundwater systems, in conjunction with surface water reservoirs and flows, play a critical role in regulating and redistributing water resources between water-rich and water-stressed regions. Acting as a natural buffer, groundwater helps mitigate the impacts of both climate change and human activities by sustaining a relatively stable outflow from terrestrial water storage (e.g., Ndehedehe et *al.*, 2021). However, research by Genereux et *al.* (2013) and Ma et *al.* (2014) has shown that groundwater-dependent ecosystems can alternate between functioning as carbon sinks and carbon sources, depending on fluctuations in groundwater levels (GWL). Additionally, the quantity and travel time of groundwater flow under climate change scenarios have been reliably assessed in some studies (Jing et *al.*, 2020). Despite these advances, further research is needed, particularly in West Africa, to understand how persistent GWL declines—driven by both climate variability and land cover changes—affect the carbon cycle and contribute to localized warming in groundwater-related ecosystems. The ability to predict changes in GWL has been evaluated using a combination of hydrospheric indicators (e.g., soil moisture, vegetation water content, precipitation) and atmospheric drivers (e.g., humidity, atmospheric boundary layer [ABL], ENSO, AMO), often through machine learning and deep learning approaches (e.g., Kalu et *al.*, 2022; Koster & Walker, 2015; Oussou et *al.*, 2022). Although subsurface flows are generally stable over time, groundwater-to-atmosphere (G2A) exchanges are not insignificant (Condon et *al.*, 2021), and their delayed feedbacks influence both the quantity and quality of hydrologic and atmospheric components (Maxwell & Kollet, 2008; Erler et *al.*, 2019; Sorensen et *al.*, 2021). Improving and systematically documenting these interactions can enhance our understanding of aquifer system sensitivities to land surface processes—particularly those driven by climate change—and inform more effective water resource and climate-related decision-making, especially in densely populated regions.

2.8 Greenhouse gas emissions under Groundwater-Atmosphere modeling

The terrestrial ecosystem in WA is not excepted regarding the greenhouse gases emission especially the carbon exchange print on the environmental disruption and climate warming. During the wet-to-dry transition periods, it is reported that the carbon sink driven by biomass regrowth in the rainy season is replaced by the carbon release which prevails in the dry season (Quansah et *al.*, 2015) in West African Savanna. Although, a sudden drop in the precipitation rate might mark severe decrease in the ecosystem respiration and therefore be considered a primary

predictor of CO_2 rate increase in the atmosphere, it is yet to be apprehended to what surface or subsurface factor this critical role is handover to in the dry season. This highlights the unprecedented need to assess whether the dry season carbon rate increase is driven by exogenous carbon importation due to atmospheric global circulation or in situ land surface or subsurface fluxes. The latter options are foreseen by Quansah et *al.* (2015) in which it is suggested that factors related to the soil might enhance the ecosystem respiration.

There are two acknowledged major systems in WA that define the CO_2 fluxes inter-annual, seasonal and diurnal trends year in year out in form of the terrestrial ecosystem influenced by meteorological forcings and anthropogenic activities (Ciais et *al.*, 2011; Janssens et *al.*, 2003). The Land Cover Land Use (LCLU) is the main carbon uptake and release component in the terrestrial ecosystem depending on the vegetation greenness and drives the energy balance (Quansah et *al.*, 2015). It is argued that the ecosystem whether natural or influenced by human activities switches from carbon sink in rainy season to carbon source in dry season but the annual budget fluctuation in terms of inner-annual sink versus source time span and inter-annual storage deficit in the past years in the Sudanian savanna is required for climate change related decision making. In fact, the Quantile Function of Storage (QFS) can be used as a tool to efficiently monitor the sink/source variability and how ecosystems degradation impacts carbon release and its concentration change in the atmosphere. Although valuable actions have been taken to reduce the lack of high confidence evidences about the contribution of the carbon budget of the Sudanian Savanna to the global budget, there is an inevitable fact that different LCLU and local climate condition display different energy, water and carbon fluxes. And this is even exacerbated in the climate change era where the greenhouse gases effects related to carbon release from subsidies is reported to increase (IPCC AR6, 2022 in SPM).

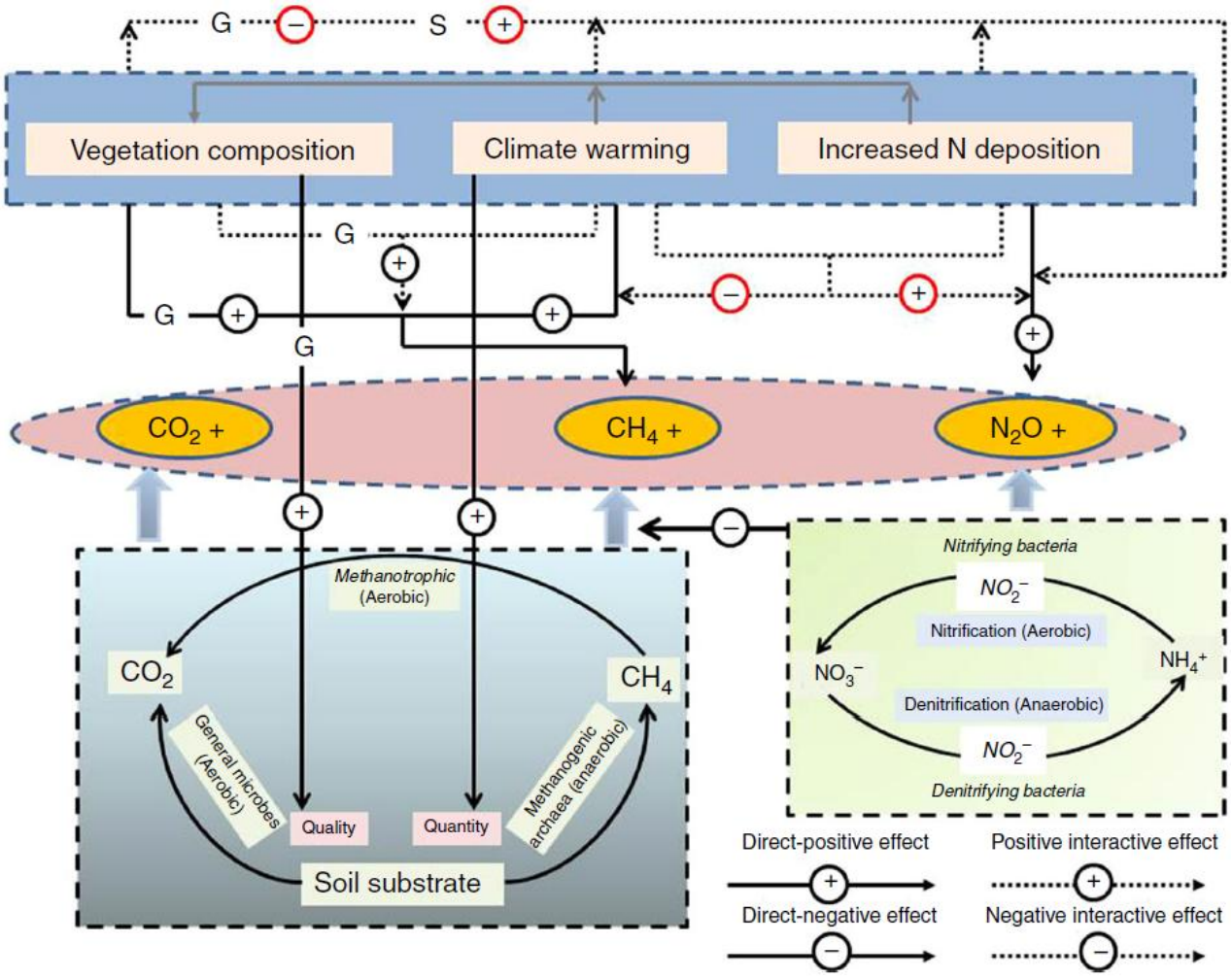

Figure 2.6: Conceptual schematic of CH_4, N_2O, and CO_2 fluxes in wetlands under N deposition, potential warming, and plant community composition (see Luan et *al.*, 2019).

Limitations can be placed on the carbon fluxes because of reduced sunlight required for photosynthesis during the rainy season and this infers that though plants activities might be triggered by precipitation for carbon uptake, the light availability is reported to arguably drive the rate in the Sudanian savanna (Berger et *al.*, 2019). These two factors added to the land use greenness are significant contributors to the carbon source versus sink strength in the region. However, the question about the strongest driver of the Net Ecosystem Exchange (NEE) of CO_2 is yet to be elucidated and the ambiguity of its' spatial and temporal pattern remains a challenge. It is fairly recommendable for better insight into carbon release issues in the study area that existing factors from each Earth system component including subsurface should be explored and relate to the carbon concentration change signals. To handle this, different methods such as the original signal decomposition into sub-domains using Principal Component Analysis (PCA), Independent Component Analysis (ICA), and Rotated Component Analysis (RCA) have proved their efficiency in revealing the hidden patterns of variability embedded in a particular variable. These multivariate statistics are widely reported methods for high-dimension data matrix reduction to lower dimension or mixed signals separation (Ndehedehe et *al.*, 2018).

Throughout seasons, water and energy limitations are reported to exercise significant control over the biosphere-precipitation feedbacks in the Sudanian savanna (Klein et *al.*, 2017, Green et *al.*, 2017 in Bliefernicht et *al.*, 2018). And the carbon rate in the atmosphere switches from sequestration to release when the season changes from wet to dry whatever the land cover type in the study area (Berger et *al.*, 2019; Quansah et *al.*, 2015). Although, the net warming and cooling effects of the atmosphere is associated respectively with carbon losses and uptake increase, it is fairly a critical question to find out the carbon rate enhancement (sink/source) ability of the rain in different land use conditions. That is, which association of rain duration, amount, and intensity perform best in enhancing the carbon concentration in a particular land use type?

From carbon fixation to biomass and yield estimation, the Production Efficiency Model according to Montheith (1972 and 1977) is well established for GPP and NPP assessment. But the widely reported error associated to the estimation when compared to Eddy Covariance measurements has remained a daunting task since the best structural optimization of the model is yet to be archived (Zhang et *al.*, 2015). This global endeavor to reach less error prone equations have reached moved from factor to factor (fPAR, PAR, LUE) and the light use efficiency parameter is known as a significant contributor to the error budget in the GPP models based on Remote Sensing products (Gitelson et *al.*, 2015). The environmental stress scalars integration to

the LUE model for GPP computing has been limited so far to the land surface and atmospheric factors (Wellington et *al.*, 2022; Zhang et *al.*, 2015). This is reflected in the required inputs (Temperature, soil, precipitation) of the widely adopted models. Zhang et *al.* (2015) evidenced the gain in accuracy of GPP estimation in different climate conditions using structural optimization of the LUE models. Not only that, the evaluation of LUE models for better error reduction using environmental stress scalars based on the Carnegie-Ames-Stanford approach (CASA), Global Production Efficiency Model (GLO-PEM), Vegetation Photosynthesis Model (VPM), and Eddy Covariance-Light Use Efficiency model (EC-LUE) has remained a challenge and the integration of other Earth system component (subsurface factors) is yet to be explored. That is, adding the subsurface and surface variables such as groundwater level and land subsidence to the reported stressors to verify the improvement in the GPP and NPP estimation accuracy is not less useful as the scientific debate on the aforementioned issue is yet to be cleared. Although, these stress scalars might be less regarded in humanly influenced environments like irrigated cropland, their control over carbon production in other land use type is not negligible (Wellington et *al.*, 2022).

Human activities such as land use and land management have led to a steady increase in the atmospheric concentration of major greenhouse gases, including N_2O, and CH_4, over recent decades, raising significant concerns about global warming (Canadell et *al.*, 2021; Guug et *al.*, 2025; Tharammal et *al.*, 2019). The cumulative effects of the carbon dioxide emission have pushed the threshold of the atmospheric CO_2 concentration to 414 mmol mol^{-1} (NOAA, 2020). A score of factors is identified as ways the terrestrial system influences the atmosphere, especially the net ecosystem exchange (NEE) of the plant and soil (Humphrey et *al.*, 2021). While the environmental impacts of CO_2 emissions are well documented (Baldocchi, 2003), the contributions of nitrous oxide (N_2O) and methane (CH_4) to global warming potential (GWP) are even greater per molecule—yet their monitoring, especially in West Africa, remains limited

With a global warming potential of 25 times that of carbon dioxide and a lifetime span of less than a decade (Canadell et *al.*, 2021), the level of the atmospheric CH_4 concentration between the pre-industrial era and now has reached 1879 nmol mol^{-1}(NOAA, 2020). CH_4 emissions from agriculture, livestock breeding, and manure management (Heilig et *al.*, 1994) is widely reported however the contribution from rainfed farming in West Africa is yet to be thoroughly investigated. The biological and environmental factors that affect CH_4 emissions are many (Xu et *al.*, 2016) but soil moisture is one of the most significant (Dutaur & Verchot, 2007). Notwithstanding the

aforementioned evidence, further clarification in uncovered or poorly covered areas (i.e., West Africa) is necessary for decision-making.

The global endeavour for climate change adaptation and mitigation is mainly focused on the carbon dioxide emission but the global warming potential (GWP) of nitrous oxide (N_2O) is reported 265 times higher with more than a century life span (NOAA, 2020; Pachauri et *al.*, 2014). The highest rate of total N_2O emissions due to human activities is in the agricultural sector (Tian et *al.*, 2020; Grossi et *al.*, 2018). N_2O emissions on agricultural soils are a direct consequence of animal excreta and fertilizer applications (Flechard et *al.*, 2007). The needs for organic nitrogen fertilizers vary from crop's yield improvement to intensive grass growth simulation for large-scale grazing events (Murphy et *al.*, 2022). Two types of nitrogen (N) spreading responsible for N_2O losses increase are the cumulative effects of fertilizer application on top of animal excreta and on urine and dung deposit (Carpinelli et *al.*, 2020; Maire et *al.*, 2018; Hyde et *al.*, 2016; Jarvis et *al.*, 1995). The ratio of N_2O release to uptake is therefore further exacerbated at the affected spots when both the plant N demand and soil microclimatic conditions tilt the balance in the emission direction (O'connell et *al.*, 2004).

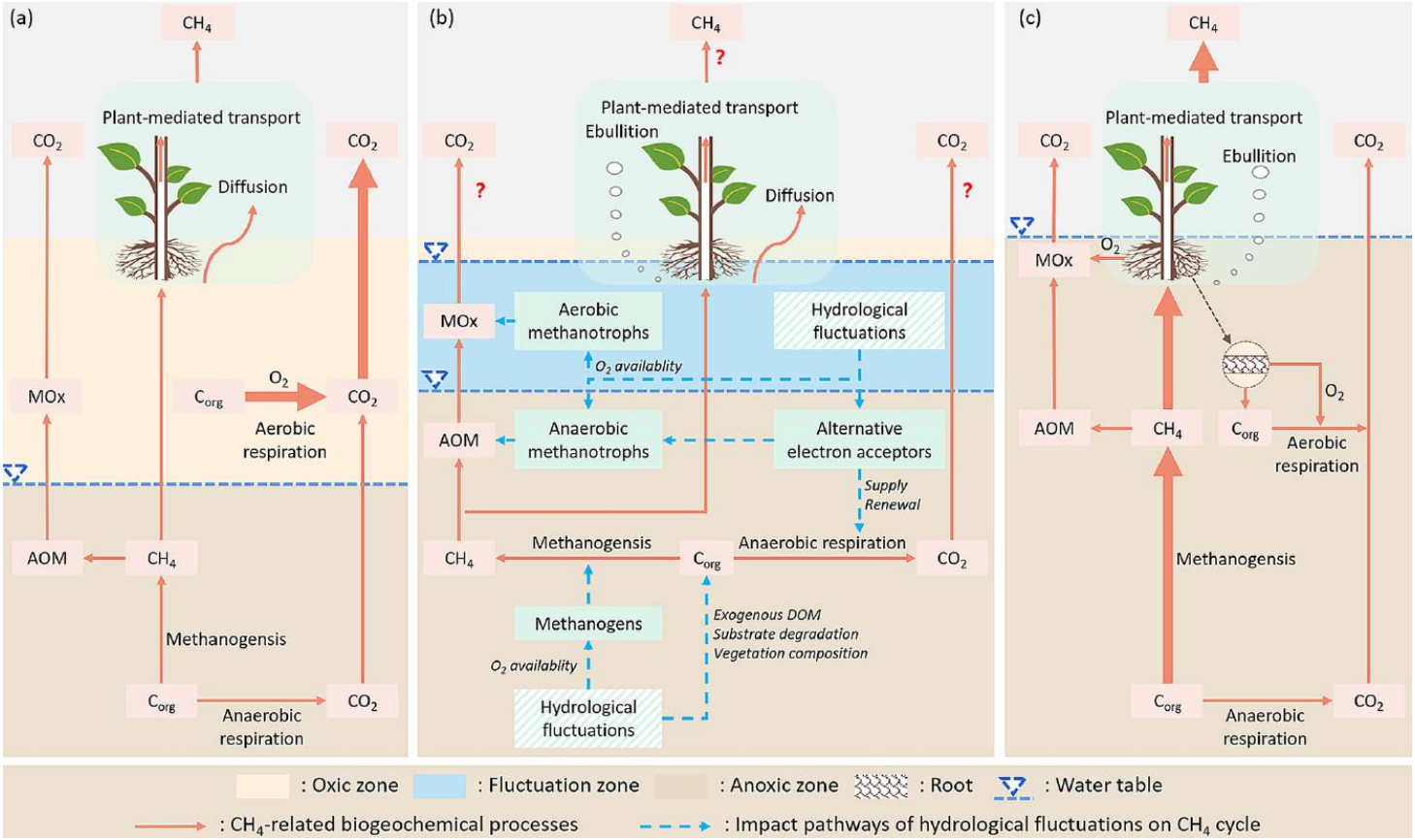

Figure 2.7: Methane (CH_4) cycle response to different hydrological scenarios in wetlands (see Cui et *al.*, 2024).

2.9 Current state of observational data availability for Groundwater-Atmosphere models validation in West Africa

Most of the environmental, hydrological, and hydrometeorological studies rely on the traditional concept of observational systems, hydrological observatories or advanced hydrometeorological systems. Today's statistics reveal at the global level a non-negligible progress in covering poorly gauged areas and a growing attention towards interdisciplinary research (Blöschl et *al.*, 2016). Despite the compelling necessity to achieve this purpose in WA because of increasing weather extremes, climate hazards, and water-food scarcity (IPCC AR6, 2022), the high cost required for hydrometeorological instruments acquisition has placed a serious limitation on WA. Notwithstanding these issues, since 1980s two types of international research projects have benefited the region like the short-term period (less than 3 years) field experiments focusing on energy balance (Sahelian Energy Balance Experiment – SEBEX, Wallace et *al.*1991, Kahan et *al.*, 2006), micrometeorology (Nigerian Micrometeorological Experiment – NIMEX, Jegede et *al.*, 2004, Mauder et *al.*, 2007), African Monsoon Analysis (NASA field campaign of the African Monsoon Multidisciplinary Analysis – NAMMA, Smith et *al.*, 2012), precipitation (Estimation of Precipitation by Satellite-Niger experiment – EPSAT-Niger, Lebel et *al.*, 1992), and Hydrology (Hydrologic Pilot Experiment in the Sahel – HAPEX-Sahel, Goutorbe et *al.*, 1994, Lebel et *al.*, 1997). And the relatively long-term (greater than 3 years) observation networks such as the African Monsoon Multidisciplinary Analysis (AMMA) program established in three countries (Benin, Niger, and Mali), the Dahra test in Senegal, and the WASCAL observatories which complete operation remains a challenge for the host stakeholders.

The global south unlike the north benefits less from the global endeavour for fluxes monitoring. In fact, there is a compelling limitation of climate stations and long-term measurements are rare (Ceperley et *al.*, 2017). In fact, the fluxes monitoring especially in the semi-arid savanna grasslands are still not thoroughly explored (Sjöström et *al.*, 2013; Tagesson et *al.*, 2015) and tropical savanna ecosystems are yet to be extensively studied compared to the tropical rain forests (Rodrigues et *al.*, 2013). The beginning of the 21st century has seen an increase in flux monitoring in WA using different technics in diverse climatic conditions and land use. However, the first longest series by EC method measuring CO2 and energy fluxes in the Sudanian savanna of West Africa is traced back to 2008 (Brümmer et *al.*, 2009). The energy components were not all measured back then in tropical West Africa (Mauder et *al.*, 2007b). The

experiments were based on the flux-gradient similarity (Jegede et *al.*, 2005; Balogun et *al.*, 2002a), assuming a closed energy balance for the Bowen ratio method (Bowen, 1926; Ohmura, 1982) and the modified Bowen ratio (Liu & Foken, 2001; Balogun et *al.*, 2002b).

A score of experiments have been setup for surface energy balance assessment in WA such as the Large Aperture Scintillometer (LAS), radiometer, and EC method implemented in the Volta basin for seasonal cycle analysis (Schüttemeyer at *al.,* 2006). In a tropical climate (Ile-Ife, Nigeria), the components of the energy were measured for the first time using a micro-meteorological experiment during the seasonal dry to wet transition period in the first quarter of 2004 (Mauder et *al.*, 2007b). The EC fluxes monitoring experiment in an undisturbed south Sudanese savanna was undertaken for energy and carbon assessment for two years in Burkina-Faso (Brümmer et *al.*, 2009). Further, the area-averaged sensible and latent heat fluxes of the Wankama catchment in Niamey (Niger) were estimated with LAS Scintillometer using an aggregation scheme covering three types of vegetation and the result compared to EC measurements (Ezzahar et *al.*, 2009). The Scintillometer technic combined with EC method was deployed during the end of the dry season 2006 in Northern Benin and turbulent heat fluxes were measured (Guyot et *al.*, 2009). The climate fluctuations and their implication on energy fluxes, water cycle, and vegetation was assessed at Gourma observatory with EC stations in Mali (Mougin et *al.*, 2009). Furthermore, in a semi-arid Sahelian climate, the energy balance components especially the vertical flux of a millet field and semi-natural fallow plot was monitored with EC stations in Wankama catchment (West Niger) over two years. The land use control over the energy balance closure is evidenced for the Sahel in Timouk et *al.* (2009).

The West African monsoon seasonal cycle and the related surface turbulence of the Planetary Boundary Layer in 2006 was observed with the EC method in the Northern Benin (Lohou et *al.*, 2010). The network of FLUXNET measurements sites is upscaled to the global level with ML algorithms and model tree ensembles (MTE), and the final product was proved useful for the West African climate (Jung et *al.*, 2011). The evaporative fraction, a product of the surface turbulence is derived from Remote Sensing products and related to the ground heat flux employing a given parameterization scheme for four EC sites between 2005 and 2007 in different climatic condition (Tanguy et *al.*, 2012). The gross primary productivity (GPP) from 12 EC stations in Africa including one from a grassland/shrubland of Bontioli reserve (Burkina-Faso) served as reference to evaluate the remotely sensed GPP of the MODIS satellite (Sjöström et *al.*, 2013). Tagesson et *al.* (2015) investigated the climate change in Senegal and its impact on the

environment in a semi-arid savanna grassland. The carbon, water, and energy fluxes of the ecosystem is explored with the EC method. Also, the accuracy of the Coupled Model Intercomparison Project Phase 5 (CMIP5) in simulating the latent heat is assessed at the global level with 240 EC sites extending from 2000 to 2006 (Yao et *al.*, 2016) with evidences for WA. Ceperley et *al.* (2017) demostrated that the turbulent fluxes through the evaporative fraction is influenced by the land cover health in a small catchment (Burkina-Faso) which added to the soil moisture gives a reliable prediction of the evaporation.

The EC technique is deployed in numerous ecosystems for relatively long period of observation (Mauder et *al.*, 2013; Aubinet et *al.*, 2012) in Europe (Integrated Carbon Observatory System – ICOS, www.icos-infrastructure.eu), in Germany (Terrestrial Environmental Observatories, www.tereno.net), and in US (National Ecosystem Observatory Network, www.neoninc.org). The limitation related to long-term fluxes monitoring in WA is well reported (Bliefernicht et *al.*, 2018) and the experiments setup lack of required resources to sustain the observation and provide reliable measurement. Different land cover types fluxes exchange in the Sahelian region is observed through the Sahelian Energy Balance Experiment (SEBEX) with the purpose in the one hand to measure directly the energy available, evaporation, and the sensible heat flux; and in other hand to evaluate Satellite Remote Sensing efficiency in estimating energy fluxes for regional climate forecasting (Wallace et *al.*, 1991). Improving the global circulation models (GCMs) parameterization was one of the targets for deploying the Hydrologic Atmospheric Pilot Experiment in the Sahel (HAPEX-Sahel). Not only that, the West Niger area was provided with a relatively large amount of data and study outputs (Dolman et *al.*, 1997; Goutorbe et *al.*, 1997). The land-atmosphere processes of the study area are assessed at the large scale with the aggregation of field measurements, Remote Sensing, hydrological and meteorological modeling (Goutorbe et *al.*, 1994). Two main limitations were underlined about the experiment by Ramier et *al.* (2009): the experiments' spatial placement was dispersed and the time period devoted to the observation was short (end of 1992 rainy season). Further, the Nigerian micro-meteorological Experiment (NIMEX) assessed the energy fluxes in a tropical climate of WA with different types of method such as the EC measurement (Jegede et *al.*, 2005; Mauder et *al.*, 2007b).

The water resources management was the main focus for the GLOWA-Volta project "Sustainable Use of Water Resources: Intensified Land Use, Rainfall Variability, and Water Demands in the Volta Basin in the early 21st century providing science-based decision-making

tools for development, integrated, and sustainable water use (Van de Giesen et *al.*, 2001; Schüttemeyer et *al.*, 2006). Both precipitation and evaporation were measured and simulated to spatially understand water availability and feedbacks in WA, particularly in the Volta basin. Also, the nexus of soil, vegetation, and anthropogenic activities on climate and hydrology in terms of land use change impact is assessed. The project analysed various aspects of water resources management (Hydrology and water use) from the legal, political, and institutional perspective to spatial and temporal availability, use, and demand. It covered complex scenario simulations for decision-making and technology integration (BMBF, 2005).

The African Monsoon Multidisciplinary Analysis (AMMA) project is one of the early initiatives to investigate thoroughly the West African Monsoon (WAM) in terms of land, ocean, and atmosphere interactions and feedbacks (AMMA-ISSC, 2005; Redelsperger et *al.*, 2006; Guyot et *al.*, 2009; Galle et *al.*, 2018). Therefore, experiments are setup for interdisciplinary analysis in a joint global endeavour. More, a long-term variability of the WAM dynamics, land surface processes, and rainfall is undertaken through the "Couplage de l'Atmosphère Tropicale et du Cycle Hydrologique", a component of AMMA (Lebel et *al.*, 2009; Timouk et *al.*, 2009). Three bioclimatic zones, namely North-Guinean, Sahel, and Sudan, with different annual rainfall, are extensively assessed with three mesoscale sites located in Benin, Niger, and Mali (Lebel et *al.*, 2009; Galle et *al.*, 2018).

The West African Science Service on Climate Change and Adapted Land Use (WASCAL) program launched a hydrometeorological data collect initiative since 2012 using climate and EC stations. The water, energy, and greenhouse gases of the Sudanian savanna of WA are monitored with the intent in one hand to evaluate land use change controls over climate, and climate change social and ecological impacts. In other hand, decision making strategies are provided for adaptation and mitigation. To achieve that purpose, more than 30 meteorological variables in sub-hourly temporal resolution are measured at different sites with a growing number instrumentation for particularly greenhouse gases (CO2, N2O, and CH4). The different types of land use considered are nature reserve/near natural, cropland, a mixture of fallow, and degraded grassland which indicates the vegetation greenness gradient of the savanna (Bliefernicht et *al.*, 2013; Quansah et *al.*, 2015; Bliefernicht et *al.*, 2022). The past publications that used the aforementioned dataset provided details and relevant information about the EC stations. The advantages offered by the EC instrumentation for micro-meteorological studies in WA are multiple as longtime unexplored land surface fluxes exchange in the region is now revealed

(Bliefernicht et *al.*, 2013, McGloin et *al.*, 2018). This adds up to the existing global network such as FLUXNET (Baldocchi et *al.*, 2001) and is a reliable data source for multi-discipline analysis and models' validation (Stöckli et *al.*, 2008; Jaeger et *al.*, 2009 in Franssen et *al.*, 2010).

Chapter Three

Materials and Methods

3.1 Sensitivity of water fluxes to subsurface flow parameterization schemes using a groundwater-enhanced Weather Research Forecast Hydro modeling system

3.1.1 Study area

The area of interest is selected based on the data availability and extends between the longitudes 5°37.8' W and 4°6.6' E and the latitudes 4°43.8' N and 15°51.0' N (Figure 3.1). It encompasses part of the climatic zones in the region, namely the Guinea Coast, the Savannah, and the Sahel. It covers fully West African countries like Benin, Togo, Ghana, and Burkina Faso; and partly Ivory Coast (12.2% of the study area), Niger (9%), Mali (13.3%), and Nigeria (5.2%). The largest basin within the area is the Volta catchment which drains approximately 30.7% of the study area. The two main physical features bordering the area are the Sahara Desert and the Atlantic Ocean respectively in the north and the south (Menz, 2010). The hydrography network drains the rainfall from the northern part to the southern coast through multiple rivers like the Volta and Pra Rivers in Ghana, Comoe, and Bandama in Ivory Coast, Oueme and Mono in Benin and others. A portion of the third-longest river (Niger River) traverses partly the upper region of the study area where its tributaries extend to the neighboring countries.

The yearly deployment of the Inter-tropical Discontinuity (ITD) drives rainfall variability across West Africa (Aryee et *al.*, 2024; Lavaysse et *al.*, 2009). The annual rainfall varies from 1250 to 1500 mm in the subtropical climate of the Guinea Coast, 600 to 1200 mm in the semi-arid region of the Savannah, and 150 to 600 mm in the Sahel. From rainfall onset to cessation, two peaks of rainfall are generally recorded in the south and one in the north. For instance, the imprint of the monsoon jump and Dahomey gap are reflected in the spatial variability of the rainfall in the region. The North-South gradient in the yearly rainfall amount is consequential as it is reflected in the spatial distribution of vital human activities intensity like agriculture, livestock breeding, water supply, and others.

At the regional level, the soil and geological features cannot be exhaustively detailed because of their complexity and the need for specialized descriptions which can change between countries and even experts. Nevertheless, the simplified maps existing in the literature give a hint for an overview. For instance, the State Soil Geographic Database (STATSGO; Miller & White, 1998) indicates that the sandy clay loam, sandy loam, and loam soils as the dominating soil types

in the region. The sandy loam soils are more abundant in the sedimentary basins like the Coastal Sedimentary Basin, the Kandi Sedimentary Basin, and the Volta Sedimentary Basin. In basement areas which cover 65.2% of the study area, the sandy clay loam soils occupy the first rank. Metamorphic rocks cover the largest part of the study area based on the global lithological database (GliM; Hartmann & Moosdorf, 2012), and constitute matrices where fractured groundwater systems occur. The unconsolidated sediments and other sedimentary rocks are found in the sedimentary basin where groundwater systems' depths are more significant.

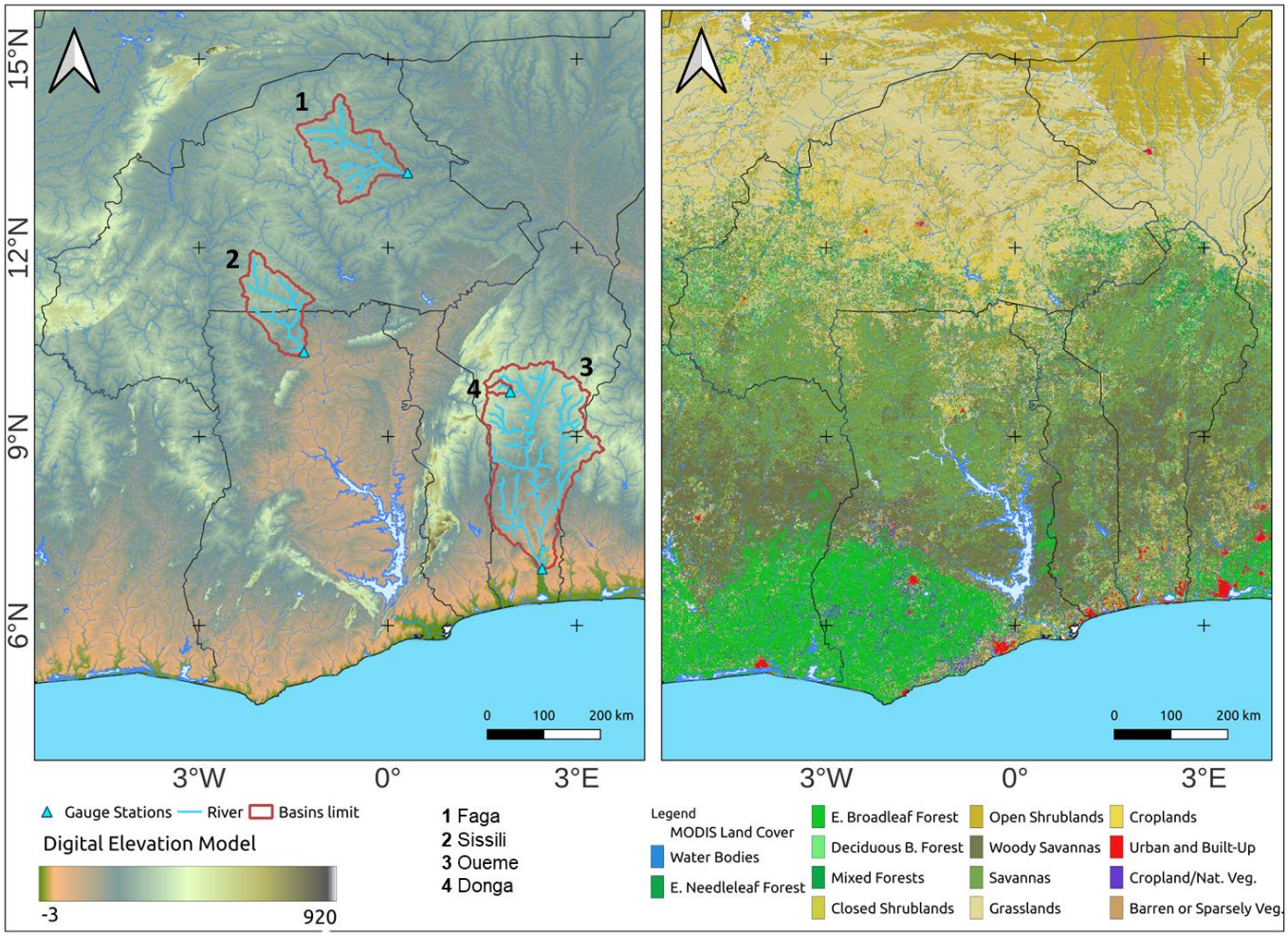

Figure 3.1: Study area represented by the digital elevation model of HydroShed (Lehner et *al.*, 2008; Left; elevation is indicated in metres) and land cover maps of MODIS (Friedl et *al.*, 2010; Right) with countries limits (black), catchments (red), river gauges (blue triangle), and the river network (light blue). Four basins are represented (Faga, Sissili, Oueme, and Donga).

3.1.2 Dataset

3.1.2.1 On-site observations

The energy balance components, soil moisture, and other climatic data are gathered as benchmarks for the simulations' validation. They are monitored by the AMMA-CATCH project and the WASCAL observatory through the CONCERT project. The Eddy Covariance method is employed at the three sites of the CONCERT project to measure the turbulent fluxes and a set of other climatic variables. The diurnal cycle of the energy fluxes is compared to the simulated in the dry season from 1st to 3rd January 2013. The latent heat flux is used to compute the potential evapotranspiration (PET) which is done with the Python package PyEt (Vremec et *al.*, 2024; Vremec et *al.*, 2023). The tool offers 21 approaches for the computation but only three are employed in this study namely Penman (Penman, 1948), FAO-56 (Allen et *al.*, 1998), and Priestley-Taylor (Priestley and Taylor, 1972). It requires climatic variables such as the temperature (°C), the solar radiation (MJ m^{-2} day^{-1}), the relative humidity (%), the wind speed (m/s), and the height of the wind measurement. The PET is further transformed into the actual evapotranspiration (AET) by combining it with the crop coefficient (K_c; Kamble et *al.*, 2013; Eq. 3.1) estimated from the Normalized Difference Vegetation Index (NDVI) of the Moderate Resolution Imaging Spectroradiometer (MODIS) mission (Friedl et *al.*, 2002). This NDVI dataset is chosen mainly because it has been widely used and has a relatively long period (2002 to present). The AET is computed using a simple linear equation suggested by Kamble et *al.* (2013):

$$KcNDVI = 1.457 * NDVI - 0.1725 \text{ (Eq. 1); and } AET = KcNDVI * PET \text{ (Eq. 3.1)}$$

The choice of the three is to have a broader appreciation of the accuracy of the simulated evapotranspiration. The soil moisture content (%) is monitored at different depths and locations at some sites, but only the first layer is considered. The river discharge data are obtained from the Global Runoff Data Center website (https://grdc.bafg.de/) and the ''Direction General de l'Eau'' of Benin.

3.1.2.2 ERA5-Land Reanalysis

The meteorological forcing data used to drive the WRF-Hydro model in this study is derived from the ERA5-Land reanalysis provided by the European Centre for Medium-Range Weather Forecasts (ECMWF) (https://cds.climate.copernicus.eu). ERA5-Land is an enhanced version of the earlier ERA5, which itself replaced the ERA-Interim dataset. It offers improved

precipitation accuracy (Nogueira, 2020) and features reduced dependence on external data sources during near-real-time production (Muñoz-Sabater et al., 2021). This global dataset provides meteorological variables at a 0.1° horizontal resolution (approximately 9 km) and includes four surface model levels, spanning vertically from 289 cm below the surface to 2 m above ground level. It offers an hourly temporal resolution and covers the period from January 1950 to the present. The specific ERA5-Land variables utilized include:10 m u and v wind components (m s^{-1}), 2 m temperature (K), 2 m dewpoint temperature (K), Surface pressure (Pa), Downward shortwave radiation (J m^{-2}), Downward longwave thermal radiation (J m^{-2}), and Total precipitation (m). ERA5-Land was selected for this study due to its improved accuracy over previous reanalysis datasets and its growing adoption in hydrological modeling (Dalla Torre et al., 2024) and land surface modeling (Draeger et al., 2023).

3.1.2.3 Remote Sensing products

a. GLEAM dataset

The skill of the simulated evapotranspiration from the 3 schemes is assessed using the Global Land Evaporation Amsterdam Model (GLEAM; Miralles et *al.*, 2011; Martens et *al.*, 2017). The GLEAM product is generated from satellite data with a set of algorithms and provides 10 variables including the actual evapotranspiration (AET, mm/day) used in this study for validation (www.gleam.eu). It is a semi-empirical model used in many studies for validation. The GLEAM version 3 produced in 2021 uses a new data assimilation scheme validated by Martens et *al.* (2017) and both the evaporative stress functions and water balance module were updated. Despite the difference in the spatial resolution with the present simulations, the dataset is chosen because it has been used in similar studies and found reliable for investigating evapotranspiration in various climate systems.

b. ESA-CCI Soil Moisture

The soil moisture data from the European Space Agency Climate Change Initiative (ESA-CCI; http://www.esa-cci.org/) blends active and passive microwave products using proportional weights to the signal-to-noise ratio (SNR). The triple collocation (TC) analysis is applied to retrieve the soil moisture in areas where TC based SNR estimates are available. In areas with no TC based SNR, a polynomial regression of those estimates and the Vegetation Optical Depth (VOD) is employed to compute the soil moisture. The dataset is in three types based on the sensors namely the Passive, and Combined which are in the volumetric unit (m^3 m^{-3}), and the

Active in the percentage of saturation (%). It benefited from the harmonization of different sensors and required thorough scaling procedures using the cumulative distribution function (CDF-) matching approach. For the data accuracy evaluation, the error standard deviation is computed and made available as soil moisture uncertainty. The simulated soil moisture is compared to these products for domain-level evaluation as undertaken in past studies (Eini et *al.*, 2023; Seo & Dirmeyer, 2022).

3.1.3 Methods

3.1.3.1 Description of the WRF-Hydro hydrological model

The distributed WRF-Hydro model is an enhanced representation of the Weather Research and Forecasting (WRF) model to count for the hydrological processes occurring from the land surface to a few depths of the soil column. It improves on past vertically solved hydrological models and employs a set of lateral water routing schemes to compute the overland, surface, and subsurface flow. The basic concept for the occurrence of both surface flow and subsurface flow in the WRF-Hydro model is that quantifiable flux is generated if the maximum retention depth is reached in the grid cell and the maximum humidity capacity of a soil layer is exceeded (Cerbelaud et *al.*, 2022). Under persisting rainfall, the pounded water increases in depth at the land surface and is later partitioned into evaporation and infiltration through the vertical routing scheme of Noah-MP. The channel routing (1D) and 2D overland flow schemes are interconnected so that routing the flow over the land surface if a channel grid cell is reached and the surface water is greater than the local retention depth, the excess is routed through the channel model. The two water flow routing processes are implemented with simplified Saint-Venant equations in form of the diffusive wave equation of shallow water models (Hingray et *al.*, 2015). The topographic effect on the soil layers is combined with the permeability and saturated soil depth to calculate the subsurface flow (Gochis et *al.*, 2013). The model is forced in offline mode using gridded reanalysis products presented above in section 3. The required forcing variables namely the incoming shortwave radiation, incoming longwave radiation, specific humidity, air temperature, surface pressure, and near surface u and v wind components are employed as atmospheric input. The Land Surface Model (LSM) used with WRF-Hydro is Noah LSM with multiple parameterization options (Noah-MP; Niu et *al.*, 2011). The spatial resolution of the Noah-MP is

coarse compared to the WRF-Hydro horizontal grid spacing and has four soil layers of 0.1, 0.4, 1, and 2 m depths.

3.1.3.2 Experiments setup overview

The model setup is undertaken for the study area in the offline mode encompassing three climatic zones (Guinea, Sudanian, and Sahel) with a spatial coverage of 1312500 km^2. Though the application of the model to this region was done in past studies, the evaluation of an improved groundwater scheme offers further variables analysis, an assessment of the subsurface and land surface interactions is therefore made possible. The study area is defined based on the field measurement availability from past and ongoing scientific and government projects focusing on water, energy and greenhouse gas fluxes monitoring in West Africa (Fig. 3.1). To mention some, the AMMA-CATCH project (Galle et *al.*, 2018; AMMA-CATCH, 1990), the WASCAL observatory through the CONCERT project (Bliefernicht et *al.*, 2018; Berger et *al.*, 2019), the CSIR-Water Research Institute of Ghana, the "Direction General de l'Eau" of Benin and many others have built significant hydro-meteorological and hydrogeological databases which serve as benchmark for the validation of the model simulations. In the WRF-Hydro framework, the required inputs can be categorized into static input including variables like the topography, the spatially distributed soil and land cover information, and the meteorological forcing. The regional characteristics of the study area is implemented into the model by relating both the vegetation parameters and soil hydrology parameters to respectively the land cover and soil maps. Regarding the soil and subsurface processes representation, further detail is provided in the model schemes description (Table 1). The MODIS modified IGBP land cover product provided in the model is used for the three simulations (Friedl et *al.*, 2010). Further, the 1-km STATSGO database (Miller and White, 1998) made of 19 soil types which is provided in the default WRF-Hydro model settings is used with the corresponding soil hydraulic parameters estimated based on the suggestions of Cosby et *al.* (1984).

Table 3.1: Model setup description of WRF-Hydro and Noah-MP

Objects	Description
Hydrological Model	WRF-hydro in offline mode
Land Surface Model	Noah-MP
Forcing	ERA5-Land of 0.1° resolution
Horizontal resolution	1 km and 250 m respectively for the LSM and Routing
LSM Grid points	1050 X 1250
Routing Grid points	4200 X 5000
Input time step	Hourly
Output time step	24h
Simulation period	01 January 2009 – 31 December 2022

The model spatial discretization is 1km resolution in x and y dimension making it 1050 X 1250 cells for the LSM and 250 m resolution for the routing sub-grid; hence the aggregation factor is 4. The HydroSHED digital elevation model (DEM) serves as the land surface topography to create the watersheds and drainage network. The generated river network accuracy is verified and adjusted based on high resolution satellite images until the best representation is obtained. Initial and boundary conditions are derived from the ERA5-Land reanalysis dataset. More details are provided on the forcing in the data description section 3.

3.1.3.4 Default Option or Free drainage parameterization

The original surface and subsurface runoff condition which is defined as the default setting and free drainage in Noah-MP serves in this study as reference parameterization for the options evaluation. In this representation of the soil column, the infiltration from the land surface to the soil is scaled with three global parameters namely REFKDT, REFDK, and SLOPE (Eq. 3.2 & 3.3).

$$Q_{surface} = Q_{wat} - I_{max} \text{ (Eq. 3.2)}$$

And

$$I_{max} = Q_{wat} * \frac{D[1 - \exp(-kdt * \delta_t)]}{Q_{wat} + D[1 - \exp(-kdt * \delta_t)]} \ (Eq. 3.3)$$

The surface runoff $Q_{surface}$ is computed by subtracting the soil infiltration rates I_{max} from the water input rates Q_{wat} into the soil. The Infiltration/exfiltration rates into and out of the soil are a function of the liquid soil moisture deficit of the model soil column, the time between two model time steps (δ_t), the saturated permeability coefficient (K_{sat}), the reference value (K_{ref}) for the saturated permeability coefficient (REFDK) and the REFKDT parameter (kdt_{ref}). The REFDK of $2x10^{-6}$ m/s (silty-clay-loam) is chosen as default value. The liquid soil moisture deficit (Eq. 3.4 & 3.5) is written as follows:

$$D = \sum_{i=1}^{4} \Delta Z_i(\theta_{sat} - \theta_i) \text{ (Eq. 3.4)}$$

And

$$kdt = kdt_{ref} * \frac{K_{sat}}{K_{ref}} \text{(Eq. 3.5)}$$

The third global parameter SLOPE is defined as a scaling factor of the percolation Q_{perc}. This explains the drainage of water from the bottom of the soil layer and approximates the rate at which the drainage from the bottom occurs (Eq. 3.6). In this free drainage condition, the global SLOPE is set to 0.1 and the corresponding Q_{perc}in this groundwater bucket option is redistributed to the channel network.

$$Q_{perc} = SLOPE * K_4 \text{(Eq. 3.6)}$$

3.1.3.5 MMF runoff scheme

For Improved subsurface representation in LSMs, the two-dimensional MMF groundwater parameterization (Barlage et *al.*, 2015; Fan et *al.*, 2007; Fan & Miguez-Macho, 2011; Miguez-Macho et *al.*, 2008; Miguez-Macho & Fan, 2012) is implemented in Noah-MP LSM providing a process description of the upper unconfined aquifer. In fact, an additional soil layer is added below the lowest soil layer of the LSM to represent the unsaturated zone above the water table. Two major factors namely the vertical and lateral water flows in that zone and the geological characteristics define the water table depth and the groundwater flow in space and time. The one-dimensional variant of the Richard equation is implemented in Noah-MP is used for the vertical water movement simulation within the vadose zone which results in capillary rise and drainage. On the other hand, the Darcy law describes the lateral water movement in the saturated zone and further detail is taken into account using the Dupuit-Forchheimer approximations. In this case, the groundwater head gradient is related to the groundwater flux and the storage change (Eq. 3.7 & 3.8) which is computed as follows:

$$\Delta S = Recharge + Q_{lateral} - Q_{river} \text{ (Eq. 3.7)}$$

And

$$Q_{river} = R_{cond} * (h - Z_{riverbed}) \text{ (Eq. 3.8)}$$

The vertical flux from the 4th soil layer represents the recharge. The sum of the fluxes (positive or negative) from the surrounding cells is $Q_{lateral}$and the groundwater flow to rivers Q_{river}which is a function of the elevation of the river bed within the grid cell, the water table head (h), and the river conductivity (R_{cond}). The downward fluxes from the riverbed to the groundwater table are assumed to be negligible. The surface runoff (Eq. 3.9) is computed following the TOPMODEL approach:

$$Q_{surface} = Q_{wat} * ((1 - FCR_1) * F_{sat} + FCR_1)$$ (Eq. 3.9)

FCR_1 is the impermeable pore space fraction, F_{sat} is the saturated surface fraction, and Q_{wat} (Eq. 3.10) is water input rate:

$$F_{sat} = F_{max} * e^{-0.5*f* \max(z_{wt}-2,0)}$$ (Eq. 3.10)

With f (m^{-1}) being the runoff decay factor with a constant value of 6 m^{-1}. F_{max}: a global runoff parameter represents the maximum saturated surface fraction with a default value of 0.38 in the model, and $z_{wt}$the water table depth.

The groundwater table change (Eq. 3.11) is therefore calculated as:

$$\Delta z_{wt} = \frac{\Delta S}{(\theta_{sat}-\theta_{equ})}$$ (Eq. 3.11)

The equilibrium and saturated soil moisture content respectively $\theta_{equ}$and θ_{sat}.

If $z_{wt}$is less than 2 m, the water table is within the resolved soil layers and F_{sat}default to Fmax. Therefore, the capillary rise occurs with the water table reaching the soil layers the LSM. In this case, ΔS is greater than the available pore space. A spinup routine within the MMF scheme uses annual groundwater recharge information to estimate θequ, Rcond, and $Z_{riverbed}$.

3.1.3.6 TOPMODEL runoff scheme

According to Chen and Kumar (2001) and Wolock (1993), the TOPMODEL runoff scheme (Eq. 3.12) enhances the surface saturated hydraulic conductivity $K_{sat}(0)$ to represent the surface macropores:

$$K_{sat}(0) = K_{sat}e^{fd_c}$$ (Eq. 3.12)

d_c : Depth over which macropores influence soil hydraulic conductivity. The soil texture is used to define the '' compacted '' K_{sat} (Cosby et *al.*, 1984). Based on the concept of soil surface macrospores (Beven, 1982), the d_c is set to 1m. f: the decay factor is estimated using a hydrograph recession curve by undertaking the sensitivity analysis.

Above the infiltration capacity of a given soil, the rain excess creates overland flow following the Horton mechanism which is comparable to the Dunne mechanism, the surface runoff generated on a saturated ground after a raining event. The runoff process (Eq. 3.13) is implemented using the following equation:

$$R_s = F_{sat} Q_{wat} + (1 - F_{sat}) max\big(0, (Q_{wat} - I_{max})\big)$$ (Eq. 3.13)

I_{max}: Soil infiltration capacity is controlled by both the texture and soil water content (Entekhabi and Eagleson, 1989). In the assumptions related to the TOPMODEL approaches, the second term is neglected because of the application of the surface macropore approach (Stieglitz et *al.*, 1997; Niu and Yang, 2003).

Q_{wat}: water input into the soil surface (sum of rainfall, dewfall, and snowmelt)

At grid cell level, the topographic characteristics and soil moisture at a given time define the saturated fraction F_{sat}(Eq. 3.14) which is written as follows:

$$F_{sat} = \int_{\lambda \geq (\lambda_m + f z_\nabla)} pdf\ (\lambda) d\lambda$$ (Eq. 3.14)

$\lambda = ln(\alpha / tan\, \beta)$ is the topographic index of a grid cell within the basin area and tan b the corresponding topographic slope (Quinn et *al.*, 1995; Wolock and McCabe, 1995). The average grid cell topographic index is denoted λ_m, $pdf(\lambda)$ is the probability density function of λ and the average water table depth is z_∇ (Eq. 3.15).

$$R_{sb} = \frac{a K_{sat}(0)}{f} e^{-\lambda_m} e^{-f z_\nabla}$$ (Eq. 3.15)

a: the anisotropic factor is detailed in Kumar (2004). The process is defined in a way that the 'oversaturated'' water in a given subsurface soil level is added as a capillary rise to the overlying soil layer which might be questionable as the subsurface runoff is neglected in this case.

The particularity with the TOPMODEL is how the bottom boundary condition is defined to calculate the soil moisture as the water flow from the bottom soil layer is added to the subsurface runoff. The permeability coefficient ($K(z_b)$) at the bottom is assumed to depend on the soil wetness (w_b) of the bottom layer, the bottom depth of the soil column (z_b), and the saturated permeability coefficient $K_{sat}(z_b)$ and is written as follows (Eq. 3.16):

$$K(z_b) = K_{sat}(z_b) {w_b}^{2B+3}$$ (Eq. 3.16)

The decay factor f is inversely proportional to the K_{sat} which decays exponentially with the depth resulting in very few bottom drainage. The TOPMODEL scheme solves the water table depth on the assumption that the water head at depth z (Eq. 3.17) is in equilibrium with that at the water table (z_∇) according to Chen and Kumar (2001).

$$\psi(z) - z = \psi_{sat} - z_{\nabla} \text{ (Eq. 3.17)}$$

$\psi(z)$ and ψ_{sat} represent the matric potential at depth z and saturation.

Replacing $\psi(z)$ in the previous equation using Clapp and Hornberger [1978] gives:

$$\psi_{sat}\left(\frac{\theta(z)}{\theta_{sat}}\right)^{-B} - z = \psi_{sat} - z_{\nabla} \text{ (Eq. 3.18)}$$

$\theta(z)$ and θ_{sat} are respectively the volumetric water content at depth z and saturation. The soil moisture profile is written as follows:

$$\theta(z) = \theta_{sat}\left(\frac{\psi_{sat}-(z_{\nabla}-z)}{\psi_{sat}}\right)^{-1/b} \text{ (Eq. 3.19)}$$

The equation below is then solved to estimate the water table depth z_{∇} :

$$D_{\theta} = \int_0^{z_{\nabla}}\left(\theta_{sat} - \theta(z)\right) dz \text{ (Eq. 3.20)}$$

D_{θ} is the column soil moisture deficit, which is calculated from the soil moisture profile as:

$$D_{\theta} = \sum_{i=1}^{10}\left(\theta_{sat} - \theta_{liq,i}\right) \Delta z_i \text{ (Eq. 3.21)}$$

$\theta_{liq,i}$ represents the ith layer volumetric liquid water content.

There are two significant assumptions associated with the water table depth estimation here which are: the soil column depth is limited to few meters and the water head throughout the column is at equilibrium. Based on the aforementioned assumptions, mainly regions with relatively shallower water table and in certain case where the soil moisture and the water table are in equilibrium, are likely to be well represented. In case of deeper water table aquifers beyond the model bottom, the water table might influence the baseflow and therefore it is decoupled from the soil moisture and considered as a lumped aquifer model like with Global Circulation Models (GCMs).

With the TOPMODEL scheme, from each soil layer, the liquid water mass is generated in proportion to the layer depth and the permeability coefficient and this is counted as the subsurface runoff.

$$R_{sb}(i) = R_{sb}(k_i \Delta z_i / \sum_{i=1}^{10} k_i \Delta z_i) \text{ (Eq. 3.22)}$$

k_i is the permeability coefficient and Δz_i is the layer depth

3.1.3.6 Performance measures

For model calibration and assessment of the simulations capability to reproduce the observed quantities, the following performance measures are used. The simulated streamflow goodness-of-fit to the observed values was assessed using the Kling-Gupta Efficiency (KGE; Kling et *al.*, 2012) and the Nash-Sutcliffe Efficiency (NSE; Nash & Sutcliffe, 1970) for the model calibration while the Percent Bias (PBIAS; %) and Root Mean Square Error (RMSE; m^3/s) served as the bias measures or error metrics. The metrics provide a quantitative evaluation of the model performance which makes them mathematically related but the difference in the meaning of their corresponding values offers a broader investigation. For instance, the KGE combines the linear correlation, mean bias, and variability bias, and NSE gives the time series variability and the magnitude of the errors ranging from minus infinity to 1. The hourly streamflow is resampled to daily for the model performance evaluation.

$$PBIAS = 100.\frac{\sum_{i=0}^{N}(S_i - O_i)}{\sum_{i=0}^{N} O_i} \ (Eq.3.23)$$

$$KGE = 1 - \sqrt{(cor-1)^2 + \left(\frac{std(S_i)}{std(O_i)} - 1\right)^2 + \left(\frac{\sum S_i}{\sum O_i} - 1\right)^2} \ (Eq.3.24)$$

$$NSE = 1 - \frac{\sum_{i=1}^{N}(S_i - O_i)^2}{\sum_{i=1}^{N}(O_i - \bar{O})^2} \ (Eq.3.25)$$

$$RMSE = \sqrt{\sum_{i=1}^{N}\frac{(S_i - O_i)^2}{N}} \ (Eq.3.26)$$

The S_i and O_i are the simulated and observed values with N the length of the series. $std(S_i)$ and $std(O_i)$ are respectively the standard deviations of the simulated and observed values and $\sum S_i$ and $\sum O_i$ are the sum of the simulated and observed values.

3.2 Impact of Idealized afforestation on water budget and energy fluxes

3.2.1 Model description and Experiment setup

The hydrological model Weather Research and Forecast Hydro system (WRF-Hydro) is developed by the National Center for Atmospheric Research (NCAR) and widely used to assess water and energy of the land surface processes. The main components are the land surface model Noah multi-parameterization (Noah-MP) and the hydrological routing schemes (Gochis et *al.* 2013; Niu et *al.*, 2011). The algorithms in WRF-Hydro can be categorized into surface and subsurface schemes for channel, reservoir, overland flow routing and groundwater bucket. The parameterization of the vertical fluxes in Noah-MP includes global parameters (GENPARM.TBL), soil parameters (SOILPARM.TBL) and vegetation parameters (MPTABLE.TBL). Further, the regionalization of parameters like REFKDT and SLOPE are recommended to improve streamflow accuracy. The two-dimensional MMF schemes (Barlage et *al.*, 2015; Miguez-Macho & Fan, 2012; Fan & Miguez-Macho, 2011; Miguez-Macho et *al.*, 2008; Fan et *al.*, 2007) adjusted to WRF-Hydro routing extensions by Rummler et *al.* (2022) is used to account for groundwater in the region. It integrates Q_{river} and Q_{spring} into the coupling/routing of WRF-Hydro which are respectively redistributed to the river reaches and infiltration excess.

3.2.2 Simulated afforestation scenarios

The hydrological routing of water across terrain through rivers and soil is implemented in Weather Research and Forecast Hydro model in response to fluxes and runoff from the land surface model Noah multi-parameterization (Noah-MP). In this study, the endeavor to ascertain idealized afforestation effects on water cycle and energy fluxes is executed with 6 land cover restoration options benchmarked against a reference simulation made of the current land use. The model runs were executed in standalone mode with similar default parameters. The meteorological forcings used in the model are derived from the ERA5-Land reanalysis dataset, including variables such as precipitation, near-surface air temperature, u and v wind components, humidity, surface pressure, and downward shortwave and longwave radiation. The dataset is produced by the European Centre for Medium-Range Weather Forecasts (ECMWF). The necessary ancillary data (e.g., geogrid files) required for model setup are generated using the WRF Preprocessing System (WPS). These include the modified MODIS-IGBP land cover classification (Friedl et al., 2010) and STATSGO soil data (Miller and White, 1998). For all

simulation scenarios, the model domain extends from 5°37.8′ W to 4°6.6′ E longitude and 4°43.8′ N to 15°51.0′ N latitude, with a horizontal resolution of 1 km applied to the Noah-MP Land Surface Model and 250 m used for the hydrological routing components of WRF-Hydro. The temporal resolution is set to monthly spanning from January 2012 to December 2015. This spatio-temporal resolution is preferred to assess the seasonal cycle and inter-annual variability of the fluxes under the idealized afforestation scenarios. The default soil depth of 2 m is partitioned into four layers of 0.1, 0.3, 0.6, and 1 m are adopted in this study. The model is calibrated in its default runoff option (Free Drainage) over the Donga catchment for a time period between 2009 to 2011 (Oussou et *al.* 2025 in review).

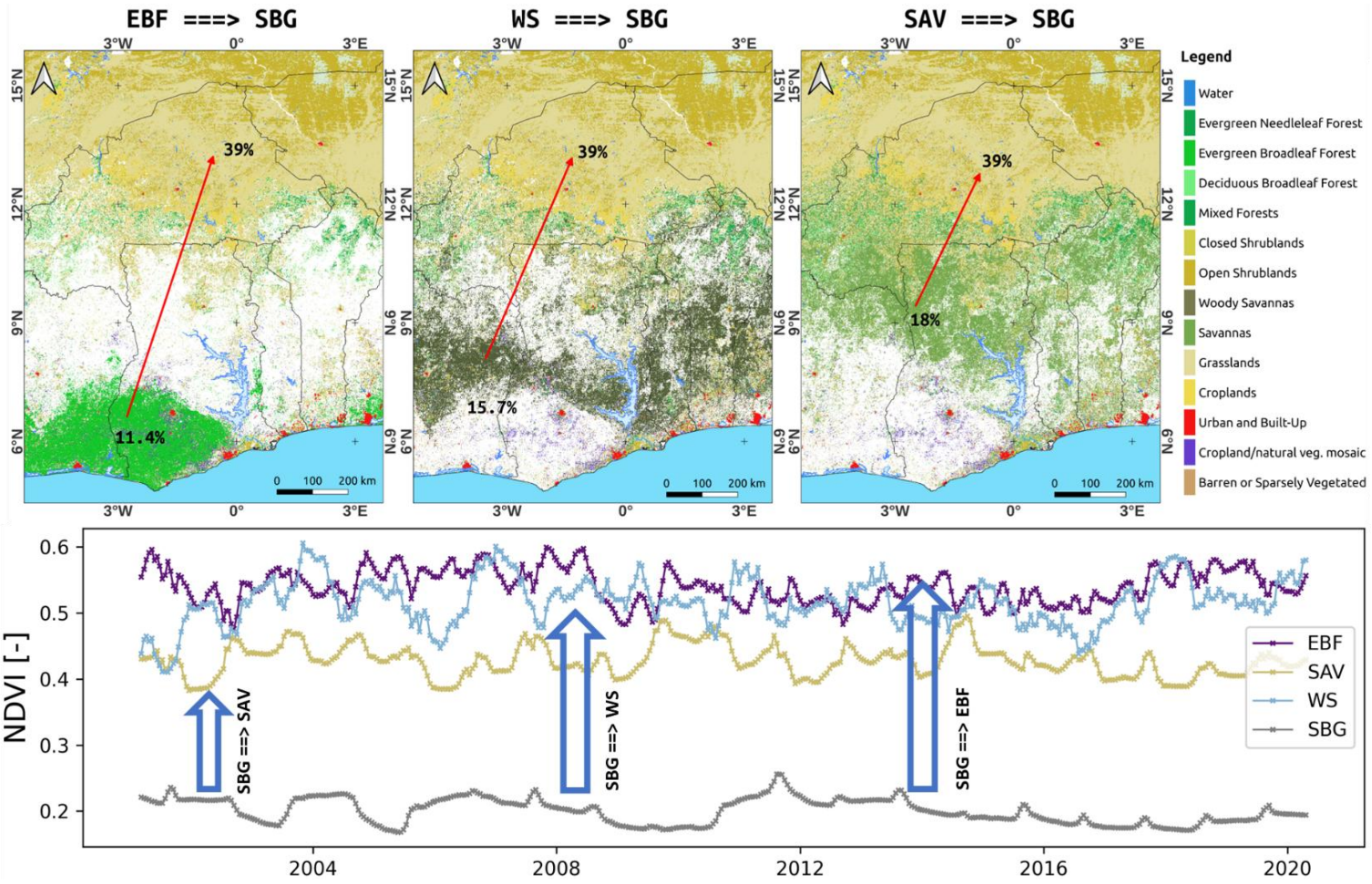

Figure 3.2: Description of the idealized afforestation undertaken for the region

The routing algorithm solves a simplified Saint Venant equation and requires the topography as a critical input. Therefore, the HydroShed digital elevation model (Lehner et *al.*, 2008) is used to replicate the spatial distribution of the stream channel and overland roughness. The adopted afforestation approach consists of three idealized regreening of the current land use. The shrubland, bare soil, and grassland (SBG) in MODIS-IGBP land cover is substituted by the Evergreen Broadleaf Forest (EBF), Savanna (SAV), and Woody Savanna (WS; Fig. 3.2). The purpose of regreening the degraded land is to mimic the effects of Africa's Great Green Wall initiative (PAGGW, 2018; Zeng, 2003) in the region and evaluate the potential change of water cycle and energy balance. GGW refers to the afforestation project targeting the Sahelian region within 100 mm to 400 mm annual rainfall. It was initially an ambition to build a "wall of tree '' covering 7000 km from Senegal to Djibouti but changed later on to different foreseeable actions to improve the living conditions of the inhabitant of the Sahel (Turner et *al.*, 2021). To evaluate the potential changes, the default vegetation parameters of the degraded land (SBG) in Noah-MP look up table are replaced by EBF, SAV, and WS parameters. This idealized afforestation improves in average the Normalized Difference Vegetation Index (NDVI) in the study area from 0.21±0.1 to 0.4±0.1 for SAV, 0.48±0.1 for WS, and to 0.53±0.1 for EBF (Fig. 3.2). Similar idealized afforestation approach was employed by Arnault et *al.* (2023) in East Africa. It provides a valuable insight into the potential risk and can guide decision making for natural resources preservation and restoration. The dynamic vegetation schemes in Noah-MP LSM uses vegetation equation developed by Dickinson et *al.* (1998) to predict the Leaf Area Index (LAI), Stem Area Index (SAI), and fractional vegetated area (FVEG) and the Ball-Berry model for stomatal resistance (Ball et *al.*, 1987). The model switches to LAI and FVEG values in the Noah-MP look up table when the dynamic vegetation scheme is off. The vegetation physical options in the LSM have different effects on the fluxes (Hosseini et *al.*, 2022) and water (Arnault et *al.* 2023; Mortey et *al.*, 2024) however the effects on subsurface water dynamics are yet to be thoroughly investigated. Henceforth, each idealized afforestation is simulated with the dynamic vegetation schemes off and on as described in Table 3.1. The 7 model runs are labeled as follows: the reference scenario with current land use (REF), the idealized EBF, SAV and WS afforestation with dynamic vegetation scheme off (EBF-VC, SAV-VC, and WS-VC) and on (EBF-VD, SAV-VD, and WS-VD). For instance, the EBF-VC experiment computes the LAI and FVEG using the Noah-MP look up table while EBF-VD calculates LAI and FVEG dynamically. The labeling convention is chosen to improve the clarify the interpretation of the results. Further, the

groundwater parameterization scheme MMF is activated to assess the response of groundwater table, recharge, and subsurface runoff to the idealized afforestation schemes.

Table 3.2: Idealized afforestation scenarios implemented in this study

Scenario ID	Afforestation	LAI	FVEG
EBF-VC	SBG afforestation with Evergreen Broadleaf Forest	Monthly values from look-up table by vegetation class	Gridded Monthly Climatology
EBF-VD	SBG afforestation with Evergreen Broadleaf Forest	Dynamic	Dynamic (calculated as function of the SAI and LAI)
SAV-VC	SBG afforestation with Savanna	Monthly values from look-up table by vegetation class	Gridded Monthly Climatology
SAV-VD	SBG afforestation with Savanna	Dynamic	Dynamic (calculated as function of the SAI and LAI)
WS-VC	SBG afforestation with Woody Savanna	Monthly values from look-up table by vegetation class	Gridded Monthly Climatology
WS-VD	SBG afforestation with Woody Savanna	Dynamic	Dynamic (calculated as function of the SAI and LAI)
REF	Current land use	-	-

3.3 Improving the depth-to-bedrock for groundwater-to-atmosphere modeling

3.3.1 Study area

Africa, the world's second-largest continent, extends from the Atlantic Ocean in the west to the Indian Ocean in the east. It is bounded by the Mediterranean Sea to the north and the Mozambique Channel to the southeast. Additional significant boundaries in the northeast are the Strait of Gibraltar, the Suez Canal, and the Strait of Suez, along with the Red Sea and the Gulf of Aden. The continent spans a wide range of climatic zones, from equatorial to temperate, influenced by variations in temperature, rainfall, and other climate-related factors. According to the Intergovernmental Panel on Climate Change (IPCC), Africa experienced a marked warming trend between 1991 and 2020, with average annual temperatures rising relative to the 1981–2010 baseline.

Climate projections suggest that Africa's mountain glaciers may disappear entirely by the 2040s, along with a likely acceleration in sea-level rise. The continent's terrain is highly diverse, featuring vast deserts such as the Sahara, Nubian, Namib, and Kalahari, as well as prominent mountain ranges like Kilimanjaro, the Atlas, the Drakensberg, the Ahaggar, and the Ethiopian Highlands. The Great Rift Valley extends from East Africa and the Red Sea northward to Syria. Several major rivers such as the Nile, Niger, Congo, Zambezi, Limpopo, and Orange play a crucial role in shaping Africa's hydrological systems. Beneath its varied surface, Africa has a complex geological structure that includes both sedimentary basins and solid rock formations. Unconsolidated sediments, such as alluvial deposits, pyroclastics, and coarse- to fine-grained materials, cover approximately 35.1% of the continent. Meanwhile, metamorphic rocks dominate the hard rock regions, making up around 27.6% of its geology, according to Börker et al. (2018) and Hartmann & Moosdorf (2012). Africa is also notable for having the most countries of any continent, typically organized into six major regions based on geography and politics. Northwest Africa includes nations such as Morocco, Algeria, Tunisia, and Libya, while Northeast Africa comprises Egypt, Sudan, South Sudan, Ethiopia, Eritrea, Djibouti, and Somalia. Central Africa consists of countries like the Central African Republic, Cameroon, Chad, Equatorial Guinea, São Tomé and Príncipe, and the Democratic Republic of Congo. In the west, countries such as Nigeria, Ghana, Mali, Senegal, and Côte d'Ivoire are part of West Africa. Southern Africa includes Angola, Namibia, South Africa, Zambia, Botswana, and Zimbabwe, while East Africa encompasses Kenya, Uganda, Rwanda, Tanzania, Malawi, and Burundi.

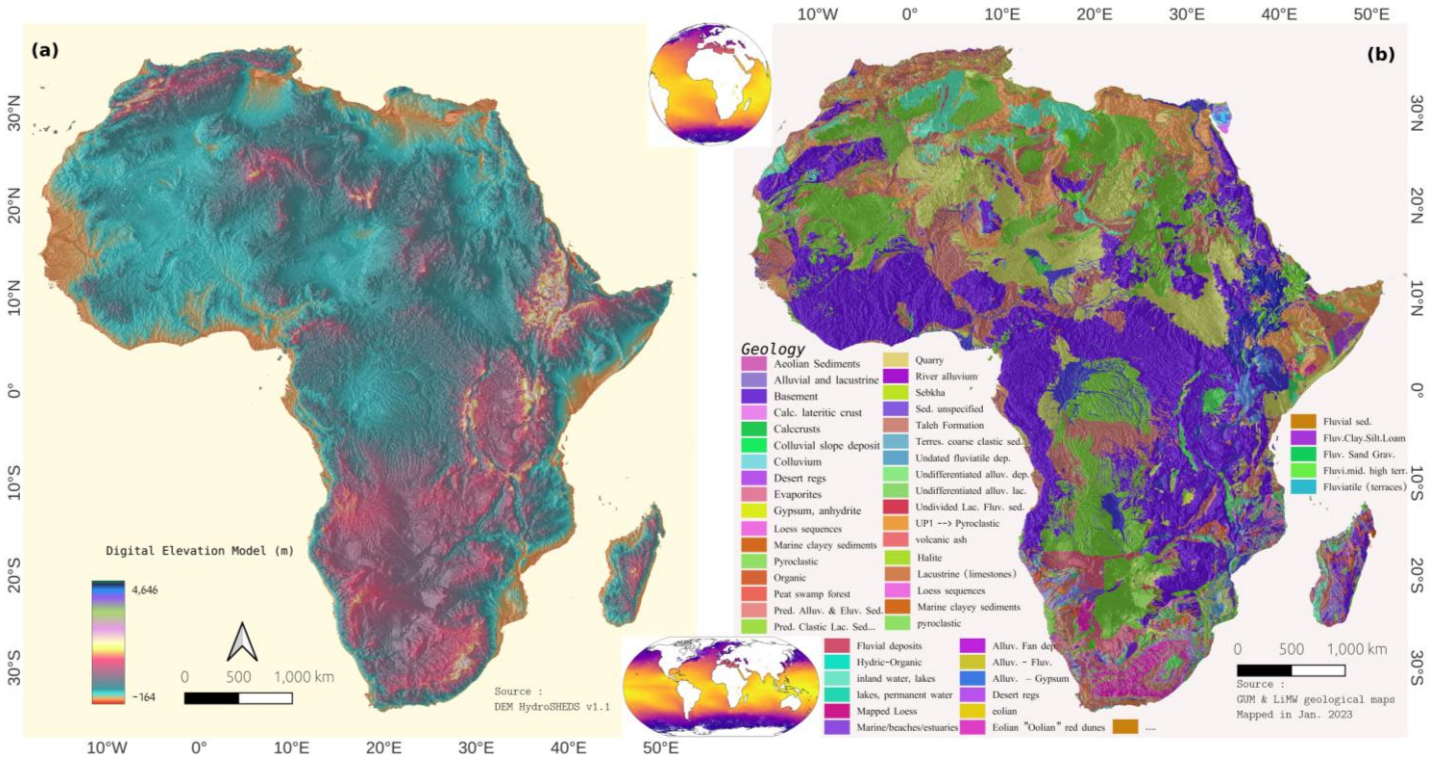

Figure 3.3: (a) The continent's topography is illustrated using the HydroSHED Digital Elevation Model (DEM), which displays the elevation distribution across Africa. (b) Geological units are derived from the Global Lithological Map (GliM) developed by Hartmann and Moosdorf (2012). The geological layer was extracted using the study area shapefile. Metamorphic units, representing basement rock, account for over 27% of the continent's surface.

3.3.2 Dataset

3.3.2.1 Depth-to-bedrock in situ data

The DTB (Depth to Bedrock) field measurements used in this study were obtained from the national integrated database maintained by the Direction Générale des Ressources en Eau (DG-Eau). This borehole dataset, assembled by engineering departments throughout the Republic of Benin, serves as a valuable and widely recognized record of borehole drilling logs, detailing the geological lithology encountered during the development of both rural and urban drinking water systems. Data collection started in the early 1950s and has progressively expanded to include the majority of towns and villages in need of drinking water supply and groundwater monitoring facilities. Over time, several certified engineering institutions have contributed to the database, starting with BRGM-ORSTOM in the late 20th century, and more recently including organizations like CANAL-EAU. Although national guidelines mandate that geophysical surveys precede all water supply drilling, there is currently no centralized database for geophysical measurements. According to Allé (2019), the absence of such data remains a major obstacle to improving well siting, as geophysical techniques such as electrical resistivity tomography could significantly enhance drilling success rates. Despite generally low success rates for borehole drilling, the national integrated database had accumulated more than 4,000 records by 2007.

During data preprocessing, biased values were systematically removed, and gaps were filled using values from the nearest boreholes. Additionally, DTB measurements located in sedimentary zones were excluded due to differing geological conditions. In such areas, groundwater system thickness can span several hundred to thousands of meters, making large-scale DTB estimation highly unreliable. As a result, the total number of usable data points was reduced from 4,241 to 4,141 due to missing or excluded values.

3.3.2.2 Domain topography

The Digital Elevation Model (DEM) used in this study was downloaded from the NASA HydroSHED website (www.hydrosheds.org/hydrosheds-core-downloads). This DEM is widely utilized due to its void-filled and corrected nature, offering relatively high accuracy. HydroSHED is the result of a collaborative effort involving multiple partners, including the U.S. Geological Survey, the International Center for Tropical Agriculture, and support from the World Wildlife Fund. The datasets and maps are derived from Shuttle Radar Topography Mission (SRTM) data

at a 3-arc-second resolution, incorporating elevation derivatives at various scales. To address areas with missing data—such as water bodies or mountainous regions affected by radar shadowing—four enhancement algorithms are applied in three processing steps: void filling, filtering, stream burning, and upscaling. Voids in the SRTM are filled using a combination of 3×3 minimum and 5×5 mean filters, followed by smoothing with a 9×9 mean filter. HydroSHED was chosen for this study because its processing algorithms are widely accepted as reliable for hydrological analysis. Additionally, its integration of smoothed, disaggregated, and blended values from the global GTOPO30 DEM ensures continuous elevation coverage without voids. The Depth to Bedrock (DTB) occurrence map, which serves as a key intermediate output in DTB mapping, is generated using this DEM.

3.3.2.3 Global depth-to-bedrock maps

The geometry of the groundwater model is essential for producing accurate simulations of groundwater systems. While several globally recognized datasets exist—developed through various methods and using different input sources they often come at relatively low spatial resolutions. Therefore, it is recommended to enhance the quality and resolution of these maps, particularly in regions with limited field data, and to explore more effective mapping techniques (Pelletier et *al.*, 2016; Shangguan et *al.*, 2017; Zamrsky et *al.*, 2018). The terms "depth to bedrock" (DTB), "drift thickness," "regolith thickness," "overburden thickness," and "R horizon soil depth" are used variably in the literature, depending on the disciplinary context and interpretation (Miller and White, 1998; Tesfa et *al.*, 2009; Karlsson et *al.*, 2014; Shangguan et *al.*, 2017). In this study, the term "depth to bedrock" is preferred and is defined as the vertical distance from the land surface to the interface between consolidated hard rock and any unconsolidated material such as saprolite, alterite, or weathered regolith (Jain, 2014; Lachassagne et al., 2021).

This interpretation aligns with practical field observations, particularly in hard-rock regions, where drilling companies typically switch from rotary drilling to the down-the-hole hammer technique (commonly known as marteau fond de trou) upon reaching bedrock. Although there is no universally agreed-upon definition, Lachassagne et *al.* (2021) suggest that in fractured rock aquifer systems, the depth to bedrock typically ranges from the surface to approximately 100 meters. In contrast, studies focused on land surface modeling such as those by Jain (2014) and Shangguan et *al.* (2017) report much greater depths, sometimes extending to several thousand meters in sedimentary basins. This study adopts the definition put forward by Lachassagne and

colleagues, as it is consistent with both previous research and the depth-to-bedrock dataset analyzed here.

3.3.3 Methods

3.3.3.1 Groundwater systems thickness estimate

To differentiate local aquifer systems in valleys from extensive alluvial aquifers found in major floodplains and mountain ranges, de Graaf et al. (2015, 2017, and 2019) developed an algorithm that uses elevation data and the drainage network for its calculations. The method assumes that a model cell is classified as an alluvial aquifer if the elevation difference between it and the adjacent downstream cell is 15 meters or less. If the elevation difference exceeds this threshold, the cell is categorized as part of mountain ranges, which are characterized by secondary permeability in hard rock regions and generally have very thin alteration layers. In fluvial systems and deltas, sediment deposition occurs such that both sediment grain size and volume increase toward the main gradient, which corresponds to the transverse axis (Fig. 4.30). The variation in alluvial aquifer depth is estimated by measuring the relative elevation difference between any point near the river and the point farthest along the transverse axis (de Graaf et al., 2015). A log-normal distribution of these standardized relative elevations is used to represent the aquifer thickness distribution. The relative elevation difference is calculated for each cell within the alluvial aquifer using the following formulation:

$$F'(x) = 1 - \frac{F(x) - F_{min}}{F_{max} - F_{min}} \text{ (Eq. 3.27)}$$

The elevation difference between a given cell at location x and its neighboring downstream cell is denoted as F(x), with F_min and F_max representing the minimum and maximum differences, respectively. The graphical depiction of F'(x) illustrates that the thickness of alluvial groundwater systems increases from the edge toward the main streamline. The z-score corresponding to this distribution is expressed as follows:

$$Z(x) = G^{-1}\big(F'(x)\big) \text{ (Eq. 3.28)}$$

G^{-1} represents the inverse standard normal distribution.

The natural logarithm of the thickness (lnD) derived from historical well log data is averaged to characterize the alluvial aquifer layers, which follow a log-normal distribution since their

thickness is always greater than zero. The lnD values are uniformly sampled across the thickness range and expressed as follows:

$$\overline{lnD} = U(10{:}\,100) \text{ (Eq. 3.29)}$$

lnD ranges from 10 to 100, where U is the random value.

A second parameter derived from the range of groundwater system thicknesses in the study area, based on previous studies, is the average coefficient of determination, which is assigned a fixed value. The spatial distribution of aquifer thickness is then calculated using the average value of ¯lnD, sampled from a uniform distribution U(10,100), in combination with the fixed coefficient of determination and the topography-dependent standard normal variable Z(x) (de Graaf et al., 2019). The corresponding equation is given as follows:

$$Y(x) = \overline{lnD}\left(1 + Cv_{\overline{lnD}}Z(x)\right) \text{ (Eq. 3.30)}$$

$$D(x) = e^{Y(x)} \text{ (Eq. 3.31)}$$

$Y(x)$ and $D(x)$ are random.

The spatial distribution of thickness for the deeper, more extensive alluvial groundwater systems is estimated using the same approach applied to the shallow alluvial systems (Fig. 4.30). The average lnD transformed values are sampled from the thickness range of deep layers reported in previous studies. These estimated thickness values are then compared with existing depth-to-bedrock (DTB) datasets (Pelletier et al., 2016; de Graaf et al., 2015; Shangguan et al., 2017).

As part of the study's objectives, the effectiveness of the method used to estimate DTB is assessed by modifying the final steps of the procedure outlined by de Graaf et al. (2015). To this end, a set of equations is proposed that combine a selected percentile from field-measured DTB values with either a logarithmic or exponential function (Table 3.3). While the exponential function is inspired by the final equation in the original method, the logarithmic function is considered more appropriate due to the characteristic shape of eroded hard-rock formations. Consequently, only the logarithmic functions $\log_2$ and ln are used, as they exhibit faster growth rates than $\log_{10}$, which appears to be less suitable. To eliminate negative DTB estimates, the absolute value of the minimum z-score is added to the z-score itself before multiplying by the selected DTB percentile. This adjustment is only applied if the minimum value of Z(x)is negative.

Table 3.3: An overview of the formulas and functions evaluated for DTB estimation in this study.

$\boldsymbol{log_2()}$	$\mathbf{ln}\ ()$	$\mathbf{2}^{()}$	$\boldsymbol{e}^{()}$
$\boldsymbol{P_{10}}$ $* \begin{cases} (\boldsymbol{log_2}(\boldsymbol{Z_{(x)}}) + \lvert\mathbf{min}\ (\boldsymbol{log_2}(\boldsymbol{Z_{(x)}})\rvert)\ (\boldsymbol{a}) \\ \boldsymbol{log_2}(\boldsymbol{Z_{(x)}})\ (\boldsymbol{b}) \end{cases}$ (Eq. 3.32)	$P_{10} * \begin{cases} (ln(Z_{(x)}) + \lvert\min\ (ln(Z_{(x)})\rvert)\ (a) \\ ln(Z_{(x)})\ (b) \end{cases}$ (Eq. 3.36)	-	-
$\boldsymbol{P_{25}} * \begin{cases} (\boldsymbol{log_2}(\boldsymbol{Z_{(x)}}) + \lvert\mathbf{min}\ (\boldsymbol{log_2}(\boldsymbol{Z_{(x)}})\rvert)\ (\boldsymbol{a}) \\ \boldsymbol{log_2}(\boldsymbol{Z_{(x)}})\ (\boldsymbol{b}) \end{cases}$ (Eq. 3.33)	$P_{25} * \begin{cases} (ln(Z_{(x)}) + \lvert\min\ (ln(Z_{(x)})\rvert)\ (a) \\ ln(Z_{(x)})\ (b) \end{cases}$ (Eq. 3.37)	-	-
$\boldsymbol{P_{50}} * \begin{cases} (\boldsymbol{log_2}(\boldsymbol{Z_{(x)}}) + \lvert\mathbf{min}\ (\boldsymbol{log_2}(\boldsymbol{Z_{(x)}})\rvert)\ (\boldsymbol{a}) \\ \boldsymbol{log_2}(\boldsymbol{Z_{(x)}})\ (\boldsymbol{b}) \end{cases}$ (Eq. 3.34)	$P_{50} * \begin{cases} (ln(Z_{(x)}) + \lvert\min\ (ln(Z_{(x)})\rvert)\ (a) \\ ln(Z_{(x)})\ (b) \end{cases}$ (Eq. 3.38)	$P_{50} * 2^{Z_{(x)}}$ (Eq. 3.40)	$P_{50} * e^{Z_{(x)}}$ (Eq. 3.43)
$\boldsymbol{P_{75}} * \begin{cases} (\boldsymbol{log_2}(\boldsymbol{Z_{(x)}}) + \lvert\mathbf{min}\ (\boldsymbol{log_2}(\boldsymbol{Z_{(x)}})\rvert)\ (\boldsymbol{a}) \\ \boldsymbol{log_2}(\boldsymbol{Z_{(x)}})\ (\boldsymbol{b}) \end{cases}$ (Eq. 3.35)	$P_{75} * \begin{cases} (ln(Z_{(x)}) + \lvert\min\ (ln(Z_{(x)})\rvert)\ (a) \\ ln(Z_{(x)})\ (b) \end{cases}$ (Eq. 3.39)	$P_{75} * 2^{Z_{(x)}}$ (Eq. 3.41)	$P_{75} * e^{Z_{(x)}}$ (Eq. 3.44)
-	-	$P_{90} * 2^{Z_{(x)}}$ (Eq. 3.42)	$P_{90} * e^{Z_{(x)}}$ (Eq. 3.45)

If $\min(log_2(Z_{(x)})) < 0$ or $\min(ln(Z_{(x)})) < 0$ then (a) and (b) if greater than 0. P_{10}, P_{25}, P_{50}, P_{75}, and P_{90} are respectively the 10th, 25th, 50th, 75th, and 90th percentiles of the DTB measurements. As proposed by Lachassagne et *al.* (2021), with a maximum DTB of 100 meters, the estimation is carried out using the following equation.:

$$DTB = 100 * Z_{(x)} \quad (Eq.\ 3.46)$$

3.3.3.2 Test case

The ParFlow model employs the Richard equation to solve groundwater flow in variably saturated systems which integrate both the subsurface and land surface of the Earth System (Kollet and Maxwell, 2006; Maxwell, 2013; Kuffour et *al.*, 2020). The free surface boundary condition is also captured through the two-dimensional overland flow and coupled to the Common Land Model (CLM) which simulates the water and energy fluxes (Naz et *al.*, 2023). The model setup is undertaken for the Nazinga catchment located near the border between Burkina Faso and Ghana extending from 11˚5' to 11˚12' latitudes and 1˚38.55' to 1˚33.15' longitudes (Fig. 2d). The semi-arid climate in the catchment is characteristic of the transition from the Sahelian to the Sudanian climate. The annual average rainfall reaches 994 mm/y (Bliefernicht et *al.*, 2022) with the mean temperature fluctuating from 22˚C in the raining season to 38˚C in dry season. The Nazinga Park is a natural reserve allocated for tourism and the indigenous communities mainly live on agriculture, livestock breeding and harnessing natural resources. The selection of the catchment is justified by the presence of an Eddy Covariance station, established in 2012 by the WASCAL CONCERT project, for monitoring water, energy, and greenhouse gas fluxes. This type of station is unique in the region as more than a hundred hydrometeorological variables are sensed or computed for the natural reserve.

The test case implemented in this section is undertaken to assess the overall accuracy of the computed DTB at a local scale. The model setup covers 100 km^2 around the Nazinga EC station with a horizontal resolution of approximately 30 m. The number of grid cells in both x and y directions is 334 and the vertical dimension is 10 grid cells with 4 attributed to the soil layer. The 1115560 grid cells are solved at hourly time step from January to February 2014. This corresponds to approximately 768 hours and it should be noticed that the simulation period is selected mainly to test the model's skill in replicating the fluxes. Although the noticeable deviations of the simulation from onsite measurements in representing certain water and energy

fluxes, the overall pattern of the components is reasonably well captured. This confirms the reliable skill of the surface and subsurface model coupling offered by PF-CLM in the study area. Further, the focus of this test case is also to assess the reliability of the watershed bottom representation using the overall average of DTB which fluctuates around 25 m (Fig. 2f). The necessity to undertake the model calibration and evaluate the discrepancies in the parameters is widely reported (Bijak & Hilton, 2022; Reinecke et *al.*, 2019) however this is not the focus of this study. The aim is not to make predictions, but rather to identify and analyze the key water and energy processes occurring within the watershed.

The model setup requires mainly two types of datasets: the static data and the meteorological forcing. In this case, the static variables consist of standard land surface datasets, including the digital elevation model (DEM, Fig. 2e), land cover (Fig. 2c), soil types (Fig. 2b), and geological units (Fig. 2a) that characterize the subsurface. Surface elevation in the study area ranges from 266 to 322 meters. The DEM, obtained from the HydroSHED website, is used to calculate slopes in both the x and y directions, which are necessary inputs for the PF-CLM model. The Moderate Resolution Imaging Spectroradiometer (MODIS) mission (Friedl et *al.*, 2002) land cover map was employed to represent the land management practices occurring in the study area which affect the spatial distribution of the fluxes. Although the Nazinga Park is officially labeled as a natural reserve, the MODIS land cover indicates a mixt of Evergreen Broadleaf Forest, Evergreen Needleleaf Forest, Savanna, woody Savanna, shrubland, and grassland with the latter ones making a significant proportion of the present domain (Fig. 2c). The soil types are obtained by clipping the HWSD FAO soil spatial database and this results in two soil classes coded 1536 and 1540 representing wet soils with an irreversibly hardening mixture of clay, quartz, and iron in the subsoil (Fig. 2b). Additionally, the geological unit is obtained from the GLHYMPS database, which identifies a single type classified as basement rock, as referenced in the GUM spatial database by Gleeson et *al.* (2011) and Börker et *al.* (2018). The recent version of the global database of groundwater systems' transmissivity is used in this data-scarce area where detailed subsurface representations require thorough fieldwork. The attribute table of the GLHYMPS shapefile contains the near-surface global permeability in logK format which is multiplied by 100 to obtain integer values (e.g. -1341). To convert these values from permeability (m^2) to hydraulic conductivity (m/s), the $logK$ values are first exponentiated using the expression $10^{k/100}$, then multiplied by the ratio of fluid density multiplied by gravitational acceleration to dynamic viscosity ($\frac{\rho * g}{\mu}$), where ρ represents fluid density in kilograms per cubic meter (kg/m^3), g is

gravitational acceleration in meters per second squared (m/s^2), and μ denotes dynamic viscosity in pascal-seconds (Pa·s).

The meteorological variables downloaded for the model forcing are ERA5-Land products accessible from the European Centre for Medium-Range Weather Forecasts (ECMWF) website (https://cds.climate.copernicus.eu/). These variables are total precipitation (m), 2m temperature (K), surface pressure (Pa), water-vapor specific humidity (kg/kg), longwave radiation downwards ($J\ m^{-2}$), shortwave radiation downwards ($J\ m^{-2}$), 10m u and v components of wind ($m\ s^{-1}$). The spatial resolution of the dataset is 0.1˚ which is regridded to 30 m using the bilinear interpolation implemented in the python package xESMF (https://xesmf.readthedocs.io/en/stable/). The variables are renamed to align with the input requirements of PF-CLM, and the resulting datasets are converted into ParFlow binary files (.pfb). For example, the variables originally labeled RAINRATE and Q2D for precipitation and surface pressure are renamed to APCP and Press, respectively. The simulation uses an hourly time step, covering the period from January to February 2014.

The simulated fluxes' accuracy in reproducing the ground truth is assessed using widely accepted error metrics such as Root Mean Square Error (RMSE), the Pearson Correlation Coefficient (PCC), Nash–Sutcliffe Efficiency (NSE), and Percentage of bias (PBIAS). The computed metrics are derived using open-source prediction fitness evaluator implemented in the Python packages ‘’hydroeval‘’ (Hallouin, 2021) and others like Scipy (Virtanen et *al.*, 2020) and Statsmodel (Seabold and Perktold, 2010).

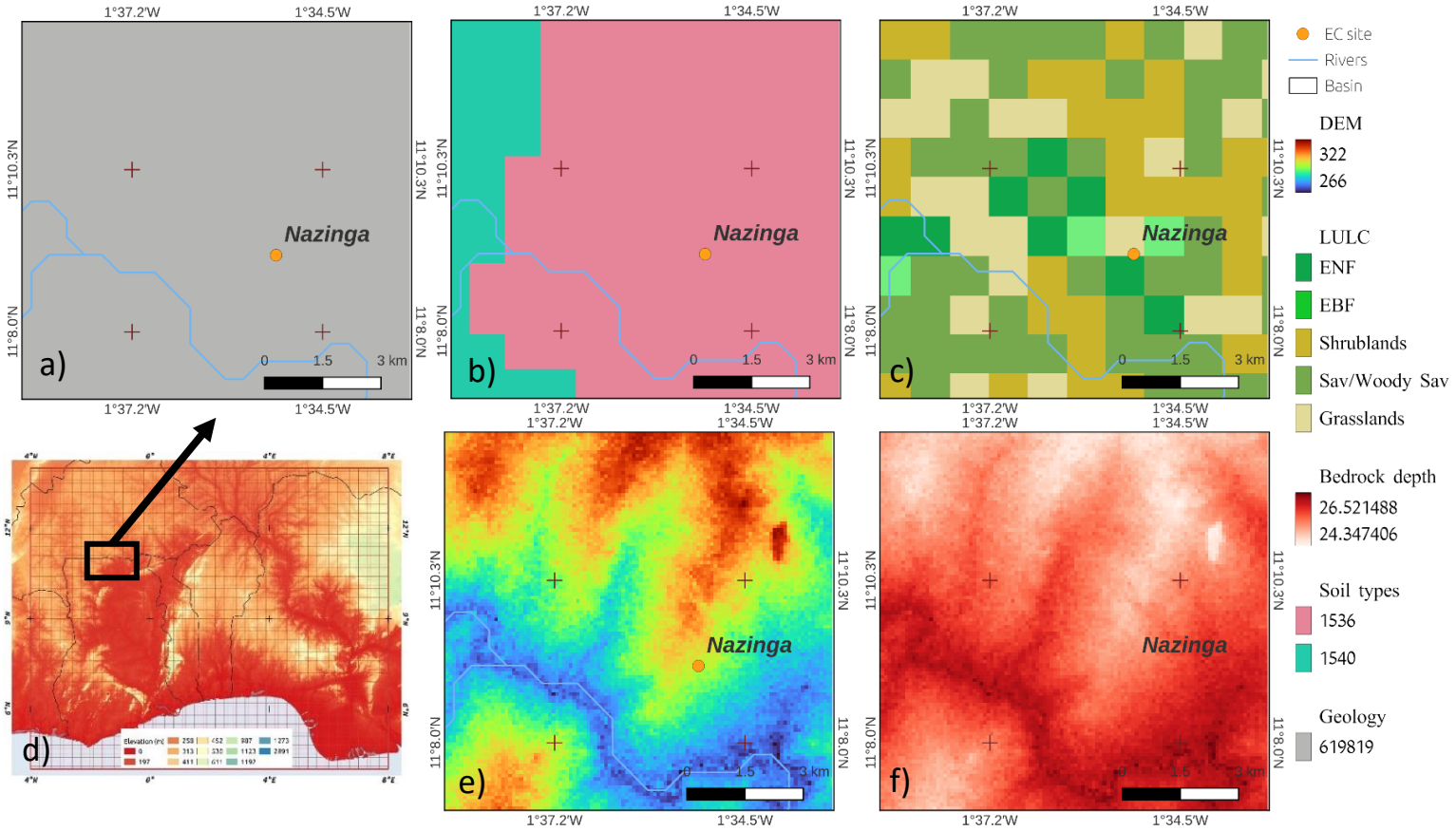

Figure 3.4: Digital elevation model (e), depth to bedrock (f), MODIS land cover (c), FAO soil types (b), basement hard rock geology (a), and the topography of a section of West Africa are shown, with a black box marking the Nazinga reserve and an arrow pointing to the specific study area (d).

3.4 Evaluation of Fractured Groundwater systems' influence on water and energy fluxes

3.4.1 Study area

The Donga subbasin is located in the North of Djougou in Northern Benin and covers approximately 600 km^2. It is a water and energy flux monitoring supersite equipped with hydrometeorological instruments by the African Monsoon Multidisciplinary Analysis - Coupling the Tropical Atmosphere and the Hydrological Cycle" (AMMA-CATCH) project in the Sudanian climate. Past reports highlighted the temporal fluctuations of the mean annual rainfall between 1190 mm (Lelay and Galle, 2005) and 1364 to 1534 mm (2008-2010, Mamadou et *al.*, 2016) extending from April to October. The seasonal dynamics of the Intertropical Convergence Zone (ITCZ) control the rainfall onset and cessation, and the study domain is subjected to the Sudanian climate (Sultan and Janicot, 2003). The change in absolute humidity separates the dry from the wet season. Less than 6 g m^{-3} of absolute humidity indicates the dry season, while in the wet season, the value is above 16 g m^{-3}. Approximately 90% of the annual precipitation is recorded between April and October, and 70% after the monsoon onset (July-October).

The metamorphic crystalline bedrock at the bottom of the domain is covered by the saprolite and a relatively flat landscape which altitude varies from 450 to 550 m with an average slope of 3%. The soil top layers within 40 to 60 cm are made of sandy loam and loamy sand (Mamadou et *al.*, 2016), also characterized as ferric lixisols by Faure and Volkoff (1998). These high-permeability soils fall within the widely reported tropical soil in the region (de Condappa et *al.*, 2008) and lie on top of the weathered clayey layers supported by the bedrock.

The natural ecosystem is not exempt from the reported land use degradation in the region (Grinblat et *al.*, 2015), with 53% of the domain occupied by herbaceous fallow, shrubland, and cropland (Seghieri et *al.*, 2009). The same study reported 47% of the woodland with sparsely scattered trees. In Northern Benin, food production from rainfed agriculture is made of annual crops (e.g., groundnuts, maize, cassava), which are rotated according to the agricultural practices. As mentioned above, the rainfall seasonality drives the fallow land regreening from scattered shrubland to dense herbaceous vegetation of 2.5 m (C4 plant) in October. The dominant vegetation species documented by Seghieri et *al.* (2009) and Houeto et *al.* (2012) are predominantly C3 plants, namely Isoberlinia doka and Burkea Africana, Isoberlinia tomentuosa, and Vitellaria paradoxa.

3.4.2 Methodology

3.4.2.1 ParFlow-CLM model approach

The model ParFlow-CLM solves the energy and mass balance equations both at the land surface and the subsurface (Maxwell and Miller, 2005). The coupled model is an enhanced representation of the Earth system which is an integrated and distributed hydrological model. The energy fluxes namely the turbulent fluxes, ground heat flux, evaporation and others are simulated with CLM and the water flow in the unsaturated and saturated zones with Parflow. In the past decades, the two have been extensively described, and the focus here is to provide only necessary processes engaged in this study. The energy balance equation serves as a primary basis to elucidate the fluxes exchange and is written as follows:

$$R_n(\theta) = SH(\theta) + LE(\theta) + G(\theta) \quad \text{(Eq. 3.47)}$$

R_n : The net radiation (W m^{-2}), H: sensible heat (W m^{-2}), LE : latent heat, and G the ground heat fluxes.

The change in each energy component depends on the soil moisture θ (kg/kg) in the first soil levels. The sensible energy flux is decomposed into the bare ground heat H_g and vegetation heat H_c :

$$SH = H_g + H_c \text{(Eq. 3.48)}$$

$$\text{with } H_c = \sigma_f L_{SAI} \rho_a c_p r_b \left(T_c - T_{af}\right) \text{ (Eq. 3.49)}$$

$$\text{and } H_g = \sigma_f \rho_a c_p C_{soilc} u_{af} \left(T_g - T_{af}\right) \text{ (Eq. 3.50)}$$

L_{SAI} : the stem plus leaf area index (m^2 m^{-2}), r_b: the leaf boundary resistance (sm^{-1}), σ_f : the vegetation fraction (unitless), c_p: the specific heat of dry air (J.kg^{-1} K^{-2}), ρ_a : the intrinsic density of air (kg m^{-3}), u_{af} : the magnitude of the wind velocity incident on the leaves (unitless), C_{soilc} : the transfer coefficient between the canopy air and land surface, T_g and $T_c$are respectively the ground surface and leaf temperature (K), and T_{af} : the air temperature in the canopy space (K).

The latent heat is a function of the sum of evaporation from the ground and the transpiration from the vegetation (E_g and E_c in kg.m^{-2}s^{-1}), and latent heat of evaporation (J.kg^{-1}):

$$LE = L_v E \text{ (Eq. 3.51)}$$

with $E = E_c + E_g$ (Eq. 3.52)

and $E_g = \rho_a \frac{q_g - q_a}{r_d}$ (Eq. 3.53)

q_a: the air specific humidity (kg.kg^{-1}) at reference height z_q which is derived from the forcing, q_g : the air specific humidity at the ground surface (kg.kg^{-1}), and r_d : the aerodynamic resistance of evaporation between the atmosphere.

Further, the transpiration from the vegetation E_c is decomposed into the transpiration E_{tr} and evaporation from wet foliage E_w (kg.m^{-2}s^{-1})

$$E = E_w + E_{tr} \text{(Eq. 3.54)}$$

with $E_{tr} = \sigma_f L_{SAI} \delta\left(E_f{}^{pot}\right) L_d \frac{r_b}{r_b + r_s}$ (Eq. 3.55)

and $E_w = \sigma_f L_{SAI}\left[1 - \delta\left(E_f{}^{pot}\right)(1 - L\tilde{}_w) E_f{}^{pot}\right]$ (Eq. 3.56)

δ : the step function (zero for zero and negative arguments and one for positive arguments), L_d: the dry fraction of foliage surface (unitless), r_s: the stomatal resistance (sm^{-1}), r_b: the conductance of heat and vapor flux from leaves (sm^{-1}), $L\tilde{}_w$: the wetted fraction of the canopy and $E_f{}^{pot}$: the potential evaporation from wet foliage (kg.m^{-2}s^{-1}).

The transient heat conduction in one dimension is used to compute the ground heat flux G and is written as:

$$G = \lambda \nabla T \text{ (Eq. 3.57)}$$

T : the subsurface temperature (K) and λ : the thermal conductivity of the soil (W m^{-1}K^{-1})

The balance between the incoming and outgoing radiation is defined as the net radiation () and written as:

$$R_n = S_{n,c} + S_{n,g} + L_a{}^{\downarrow} - L^{\uparrow} \text{(Eq. 3.58)}$$

$S_{n,c}$: the solar radiation absorbed by the vegetation (Wm^{-2}), $S_{n,g}$: the solar radiation adsorbed by the ground (Wm^{-2}), $L_a{}^{\downarrow}$: the incoming longwave radiation (Wm^{-2}), and $L^{\uparrow}$: the outgoing longwave radiation (Wm^{-2}).

The absorbed solar radiation ($S_{n,c}$ and $S_{n,g}$) is further parameterized in the CLM using:

$$S_{n,c} = \sigma_f \sum_{\wedge,\mu} F_{\wedge,\mu} S^{\downarrow}{}_{\wedge,\mu} \quad \text{(Eq. 3.59)}$$

$$S_{n,g} = S_n - S_{n,c} \quad \text{(Eq. 3.60)}$$

$$S_n = \sum_{\wedge,\mu} \left(1 - \bar{\alpha}_{\Delta,\mu}\right) S^{\downarrow}{}_{\wedge,\mu} \quad \text{(Eq. 3.61)}$$

$F_{\wedge,\mu}$: the fraction of solar radiation absorbed by canopy (unitless), $S^{\downarrow}{}_{\wedge,\mu}$: the component of the visible solar radiation (beam and diffuse), near-infrared (beam and diffuse), S_n : the net solar radiation absorbed by the land surface (Wm^{-2}), and $\bar{\alpha}_{\Delta,\mu}$: the weighted surface albedo over the grid cell.

Regarding the subsurface water dynamics, the mass balance equation below is used:

$$S_s \theta \frac{\partial \psi}{\partial t} + \frac{\partial \theta(\psi)}{\partial t} = \nabla . q(T) + q_s(\theta) \text{ (Eq. 3.62)}$$

S_s : the specific storage (m^{-1}), ψ : the soil pressure head (m), q_s : the source/sink term (s^{-1}), q : the water flux (ms^{-1}), t : the time (s)

In the first few meters soil depth, the general source/sink term can also be written as :

$$q_s = LE(\theta) + q_g(\theta) \text{ (Eq. 3.63)}$$

q_g : the infiltration from the precipitation, surface runoff and canopy throughfall (s^{-1}).

Therefore, the interactions between the subsurface and the land surface through the energy and mass transport is described through the nonlinear source q_s and the energy fluxes depending on the soil moisture (θ). The parameterization of the energy components ($R_n(\theta)$, $H(\theta)$, and $G(\theta)$), the source term $q_s(\theta)$, $q(T)$ and $\theta(\psi)$ and associated assumptions define mainly the accuracy of the coupled model. For instance, the convective component in the ground heat flux G is overlooked as the water flux q is deemed independent of the subsurface temperature T. In other word, the permeability coefficient of the vapor transport through the subsurface layers is counted for in the approximations of the ground evaporation.

3.4.2.2 Eddy Covariance Fluxes

An innovative way of monitoring the water, energy and greenhouse gases is the EC method which is proved reliable to understand the fluxes exchange between land surface and the atmosphere (Sjöström et *al.*, 2013; Gebler et *al.*, 2015). The Planetary boundary layer dynamics through turbulent fluxes (Baldocchi et *al.*, 1988; Swinbank, 1951; Mauder & Foken, 2006; Verma, 1990; Soltani et *al.*, 2018) and flux footprint information (Schmid, 1994) can be measured with relatively high accuracy using the EC method. Because of that, flux monitoring sites in many areas have adopted this method for various purposes like Earth system models validation, climate observation, and hydrological modeling. This method offers a measurement time scales as low as in seconds making the hydrometeorological processes observation arguably easy (Foken et *al.*, 2011; Soltani et *al.*, 2018). The EC method is basically implemented by measuring at high frequency the vertical wind velocity, the Sonic temperature and the gases density of the water vapor or CO_2 (McGloin et *al.*, 2018). The fluctuations of the vertical wind (m/s) and the air temperature (C) combined in one hand with the density of air (kg/m3) and specific heat of air (J/kg K) gives the sensible heat flux (H) and in other hand the vertical wind (m/s) and the specific humidity (Kg/Kg) with the latent heat of vaporization and the density of air is the latent heat flux (Finnigan, 1994). Achieving less error in the measurement is defined between avoiding a shorter block averages of time responsible of the loss of the longwave fluxes components and having a stationary measurement condition which time step is conventionally set to 30 minutes (Finnigan et *al.*, 2003; Foken, 2006). Nevertheless, one of the limitations in this method is related to the chosen time step as non-propagating eddies and low frequency motions are hardly captured (Lee & Black, 1993; Mahrt, 1998). The Reynolds decomposition is used as the basis in the EC method for the turbulent fluxes' calculation; that is the covariance between the vertical wind velocity and the concentration of a scalar (water vapour and air temperature) at a given location and time is what defines the estimated vertical flux (Mauder & Foken, 2015). The density and specific heat of air multiply by the covariance between the vertical wind components and the fluctuation in the air temperature gives the sensible heat flux while the density of air and latent heat of evaporation multiply by the covariance between the fluctuations in the vertical wind component and the specific humidity gives the latent heat flux (Soltani et *al.*, 2018; Eder et *al.*, 2014). The equations for the two turbulent fluxes (Kaimal & Finnigan, 1994) are written as follows:

$$SH = \bar{q} C_p \overline{W'T'} \quad \text{(Eq. 3.64)}$$

and

$$LE = \bar{q} L_v \overline{W'q'} \text{ (Eq. 3.65)}$$

where air density (Kg/m^3), specific heat of air (J/Kg K), latent heat of evaporation (J/Kg), fluctuations in the air temperature (°C), vertical wind component (m/s), and specific humidity (Kg/Kg) are respectively $\bar{q}$, C_p, L_v, T', W', and q'.

Many studies have reported the persisting Energy Balance Closure problem related to the EC method (Story et *al.*, 2013; Foken, 2008). The fact is that the turbulent and ground heat fluxes do not match up to the measured net radiation (Foken et *al.*, 2006; Foken et *al.*, 2011, Mauder et *al.*, 2017). According to the law of energy conservation, the sum of the fluxes approximates 0 which is rarely the case and has remained a key research question.

$$R_n - LE - SH - GH \approx 0 \text{ (Eq. 3.66)}$$

The estimated energy gap in past studies is 10-30% (Stoy et *al.*, 2013), with isolated cases where the lower gap was recorded (Ose, 1999). This issue has placed a significant limitation on the reliability of the approach. Because of the heterogeneity of the land surface below the planetary boundary layer, large-scale eddies occur as secondary circulation and are widely reported as the main source of the energy gap. Mauder et *al.* (2007a) confirmed that homogeneous land covers behave as an ideal condition for the EBC, while a very heterogeneous surface exacerbates the EBC residuals (10-15% and 25-35%). The EC method uses the short-period wind direction (u, v, and w) for turbulent fluxes estimation, which is not suitable for detecting large-scale eddies. It is less likely for a single location-based measurement to detect the heat fluxes induced by large-scale eddies. The area averaging measurement approach and land surface model reduce the EBC gap (Liu et *al.*, 2011; Foken et *al.*, 2008; Stoy et *al.*, 2013) as they integrate the landscape influence. Further, the energy balance residual can be reduced if long-term integrated fluxes are considered (Mauder and Foken, 2006), likewise organized turbulent structures (Kenda et *al.*, 2004). This study endeavors to ascertain the contribution of the subsurface configuration on the fluxes as the aforementioned factors are solely land-atmosphere related. We evaluated the sensitivity of the fluxes to the geological lineaments of the critical zone in Donga catchment. Further, the effect on the evaporative fraction (EF) and latent heat of evaporation is also assessed. The EF is written as follows:

$$EF = \frac{LH}{LH+SH} \text{ (Eq. 3.67)}$$

And the latent heat of vaporization is computed as follows:

$$L_v = \frac{LE}{E} \quad \text{(Eq. 3.68)}$$

3.4.2.3 Fractured groundwater systems descriptions

The principal circulation medium in fracture-rock groundwater systems which by definition extends to soft rocks and others alike is mainly controlled by the fractures and fissures network (Troeger & Chambel, 2021). Also known as secondary porosity groundwater systems, they are characterized by faults, fissures, joints and others derived from hard-rock breakdown. Groundwater flow in these weathered geological conditions is defined by the hydrodynamic properties of the saprolite and the fractures. There is a widely recognized challenge that makes hard-rock groundwater systems identification difficult almost everywhere, that is the chaotic nature of the changes in the groundwater flow from porous medium to directional which drives wells' productivity (Krasny, 1996; Lachassagne et *al.*, 2011). Even in deep layers, the Aspo Hard Rock Lab in Sweden (Knutsson, 1998) reported a well-developed network which turns out to be a very low productivity fractured aquifer. The remote sensing products (e.g., Landsat images) are widely reported as reliable tools for locating and mapping these linear features.

The geological lineaments are derived from Earth Observation (EO) products in form of linear features (Rahnama and Gloaguen 2014a, b). The frequency and spatial domain approaches are used to enhance linear elements in a satellite image by increasing the contrast between a given linear element and its surroundings. To detect these high frequency features, either the optimal filter (Canny), Laplacian filter (LOG) or gradient filters (Sobel and Prewitt) are applied. The geological lineaments are retrieved after differentiation, smoothing, and labeling of the linear features (Oussou et *al.*, 2020, 2019; Stanislawski et *al.* 2018). The dataset employed in this study is obtained from Oussou et *al.* (2022, 2020, and 2019) which are derived from digital elevation models, optical, and radar multispectral images. The geological lineaments are corrected and displayed in Figure 3.5. The accurate mapping of the lineament is critical for borehole sitting in the relatively low groundwater systems' productivity regions. The directional groundwater flow in basements is identified using the lineaments as spatial indicators of high subsurface flow hotspots. The section 3.5 highlights the implementation of their hydraulic properties in the model setup.

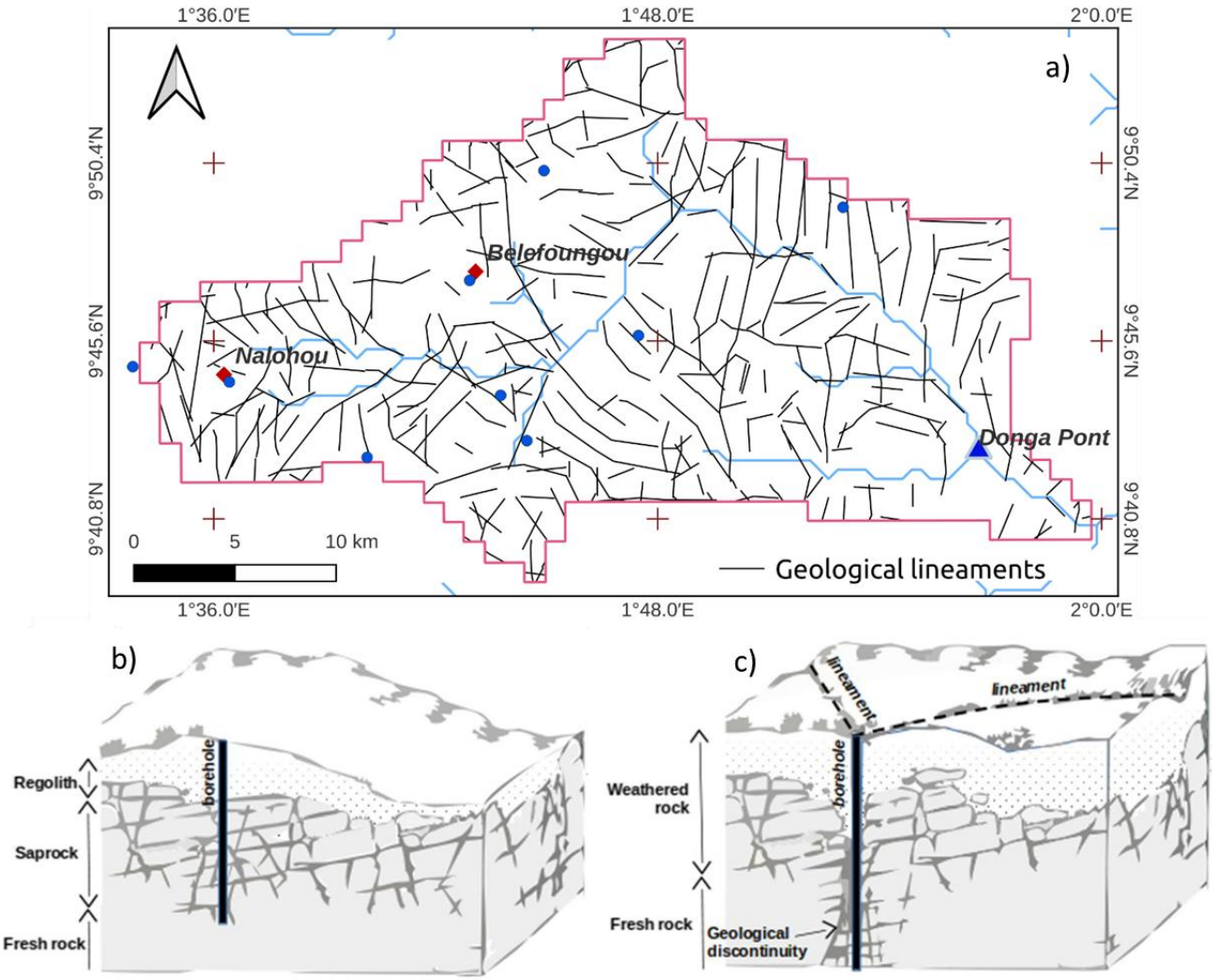

Figure 3.5: Lineament map of Donga basin (a), and vertical profiles of a typical hardrock aquifer (b and c) modified from Lachassagne et *al.* (2011) and MacDonald et *al.* (2005) in Adeotan et *al.* (2025).

3.4.2.4 Model setup and domain description

The evaluation of the groundwater flow and its interaction with land surface fluxes is undertaken using the coupled hydrological model ParFlow-CLM (Kollet and Maxwell, 2006; Maxwell, 2013; Kuffour et *al.*, 2020). The subsurface model solves the Richards equation within a three-dimensional variably saturated system. It uses the kinematic wave equation to simulate overland flow (Kollet & Maxwell, 2006) and is coupled with the Common Land Model (CLM; Dai et *al.*, 2003) to compute water and energy balances (Maxwell & Miller, 2005). The land surface component supplies key surface fluxes and variables, including turbulent heat fluxes, ground heat flux, outgoing longwave radiation, evapotranspiration, soil and canopy evaporation, plant transpiration, soil temperature, and freeze–thaw dynamics.

The domain setup is the Donga catchment located in the Donga department of Benin, with a rectangular coverage of 27 x 47 km^2. It extends from 1°33’ E to 2°00’ E longitudes and 9°35’ N to 9°57’ N latitudes. The predominant soil type is the ferruginous soil on hard rock (Fig. 3.6). The humid subtropical climate zone has a unimodal rainy season driven by the northeast and southeast trade winds convergence (Intertropical Convergence Zone - ITCZ) and a dry season from November to March. The annual rainfall is estimated between 700 and 1400 mm (Galle et *al.*, 2018; USGS, 2020a and b), with an average temperature of 25°C (Herzog et *al.*, 2021). The rainfall gradient is south-north, and the highest rates are recorded towards the coast. The study area is equipped by the project African Monsoon Multidisciplinary Analysis - Coupling the Tropical Atmosphere and the Hydrological Cycle" (AMMA-CATCH) since 1997, it is a component of a mesoscale observatory network which focuses on climate, water cycle and land cover monitoring. Multiple parameters are measured, but this study used streamflow, water level, water and energy fluxes, and soil moisture for the model assessment. The catchment lies on fractured groundwater systems (Fig. 3.5) which are mainly exploited for drinking water supply. Therefore, this study endeavors to ascertain the influence of the geological lineaments on water and energy balances. The active modeling domain spans the entire basin, covering an area of 576 km^2 with a spatial resolution of 75 meters. It consists of 627 grid cells in the x-direction and 360 in the y-direction, while the vertical dimension includes 10 layers, with the top four representing soil layers. The model runs on an hourly time step for the full year of 2014, from January to December. This PF-CLM configuration is designed to evaluate the role of fractured groundwater systems in influencing water and energy balances, aiming to provide a comprehensive understanding of how subsurface characteristics affect land surface processes. A spin-up

simulation is performed over several years until dynamic equilibrium is achieved, defined by a total storage change of less than 2%, in line with previous studies (O'Neill et al., 2021; Naz et al., 2023). The pressure files of the initial steady-state are used as input for the simulations.

The static variables used for the model setup include the digital elevation model (DEM), soil type data, land cover, and a geological map with associated groundwater permeability attributes. The DEM, sourced from the HydroSHED database (Lehner et al., 2008), is used to define the domain geometry solid file (pfsol) and to calculate slope values in both x and y directions. Soil types are obtained from the FAO Harmonized World Soil Database v2.0 (HWSD; Fischer et al., 2008) at a spatial resolution of 1 km, with two soil classes (15 and 17) identified in the study area. Although a more detailed representation of soil types could enhance model performance, this is beyond the scope of the current study. The domain's indicator field is constructed using the soil data along with aquifer layers derived from the GLobal HYdrogeology MaPS (GLHYMPS) dataset on permeability and porosity (Gleeson et al., 2011). Across the entire domain, the estimated hydraulic conductivity is 2.9×10^{-4} m/h (see Table 3.4). Geological lineaments are incorporated based on their horizontal and vertical positions, as further explained in Section 3.5. Additionally, land use data from the Moderate Resolution Imaging Spectroradiometer (MODIS) are processed to generate the drv_clmin input file required by the CLM model, along with the associated vegm and vegp files.

The meteorological forcing data used to drive the ParFlow-CLM model are sourced from the ERA5-Land reanalysis dataset provided by the European Centre for Medium-Range Weather Forecasts (ECMWF) (Muñoz-Sabater et *al.*, 2021). The variables extracted include downward shortwave and longwave radiation (J m^{-2}), 2-meter air temperature (K), specific humidity (kg/kg), 10-meter u and v wind components (m/s), and surface pressure (Pa). In addition, daily rainfall data from 12 meteorological stations—Adio, Baba, Bira, Dogue, Gnonganbi, Gountia, Kolokonde, Koukoubou, Nalohou 2, Nalohou 3, Nangatchouri, Penessoulou, and Tebou—are obtained from the AMMA-CATCH project database (Lebel et *al.*, 2009). With the geographic coordinates of the stations, the time series are regionalized using the Scipy package function "Interpolate" and converted to ParFlow binary file. The temporal resolution is set to hourly, and the simulation period extends from January to December 2014.

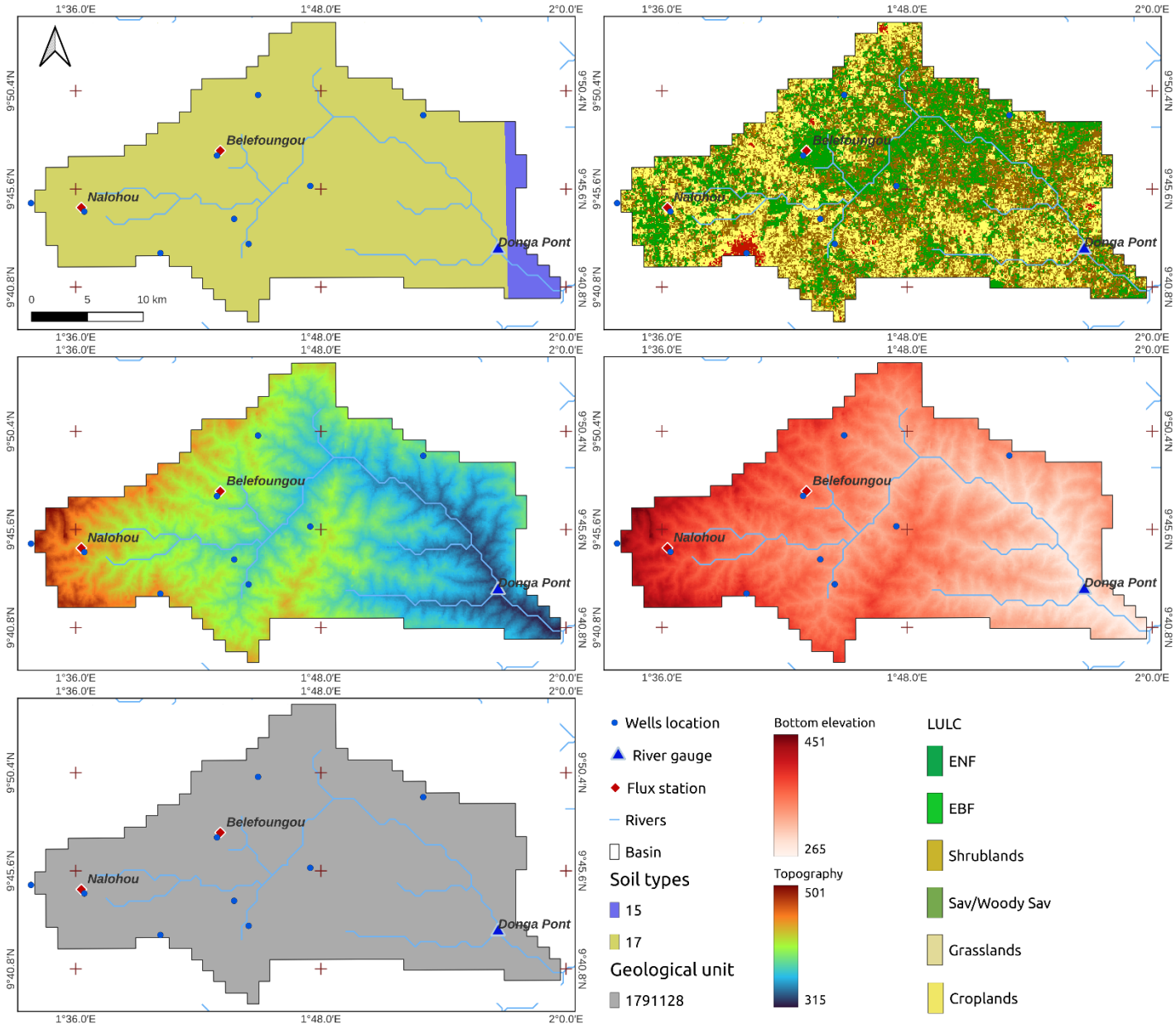

Figure 3.6: Digital elevation model, depth to bedrock, MODIS land cover, FAO soil types, basement hard rock geology, and the topography of Donga basin.

3.4.2.5 Simulated scenarios

The ability of a given model to simulate the groundwater head, the lateral groundwater flow and groundwater-surface water interactions depends on how accurately the groundwater systems' properties are represented. Attempts to accurately map aquifer properties at the global level like GLobal HYdrogeology MaPS versions 1 and 2 (GLHYMPS; Gleeson et *al.*, 2014; Huscroft et *al.*, 2018) still require improvement at the local scale. GLHYMPS is based on a global-scale lithology map with poor spatial variability which does not reflect the complexity of the geological features at the local scale. These permeability coefficient products are the only available at a global scale for the upper 100 m of the subsurface. However, they are reported to contain discrepancies such as biases towards lower permeability (Gleeson et *al.*, 2014; Huscroft et *al.*, 2018) and inconsistency in regions where permeability shifts up to an order of magnitude. Part of the errors is attributed to the accuracy of the global lithological map database GliM (Hartmann & Moosdorf, 2012), which is assembled at a target scale of 1:1000000 and has a considerable influence on the GW models' water table depths, fluctuations, and head (Reinecke et *al.*, 2019).

The land-subsurface interactions due to the fractures' permeability coefficient are investigated in this study. Five simulation experiments are undertaken to evaluate the influence of the fractured subsurface on water and energy fluxes. The geological lineaments mapped in section 3.3 are converted to raster format using QGIS tool "Rasterize''. The 2D array is used to select the corresponding position in the 3D indicator field which features the geometry for Parflow model. As the z direction is made of 10 grid cells (see section 3.4), the geological lineaments were extended from the bottom (hard rock) to the last 6^{th} cell below the 4 soil layers. The reference scenario is the simulation with a constant permeability coefficient for the entire subsurface derived from GLHYMPS database (Huscroft et *al.*, 2018). For the remaining scenarios, the fractures are assigned permeability values (see Table 3.4) following the textbook practices and the suggestions by Freeze and Cherry (1979). The choice of these permeability values is mainly because the authors made a clear distinction between the grain sizes which serves the purpose of this study. With the lowest permeability attributed to clayey fractures and high values to sandy ones, the magnitude of the effect of fractures on land surface fluxes can be ascertained as the permeability coefficient plays a critical role in PF-CLM model. Gleeson et *al.* (2011) updated Freeze and Cherry (1979) findings by attributing to different lithologies the geometric regional-scale mean permeability. However, the hydrolithologic and lithologic classes

used are generalization of a rather complex geological units which are quite difficult to exhaustively map let alone their hydrogeological properties.

The tested scenarios are based on the assumption that fracture formation under tectonic actions can result in different types of geological discontinuity. That is, after the hard rock breakdown, the debris from the erosion that fills the discontinuity can vary from low permeability rocks (clay) to high permeability (e.g., sand or gravel). This study endeavors to ascertain the impact of these options on water and energy fluxes. Therefore, it identifies the best fit for the Donga catchment and broadens the assessment of the impact of improved subsurface representation in land surface models (LSM). The scenarios assume a uniform distribution of the fracture permeability coefficient which can be perceived as an idealistic scenario.

Table 3.4: Tested scenarios with corresponding permeability values and description.

Scenarios ID	Permeability (m^2)	Description	Reference
REF	$7.9\ 10^{-15}$	GLHYMPS 2.0: a global scale hydrogeological properties database	Gleeson et *al.*, 2014; Huscroft et *al.*, 2018
High K	10^{-10} - 10^{-7} ($10^{-8.5}$)	Gravel: high permeability	Freeze and Cherry (1979); Gleeson et *al.* (2011)
Moderate K	10^{-13} - 10^{-9} (10^{-11})	Sand: moderate to high permeability	Freeze and Cherry (1979); Gleeson et *al.* (2011)
Low K	10^{-19} - 10^{-16} ($10^{-17.5}$)	Clay: Low permeability	Freeze and Cherry (1979); Gleeson et *al.* (2011)

3.4.2.6 Evaluation approach

The performance of the simulated scenarios is evaluated with widely reported metrics, namely the Kling–Gupta efficiency (KGE), Pearson Correlation Coefficient (R), and the percent bias (PBIAS). The R captures the monotonic relationship between the simulated and observed values, while KGE highlights the similarity. KGE includes the linear agreement, and biases in the mean and variability with stronger performance values close to 1. The PBIAS (%) gives the average tendency of the simulations to overestimate or underestimate the observed values. The simulations are compared to observations from the AMMA-CATCH project (fluxes and streamflow), remote sensing (ESA CCI soil moisture, GRACE TWS), and reanalysis products (GLEAM evapotranspiration and soil moisture). The KGE, R, and PBIAS are calculated as follows:

$$KGE = 1 - \sqrt{(corr - 1)^2 + \left(\frac{std(y_i)}{std(x_i)} - 1\right)^2 + \left(\frac{\sum y_i}{\sum x_i} - 1\right)^2} \text{ (Eq. 3.69)}$$

$$R = \frac{\sum(x_i - \bar{x})(y_i - \bar{y})}{\sqrt{\sum(x_i - \bar{x})^2 \sum(y_i - \bar{y})^2}} \text{ (Eq. 3.70)}$$

$$PBIAS = 100.\frac{\sum_{i=0}^{N}(y_i - x_i)}{\sum_{i=0}^{N} x_i} \text{ (Eq. 3.71)}$$

y_i: Simulated values, x_i: Observed values, N: length of the series, $std(y_i)$: standard deviation of simulated values and $std(x_i)$: standard deviation of observed values, $\sum y_i$ and $\sum x_i$ are the sum of the simulated and observed values, and $corr$: correlation coefficient.

Further, the centered root mean square difference (cRMSD) and the percent change (PC) are used to assess the change in water and energy fluxes under the scenarios C1, C2, C3, and C4 compared to C0. The cRMSD is a modified form of RMSD and is written as follows:

$$cRMSD = \sqrt{\frac{1}{N}\sum_{i=1}^{N}[(x_i - \bar{x}) - (y_i - \bar{y})]^2} \text{ (Eq. 3.72)}$$

And

$$MSD = RMSD^2 = \frac{1}{N}\sum_{i}^{N}(x_i - y_i)^2 \text{ (Eq. 3.73)}$$

The relative change of simulations to the reference is computed as follows:

$$PC = \frac{Sim - REF}{REF} * 100 \text{ (Eq. 3.74)}$$

The reference simulation (REF) corresponds to the scenario C0. The variables used for the impact analysis are energy fluxes (sensible heat, latent heat, ground heat, and outgoing longwave radiation), energy balance closure (EBC), evaporative fraction (EF), latent heat of vaporization (L_v), soil moisture, evapotranspiration, groundwater table depth (WTD), terrestrial water storage (TWS), and streamflow.

3.5 Impact of Climate projections on groundwater recharge, levels, surface water storge

The uncertainties related to the influence of future climate change projections on groundwater resources are yet to be thoroughly clarified. Therefore, this study investigates the potential changes in groundwater recharge, levels, surface water storage, and overland flow in the Donga basin. Five Global Circulation Models (GCMs) are used under two different Shared Socioeconomic Pathways (SSP1-2.6, SSP5-8.5). The purpose is to evaluate the groundwater resources' response to different warming scenarios. As commonly used in past studies, the projected variables (e.g., Precipitation) from the GCMs are added to other required variables (e.g., Wind and surface pressure) for running the integrated hydrological model Parflow-CLM. The domain description and model setup are described in the sections 3.4.2.4.

3.5.1 Climate scenarios

The climate variables from future projections are derived from five GCMs namely GFDL-ESM4, HadGEM3-GC31-LL, IPSL-CM6A-LR, MIROC6, and NorESM2-MM provided by the sixth phase of the Coupled Model Intercomparison Project (CMIP6). The precipitation and temperature variables are retrieved from the Climate Data Store (CDS) website. The two Shared Socioeconomic Pathways (SSP1-2.6 and SSP5-8.5) are chosen to evaluate the spread between the low and high emissions. The future climate forcing covers the historical period and the end of the century. The downloaded climate variables are regridded to 75 m horizontal resolution to match the model setup described in the above section. Likewise, the temporal resolution is resampled from daily to hourly. As the model is run at a hourly time step, a synthetic diurnal cycle is added while converting the daily temperature is hourly. The regridding of the downloaded variables is done with the Python Package xESMF. The baseline scenario used to represent the current climate covers 1850 to 2014, which serves as a reference simulation. The differences between the end-of-century projections (2050-2099) and the baseline are computed for each of the simulated subsurface variables (groundwater recharge, levels, surface storage, and overland flow). As described in Table 3.5, the choice of the five GCMs under the two SSP1-2.6 and SSP5-8.5 provides the possibility to assess uncertainties in the model projections and the spread of the projected change at the end of the century. A total model run of 15 is undertaken to achieve the aforementioned scenarios.

Table 3.5: Time periods of Global warming in the GCMs under SSP1-2.6 and SSP5-8.5

	GFDL-ESM4	**HadGEM3-GC31-LL**	**IPSL-CM6A-LR**	**MIROC6**	**NorESM2-MM**
Historical	1850-2014	1850-2014	1850-2014	1850-2014	1850-2014
SSP1-2.6	2050-2099	2050-2099	2050-2099	2050-2099	2050-2099
SSP5-8.5	2050-2099	2050-2099	2050-2099	2050-2099	2050-2099

3.6 Soil N_2O and CH_4 emissions in contrasting land use of the Sudanian savanna

3.6.1 Study region and sites description

This study was undertaken at four contrasting greenhouse gases monitoring locations in the Sudanian savanna, Northern Region, Ghana for two consecutive rainy seasons (2023 and 2024; see Fig. 3.7). The land use types are cropland (Kayoro), semi-degraded grassland (Gorigo), rainfed paddy rice fields (Janga) and a protected savanna woodland within a national forest reserve (Mole Park). The monitoring locations are part of the WASCAL-hydrometeorological observatory installed in the last decade (Bliefernicht et *al.*, 2018; Berger et *al.*, 2019; Guug et *al.*, 2025). This region is intensively used for agriculture practices. The natural savanna vegetation was therefore strongly converted to different agricultural systems in this region over the past decades Water, energy and carbon fluxes at the different sites are monitored with the Eddy Covariance method (Quansah et al, 2015, Berger et *al.*, 2019 and Guug et *al.*, 2025) since 2013 at Kayoro, 2017 at Gorigo, 2022 at Janga, and 2023 at Mole Park. In addition, chamber measurements were taken at these sites in 2023 and 2024 to further ascertain the N_2O, CH_4, and CO_2 fluxes (Fig. 3.8).

The geographic boundaries of the area extend from latitude 9º26.4'N to 11º12.4'N and longitude 2º12'W to 0º.41.4'W with the altitude varying from 93 to 488 m. The seasonal cycle of rainfall is strongly linked to the movement of rainfall belt of the West African Monsoon determing the rainfall onset and cessation (Sultan and Janicot, 2003, Nicholson 2013). The annual rainfall is monomodal in the southern Sudanian savanna extending between May and October. The mean annual precipitation ranges between 900 mm and 1100 mm (Bliefernicht et *al.*, 2018; Bliefernicht et *al.*, 2022). The annual average air temperature varies between 26 and 33°C. Different dominant vegetation species are reported in the area such as *Lannea microcarpa*, *Adansonia*, and *Parkia biglobosa* (Quansah et *al.*, 2015). Near the flux tower, the cultivated crops in 2023 and 2024 are soybean and groundnut at the cropland site (Kayoro). Further site characteristics about Kayoro and Gorigo are given by Bliefernicht et *al.* (2018) and Mole Park and Janga in Guug et *al.* (2025). During the gas sampling period, the cropland was ploughed and fertilized after applying a selective herbicide (Glyphosate 410g/L SL) on the 18th July 2023 and 24th June 2024 at the cropland site. Likewise, the rice fields was subjected to similar agricultural practices on the 25th July 2023 and 26th June 2024. The local community undertook a low-intensity mixed grazing of livestock (cattle and sheep) at the grassland site.

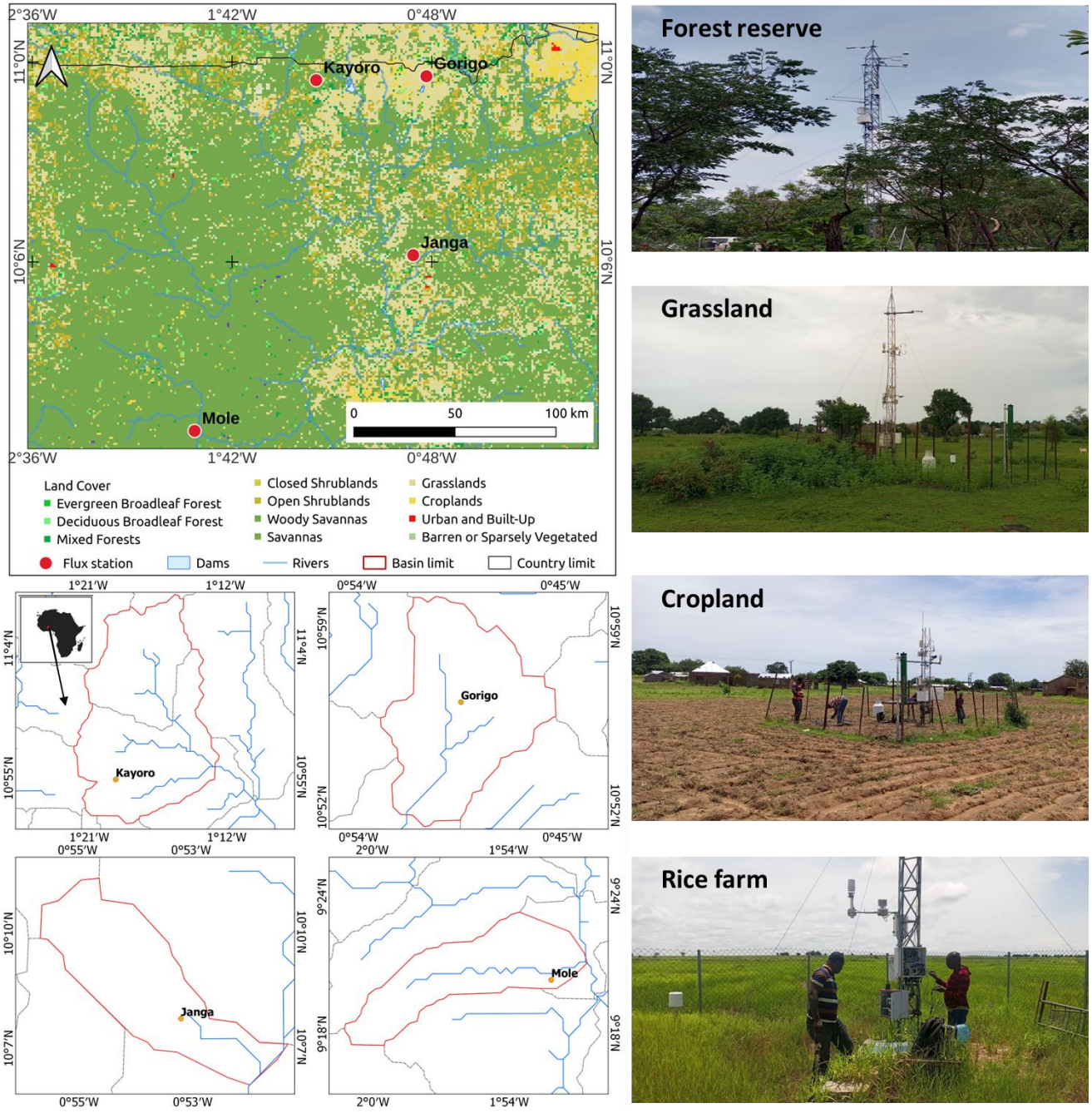

Figure 3.7: Study region and the four monitoring sites Kayoro "cropland", Gorigo "grassland", Janga "rice fields" and Mole Park "forest reserve"

3.6.2 Procedures of the field GHG measurement

3.6.2.1 Experimental design

The field campaign with the chamber measurements was done in 2023 and 2024 on a weekly basis covering the peak monsoon period and therefore the main vegetation and cultivation period in this region (Fig. 2). The first samples were collected at Kayoro, Gorigo and Janga by the end of May 2023 (29th of May 2023). The sampling at the Mole Park started end of July 2023. The sampling was always done in the morning, between 9 and 11 AM, when the turbulent fluxes of the planetary boundary layer deploy progressively until the highest around the noon time. Because of this time constraint and the average distance (105±50 km) to the EC sites, the gas sampling is undertaken for each site per day. The sampling is done at Gorigo, Kayoro, and Janga from Monday to Wednesday and the Mole Park gas sample is collected later during the week.

The chamber-based measurement of greenhouse gases is deployed in various ecosystems in the last decades and the experimental design changes based on the purpose of specific studies (Maier et *al.*, 2022; Murphy et *al.*, 2022). In this study, the designed chamber is made of two parts: the collar and the intransparent lid. It is a 37 x 26.7 cm size collar which is implanted at 10 m from the EC tower. Five sub-trial points (chambers) are deployed at each site to ascertain the spatial variability. The first is located at the north (0N) and the following at the interval of 72 degree.

Figure 3.8: Chamber-based greenhouse gas sampling plots; closed (middle) and opened for soil moisture and temperature measurements (left and right) in a rice field at Janga, Upper-East Ghana

3.6.2.2 Chamber sampling and analysis

De Klein & Harvey (2015) described the static chamber method for the N_2O measurements. In this study, the plastic collar of the chamber is inserted into the ground at 2-5 centimeters depth and left on the field throughout the measurement periods. The average head space volume is approximately 20L. The sampling starts with the soil moisture and temperature measurement for each sub-trial chamber. For 20 minutes, the chambers are closed and the gas sample is taken at 5, 10, 15 and 20 minutes at the top of the chamber through a rubber septum. A 50 mL poly-propylene syringe attached to a hypodermic needle is used to extract the air from the closed chamber. The gas sample is then transferred into a sealed and pre-evacuated glass exetainer of 10 mL. The choice of the sampling period (9:00 to 11:00 AM) is based on the suggestions that 94 to 101% of the "true" seasonal emissions is captured early in the morning and evening (Weller et *al.*, 2015; Charteris et *al.*, 2020). The weekly sampling is undertaken almost the same day for each site throughout the measurement period on different days of the week.

During the sampling, 50 ml of air is taken from the chamber using a syringe; 70 percent of the sample is used to flush the vial, after which the remaining 15 mL is injected with a slight overpressure in the 10 mL vial (see Calvo-Rodriguez et *al.*, 2020).

At the end of the sampling process, the chambers' height, soil moisture, and temperature are measured. The gas fluxes are computed as follows:

$$F_{CH} = \frac{d_q}{d_t} \times \frac{V \times P \times M_w}{R \times T} \times \frac{60}{A \times 1000} \quad Eq.(3.75)$$

$\frac{d_q}{d_t}$: change in the mixing ratio over time (ppb min^{-1} or ppm min^{-1}) resulting from the linear fit, T: average temperature during sampling (°K), P: long-term average air pressure of the site (Pa), V: chamber volume (m^3), Mw = 12 for CO_2 and CH_4 and Mw = 28 for N_2O (g mol−1), A is the surface area of the chamber (m^2) and R is the universal gas constant (J mol^{-1} $°K^{-1}$).

The monthly means were calculated for each land use after the quality control which is made of two main criteria. In case the calculated flux is an outlier, the estimated flux is benchmarked against the temporal average from previous values and a measurement is considered valid if the coefficient of determination is greater than 0.8, 0.6, and 0.6 respectively for CO_2, CH_4, and N_2O fluxes. If the coefficient is less than 0.8 for the CO_2 flux, the calculated fluxes for the

site that week are altogether rejected. The fluxes are valid if the coefficient is greater than 0.8 for CO_2 flux and 0.6 for N_2O and CH_4 fluxes (e.g., Calvo-Rodriguez et *al.*, 2020).

3.6.2.3 Soil moisture and temperature measurements

Each gas sampling procedure is preceded by the soil volumetric water content (VWC) and temperature measurement. The soil thermometer and moisture sensor are implanted inside the chamber collar and the values are read on the device screen. Following the recommendation of Werner et *al.* (2014), the soil water-filled pore space (WFPS) is calculated using VWC values.

3.6.2.4 Soil sampling and analysis

Before the GHG sampling, soil core samples are collected at 5 different depths (0-5cm, 5-10cm, 15-20cm, 30-35cm, 45-50cm) with four soil profiles per depth at each site (Table S2). The soil physicochemical properties were measured at Janga, Kayoro, and Gorigo (n=45). The nitrogen content and soil organic carbon are measured at KIT IMK-IFU laboratory. The bulk density (BD) is calculated for each soil sample dried at 105˚C for 24h. The soil volumetric water content and BD values are used to calculate the soil water filled pore space (WFPS) following the suggestions of Werner et *al.* (2014).

$$WFPS[\%] = \frac{W_{vol}}{\left(1 - \frac{BD}{2.65}\right)} Eq.(3.76)$$

$W_{vol}$is the volumetric water content, BD the bulk density [$g\ cm^{-3}$], and 2.65 the particle density [$g\ cm^{-3}$].

The isotopic signature of carbon (δ13C) and nitrogen (δ15N) of each sample are also measured. The isotope Ratio Mass Spectrometry test AIL-1.1c (2015-02) used for the analysis is a flexibly accredited method by the European standard DIN EN ISO/IEC 17025:2018. The analysis of the ratios of the stable carbon isotope $\delta^{13}C/\delta^{12}C$ shows altogether a higher rate of $\delta^{12}C$ at the three managed sites originating from a mixture of C3 and C4 plants with dominance towards C4 (Fig. S1). For all the sites, the ratios oscillate from -19.9 to -14.3‰ with respectively an average of -17.29±0.1, -17.93±0.11, and -17.48±0.1 for the grassland, cropland, and rice fields. Similar ranges between -24 and -13‰ at a grassland, -18 and –15‰ at a maize field, and –17 and -15‰ are obtained by Gerschlauer et *al.*, (2019) at Kilimanjaro mount. The carbon ratio increases slightly with the depth at the grassland and cropland sites while the values remain in the same

range at the rice fields. Unlike the low nitrogen content, the carbon content is relatively moderate to low with $\delta^{13}C$ averages of 0.23±0.0%, 0.23±0.1%, and 0.47±0.2% respectively.

Table 3.6: Descriptions of the investigated sites: altitude, annual precipitation (AP), mean annual air temperature (MAT), soil organic carbon (SOC), soil nitrogen (Ntot), soil carbon to nitrogen ratio (C/N), N fertilization rate (Nr), bulk density (BD), texture (%), and soil types. The parameters refer to soil depth from 0 to 50 cm. The values are derived from Eddy Covariance measurements and reanalysis products (*) because of missing data. Further details about the sites are provided in Quansah et *al.* (2015), Bliefernicht et *al.* (2018), and Berger et *al.* (2019).

Site name	**Land cover**	**Altitude (m)**	**AP (mm)**		**MAT (°C)**		**$\delta^{13}C/\delta^{12}C$ (‰)**	**Soil C (%)**	**Ntot (%)**	**C/N**	**Nr**	**BD (g/cm3)**	**Texture (%) sand/silt/clay**
			2023	2024	2023	2024							
Mole	Forest	159	1029*	889*	28.36*	28.63*	-	1.62±0.35	0.154±0.03	10.64	-	-	-
Gorigo	Grassland	217	952*	1042*	28.97	32.55	-17.29±0.1	0.32±0.015	0.04±0.0	8	-	1.66±0.11	-
Kayoro	Cropland	292	959*	877.9	29.99	29.57	-17.93±0.1	0.39±0.11	0.046±0.012	8.48	Low	1.65±0.08	770.9/20.05/2.87
Janga	Rice fields	118	883*	1011*	26.05	26.52	-17.48±0.1	0.62±0.092	0.057±0.005	10.88	Low	1.53±0.09	-

3.6.2.5 Statistical Analysis

The sampling period extends from May to October for the two consecutive years. The annual and monthly means are calculated for each year for comparative analysis. The Kolmogorov-Smirnov test is used to evaluate the normality of the variables. The paired t-test is used to assess the difference between the sites and years. The environmental controls over the GHG fluxes at each site are evaluated using the multiple stepwise regression analysis. The factors considered are WFPS and soil temperature. The data processing is done in Python with modules such as Scipy, Pandas, and Statsmodels.

Table 3.7: Descriptive statistics of the seasonal N_2O and CH_4 fluxes, soil temperature (T_{soil}), water filled pore space (WFPS) of the four sites for the two years. The values are in kg C/N ha^{-1} $season^{-1}$ and the monthly averages are reported in μg C m^{-2} h^{-1} (see Table S1). The period of the season considered for the seasonal mean computation is from June to October.

	Ecosystem	Seasonal mean		Min		Max		Median	
		2023	2024	2023	2024	2023	2024	2023	2024
CH_4 [kg C ha^{-1} $season^{-1}$]	Forest	-0.019±0.2	-0.42±0.13	-33.08	-33.8	13.72	29.13	4.92	-13.86
	Grassland	0.53±0.35	0.37±0.13	-24.13	-16.15	73.58	64.25	13.49	8.04
	Cropland	-0.065±0.2	-0.074±0.14	-27.46	-17.35	18.13	15.56	-4.79	-3.45
	Rice fields	0.69±0.17	0.82±0.22	-17.23	-40.18	140.07	233.9	14.6	5.47
N_2O [kg N ha^{-1} $season^{-1}$]	Forest	0.12±0.1	0.011±0.11	-9.31	-10.56	12.1	9.27	6.32	-1.37
	Grassland	0.05±0.16	0.1±0.02	-13.21	-9.65	14.14	21	3.3	3.25
	Cropland	0.12±0.18	0.1±0.08	-12.18	-15.84	16.51	29.63	6.11	2.55
	Rice fields	0.08±0.24	0.16±0.31	-9.74	-11.09	12.59	33.93	3.65	4.66
SM [%]	Forest	16.59±4.3	10.55±0.0	7.9	10.55	23.55	10.55	18.1	10.55
	Grassland	19.78±8.95	18.61±8.02	0.1	4.3	40.15	33.95	19.45	17.125
	Cropland	11.97±5.29	10.56±6.01	0.5	0.3	22.3	21.25	12.85	11.25
	Rice fields	25.41±11.7	17.18±10.5	0.5	5.35	39.15	36.15	31.6	14.25
T_{soil} [°C]	Forest	28.43±0.46	28.3±0.0	26.45	26.45	31.05	30.15	27.82	27.87
	Grassland	29.81±1.48	31.26±2.86	26.75	28.5	32.35	40.9	29.92	30.25
	Cropland	29.19±2.91	31.41±2.78	24.8	27.65	34.5	37.75	28.5	31.22
	Rice fields	30.78±2.34	31.42±2.51	27.75	26.95	36.25	34.75	30.25	32
WFPS [%]	Forest	-	-	-	-	-	-	-	-
	Grassland	53.05±24.0	49.9±21.5	0.26	11.52	107.65	91.02	52.15	45.91
	Cropland	32.11±4.48	28.33±16.2	1.32	0.79	59.27	56.48	34.15	29.9
	Rice fields	59.99±27.6	40.56±24.91	1.18	12.63	92.42	85.34	74.6	33.64

3.7 Sensitivity of soil N_2O, CH_4, and CO_2 fluxes to water table dynamics

3.7.1 Model descriptions

The Joint UK Land Environment Simulator (JULES) as a state-of-the-art Earth System Model (ESM) is used in its modified version, named JULES-Microbe, to evaluate the impact of water table dynamics on wetland greenhouse gas emissions in the region. Both JULES and JULES-Microbe are described in sections 3.2 and 3.4. The tested scenarios are also presented in section 3.7.4.

3.7.2 Joint UK Land Environment Simulator

JULES is a widely reported community model in the UK Earth System Model (UKESM, Sellar et *al.*, 2019). It simulates water and heat fluxes, snowpack dynamics, soil biogeochemistry, vegetation dynamics, energy balance, nitrogen and carbon fluxes (Burke, Chadburn, & Ekici, 2017; Best et *al.*, 2011; Wiltshire et *al.*, 2020). A detailed description of JULES is provided in two parts in Best et *al.* (2011) and Clark et *al.* (2011), and was used in the Global Carbon Project (Friedlingstein et *al.*, 2019) and the Inter-Sectoral Model Intercomparison Project (Rosenzweig et *al.*, 2017). Global projections of multiple variables are undertaken in with JULES for example for methane and carbon emission, and future hydrology (Comyn-Platt et *al.*, 2018; Gedney et *al.*, 2019). The model is preferred to achieve the objective of this study as it provides schemes and necessary variables to link the water table dynamics to wetland greenhouse gas emissions. The methane emission is computed in JULES though the wetland methane scheme. It requires substrate availability (C), and soil temperature (T) which are multiplied by saturated fraction to obtain the methane emission of the grid box (Gedney et *al.*, 2004). Comyn-Platt et *al.* (2018) updated the scheme providing the computation of the emission from multiple vertical soil layers. The total emission is calculated by adding the fluxes from the layers. The oxidation is empirically represented as an exponential decay factor (τ) to weight the sum of methane production from the layers (Equation 1). A major factor in methane emission namely root exudates is neglected in the scheme as it focuses on methane production from soil carbon. Gedney et *al.* (2019) reported multiple ways the substrate can be used for methane emission. The equation below indicates methane emitted from the saturated area of the soil layer ith :

$$F_{CH_4}, i = k_1 C_i A(T_i, Q) \exp(-\tau z_i) dz_i \quad \text{(Eq. 3.77)}$$

With z_i : depths at center of the soil layers, dz_i: layer thickness, and A: Arrhenius function written as follows:

$$A(T, Q) = Q^{0.1T/(1-{}^{T}/_{T_0})} \quad \text{(Eq. 3.78)}$$

With T: Temperature (C), T_0: temperature at absolute zero, Q: equivalent to Q_{10} generally adopted in ecological modeling.

3.7.3 JULES-Microbe setup

The JULES-Microbe scheme is extensively described in Chadburn et *al.* (2020). It simulates the methane emission from the methanogens or methanogenic archea, a group of microorganisms that produces methane in anoxic conditions (Garcia et *al.*, 2000). Dissolved substrate from organic material is transformed into carbon dioxide, methane, and methanogenic microbial biomass. The substrate source in JULES-Microbe is soil organic carbon which is one amount many others not included in the scheme. Hydrolysis is reported as the rate-limiting step (Mata-Alvarez et *al.*, 2000) for the decomposition of the soil organic matter to dissolved substrate which occurs in many stages (Christy et *al.*, 2014). JULES-Microbe simulates the decomposition by hydrolytic microorganisms, a chemical process which does not include the methane emission by the methanogens. The rate of microbial respiration and biomass governs the consumption of the dissolved substrate. Higher of microbial respiration is associated with increase in the level of microbial activity, temperature, and substrate availability. Carbon dioxide and methane emissions, and growth of methanogenic biomass are the derived products from the consumption of the substrate. The level of microbial activity varies between poor and good growth conditions where the later one is associated with higher temperature and substrate.

The sensitivity of the greenhouse gas fluxes (CH_4, N_2O, and CO_2) to the water table configuration in the region is assessed with the scenarios described in Table 3.8. The purpose is to ascertain its' contribution of the emissions. The metrics used to evaluate the difference are KGE, PBIAS, and BIAS described in section 3.1.3.7.

Table 3.8: Scenarios for the evaluation of the impact water table dynamics on greenhouse gas fluxes.

Scenario ID	Scheme Type	Water Table Setting	Target System	Scientific Basis / Source	Expected Biogeochemical Response
S1	*Prescribed Static*	-10 cm below surface	Boreal fen, mesic peat	Moore & Knowles (1989); Turetsky et *al.* (2008)	High CH_4, moderate CO_2/N_2O
S2	*Prescribed Static*	-40 cm below surface	Moderately drained peat	Heinemeyer et *al.* (2010); Grant et *al.* (2019)	Moderate CH_4, higher CO_2
S3	*Prescribed Static*	-80 cm below surface	Upland organic soils	Treat et *al.* (2015); Wieder et *al.* (2019)	Low CH_4, high CO_2/N_2O
S4	*Prescribed Static*	Surface level (0 cm)	Permanently saturated wetland	Ringeval et *al.* (2012); Tootchi et *al.* (2020)	Peak CH_4, low CO_2, rising N_2O
S5	*Prescribed Static*	+5 cm above surface (flooded)	Tropical swamp forest	Pangala et *al.* (2017); Methane feedback CMIP6 work	High CH_4 ebullition, low CO_2
S6	*Dynamic Event-based*	–10 to –80 cm event-driven drop (drought scenario)	Drained peatland	Knox et *al.* (2015); Helbig et *al.* (2020); WETCHIMP simulation strategies	CH_4 collapse, CO_2 pulse, N_2O spike
S7	*Dynamic Rising WTD*	–80 to 0 cm rise (rewetting/restoration)	Peatland restoration	Günther et *al.* (2020); Laine et *al.* (2021); Peatland Code UK	CH_4 increase, CO_2 decrease
S8	*TOPMODEL-derived*	Topographic wetness index (TWI) driven WTD	Large-scale catchment	Gedney & Cox (2003); Clark et *al.* (2011); JULES-ES configuration	Realistic wetland distribution, patchy GHG emissions

Chapter Four

Results and Discussion

4.1 Sensitivity of water fluxes to subsurface flow parameterization schemes in West Africa

4.1.1 Model calibration

The scarcity of streamflow records places a significant limitation on the WRF-hydro model calibration in the study area as reported by Arnault et *al.* (2016), Naabil et *al.* (2017), and Quenum et *al.* (2022). The models' hydrological parameters selection is a critical step. From the literature, past works that dealt with this issue have provided considerable insight into the range of values suitable for the main parameters namely the runoff infiltration partitioning parameter (REFKDT) and surface and channel roughness parameter (Manning's roughness, n) at basin scale. But, transferring past calibrated parameter values to other gauges still encounters a representativity challenge due to the peculiar characteristics of each hydrological unit even at the local scale. The model calibration in the present study is undertaken on the Donga catchment where streamflow data is available (see location in Fig. 3.1) using the FD scheme. The year 2009 is used for the model spinup, 2010 is chosen for the calibration following suggestions in the literature (Senatore et *al.*, 2015; Quenum et *al.*, 2022), and the remaining period for the model validation. For improved streamflow simulation, the first step of the model calibration is done by evaluating the model performance in response to a similar range of values for the REFKDT parameter (see Table 4.1b, Fig. 4.3a-b), as suggested in prior studies. The adopted approach is to change the infiltration scaling value for the entire domain as a global parameter. The remark at this first stage is that with the tested REFKDT value, the precision metrics KGE and NSE reach up to 0.66 and 0.49, respectively, with the PBIAS values ranging between -15.04 and 6.48. For a REFKDT value greater or equal to 0.1, the model underestimates the streamflow while the tested value of 0.02 results in an overestimation. From the lower REFKDT values to higher one (0.02 to 3), the RMSE reduces progressively from 339.4 m^3/s to 132.3 m^3/s.

The model calibration through the parameters' regionalization is encouraged in recent descriptive reports of WRF-Hydro (Niu et *al.*, 2011). Therefore, as infiltration scaling factor, this study computed a spatially-distributed infiltration rate (see Fig. 4.1) using the soil hydrologic group (A, B, C, and D), the terrain slope, and the MODIS/IGBP land cover map (20 classes). The hydrologic group is derived from the soil texture map according to the recommendation of the US Soil Conservation Services (SCS) and the slope calculated from the DEM at the native land

model resolution is classified into 3 categories (low, medium and high slope). The layers are extracted from the geogrid file and the infiltration rate is mapped using the Rational Method Runoff coefficient (Baiamonte, 2020; USDA, 2007; Soil Conservation Service, 1983). The infiltration rate is assigned from the 240 sub-classes resulting from the combination of the three map categories with values ranging from 0.1 to 0.99. With the regionalized REFKDT, the KGE increases to 0.68 while the NSE remains at 0.49 with a PBIAS value of -12.0 and RMSE of 133.6 m^3/s (see Table 4.1b, Fig. 4.3a-b).

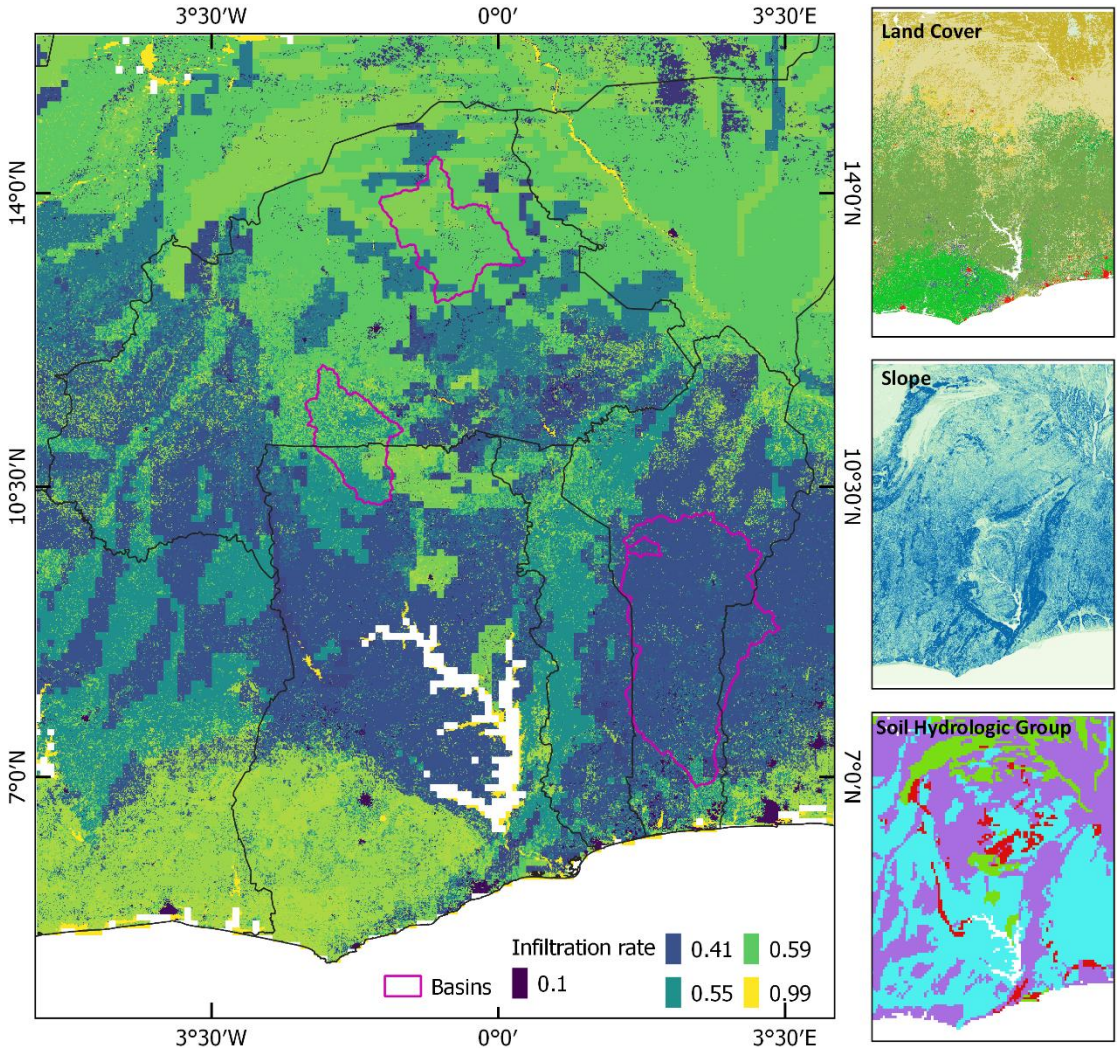

Figure 4.1: Infiltration rate map computed using soil hydrologic group, slope, and land cover (shown on the right side) for the REFKDT regionalization. The different color in the soil hydrologic group map indicates the classes (A, B, C, and D).

Small changes in the channel routing parameters are reported to significantly influence the simulated streamflow. Each segment of the channel network is indexed with the channel parameters (see Table 4.1b) by attributing same values to similar stream order in the routing scheme. The caveat is that the topographic complexity creates disparities in the channel network making each one different from any other. The streams Manning's coefficient (MannN) and the surface roughness scaling factor (OVROUGHRTFAC) are often used as a global parameter to represent the topographic roughness influence on the overland flow and streamflow of the catchment. The accurate computation of the roughness parameters (OVROUGHRTFAC and MannN) is significant for the overland flow formulation because even micro-topography affects the flood wave dynamic. The surface overland flow routing is defined based on the continuity and momentum equations (see WRF Hydro user guide) and the momentum loss of the overland flow is implemented using the Manning's or Chezy resistance equation:

$$q_x = \alpha_x h^{\beta} \quad \text{(Eq. 4.1)}$$

where $q_x$is the unit discharge in x direction from the two-dimensional continuity equation for a flood wave. It takes into account the friction slope both in x and y directions (Sfx, Sfy) which is a function of the terrain slope and the surface water depth variation:

$$\alpha_x = \frac{S_{fx}^{1/2}}{n_{OV}} \text{ (Eq. 64)}; \quad \beta = \frac{5}{3} \text{ and } \quad S_{fx} = S_{ox} - \frac{\partial h}{\partial x} \text{ (Eq. 4.2)}$$

The tunable parameter $n_{OV}$is the roughness coefficient of the land surface with a default value equal to 1 (OVROUGHRTFAC) which is used in the first step of the model calibration. The roughness parameter (OVROUGHRTFAC) is evaluated by tuning values ranging from 0.2 to 0.8 (see Table 4.1b, Fig. 4.3a-b) and a 2D spatially distributed roughness map using the regionalized REFKDT. The Topography Roughness Index (TRI) describes the topographic gradient change from hillside to the channel and is used in this study to evaluate its efficiency in improving the streamflow simulation. A python code is written to compute the TRI (Fig. 4.2) and the simulated streamflow time series are compared.

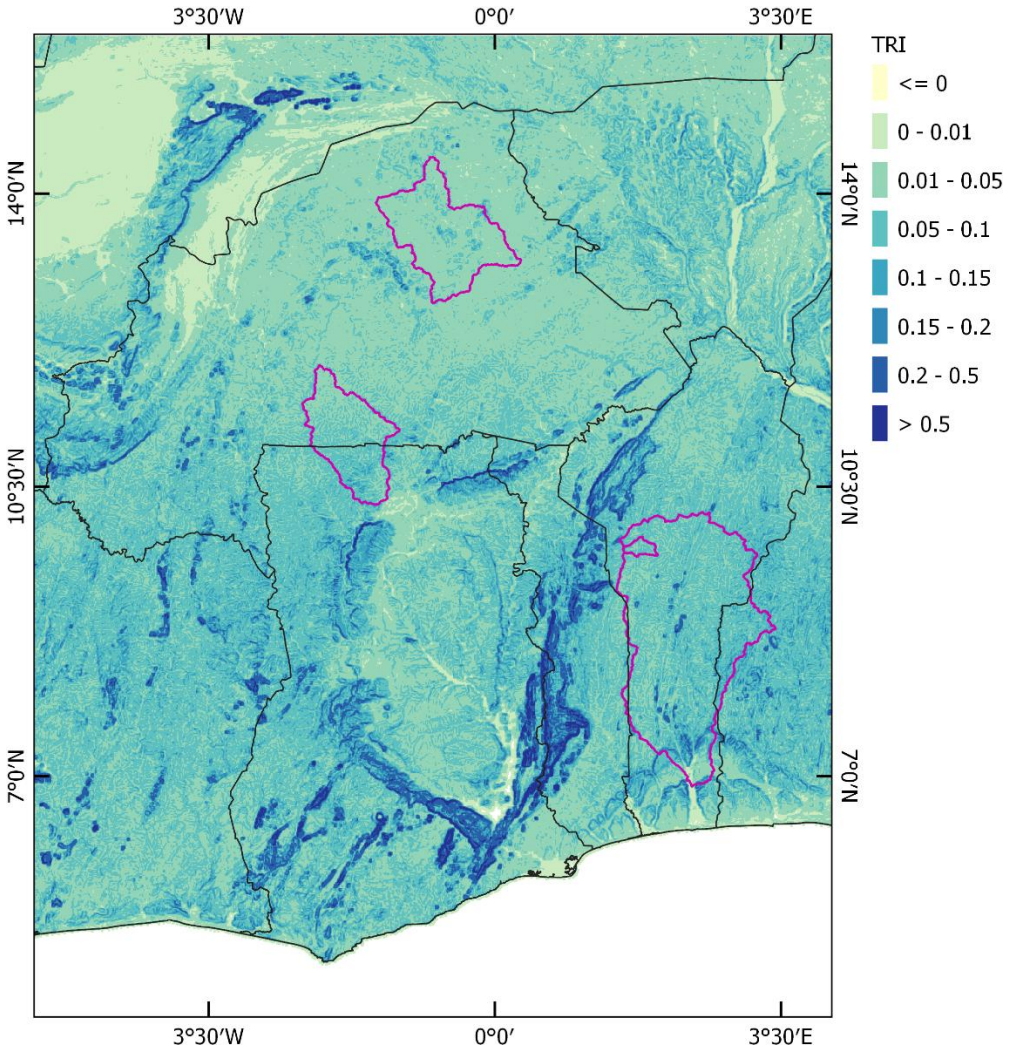

Figure 4.2: Topography Roughness Index (TRI) map used for the regionalized surface roughness scaling factor OVROUGHRTFAC. The dark blue indicates high roughness values.

It turns out that the performance of the model with the different parameterizations of OVROUGHRTFAC is quite similar with KGE and NSE values approximating respectively 0.68 and 0.49. More, the PBIAS and RMSE values fluctuate around -12 and 133 m^3/s revealing that despite the reasonable performance in the Donga catchment, the TRI does not increase significantly the accuracy of the simulated streamflow but appears among the best performing results.

The calibration process is continued with the investigation of the Beta parameter (BEXP), the Saturated value of soil moisture (SMCMAX), and the Saturated soil permeability coefficient (DKSAT) which are spatially distributed with respective default mean and standard deviation of 6.8±0.9, 0.4±0.01, and 4.3e-6±6.4e-7. To preserve the spatial heterogeneity of these parameters, the proposed calibration consists in shifting the default values by a multiple of its standard deviation. For instance, the distributed BEXP is decreased by 6, 5, 4, 3, and 2 times the standard deviation and increased by 2 and 4 times to investigate how the simulated streamflow is improved. The results indicate that the highest performance is achieved with the BEXP-3STD and the metrics KGE and NSE values are respectively 0.74 and 0.57. The PBIAS value of 1.91% is the lowest recorded with a RMSE of 112.5 m^3/s. It is remarkable that for the tested BEXP values below and above BEXP-3STD, the model performance decreases significantly towards the lowest values reaching KGE and NSE respectively of 0.21 and 0.37, and PBIAS and RMSE of 76% and 165.26 m^3/s; and less significantly towards the highest BEXP with the KGE, NSE PBIAS, and RMSE values of respectively 0.66, 0.46, -18.1%, and 140.2 m^3/s. The lowest BEXP values lead to the streamflow overestimation while the highest lead to underestimation.

The SMCMAX parameter is also calibrated in a similar manner and it turns out that the best performance of the model is recorded with SMCMAX-2STD where the KGE, NSE, PBIAS, and RMSE values reach respectively 0.74, 0.56, 7%, and 115.3 m^3/s. Towards the lowest values of SMCMAX the model overestimates the streamflow by 33.5% with the largest RMSE of 152.3 m3/s. The corresponding KGE and NSE values are respectively 0.57 and 0.42. It underestimates the streamflow towards the highest SMCMAX where the PBIAS and RMSE reach respectively -12% and 120.6 m^3/s with KGE and NSE of 0.66 and 0.54.

The highest performance of the model with the DKSAT parameter is recorded with DKSAT-2STD where the KGE and NSE values are respectively 0.73 and 0.56 with the lowest PBIAS and RMSE of -2.1% and 115.5 m^3/s. Further, the drop of the model performance is abrupt towards the lowest DKSAT reaching 0.12 and -1.1 of KGE and NSE with a streamflow

underestimation of -27.4% and a RMSE of 554 m^3/s. The model performance towards the highest DKSAT is slightly lower with the streamflow overestimation of similar magnitude (29.3%) and KGE, NSE, and RMSE of respectively 0.63, 0.51, and 128.6 m^3/s.

Table 4.1a: Channel parameters per stream order

Stream Order	Bw	HLINK	ChSSlp	MannN	Averaged TRI
1	1.6	0.02	0.03	0.09	0.045
2	2.4	0.02	0.03	0.07	0.043
3	3.5	0.02	0.03	0.06	0.042
4	5.3	0.03	0.04	0.05	0.04
5	7.4	0.03	0.04	0.04	0.04
6	11	0.03	0.04	0.03	0.031
7	14	0.03	0.04	0.03	-
8	16	0.1	0.04	0.02	-
9	26	0.3	0.05	0.02	-
10	110	0.3	0.1	0.02	-

Table 4.1b: Model calibration metrics

Parameter	KGE	NSE	PBIAS	RMSE	Parameter	KGE	NSE	PBIAS	RMSE
REFKDT (OVROUGHRTFAC=1)					SMCMAX (REFKDT=REG, OVROUGHRTFAC=TRI, BEXP=-3STD)				
0.02	0.44	-0.3	6.48	339.5	-10STD	0.57	0.42	33.59	152.3
0.1	0.62	0.26	-10.2	194	-6STD	0.7	0.52	19.06	125.3
0.3	0.65	0.42	-13.91	150.2	-4STD	0.73	0.55	12.69	118.5
0.5	0.66	0.46	-14.53	140.9	-2STD	**0.74**	0.56	7.05	115.3
1	0.66	0.48	-14.87	134.4	2STD	0.71	0.57	-3.1	110.8
3	0.66	0.49	-15.04	132.4	4STD	0.68	0.55	-8.18	116.4
REG	**0.68**	0.49	-12.05	133.7	6STD	0.66	0.54	-12.03	120.7
OVROUGHRTFAC (REFKDT=REG)					DKSAT (REFKDT=REG, OVROUGHRTFAC=TRI, BEXP=-3STD, SMCMAX=-2STD)				
0.2	0.68	0.49	-11.47	134	-10STD	0.12	-1.1	-27.49	554.1
0.4	0.68	0.49	-11.81	134	-4STD	0.65	0.52	-15.54	124.2
0.6	0.68	0.49	-11.94	133.8	-2STD	**0.73**	0.56	-2.12	115.6
0.8	0.68	0.49	-12.01	133.8	2STD	0.72	0.55	13.72	117.3
TRI	**0.68**	0.49	-12.16	131.9	4STD	0.7	0.54	18.86	119.9
BEXP (REFKDT=REG, OVROUGHRTFAC=TRI)					6STD	0.67	0.53	22.99	122.8
-6STD	0.21	0.37	76	165.3	10STD	0.63	0.51	29.32	128.6
-5STD	0.58	0.54	35.76	119.3	MannN (REFKDT=REG, OVROUGHRTFAC=TRI, BEXP=-3STD, SMCMAX=-2STD, DKSAT=-2STD)				
-4STD	0.73	0.57	12.04	111.2	2STD	0.73	0.56	-2.12	115.5
-3STD	**0.74**	0.57	1.91	112.6	4STD	0.73	0.56	-2.12	115.1
-2STD	0.72	0.55	-4.37	117.3	6STD	0.73	0.56	-2.11	115.3
2STD	0.66	0.46	-15.98	140.8	10STD	0.73	0.56	-2.11	114.7
4STD	0.66	0.46	-18.16	140.3	TRI	**0.74**	0.56	-2.12	115

The channel routing algorithm also uses the mass and momentum continuity equations as for the overland flow routing. In this case, the friction slope is a function of the flow rate (Q) and conveyance (K) and formulated as follows:

$$S_f = \left(\frac{Q}{K}\right)^2 \text{(Eq. 4.3)}$$

K is calculated using the Manning's equation:

$$K = \frac{C_m}{n} AR^{2/3} \text{ (Eq. 4.4)}$$

where A: the cross-sectional area, R: the hydraulic radius (A/P), P: the wetted perimeter, n: Manning's roughness coefficient, and Cm: dimensional constant (1.0 or 1.486 for SI or English units).

The Manning's roughness (n) is the controlling factor of the hydrographs' shape and assigned to each stream order in 2 different manners; that is increasing the default MannN values by multiples of the standard deviation of the list and testing the regionalized TRI. At this last step, the average roughness value per streamflow segment (2063 polylines) traversing the cells of the roughness map is extracted with the ArcGIS tool "Add Surface Information". To increase the possibility to achieve superior yield, a finer resolution of roughness map is computed using the subgrid DEM of 250m resolution instead of the native land model resolution of 1km. The default list of n values in the routing file (Route_Link.nc) of the reach-based routing methods is replaced by the extracted roughness values (Table 4.1a). Overall, the model performance increases by few digits for all tested range of MannN. The TRI yield is slightly higher (KGE: 0.74) but there is not a significant difference between the tested values.

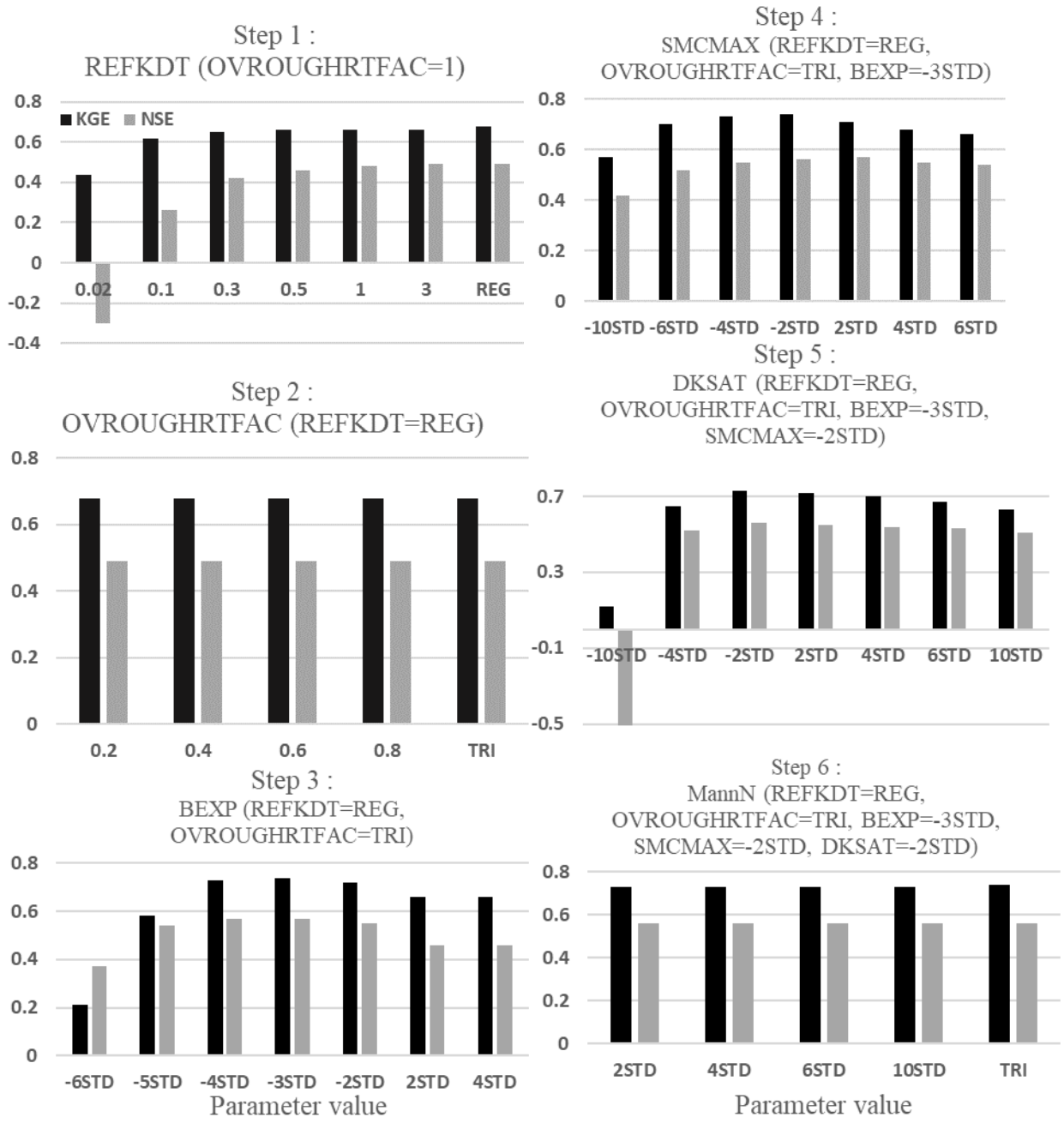

Figure 4.3a: Model calibration steps and corresponding metrics. The black and grey bars indicate respectively the KGE and NSE scores. The abbreviations are described above in section 4.4. See Figure 4.3b for further detail.

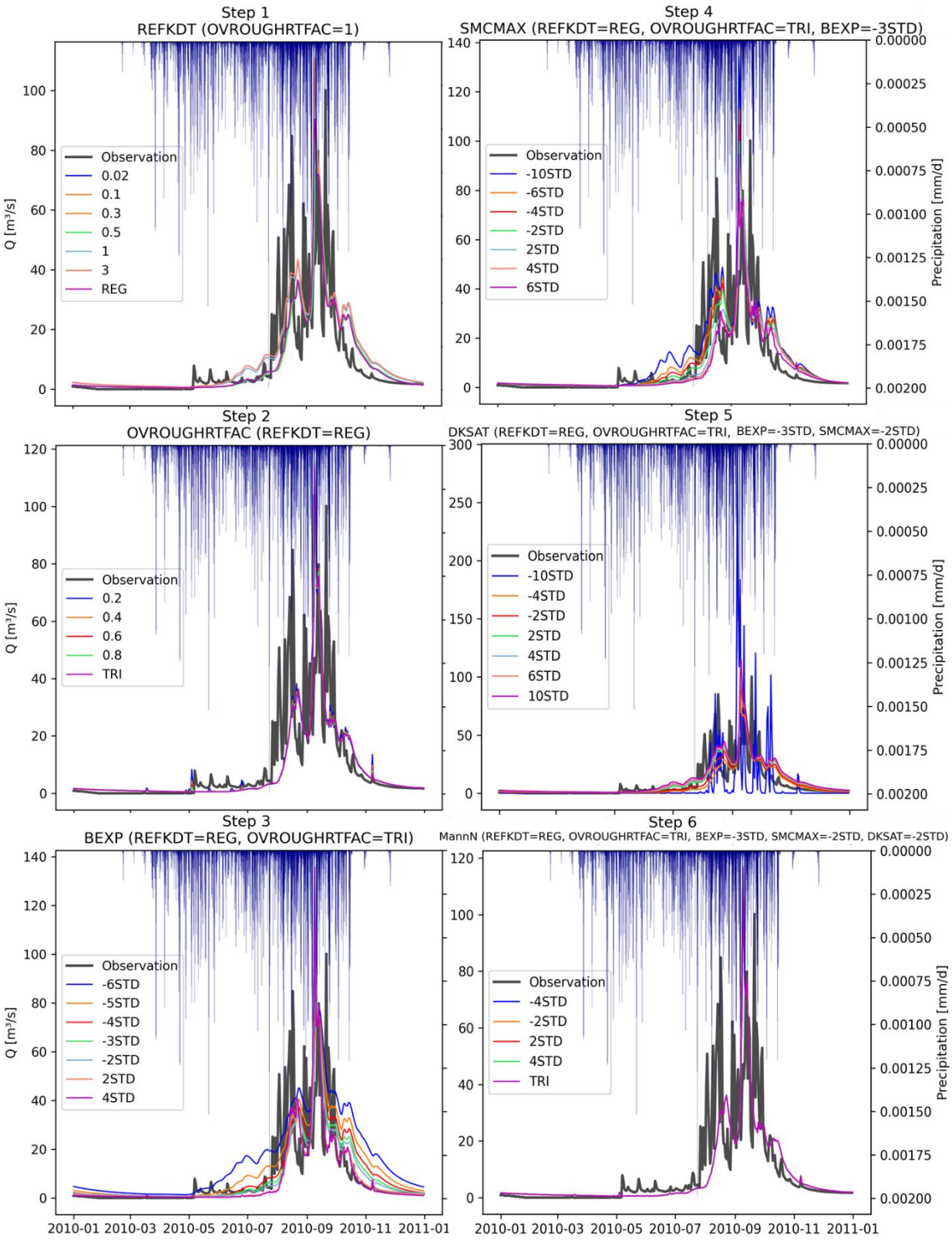

Figure 4.3b: Model calibration steps and corresponding simulations. The grey line indicates the observation.

4.1.2 Models' performance

4.1.2.1 Performance in simulating soil moisture

This study endeavors to evaluate the impact of the subsurface parameterization on the soil moisture, evapotranspiration, groundwater storage, and streamflow in West Africa using the WRF-Hydro model. Considering the benefit of improving the groundwater representation in LSMs spanning from computationally less expensive approaches (1D) to coupling variably saturated groundwater models (3D), the TOMODEL and MMF schemes resolve the upper unconfined aquifer by using the Darcy law for lateral flow and Dupuit-Forchheimer approximations. The model is calibrated for the Donga catchment using global and regionalized parameterizations to identify the optimum values required to achieve accurate streamflow simulation. The parameters are then employed to run three simulations using the schemes (FD, TOPMODEL, and MMF).

The simulated soil moisture of the three schemes is evaluated against the ESA CCI remote sensing product at the basin level for the seasonality cycle and inter-annual variability analysis (Fig. 4.4) and at the entire domain level (Fig. 4.5) with the metrics described in section 4.3. Though a slight difference can be noticed in the inter-annual variability patterns of the monthly top layer water content of FD SM, TOPMODEL SM, and MMF SM, the seasonal cycle is well reproduced for each basin. In Faga basin located in the Sahel zone, the regression metrics confirm the three schemes' skill in capturing the variability and timing of the observation with values ranging from 0.85 to 0.94 for R, 0.68 to 0.82 for KGE, and 0.36 to 0.68 for NSE (Fig. 4.5). The difference in the RMSE is negligible and the lowest value is displayed by the TOPMODEL scheme. The strong linear relationship between the models and observation confirms the lower error in the variability indicating a good performance. Overall, the three schemes' soil moisture is drier resulting in a slight underestimation in the basin. In this Sahelian climate, the two improved subsurface schemes (TOPMODEL and MMF) reveal a positive outcome for soil moisture modeling; that is in a drier condition, the role of the subsurface in sustaining soil water content is more pronounced. The three schemes' performance in the Sissili basin located in the Sudanian savanna is high with R, KGE, and NSE values respectively from 0.91 to 0.95, 0.71 to 0.76, and 0.54 to 0.74. The difference in the RMSE values is negligible, although the models underestimate the dry season soil moisture. The annual pattern of the soil moisture variability is well captured in the three simulations with the minimum residual variance recorded in the

TOPMODEL (NSE=0.74). Though the correlation coefficient R and KGE are relatively strong for the three schemes, the residual variance magnitude to the observed variance indicates FD as the less performing scheme (NSE=0.54). In wetter climatic condition of the Guinea Coast, the potential of the schemes in Oueme basin is significant with a correlation coefficient spanning from 0.94 to 0.98. The residual variance is the lowest compared to the other basins with NSE greater than 0.83 and the TOPMODEL scheme's performance is the best. The temporal variability is accurately captured as the KGE values vary between 0.81 and 0.85. The evaluation of the bias using RMSE shows the models' skill in minimizing the absolute error which is relatively low for the schemes, especially the TOPMODEL scheme. Despite the land cover simplification due to the models' grid cell size and its potential impact on the soil moisture, the schemes offer reliable outcomes for the considered climatic conditions.

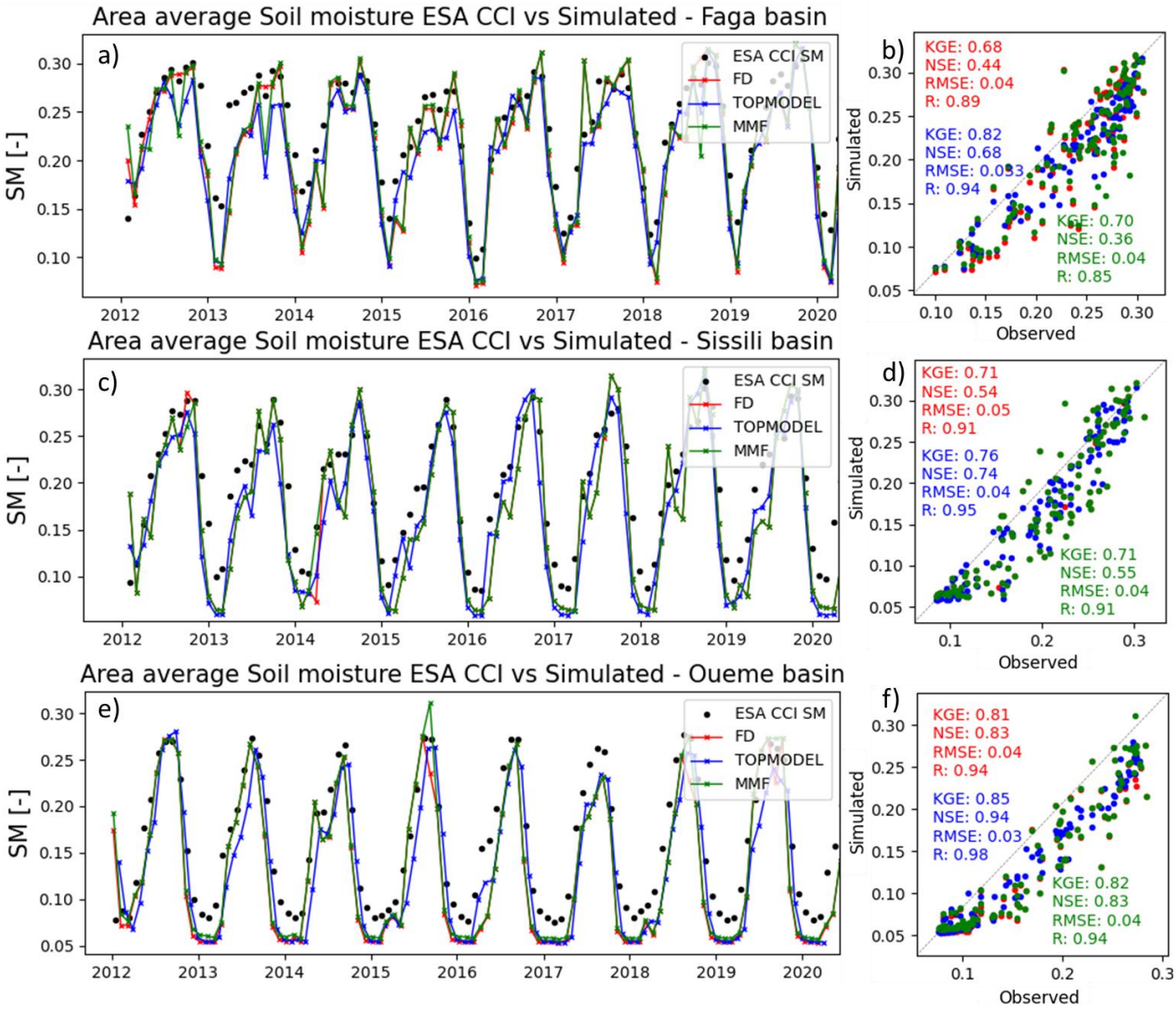

Figure 4.4: Comparison of the basin averaged soil moisture of ESA CCI SM versus simulated SM. The scatter plots and metrics of FD, TOMODEL, and MMF are in red, blue, and green.

As one of the major components for water conservation in the critical zone, the model's performance in simulating soil moisture is shown in Figures 4.5, S1, and S2. The spatial distribution of the time-averaged soil moisture shows the similarity between the reference SM and MMF SM. The widely reported south-north soil moisture gradient is well captured by MMF SM however the bias map (Fig. S1c) indicates a drier soil moisture. Although near the coast, the difference between the reference SM and MMF SM is close to zero. The linear relationship displayed in Fig. S1d shows a strong agreement (0.5 to 0.95) however the bias in Sudanian and Sahel zones oscillates around -0.05 $m^3 m^{-3}$. Altogether, the spatial correlation coefficient indicates a strong linear relationship with reference SM (0.92, 0.94, and 0.92). The impact of the improved schemes on the top layer soil moisture is negligible compared to FD SM (Fig 4.5c, 10, S1c, and S2c). Though the focus here was not on the lower layers, Wagner et *al.* (2016) argued that the subsurface improvement using dedicated hydrological models has a more pronounced effect on the lowest soil layer reducing the water content by approximately 10%. The same study confirms the present results obtained with the top soil revealing a lower impact. Despite the relatively low difference, slight changes in soil moisture can affect land surface processes (e.g., Koné et *al.*, 2022; Talib et *al.*, 2022; Robert et *al.*, 2011; Stocker et *al.*, 2018; Kunstmann & Jung, 2003). As shown in Fig. 4.12, with the MMF scheme, the sensitivity of the WRF Hydro model to subsurface parameterization is mainly significant in the riverbeds.

The spatial comparison of the simulated soil moisture versus the ESA CCI products is illustrated in Figure 4.5d-f where R, KGE, and NSE, are employed as metrics. This domain-level evaluation indicates the spatial distribution of the metrics computed on the 10-year simulation SM. For the three schemes, the spatial pattern reveals a significant score across the board with very low error. The linear relationship with the observation is strong with R values ranging from 0.5 in the Sahel to 95 in the Sudanian savanna (Fig. 4.5d, S1d, and S2d). More than 80% of the domain has KGE values greater than 0.5 whatever the scheme and this confirms their skill in representing both the seasonal cycle and inter-annual variability. Most of the highest KGE scores ($\geq$0.8) are located in the Savanna zone with the TOPMODEL SM and represented by a black dot (Fig. 4.5e, S1e, and S2e). The coastal area and the extreme north of the domain are less captured with the KGE ranging between 0.25 and 0.5. The residual variance magnitude to the observed variance confirms the skill of the TOPMODEL SM in the Savanna zone with values fluctuating between 0.5 and 1. The same cannot be inferred for the FD SM and MMF SM in the Sahel and Guinea Coast as the NSE values descend below 0.25 (Fig. 4.5f, S1f, and S2f). This implies the

less sensitivity of the two models to the two poles of the rainfall gradient. However, the two schemes' NSE values can reach 0.75 in the Savanna zone. The seasonal cycle and inter-annual variability are therefore well reproduced and no systematic errors are associated with the simulated SM. For the entire domain and whatever the scheme, the RMSE is below 0.01 m^3 m^{-3} except few grid cells with the lowest error corresponding to the highest values of KGE and NSE. There is almost no difference in the RMSE of the three schemes. For all the metrics, there is no zonation according to the soil types, land cover types, slope, or geology in the spatial distribution limiting the analysis to the climatic zones.

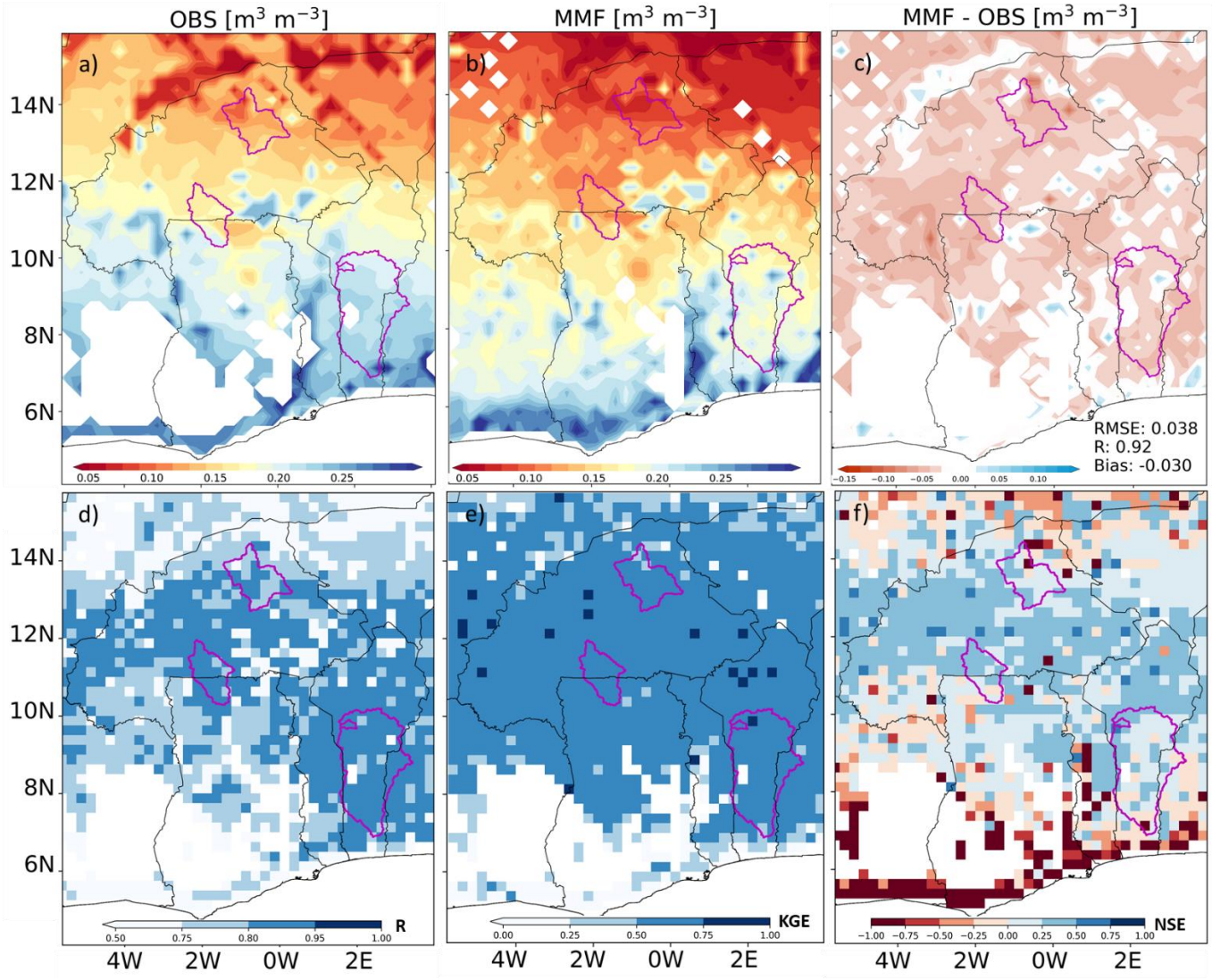

Figure 4.5: Error metrics for the domain level validation of MMF (b) soil moisture against ESA CCI soil moisture (a) with the bias (c) R (d), KGE (e), and NSE (f). The colour ramp is similar for R and KGE. Lower NSE are indicated in fading red and higher performance in fading blue. The blank areas correspond to no value in the ESA CCI product. The magenta polygons are basins. The horizontal resolution of the simulations is resampled to the ESA CCI data decreasing the subplots resolution to 0.25˚.

The simulated soil moisture of the three schemes is evaluated at site level against field measurements recorded at Eddy Covariance flux monitoring stations (Fig. 4.5) and compared to the ESA CCI remote sensing product at domain level (Fig. 4.7). The differences in the temporal patterns of FD, TOPMODEL, and MMF top layer water content are assessed at a daily resolution using as benchmark the records from the sensors positioned in the first centimeters at the EC sites (Fig. 4.5). The three schemes' estimations of the soil moisture are quite similar for each site except the Janga rice field. The MMF soil moisture is higher at this location in the dry season and during the peak of the wet season. The rice field is a topographic convergence area where the effect of the MMF scheme on the land surface water is reported to be significant (Rummler et *al.*, 2022). Although the temporal cycle is accurately simulated by the three schemes, all of them overestimate the soil moisture during the peak of the wet season. There is slight overestimation during the dry season at Kayoro, Wankama Nord, and Wankama Sud however the simulations fit well the Sumbrungu site. For the three schemes, the correlation coefficient varies between 0.32 to 0.85 and the lowest value is obtained at the forest reserve of Nazinga while the highest is recorded at Kayoro farmland (Table S2). Except the Nazinga site, the simulated soil water content from FD, TOPMODEL, and MMF indicate a higher degree of agreement with the benchmark data from the sites. The lower correlation coefficient (0.55, 0.53, and 0.41) observed at the rice of Janga is due to the data limitation as the site is recently built. The computed RMSE values for all the sites are close to 0 which further confirm the reliability of the simulated soil moisture. Nevertheless, a source of discrepancy in the evaluation of the simulated soil moisture can be attributed to the horizontal resolution (1 km) of the model grid cell which simplifies the land cover type. For instance, in the MODIS land cover layer, the savannas/woody savannas grid cell is attributed to the rice field at Janga while the Nazinga forest reserve is represented by grasslands.

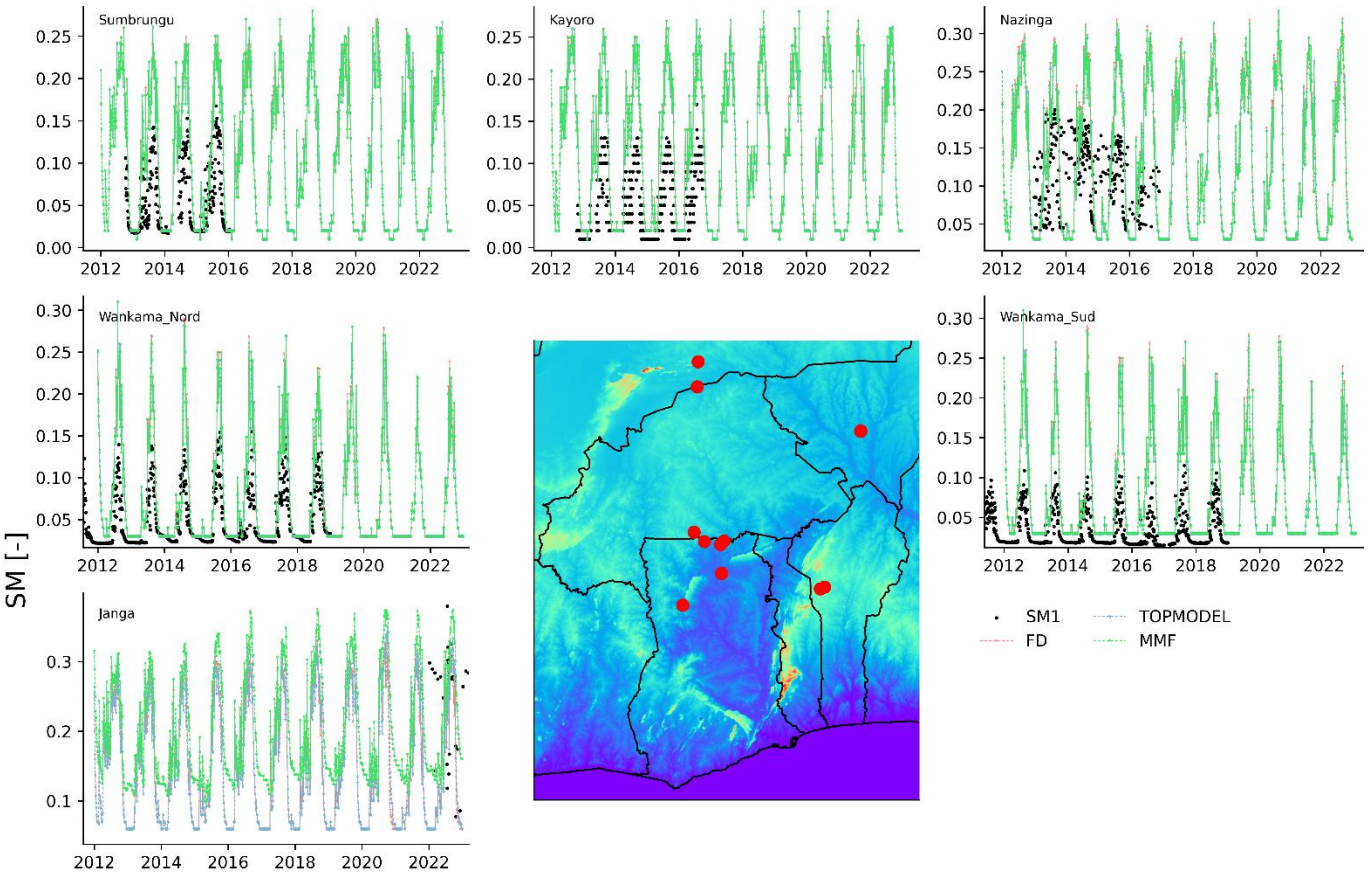

Figure 4.6: Simulated soil moisture from FD (dot line red), TOPMODEL (dash blue), MMF (dot line green) plotted against the EC sites' recorded soil moisture in the top soil layer (black dot). The stations located in the Savanna (Kayoro, Sumbrungu, Nazinga, Nalohou, and Belefoungou) and Sahel zones (Wankama Nord and Sud). The red dots on the map locate the flux monitoring sites, the black line is the countries limit (not inferring legal borders) and the image below is the HydroSHED digital elevation model of the domain.

4.1.2.2 Performance in simulating actual evapotranspiration

The sensitivity of the evapotranspiration to the improved groundwater representation in the Noah-MP LSM is also evaluated using the monthly time series computed for the three catchments (Fig. 4.8). As described in Section 2, the actual evapotranspiration is compared to the widely used GLEAM ET at basin and entire domain level. The agreement between the reference ET and the model ET is higher in Oueme catchment (Fig. 4.7f). The lowest residual variance magnitude to observed variance is recorded with the TOPMODEL ET (NSE=0.54). Further, the correlation coefficient of TOPMODEL and MMF schemes show a stronger linear relationship with the reference ET and are 0.94 and 0.93 respectively compared to the FD ET value (0.91). The ET seasonal cycle and inter-annual variability in the basin occurs consistently with the observation and KGE values span between 0.26 and 0.34. However, the schemes altogether overestimate ET in wet season and underestimate ET in the dry season. The models' performance decrease towards lower rainfall rate areas in Sissili and Faga basins. Though, the ET overestimation in the dry season in Sissili can surpass the observed by 1.5 mm d^{-1}, the dry season ET is closer. The relative magnitude of the residual variance to the observed variance is high despite the strong linear relationship with R values between 0.87 and 0.9 however MMF ET stands out with NSE and KGE values of 0.19 and 0.27 respectively. In Faga basin located in the Sahel, the models' performance altogether drops significantly nevertheless the linear relationship with the observed ET is relatively high.

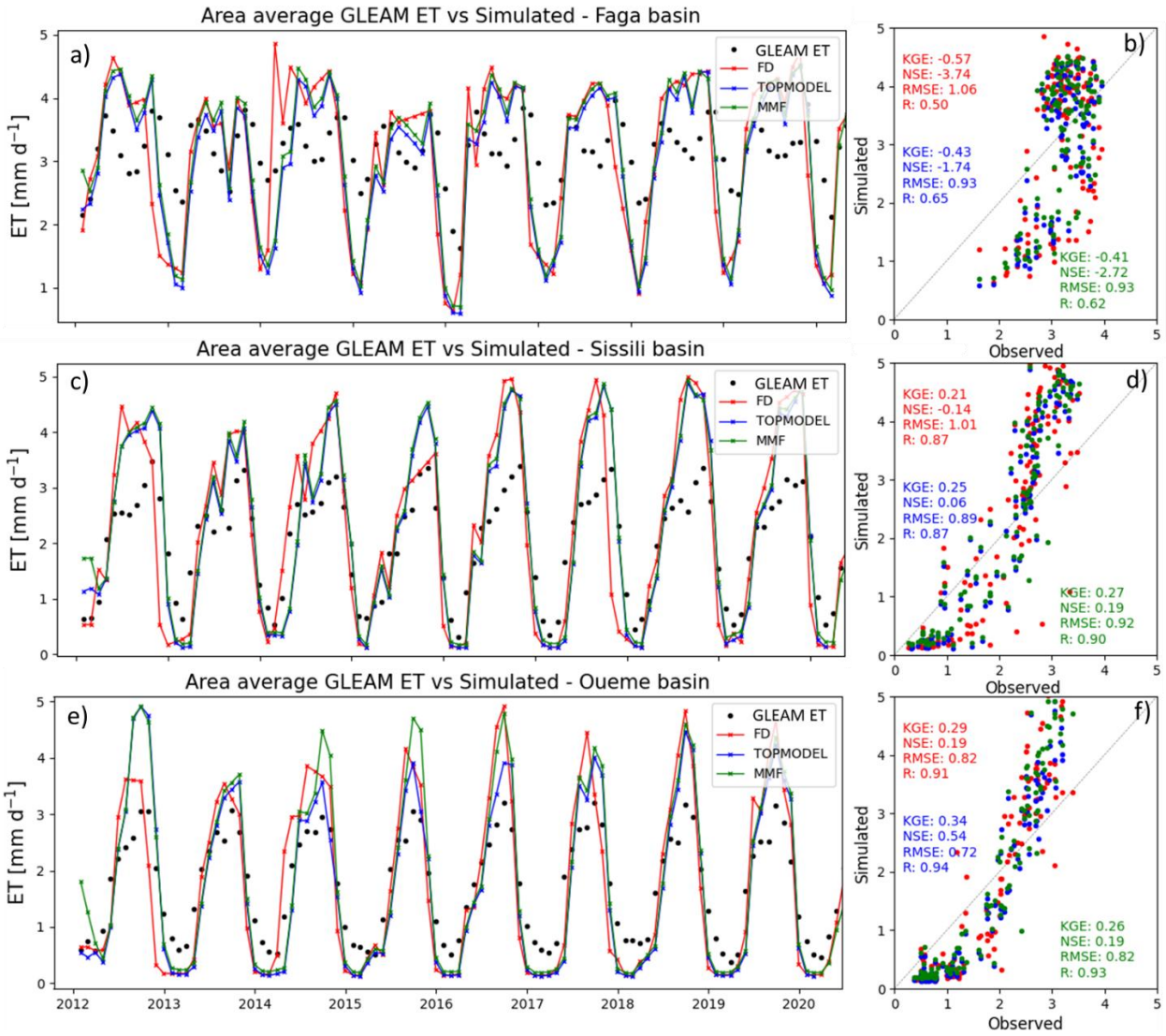

Figure 4.7: Comparison of the basin-averaged GLEAM ET versus simulated ET. The scatter plots and metrics of FD, TOMODEL, and MMF are in red, blue, and green

Except in high precipitation areas located in the Guinea Coast and mountainous zones, the deviation of FD ET from GLEAM ET is close to zero especially in the Sahel region (Fig. S3). The performance of the model is lower in the wetter regions however from the 10th to 13th latitude, the bias oscillates around 0.5 mm/d while it reaches more than 2 mm/d in the coastal area. The expected south-north trend of evapotranspiration rates is well replicated in the model with values ranging from less than 0.5 mm/d to above 4 mm/d in the rainforest located in south-west. The spatial correlation of 0.91 indicates a strong linear relationship between the FD ET and observed GLEAM ET whereas the mean bias and root mean square error reach respectively 0.5 mm/d and 0.77. The TOPMODEL ET is the closest to the observed GLEAM ET and this confirms similar analysis by Wagner, et *al.* (2016) and Arnault et *al.* (2021) using respectively the reanalysis product from Climate Prediction Center (CPC), the older version of GLEAM and the FLUXNET Model Tree Ensemble product (MTE, Jung et *al.*, 2009, 2010). In the low rates evapotranspiration areas (Sahel region), the TOPMODEL ET is slightly drier whereas below the 12th latitude, the deviation from the observation is negligible (Fig. S4). Towards high rates evapotranspiration areas in the south, the bias increases gradually as the TOPMODEL ET is wetter around 0.5 mm/d in the Sudanian savanna and above 2 mm/d near the coast. The spatial correlation coefficient indicates a strong relation between TOPMODEL ET and GLEAM ET (0.91) with the lowest mean bias of 0.02 mm/d and RMSE of 0.43 mm/d. Regarding the MMF ET, the scheme's performance is close to the observation as in the case of the TOPMODEL ET, which further demonstrates the skill of the improved subsurface schemes in reducing the well-established discrepancy associated with ET simulation in relatively wet areas (Fig. 4.8a-c and S4). However, its mean bias is higher (0.08 mm/d) compared to TOPMODEL ET. Despite the aforementioned difference, the two schemes' performance is significant and this finding corroborates the conclusion of Wagner, et *al.* (2016) which employed a fully coupled system. Remarkably, both TOPMODEL ET and MMF ET achieve RMSE of 0.43 and 0.47 which are approximately two-fold lower than FD ET.

Figure 4.8d-f, S3d-f and S4d-f show the spatial distribution of R, KGE, and NSE of the GLEAM ET versus the three simulations. It turns out that the KGE values reach more than 0.75 for FD ET, TOPMODEL ET, and MMF ET in the Sahel zone with the lowest and highest performance areas located in the central part of Mali and southern Niger. Unlike the soil water content, the highest scores of KGE are recorded in the Sahel zone and the south west evergreen forest with values ranging from 0.5 to 1. The major part of the domain displays a relatively significant KGE revealing a strong relationship between the benchmark data and the simulations.

However, the models' performance degrades gradually from the northern part until around the 9th latitude below which the disagreement accentuates especially in the south east. The linear relationship with the observation is stronger (R>0.8) in the Sahel for the three schemes especially the TOPMODEL ET. The lowest is recorded in the south-west evergreen forest where plant transpiration dominates (Fig. 4.8d). The models' accuracy in the south west evergreen forest is exceptionally high compared to the relatively low performance in the Guinea Coast. The little difference in the simulated evapotranspiration makes the NSE maps quite similar with the highest values in the Sahel zone. The highest values of NSE reach more than 0.75 in the north east of the domain but a relatively poor performance can be noticed in the 10th latitude. The major part of the domain displays RMSE values below 1.5 mm/d which confirms the reliability of the simulations to represent the evapotranspiration in the study area.

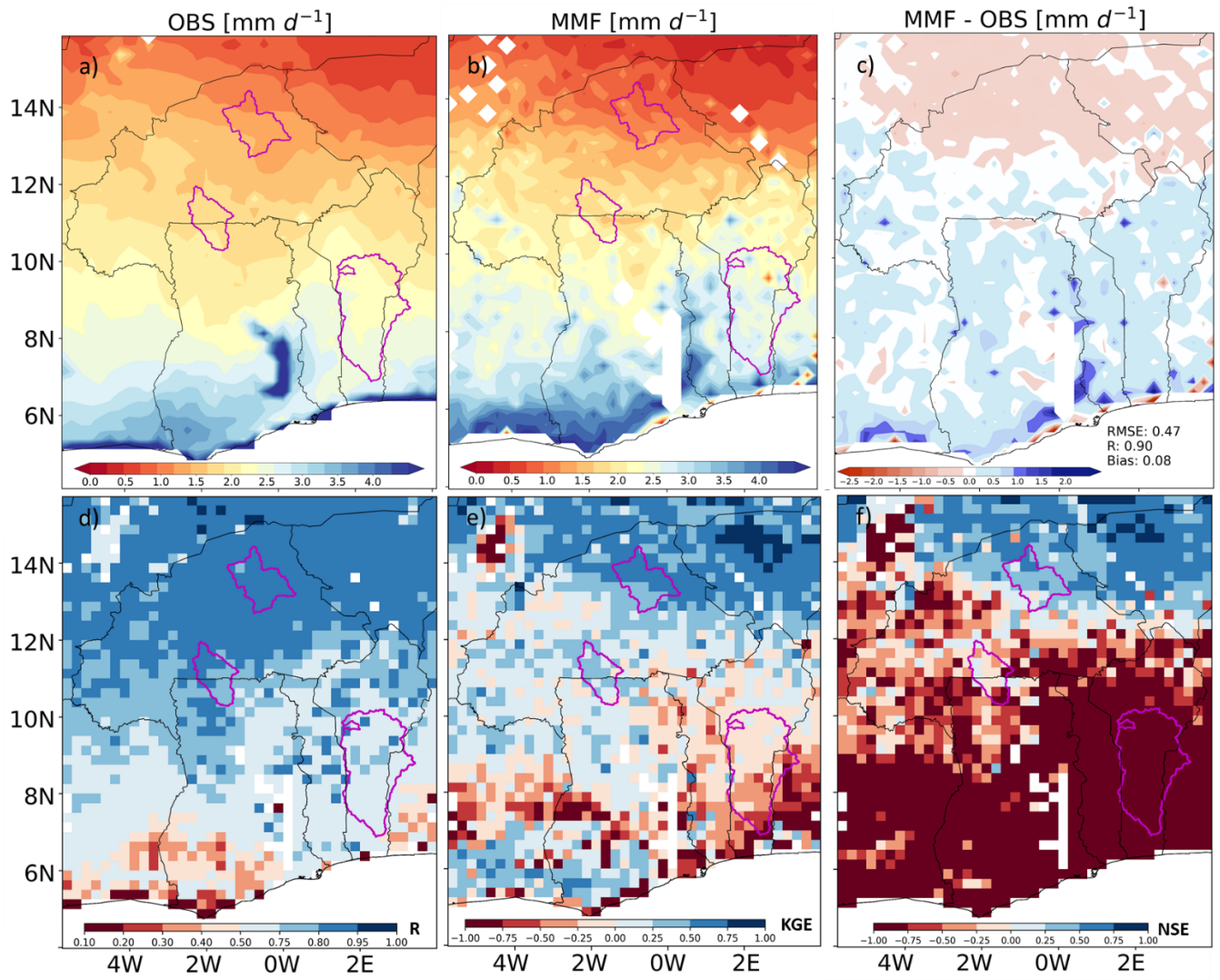

Figure 4.8: Error metrics for the domain level comparison of MMF (b) ET against GLEAM ET (a) with the bias (c) R (d), KGE (e), and NSE (f). The colour ramp is similar for R and KGE. Lower NSE is indicated in fading red and higher performance in fading blue. The horizontal resolution of the simulations is resampled to the GLEAM data.

The sensitivity of the evapotranspiration variable to the improved groundwater representation in the Noah-MP LSM is also evaluated using the daily time series computed for 7 sites where the required data are available (Fig. 4.8). As described in the section 2, the actual evapotranspiration is calculated by employing the MODIS NDVI time series and the potential evapotranspiration computed with the climatic variables from each site. For a broader perception of the actual evapotranspiration pattern, three widely reported approaches namely Penman (black dot), FAO-56 (red square), and Priestley-Taylor (magenta diamond) are used as benchmarks to evaluate the skills of the three schemes. The agreement between the reference data is significant for all the sites and the dry season low and wet season peak occur consistently with the models' outputs. It turns out that all the model configurations result into quite close evapotranspiration outputs whatever the flux monitoring site. The variability recorded with MMF scheme in the lowland areas could not be evaluated for the evapotranspiration because of the absence of required data at the Janga rice site. Overall, the three schemes underestimate the actual evapotranspiration at the Sumbrungu, Kayoro, Nazinga, Nalohou, and Belefoungou sites especially in the dry season. The amount of evapotranspiration during the peak of the wet season is better represented compared to the dry season. In contrary, the models overestimate the evapotranspiration at Wankama Nord and Wankama Sud however the sharp rise and gradual decline respectively during the growing and late season are well captured. The same is observed for the other sites as the temporal cycle is well represented. A foreseen limitation to the agreement of the models with the benchmark dataset can be attributed to the computation of the actual evapotranspiration which combines on site climatic variables with the remote sensing NDVI from MODIS. For the 7 sites, the correlation coefficient is relatively high for the 3 schemes reaching 0.75 at Wankama Nord site. The lowest correlation (0.35) is recorded at Belefoungou where there is less data available for better appreciation. Notwithstanding the little difference in the simulated evapotranspiration, it is remarkable that whatever the site, the models' results are closer to the Priestley-Taylor evapotranspiration followed by FAO-56, and Penman (Table S3). The overall average correlation coefficient is 0.61, 0.62, and 0.61 respectively for FD, TOPMODEL, and MMF. The lowest RMSE is recorded at the Wankama Nord and Sud sites (close to 0) while the average for all the sites is 0.8 mm/d. The models' performance assessed against the 3 benchmarks data is reliable and draws a relevant perspective of the expected amount of evapotranspiration in the study domain.

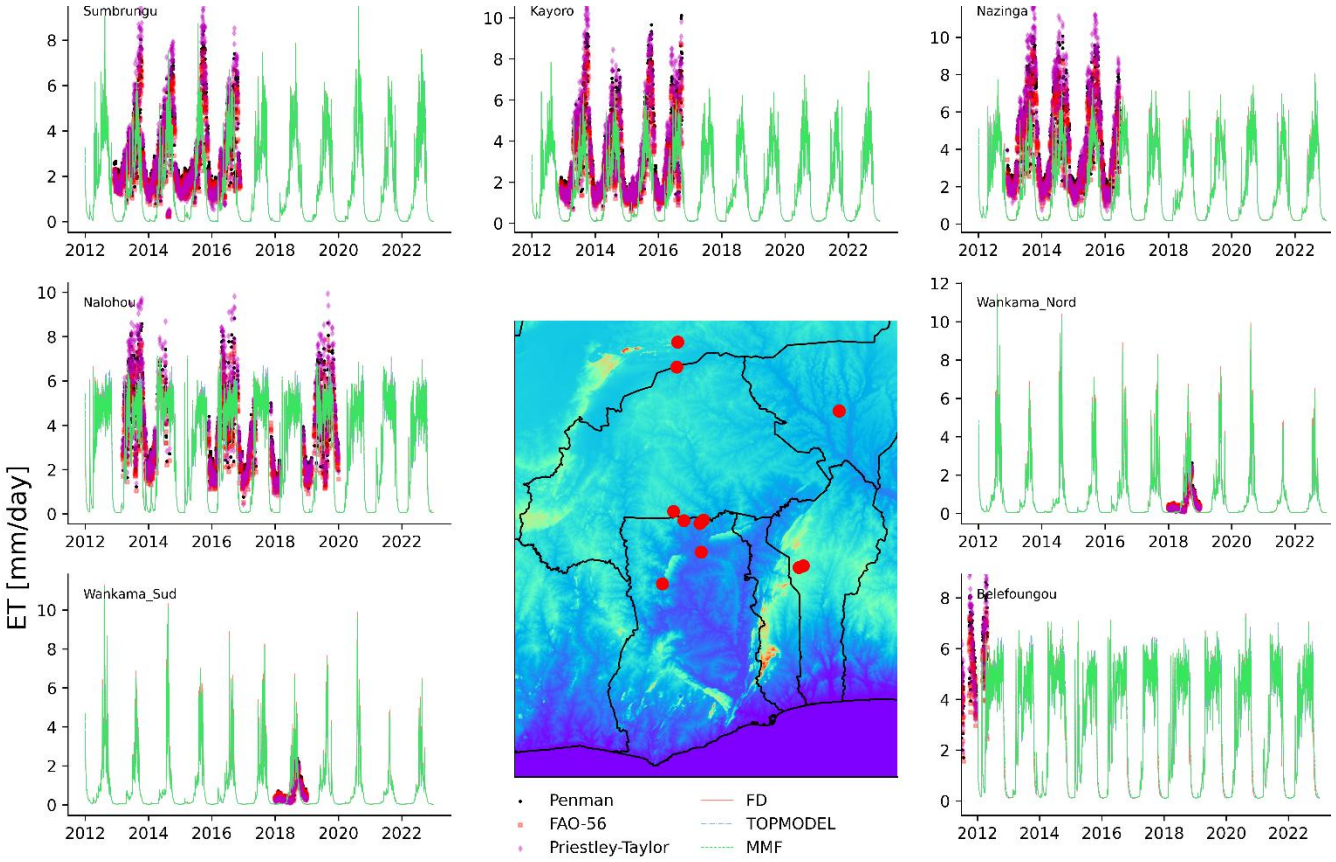

Figure 4.9: Simulated ET from FD (red), TOPMODEL (dash blue), MMF (dot line green) plotted against three computed ET using Penman (black dot), FAO-56 (red square), and Priestley-Taylor (magenta diamond) at the EC flux monitoring sites. The stations located in the Savanna (Kayoro, Sumbrungu, Nazinga, Nalohou, and Belefoungou) and Sahel zones (Wankama Nord and Sud). The red dots on the map locate the flux monitoring sites, the black line is the countries limit (not inferring legal borders) and the image below is the HydroSHED digital elevation model of the domain.

4.1.2.3 Performance in simulating energy fluxes

The three schemes' simulated energy fluxes (sensible heat, latent heat, and ground heat) and the net radiation from the forcing data are compared to the tower observations from the fluxes monitoring sites in the study domain. The models' time step is set to hourly from the 1st to 3rd of March 2013 to ascertain the differences or similarities in the diurnal cycle of the fluxes in contrasting land use conditions. The 7 monitoring sites used as benchmark are spatially distributed in the Savanna (Kayoro, Sumbrungu, Nazinga, Belefoungou, and Nalohou) and Sahel zones (Wankama Nord and Sud) and in different soil types offering a broader perspective for the models' performance evaluation. The purpose of evaluating the FD, TOPMODEL, and MMF simulations on hourly basis is significant to prove the reliability of their performance at the highest temporal resolution. It turns out that the difference in the simulated energy fluxes is negligeable whatever the monitoring site (Figure 4.10). Except from the Belefoungou site, the net radiation from both the simulations and observations matches relatively well for all the sites and the peaks occur around the noon time. For instance, at the 5 sites located in the Savanna region, the overall maximum of the net radiation fluctuates between 750 and 850 W m^{-2} while in the Sahel it reaches above 950 W m^{-2}. The correlation coefficient of the net radiation from the three simulations is the same respectively 0.95, 0.69, and 0.98 for the Nazinga, Sumbrungu, and Kayoro sites (Table S1). The shape of the diurnal cycle indicates a gradual rise and decline of the net radiation from the observations which are well captured by the simulations. The latent heat is close to 0 W m^{-2} for the three schemes replicating the observed pattern at Kayoro, Sumbrungu, and Nazinga which is expected in such period of the year in the study area. Although, the models poorly capture the latent heat at Sumbrungu site (-0.18, -0.15, and -0.12 respectively for FD, TOPMODEL, and MMF), the simulations are reliable for Nazinga and Kayoro and this is confirmed with correlation coefficient of 0.95 and 0.58 for MMF scheme, 0.95 and 0.46 for TOPMODEL, and 0.95 and 0.29 for FD. The three models overestimate the sensible heat at Kayoro and Sumbrungu reaching around 400 W m^{-2} against an observed value of 200 W m^{-2}. The difference is less accentuated at the Nazinga site where the sensible heat is slightly below 400 W m^{-2}. It is remarkable that the sensible heat rise above 0 W m^{-2} before the noon lags by one hour compared to the net radiation. The same pattern can be seen in the observations confirmed by the correlation coefficient of 0.96, 0.63, and 0.96 for MMF, TOPMODEL, and FD respectively at Nazinga, Sumbrungu, and Kayoro. The ground heat is also well captured as the degree of

agreement with the observations is strong with the highest correlation of 0.65 recorded at Sumbrungu site. In the Sahel region, the maximum values extend from 100 to 200 W m^{-2} matching the observations. It can also be noticed that the maximum from FD and MMF are lower compared to the TOPMODEL scheme. Further, at Kayoro, Sumbrungu, and Nazinga sites in the Savanna region, the ground heat is maintained below 100 W m^{-2} while it reaches 200 W m^{-2} at the western part (Nalohou and Belefoungou). The shape of the simulations replicates well the field measurement with a significant degree of agreement confirming the models' reliability in representing the ground heat at a local scale.

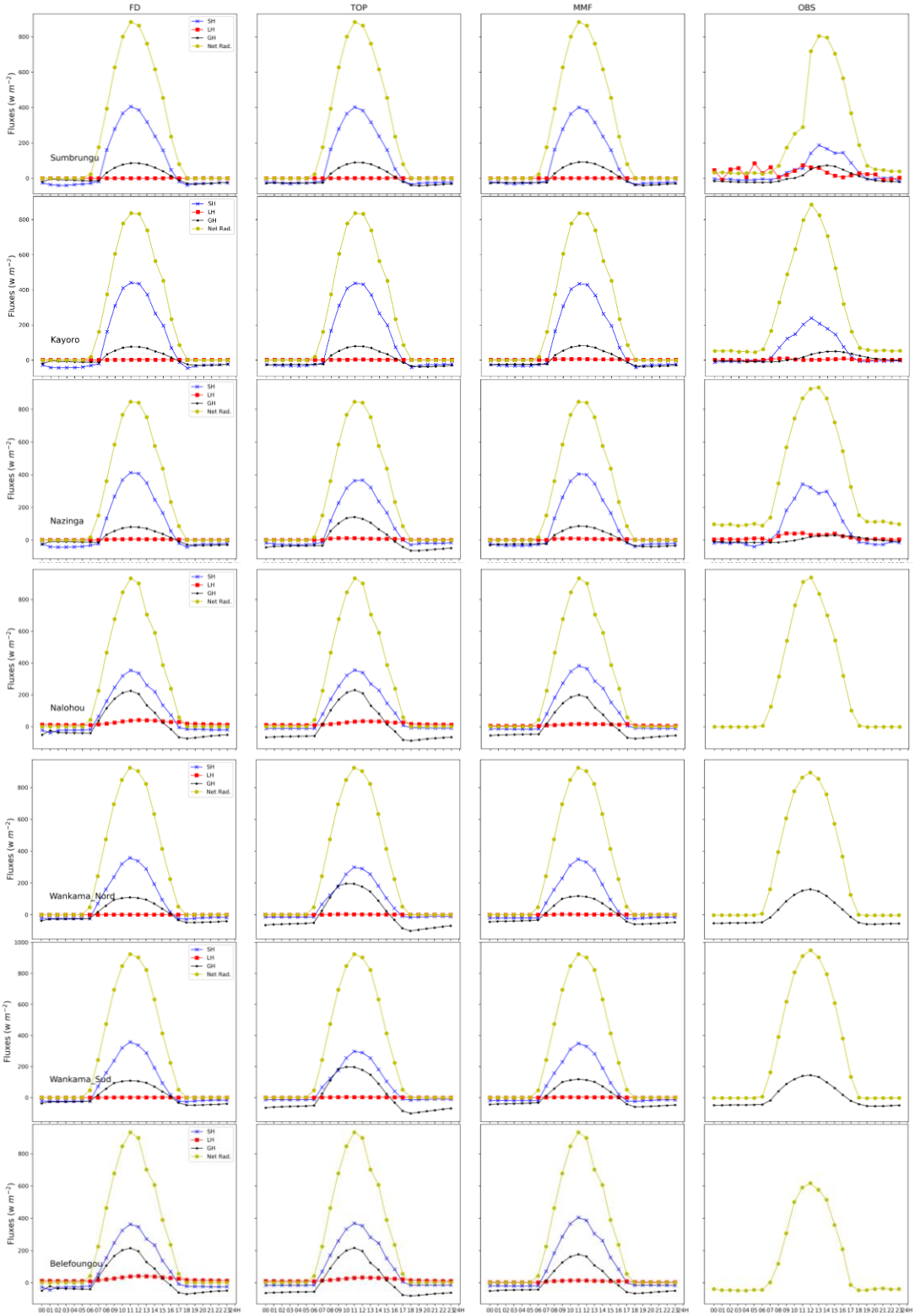

Figure 4.10: Comparison of the averaged diurnal cycle (1st to 3rd January 2013) of the simulated energy fluxes from FD, TOPMODEL, and MMF with field measurement at site level (reading from the left). The three upper sites have all the components namely latent heat (red), sensible heat (blue), ground heat (black), and net radiation (yellow). In the vertical axis, the energy fluxes are in W m^{-2} and the horizontal axis is in hourly time step. Each line indicates the sites.

4.1.2.4 Performance in simulating groundwater storage

To further apprehend the effects of the three schemes, the groundwater storage change is computed for each scheme using the water balance equation (see section 3.1) and the results are compared to the assimilated GLDAS ΔGWS (Fig. 4.11a-f, Fig. S5-6). The groundwater storage used as benchmark is aggregated to the monthly mean and the comparison is done for the period between 2013 to 2016. In the Bonou basin, the linear relationship between the simulated ΔGWS and GLDAS ΔGWS is relatively strong with R values of 0.68, 0.64, and 0.71 respectively for FD ΔGWS, TOMODEL ΔGWS, and MMF ΔGWS. Though the TOPMODEL ΔGWS is less sensitive to the seasonal variability, FD ΔGWS and MMF ΔGWS fit better with the GLDAS ΔGWS. After the rainfall cessation, the groundwater storage drops abruptly between October and January. This observed pattern is well captured with the FD and MMF ΔGWS. The residual variance magnitude to the observed ΔGWS variance is at the lowest with MMF ΔGWS (NSE=0.44, and RMSE=1494.72 mm d^{-1}). Though the maximum of ΔGWS is not captured, the overall performance is good for groundwater storage prediction in the basin. The schemes altogether indicate wetter groundwater storage compared to GLDAS ΔGWS. In the Faga basin, the schemes' performance altogether is low however linear relationship is relatively strong for TOPMODEL ΔGWS.

In the Sissili basin, the linear correlation is relatively strong with R values ranging from 0.42 to 0.64. However, the model performance is relatively low with NSE values ranging between 0.17 and 0.22. The ΔGWS of the FD and MMF are similar and capture better the observed variance compared to the TOPMODEL. The groundwater storage loss after the peak of the rainy season is followed by SM and ET decrease which together fuel the baseflow in the following dry season. From the rainfall onset to cessation, the three components increase altogether while the excess is routed through the runoff.

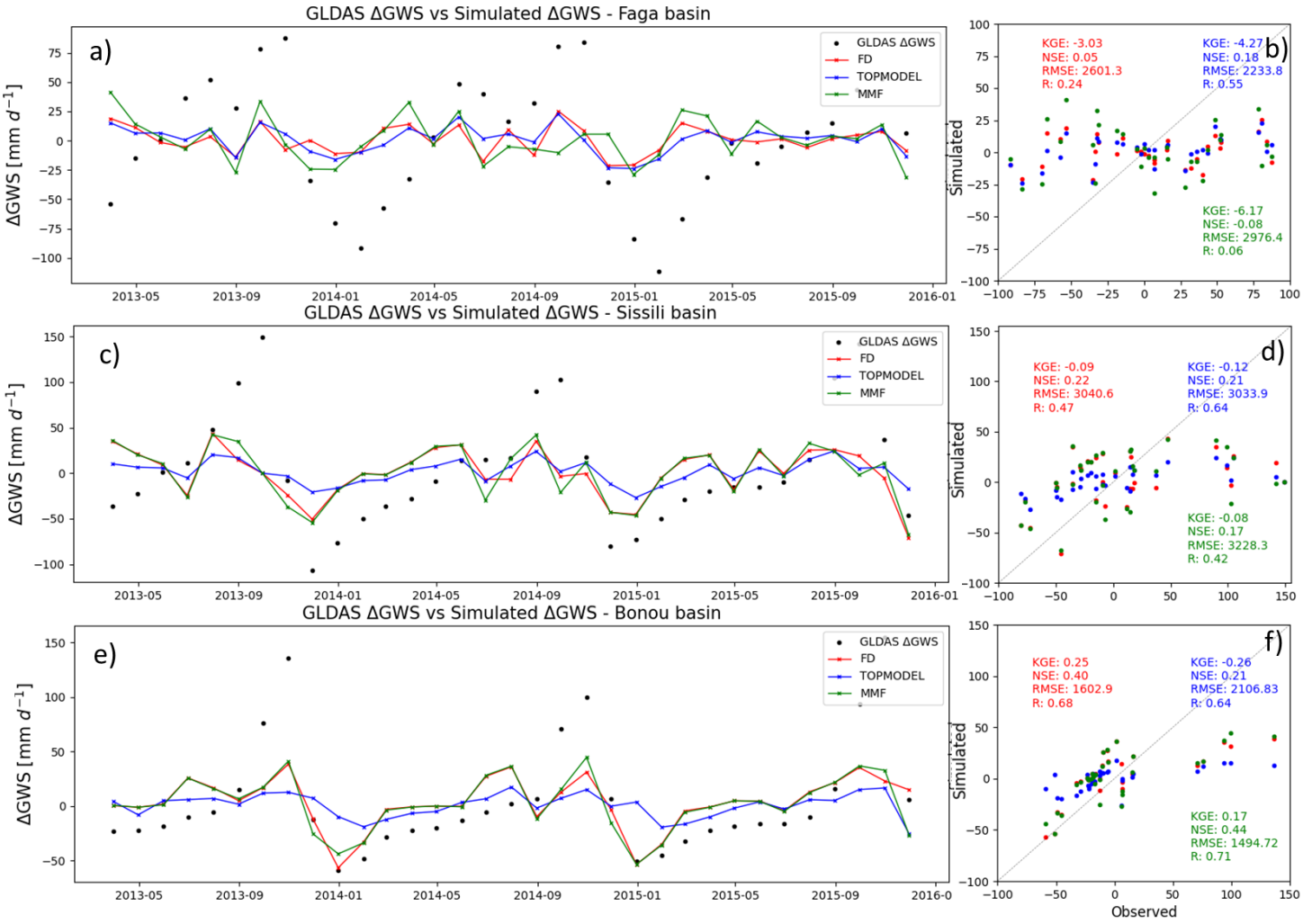

Figure 4.11: Comparison of the basin-averaged GLDAS ΔGWS versus simulated ΔGWS. The scatter plots and metrics of FD, TOMODEL, and MMF are in red, blue, and green

The spatial metrics of the models' performance in representing groundwater storage are shown in Fig. 4.12a-f and S5-S6. There is a strong agreement between the simulated ΔGWS and GLDAS ΔGWS in the Sahelian and Sudanian zones (0.25-0.75). The linear relationship weakens towards the south and this is confirmed with very low KGE and NSE (Fig. 4.12e-f) in mountainous areas and coastal forestlands. The difference is relatively high in areas with high rainfall rates. Within the evaluation period (2013-2016), the observation indicates groundwater storage decrease below the 9th latitude and the opposite in the Sahel. This trend is not captured in the simulations resulting in positive mean bias (20 to 80 mm y^{-1}) in the south and negative in north (-80 to -20 mm y^{-1}) for the schemes (Fig. 4.12c, S5c, and S6c). The relative magnitude of the residual variance compared to observed variance is high in high rainfall rates areas.

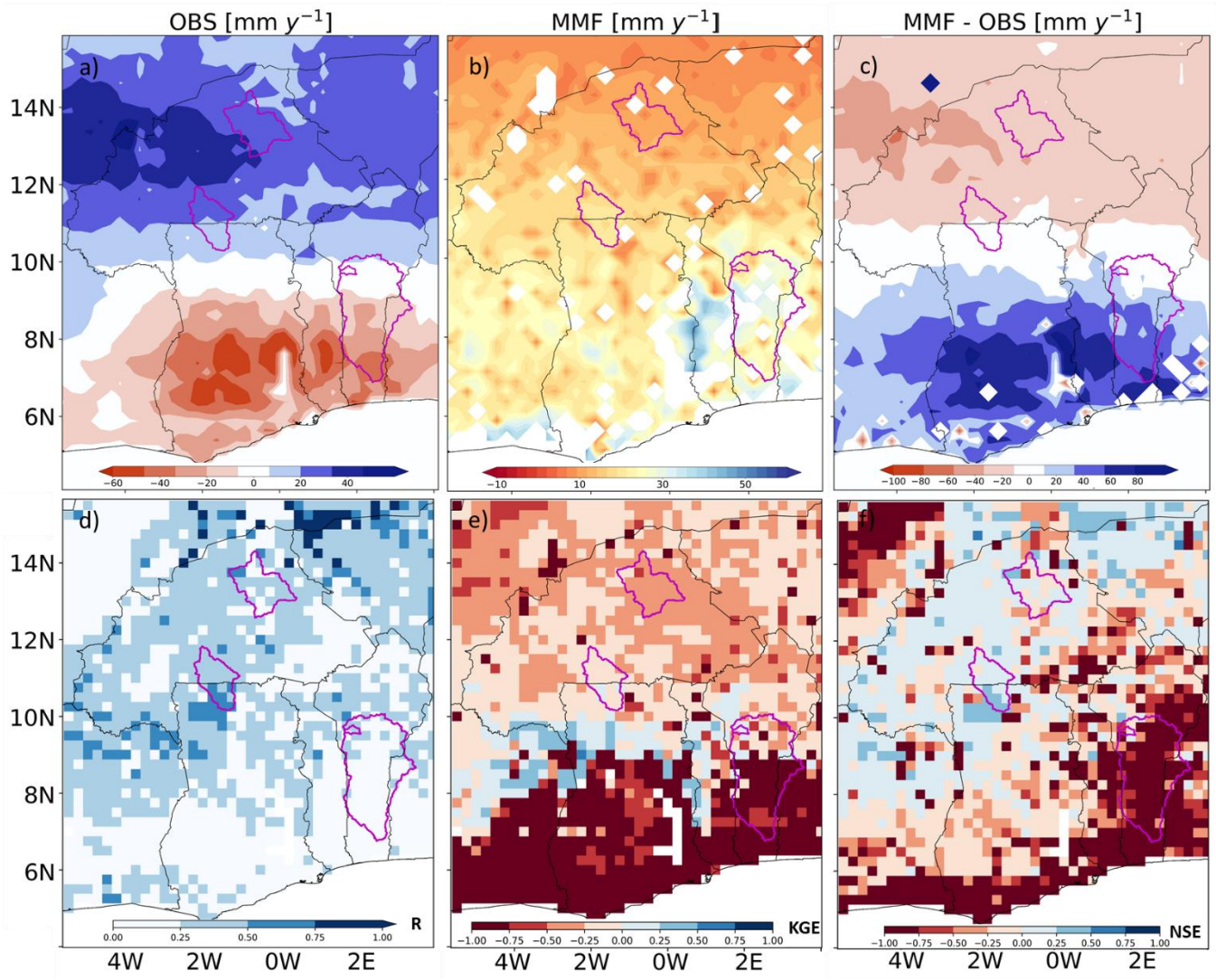

Figure 4.12: Error metrics for the domain level comparison of MMF (b) GWS against GLDAS ΔGWS (a) with the bias (c) R (d), KGE (e), and NSE (f). The colour ramp is similar for R and KGE. Lower NSE is indicated in fading red and higher performance in fading blue. The horizontal resolution of the simulations is resampled to the GLDAS ΔGWS model grid.

4.1.3 Sensitivity of water fluxes to the parameterization schemes

4.1.3.1 Soil moisture response

The average annual soil moisture of the top soil layer from the three schemes is presented in Figure 4.12 and S7. The zonal statistic using the input soil map (STATSGO; Miller & White, 1998) reveals the area average values ranging from 0.08 to 0.24, 0.08 to 0.25, and 0.08 to 0.26 respectively for FD, TOPMODEL, and MMF in the sandy clay loam soil. The spatial variability in the MMF output shows the differences in the soil moisture distribution which is strongly related to the topography and marks a significant break from the FD and TOPMODEL results. This skill demonstrated by the MMF scheme proves the expected contribution to the land surface fluxes when the groundwater lateral flow is captured in the LSM however the influence of the topography can be overestimated (Reinecke et *al.*, 2024). In the riverbeds of the study area characterized by lower slopes, the FD, TOPMODEL, and MMF schemes display respectively soil moisture values of 0.15±0.05, 0.16±0.05, and 0.17±006 m^3 m^{-3} which are overall above the values in the highlands. With the MMF scheme, the estimation increased by more than 20% compared to FD while a slight difference can be noticed with the TOPMODEL (Fig. 4.12). The results confirm a similar study undertaken by Rummler et *al.* (2022). Furthermore, the Sahelian climatic zone displays the lowest soil moisture while the highest values are recorded in the Guinea Coast. For instance, the soil moisture in the evergreen forest (South-West) ranges between 0.05 and 0.34 m^3 m^{-3} for FD, 0.06 and 0.4 m^3 m^{-3} for TOPMODEL, and 0.06 and 0.43 m^3 m^{-3} for the MMF scheme while lower values are noted in the Dahomey Gap as a result of subsequent rainfall. Therefore, the rainfall gradient mentioned in the study area section is reflected in the spatial distribution of the area-averaged soil moisture values. For instance, the simulated soil moisture displays 0.08±0.03, 0.08±0.03, and 0.09±0.03 m^3 m^{-3} respectively for FD, TOPMODEL, and MMF in the Sahel, 0.16±0.02, 0.16±0.03, and 0.17±0.03 m^3 m^{-3} in the Savannah and 0.21±0.02, 0.22±0.03, and 0.22±0.04 m^3 m^{-3} in the Guinea Coast. Based on the geological features in the GLiM database, the overall soil moisture is lower in the hard rock areas (0.16 m^3 m^{-3} for FD, TOPMODEL, and MMF) compared to the sedimentary units (0.22 m^3 m^{-3} for FD, TOPMODEL, and MMF). This geological difference in the soil moisture might indicate which type of aquifer systems are likely to contribute more to maintaining wetter soils and hence tempering the soil warming in the dry season. The reason behind this pattern deserves thorough investigation to understand how the subsurface width interacts with the land surface fluxes. Across the three schemes, the North-East/South-West mountain range dominating the study area prolongs towards

the Savannah region soil moisture values close to the results observed in the Guinea Coast climate.

The annual patterns of the area-averaged soil moisture from the FD and TOPMODEL schemes show a similar temporal variation with a dry period extending from December to May and a wet period from June to October. The MMF output displays comparative pattern with a little lower dry period indicating earlier rainfall onset (Fig. S7). In the dry months, the soil moisture is maintained below 0.17 m^3 m^{-3} with slight yearly differences while the values can reach 0.28 m^3 m^{-3} and above between July and September. Despite the improved subsurface representations, the change in the temporal pattern is almost negligeable even though a clearly add up is noticed in the spatial pattern.

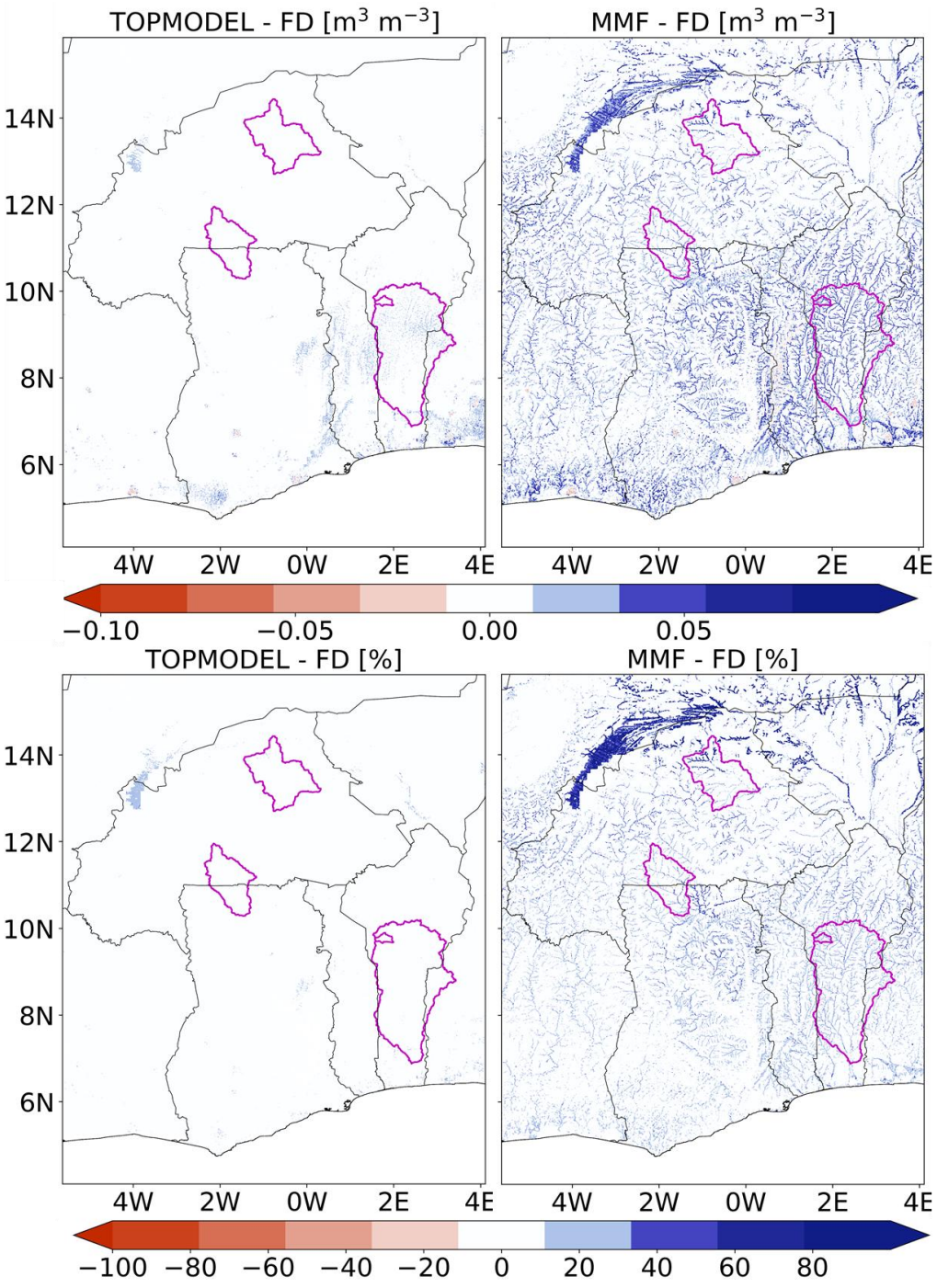

Figure 4.13: Computed relative and absolute soil moisture differences (units: $m^3\ m^{-3}$) between the TOPMODEL and FD (upper); MMF and FD (lower). The difference is negative towards the red patches showing the ET decrease under a particular scheme. The blue patches indicate an increase in ET. Countries located within the domain are delimited with a black line. The blue patch in the north-west is a bias caused by temporary wetlands of the Niger river.

4.1.3.2 Evapotranspiration response

The maps in Figure 4.13 show the absolute and relative difference of evapotranspiration (ET) compared to the free drainage scheme. The overall spatial distribution of the ET is similar with a north-south gradient. The averaged ET based on the climatic zone is 3.19, 3.15, and 3.18 mm/d in the Guinea Coast, 2.27, 2.2, and 2.25 mm/d in Savanna, and 0.96, 0.92, and 0.99 mm/d in the Sahel respectively for the FD, TOPMODEL, and MMF schemes. In the riverbeds of the domain, the ET values approximate 2.3±1 mm/d for MMF, 2.1±0.91 mm/d for TOPMODEL, and 2.15±0.91 mm/d for FD. The higher ET values and the spatial variability displayed by the MMF scheme confirm the fact that the water residence time is higher in the topographic convergence areas. In the Guinea Coast, the highest ET occurs in the evergreen forest (South-West) where the values reach 3.18±0.65, 3.15±0.66, and 3.23±0.69 mm/d and in the mountain range (3.33, 3.32, and 3.3 mm/d) respectively for FD, TOPMODEL, and MMF. The remarkable difference noted in the MMF result is its ability to capture the ET from topographic convergence areas. The difference in the simulated ET using the FD as reference shows a significant increase of more than 20% (1 to 2 mm/d) in the riverbeds for the MMF across the study domain. In the highlands of the Savanna and Sahel zones, the two improved subsurface schemes (TOPMODEL and MMF) reveal a decrease by ~5% (0 to 1 mm/d; Fig. 4.13).

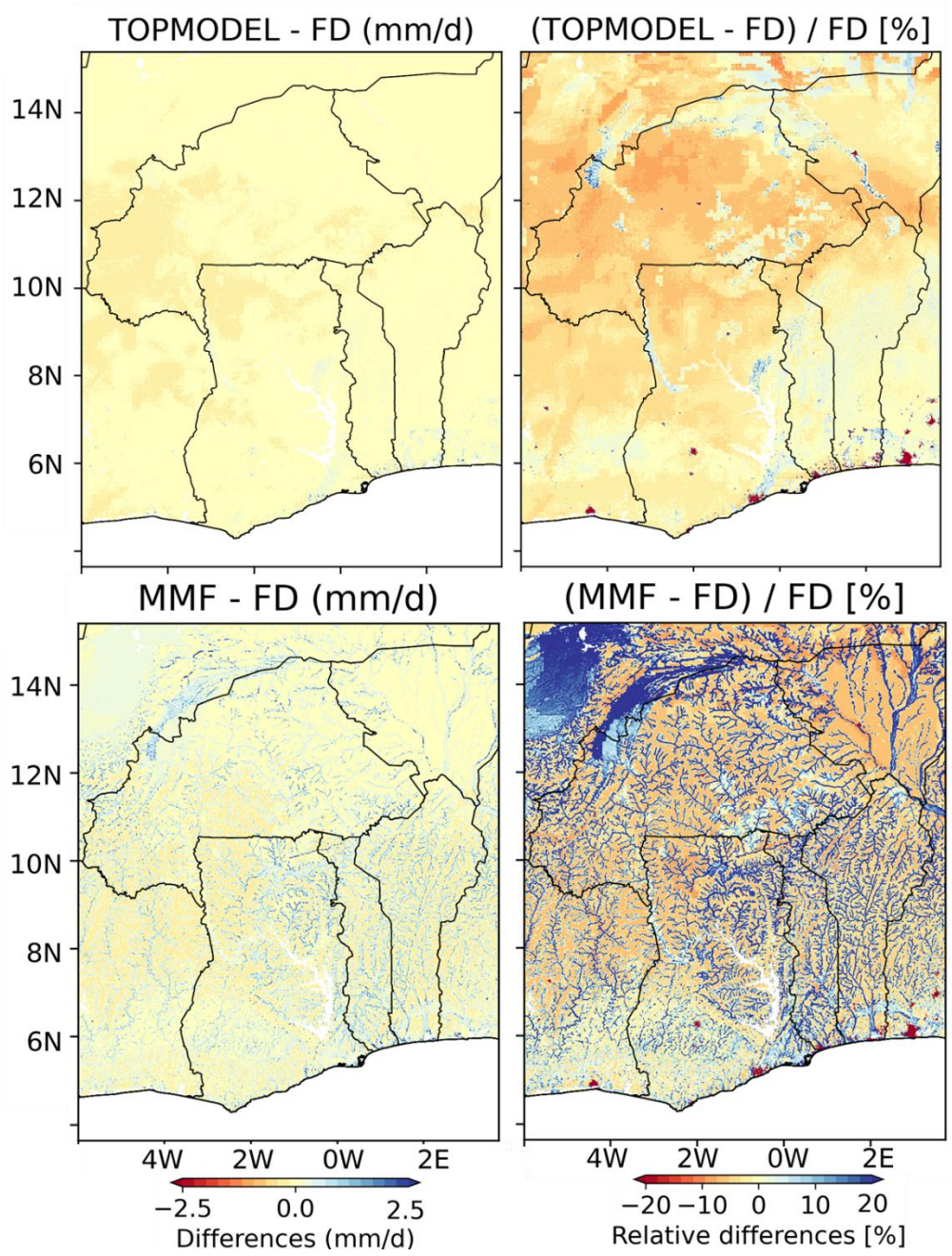

Figure 4.14: Computed relative and absolute differences of ET between the TOPMODEL and FD (upper); MMF and FD (lower). The difference is negative towards the red patches showing the ET decrease under a particular scheme. The blue patches indicate increase in ET. Countries located within the domain are delimited with black lines.

4.1.3.3 Impact on streamflow

The long-term inter-annual variability of the monthly streamflow and the corresponding evaluation metrics are shown in Figure 4.15a-d. Most of the created streamflow outlets in the domain have no observation. In this section, the impacts of the three schemes are further evaluated using the streamflow data from two gauges (Donga and Oueme Rivers). The Oueme River basin is the largest in Benin and it is gauged at different stations but the focus here is on the Bonou station located in the south (Fig. 4.15c and d). The choice of the two for the models' evaluation is justified by the relatively longer series availability. Contrary to the mitigated effect of the variably saturated model coupled to LSMs on streamflow (Wagner et *al.*, 2016), the influence of 2D groundwater parameterization (MMF and TOPMODEL) is significant. The MMF streamflow records approximately 2 folds lower mean bias in the Donga catchment while the FD and TOPMODEL are slightly different (5.97 and 6.21 mm/month). Table S1 displays the error metrics computed for the two stations and it turns out that the MMF scheme has the lowest bias at the two stations. At Donga station, the highest KGE of the improved subsurface schemes is recorded with TOPMODEL (0.65) showing its skill in capturing the observed variance (Fig. 4.15a-b). Regarding the streamflow variability, FD and TOMODEL perform well in the basin (0.68 and 0.65) but MMF displays lower KGE. The R values show a strong linear relationship across the models (0.87, 0.84, and 0.88). The models achieve a low residual variance magnitude to the observed variance with NSE values of 0.67, 0.68, and 0.57. The shape of the observation is well captured and the degree of agreement of the three schemes is acceptable and reflects the overall seasonal cycle and inter-annual variability of the streamflow in the Donga catchment. Despite, the relatively strong linear relationship in the Oueme catchment (0.82, 0.81, and 0.78), the model validation using the calibration of Donga yields significantly lower performance (Fig. 4.15c-d). However, the MMF scheme achieves the lowest mean bias (Fig. 4.15d).

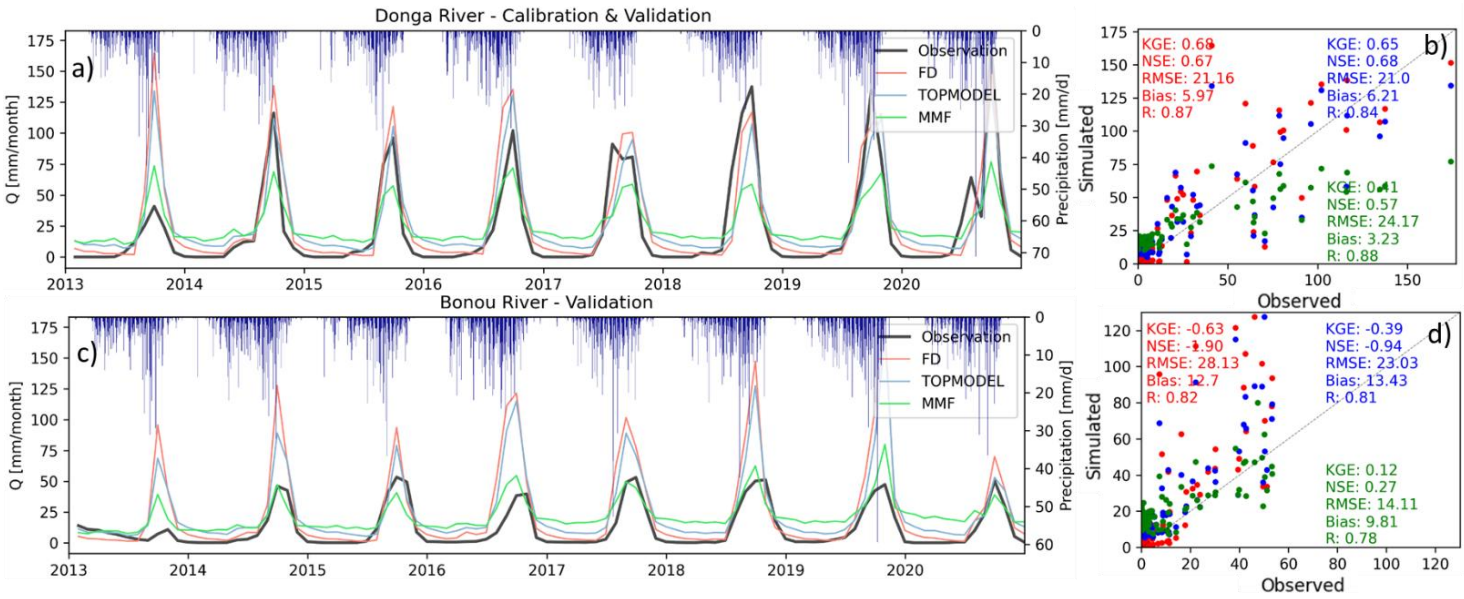

Figure 4.15: Simulated daily streamflow with FD (red), TOPMODEL (blue), and MMF (green), observation, and precipitation plotted on the secondary axis (upper) at Donga (a) and Bonou (b) stations. The corresponding metrics (e.g. KGE, R) of the simulations are displayed.

The domain level comparison with the ESA CCI soil moisture confirms the strong performance of the models as the spatial pattern indicates that more than 80% of the domain has a KGE value above 0.8 in the Savana zone. Although the Sahel zone and Guinea Coast are less captured (0.25 to 0.5), there is no systematic error recorded as the seasonal cycle and inter-annual variability are well reproduced with RMSE maintained below 0.01 m^3 m^{-3}. The MMF scheme offers a level of detail in the topographic convergence area that the FD and TOPMODEL do not. This requires further investigation to ascertain how closely it performs compared to dedicated hydrological models like MODFLOW and PARFLOW. Although the focus here was not on the lower layers, Wagner et *al.* (2016) argued that the subsurface improvement using dedicated hydrological models has a more pronounced effect on the lowest soil layer reducing the water content by approximately 10%. The same study confirms the present results obtained with the top soil revealing a lower impact (-0.03 m^3 m^{-3}) as also demonstrated by Zhang et *al.* (2024) in southern Africa. Despite the relatively low difference, slight changes in soil moisture can affect land surface processes (e.g., Koné et *al.*, 2022; Talib et *al.*, 2022; Robert et *al.*, 2011; Stocker et *al.*, 2018; Kunstmann & Jung, 2003). As shown in Fig. 10, with the MMF scheme, the sensitivity of the WRF Hydro model is mainly significant in the riverbeds.

The remarkable difference in the impact of the improved groundwater scheme of WRF-Hydro on the soil moisture is shown in the spatial heterogeneity displayed by MMF in the topographic convergence areas. That is, the MMF scheme gives a detailed representation of the soil moisture and increases the values by more than 20% (MMF minus FD) while the TOPMODEL makes almost no difference with the FD scheme. The former finding was demonstrated by Rummler et *al.* (2022) in temperate climate however recent arguments by Reinecke et *al.* (2024) stated that the influence of the topography on the simulated water table might be overblown. The rainfall gradient is reflected in the simulated soil moisture with a spatial average of 0.08, 0.16, and 0.22 m^3 m^{-3} respectively in the Sahel, Savanna, and Guinea Coast. However, there is a spatial heterogeneity based on the soil types with increased soil moisture in the North-East/South-West Mountain range and the evergreen forest located in the west.

Rafieeinasab et *al.* (2024) recently reported a reasonable agreement between the default WRF-hydro ET and GLEAM ET using cumulative distribution functions across the conterminous United States (CONUS). This study confirmed the finding and further demonstrated that improved subsurface schemes (MMF ET and TOPMODEL ET) reduce the mean bias with relatively strong performance towards low rainfall rate areas. The strong spatial correlation

obtained in this study (Fig. 8d, S3d, and S4d) confirms the findings of Zhang et *al.* (2024). Overall, the three schemes have a dry bias in the Sahel (-0.5 mm d^{-1}) and a wet bias in the Sudanian savanna and Guinea Coast compared to GLEAM ET. The FD ET displays the highest wet bias, especially in high precipitation and mountainous areas (~2 mm d^{-1}). However, the lowest mean bias values are recorded with TOPMODEL ET (0.02 mm d^{-1}) and MMF ET (0.08 mm d^{-1}). This suggests that the disagreement between the simulated and observed ET depends on precipitation rates and gradient. The spatial correlation coefficient, KGE, and NSE confirm that the three schemes capture quite well the seasonal cycle and inter-annual variability of ET with a strong linear relationship except in the southeast where higher rainfall occurs. The ET is better represented in the Sahel zone where low ET occurs with KGE ranging from 0.5 to 1. The performance degrades towards the southern part of the domain where higher ET occurs but the overall RMSE is maintained below 1.5 mm d^{-1}.

Zhang et *al.* (2024) demonstrated the sensitivity of WRF-Hydro ET in response to soil perturbations at 5 to 30%. In addition to this subsurface effect, the MMF scheme increases ET by 1 to 2 mm d^{-1} (~20%) in topographic convergence areas. There is almost no difference between the FD and TOPMODEL ET but the MMF reveals more detailed spatial heterogeneity. The evergreen forest in south west of the domain displays the highest ET of 3.18 mm/d which is expected in the area because plant activities have no water and energy limitations for photosynthesis. There is a decline in the ET moving from the coastal sedimentary basin in the southeast to the hard rock aquifer systems. While this difference requires thorough investigation, it is not overblown to argue that the groundwater systems' productivity might play a significant role in sustaining the ET, especially in the dry season. The comparative analysis against the data assimilation product of GLDAS reveals the relatively high performance of the schemes in the Bonou basin compared to lower rainfall rate basins (e.g. Faga basin). The domain-level evaluation displays high linear correlation however the trend of groundwater storage ΔGWS during the evaluation period is poorly represented. The simulated ΔGWS altogether are less sensitive to the observed seasonal variability in the Faga basin however the values are within the expected range.

The precipitation bias is reported to introduce discrepancies in simulated streamflow (Arnault et *al.*, 2016, 2021; Liu et *al.*, 2021; Quenum et *al.*, 2022; Sofokleous et *al.*, 2023) however the inter-annual variability and seasonal cycle are reasonably captured confirming the findings of Wagner et *al.* (2016). In opposition to the low effect of the fully coupled atmospheric-hydrological model system they employed; this study finds rather a significant impact of the

subsurface schemes on streamflow (Fig. 12). The models' evaluation using the streamflow from Donga and Oueme reveals the average performance of the three schemes. Despite the strong correlation coefficients, there is a contrasted performance in the simulations as the FD scheme has the highest KGE with the Donga catchment while MMF performs better with the Oueme catchment. The seasonality of the streamflow is well reproduced however the three schemes overestimate the streamflow at both stations. The amount of streamflow routed through the channels by the MMF scheme is lower than FD and TOPMODEL which are quite similar. The model calibration for the Donga catchment displays a reliable result with the KGE reaching 0.74 (Quenum et *al.*, 2022; Arnault et *al.*, 2016, 2021). Still, this study's findings demonstrate that improving the groundwater scheme of WRF-Hydro can yield better performance if both the model calibration and the groundwater parameterization focus on each catchment peculiarity.

The runtime tradeoffs incurred on one CPU node with 20 tasks per node for the improved subsurface schemes (2012-2022) are 49% and 64% compared to the FD scheme (254 hours) respectively for TOPMODEL and MMF (Fig. S12). Because of the demonstrated benefits of employing the MMF scheme in the region, the supplement ~10% runtime is fairly reasonable. Nevertheless, The MMF scheme representation of the subsurface is computationally less expensive and provides relatively accurate simulation compared to a fully-coupled land-atmosphere model with a dedicated hydrological model (e.g., MODFLOW, PARFlow). At the local scale, this performance could increase if high spatial resolution static variables (land cover, digital elevation model, and soil types) are employed. At a larger scale, its performance blurs because of the inputs' simplification, and each source of discrepancy further reduces the accuracy.

Despite the relatively good performance of the model calibration, the broader evaluation for a larger domain is limited by the data scarcity and each catchment peculiarity. That is, the efficient evaluation of the improved groundwater representation in Noah-MP requires first a thorough calibration of the model for a particular catchment, and then the parameterizations can be tested keeping in mind that the models' yield could vary based on the area of interest. Both soil moisture and evapotranspiration are underestimated in the dry period compared to the reference, this results in relatively low infiltration and high surface runoff. This might be related to inadequate vegetation parametrization in the tropics which deserves thorough investigation in future works. Further, water use for agriculture, livestock breeding, drinking water supply, and many others affect the recorded streamflow downstream and these factors are not explicitly integrated in the WRF-Hydro model.

4.2 Contrasting effects of Idealized Afforestation on water budget and energy fluxes: a WRF-Hydro modeling study over West Africa

4.2.1 Model validation

In this section, the simulated scenarios are benchmarked against remote sensing products and on-site measurement for model validation. The accuracy of the simulated variables from the reference scenario (REF) is evaluated by comparing soil moisture to ESA CCI remotely sensed soil water content, evapotranspiration to GLEAM ET, latent and sensible heat to FLUXCOM-RS heat fluxes, and streamflow to observed values from AMMA-CATCH project.

4.2.1.1 Soil moisture

The basin-averaged soil moisture from the observation and simulation is shown in Fig. 4.16. The locations are chosen to investigate the models' skill in the different climatic zones and it turns out that the KGE values are respectively 0.72, 0.71, and 0.72 for Oueme, Sissili, and Faga (Table 4.2). This strong performance is confirmed with NSE values ranging between 0.62 and 0.64. The seasonal cycle and inter-annual variability are well captured as there is a strong linear relationship between the observed and simulated values with correlation coefficients from 0.9,0 to 0.97. The model underestimates soil moisture which is shown in PBIAS values of -8.2, -19.9, and -28.2% for Oueme, Sissili, and Faga. However, the RMSE values are relatively low between 0.001 and 0.002 highlighting the reliability of the model to represent soil moisture. Further, the error metrics computed for the afforestation scenarios (EBF-VC, EBF-VD, SAV-VC, SAV-VD, WS-VC, and WS-VD) are summarized in Table 3.2.

Table 4.2: Evaluation metrics of the observation versus simulated soil moisture from the reference scenario.

Metrics	Oueme	Sissili	Faga
KGE	0.72	0.71	0.72
NSE	0.62	0.64	0.64
Pbias	-8.2	-19.9	-28.2
RMSE	0.001	0.002	0.002
R	0.90	0.97	0.96

The potential change in the soil moisture in response to the idealized afforestation experiments is evaluated in the top layer of 0.1 m over Faga, Sissili, and Oueme basins located respectively in the Sahel, Sudanian, and Guinea coast climatic conditions (Fig. 3.2). Compared to the current land use (REF) scenario, EBF-VC and WS-VC experiments decrease the mean SM by 0.2 and 0.1 mm, while the SAV-VC increases it by 0.8 mm in Faga. The three experiments increase SM by 0.1, 0.4, and 0.4 mm in Sissili. However, the scenarios reveal a decrease of mean SM by 0.5, 0.6, and 0.1 mm for EBF-VC, SAV-VC, and WS-VC in higher precipitation areas (Oueme). Higher vegetation density associated with wetter conditions in Oueme basins reveals a negative effect on soil water content as the mean SM decreases respectively by 2.1, 1.1, and 0.3% for EBF-VC, SAV-VC, and WS-VC. The experiments show a positive effect in Sissili with an increase in the mean SM of 0.8, 5.5, and 2.8%. This reveals the suitability of SAV-VC in the Sudanian climate for water conservation in the upper soil layer, which is critical for improving agricultural productivity. The potential change is rather mitigated in Faga located in drier conditions, where SAV-VC increases mean SM by 12% while EBF-VC and WS-VC decrease SM by 1.3 and 0.4%. The efficiency of the afforestation experiments is controlled by both the annual rainfall and the vegetation health (e.g. NDVI). Similar effects are observed on the minimum SM in the dry season and the maximum SM at the peak of the rainy season in Faga. However, the positive effect on mean SM is associated with a decrease of minimum SM by 0.2, 0.1, and 0.2 mm in Sissili. The effect on the maximum SM is rather mitigated because SAV-VC and WS-VC increase SM by 0.7 and 0.5 mm, while EBF-VC decreases the maximum SM by 0.7 mm. The soil water loss recorded in Oueme in response to the idealized afforestation affects the minimum and maximum SM. EBF-VC, SAV-VC, and WS-VC decrease the maximum SM by 1.2, 0.6, and 0.7 mm, and the minimum SM by 0.7 mm. Overall, the idealized afforestation experiments have a positive effect on SM in drier climatic conditions (Faga and Sissili), with the highest potential change recorded with SAV-VC.

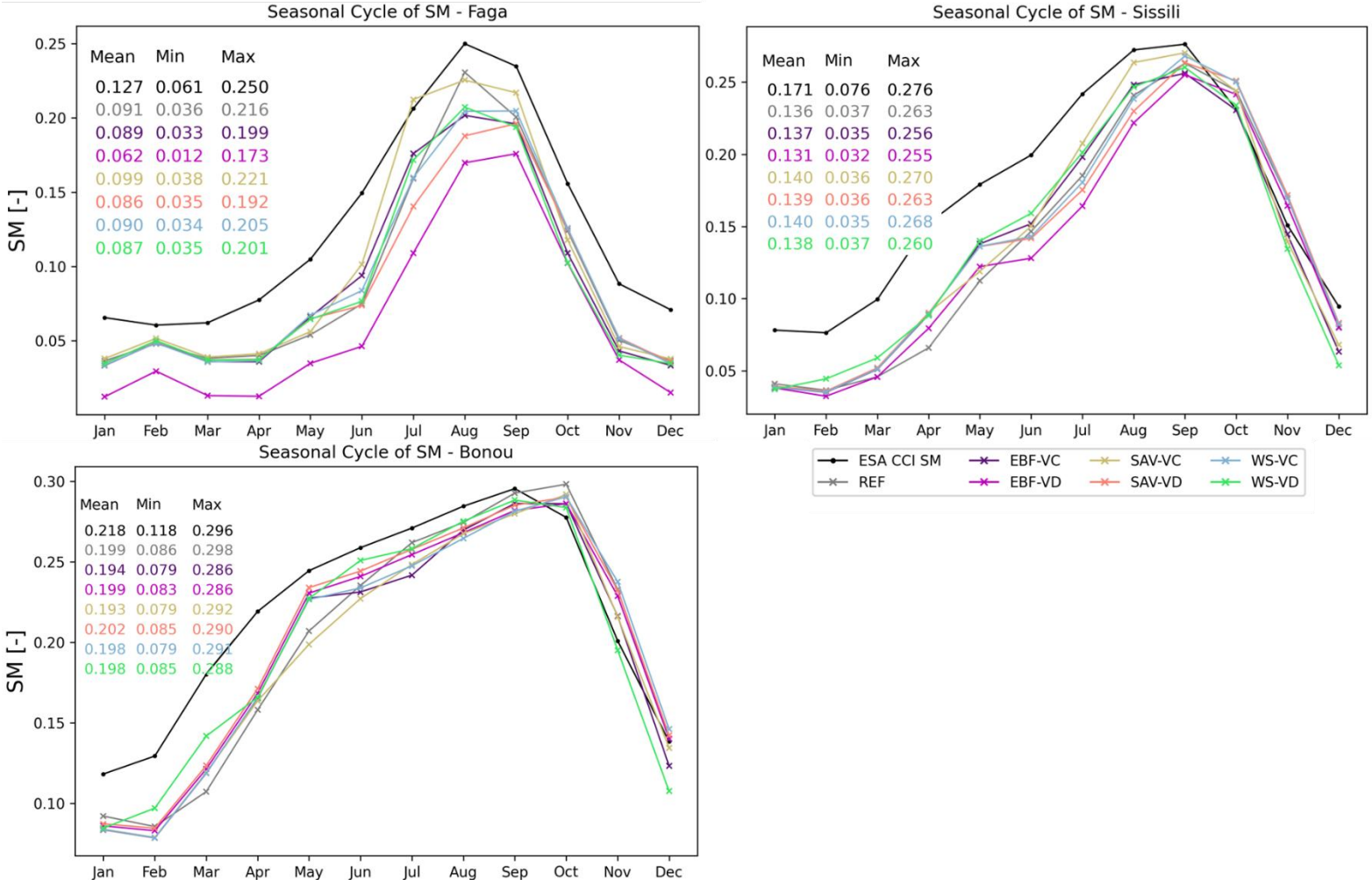

Figure 4.16: Seasonal cycle of SM under the idealized afforestation experiments and the reference scenario (REF). The graph of relative difference is added to the supplementary figures.

4.2.1.2 Evapotranspiration

The GLEAM ET is used as a reference to evaluate the simulated evapotranspiration (Fig. 4.17). Overall, the model's performance is relatively strong, confirming the range of water loss through evapotranspiration expected in the basins. The model performance is strong in Faga and Sissili with KGE values of 0.57 and 0.37. The highest performance is recorded in the lower precipitation rate areas and periods, while it decreases in wetter conditions. The linear relationship between the observed and simulated temporal pattern is strong with correlation coefficient values of 0.87, 0.92, and 0.92 respectively in Oueme, Sissli, and Faga catchments (Table 4.4). The lowest magnitude of prediction error is recorded in Faga (0.3 mm d^{-1}), followed by 0.6 and 1.0mm d^{-1} in Sissili and Oueme (Fig. 4.17). The model tends to overestimate ET during the rainy season with a significant difference ranging from 1.0 to 1.5 mm $d^{-1,}$ while it underestimates ET in the dry season with a lower difference. This systematic bias is shown in the PBIAS values of 16.9, 8.2, and -20.8% in Oueme, Sissili, and Faga. Table S2 shows the computed error metrics for all the scenarios. Discrepancies can be introduced into simulated ET in the rainy season due to higher water availability for evaporation and transpiration from bare soil and vegetation (Naz et *al.*, 2023). Higher ground temperature is associated with overestimation of ground evaporation (Jefferson & Maxwell, 2015) as a result of the sensitivity of simulated ET to soil resistance parameterization in the dry period. Further, the latent heat is significantly affected by the soil parameterization in the dry season (Kollet, 2009). For instance, a slight change in the soil permeability coefficient exacerbates ET bias. Another contributing factor to ET bias is the vapour pressure and wind speed from the meteorological forcing (Naz et *al.*, 2023).

Table 4.3: Evaluation metrics of the observation versus simulated ET from the reference scenario.

Metrics	Oueme	Sissili	Faga
KGE	-0.19	0.37	0.57
NSE	-1.15	0.37	0.55
Pbias	16.9	8.2	-20.8
RMSE	1.0	0.6	0.3
R	0.87	0.92	0.92

Figure 4.17 shows the response of the evapotranspiration (ET) to the idealized afforestation experiments in Faga, Sissili, and Oueme. Remarkably, the average ET is increased whatever the climatic condition except for SAV-VC in Sissili where a negative effect is recorded. For instance, EBF-VC, SAV-VC, and WS-VC increases the average ET by 0.25, 0.08, 0.07 mm d^{-1} in Faga. Although SAV-VC decreases average ET by 0.05 mm d^{-1} in Sissili, EBF-VC and WS-VC increase ET by 0.11 and 0.03 mm. The water loss through evapotranspiration in Oueme is 0.25, 0.22, 0.24 mm d^{-1} for respectively EBF-VC, SAV-VC, and WS-VC. Whatever the climatic condition, the experiments with dynamic vegetation scheme (EBF-VD, SAV-VD, and WS-VD) show even higher ET values. The potential water loss in Oueme reaches 10.5, 8.2, and 9.8% respectively for EBF-VC, SAV-VC, and WS-VC. In Sissili, EBF-VC and WS-VC increases average ET by 5.7 and 1.2% while SAV-VC is associated with a positive effect on ET (-8.3%) reducing significantly the water loss. The highest increase of ET occurred with EBF-VC in Faga with PBIAS value of 17.6% followed by WS-VC (6.1%) and SAV-VC (1.6%). Likewise the negative effect on average ET, the idealized afforestation experiments increase the maximum ET whatever the basin with the highest value of 0.4 mm d^{-1} (EBF-VC) in Sissili. The water stress in dry season is further accentuated in Faga by EBF-VC and WS-VC by 0.35 and 0.18 mm d^{-1}. Similar drought enhancement effect is recorded in Sissili and Oueme under intense vegetation density concurrent with higher annual rainfall.

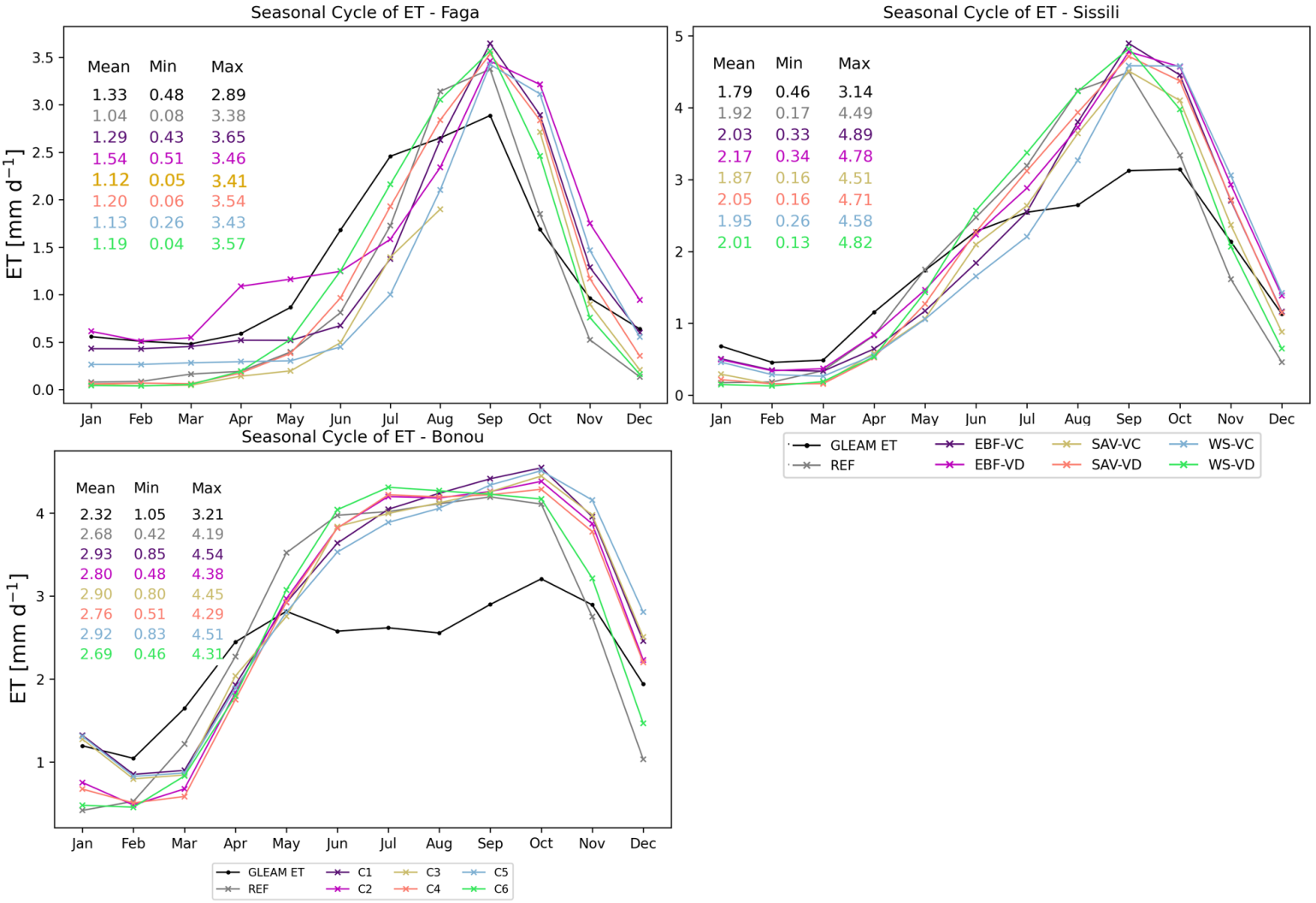

Figure 4.17: Seasonal cycle of ET under the idealized afforestation experiments and the reference scenario (REF). The graph of relative difference is added to the supplementary figures.

.

4.2.1.3 Streamflow

The simulated streamflow is assessed against on-site observation from Oueme, Sissili, and Donga (Fig. 18). The model agreement with observed streamflow is relatively strong in the Oueme and Donga basins with KGE values of 0.47 and 0.51. The results show a relatively good seasonal variability with a strong linear relationship as the correlation coefficients vary from 0.57 to 0.86 (Table 4.5). Nevertheless, the performance of the model in Sissili is weak with KGE and NSE of 0.02 and 0.14. Across the basins, overestimation of base flow occurred however the shape of the streamflow hydrographs is well replicated with PBIAS of 2, 30, and -41% respectively for Donga, Oueme, and Sissili.

Table 4.4: Evaluation metrics of the observation versus simulated streamflow from the reference scenario.

Metrics	**Oueme**	**Sissili**	**Donga**
KGE	0.47	0.02	0.51
NSE	0.51	0.14	0.63
Pbias	29.6	-41.2	1.8
RMSE	37467	1593	14
R	0.76	0.57	0.86

Reducing the amount of streamflow and delaying the occurrence of the its peak are reliable ways to tilt the water balance against water stress. It turns out that EBF-VC, SAV-VC and WS-VC experiments reduce streamflow respectively by 24%, 18%, and 21% in Donga and 31%, 26%, and 28% in Oueme. WS-VC experiment shows a negative effect on streamflow in Sissili with an increase of 2% but EBF-VC and SAV-VC decrease the average streamflow by 3% and 16%. The dynamic vegetation experiments (EBF-VD, SAV-VD, and WS-VD) demonstrate a weaker effect in reducing the streamflow however, in drier conditions, the opposite occurs in Sissili.

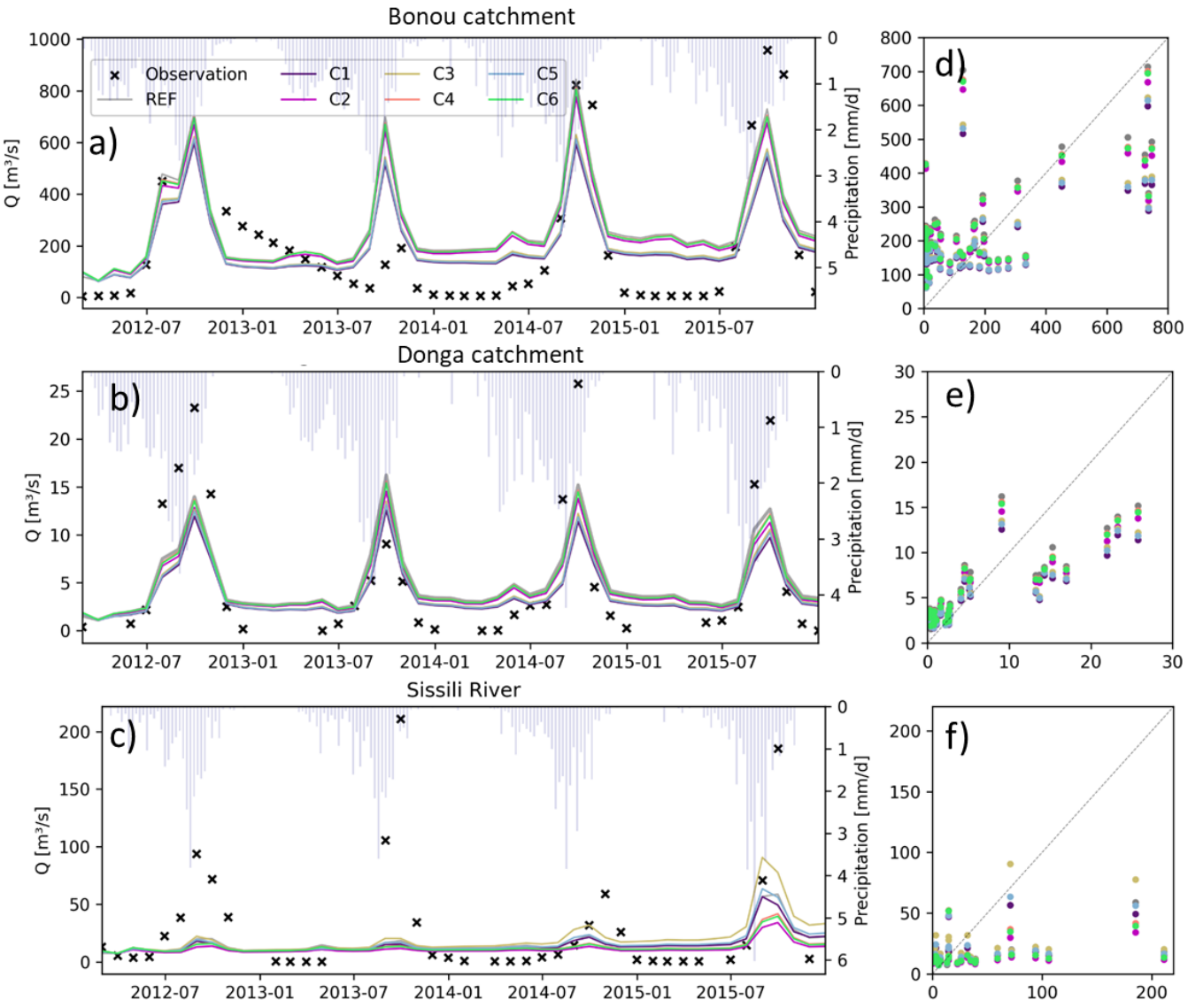

Figure 4.18: Simulated streamflow under the idealized afforestation experiments and the reference scenario (REF).

4.2.1.4 Latent heat and sensible heat

The daily turbulent fluxes from FLUXCOM-RS products (Jung et *al.*, 2019) are used to ascertain the model performance in simulating latent and sensible heat (Table 4.6). Overall, there is a strong linear relationship between the reanalysis LH and the simulation which is associated with R scores ranging from 0.92 to 0.95. The lowest RMSE is recorded in Faga (554 W m^{-2}) and the highest is reported in Oueme (2309 W m^{-2}). Figure 4.19 highlights the overestimation of the latent heat with the highest difference in terms of PBIAS reaching -59%. Despite this discrepancy, KGE scores range from 0.31 to 0.4 (Table 4.5), indicating that the pattern of the seasonal cycle is well replicated. Table S3 summarizes the performance under different afforestation scenarios.

Table 4.5: Metrics of LH and SH versus FLUXCOM-RS product

Energy component	Metrics	Oueme	Sissili	Faga
LH	KGE	0.32	0.31	0.40
	NSE	-1.95	-0.76	0.18
	Pbias	-55.9	-59.4	-55.0
	RMSE	2310	2306	554
	R	0.92	0.95	0.94
SH	KGE	-0.22	0.26	0.27
	NSE	-2.06	-0.70	-3.79
	Pbias	-64.6	-36.7	-43.1
	RMSE	1567	567	600
	R	0.52	0.68	0.47

Similar to the ET in section 5.1.2, the impact of the idealized afforestation experiments on latent heat (LH) is shown in Figure 4.19. Whatever the climatic zone, there is an increase in mean LH compared to the current land use scenario (REF). While the mean LH is 16.54 W m^{-2} in Faga with REF experiment, EBF-VC, SAV-VC and WS-VC add a further 4.9, 2.5, 2.8 W m^{-2}. Similar patterns are recorded for the three experiments in Sissili with an increase of 5.7, 1.03, and 3.1 W m^{-2}. SAV-VC experiment decreases mean LH by 0.63 W m^{-2} while EBF-VC and WS-VC increase LH by 2.71 W m^{-2} and 1.47 W m^{-2} in Oueme. The PBIAS values indicate that EBF-VC and WS-VC increase LH by 3% and 1% while SAV-VC decreases the flux by 1.8%. In water-limited conditions, the highest increase of mean LH is recorded with SAV-VC in Sissili (28%) and Faga (28.5%). The experiments increase the maximum LH in Oueme by 9.9, 2.1, and 0.73 W m^{-2} for EBF-VC, SAV-VC, and WS-VC. The opposite effect is observed in the minimum LH. Though higher latent heat is associated with a cooling effect on the land surface, it leads to higher ET, which enhances the overall water stress in the basin.

Likewise, the case of LH, there is a significant linear relationship between the simulated SH and the reanalysis SH. The correlation coefficients are 0.7, 0.7, and 0.5 in Faga, Sissili, and Oueme however the model underestimates SH by -65, -37, and -43.1%. The agreement between the simulated SH and reanalysis SH is high in Faga (KGE=0.3), while a lower performance occurs in Oueme. There is a trend in the potential change of SH in response to the experiments. For instance, EBF-VC increases mean SH by 20.6, 6.1, and 4.9 W m^{-2} respectively for Faga, Sissili, and Oueme. The corresponding PBIAS values are 10%, 12%, and 39.8%.

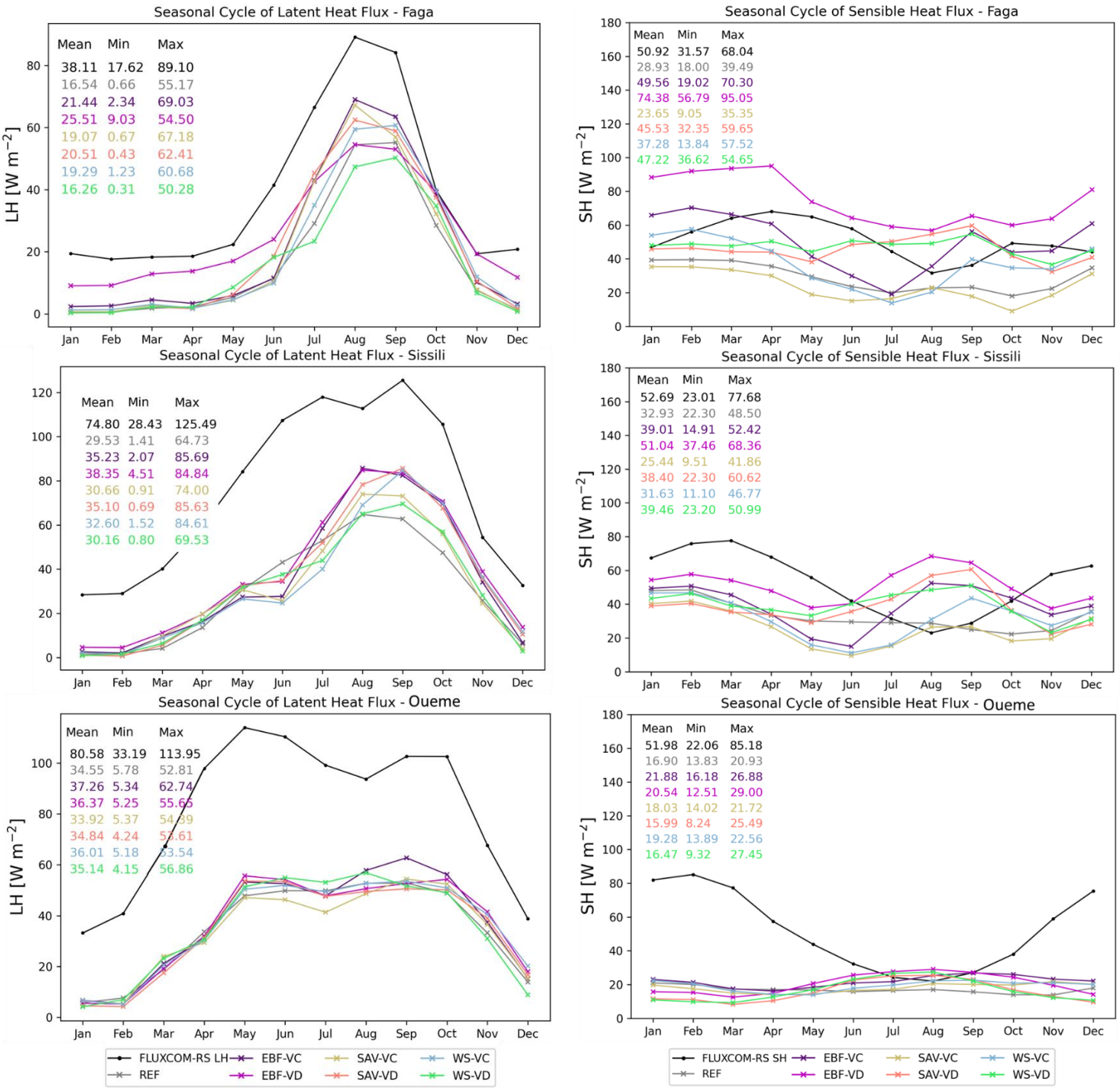

Figure 4.19: Seasonal cycle of sensible heat (SH) and latent heat (LH) under the idealized afforestation experiments and the reference scenario (REF). The graph of relative difference is added to the supplementary figures.

4.2.2 Patterns of water and energy fluxes under the idealized afforestation

4.2.2.1 Evapotranspiration and soil moisture response to different idealized afforestation

The spatial distribution of the potential change in the water cycle (ET, ΔSM, UGRF, and ZWT) and energy fluxes (LH, SH, and GH) in response to the idealized afforestation experiments is highlighted in this section. Figure 4.20 displays the differences of ET and SM between the idealized afforestation experiments and the current land use scenario (REF). Most of the areas affected by the afforestation are located above the 11th latitude (see Section 4.2). The gradient of vegetation density in the idealized experiments is reflected in their impact on the average ET. EBF-VC experiment has the highest ET increase, with the maximum occurring in Central Burkina Faso, Niger Delta, and the riverbeds (>1 mm d^{-1}). A similar spatial pattern is recorded in the WS-VC experiment with a lower potential increase of ET. However, SAV-VC decreases slightly average ET. The dynamic vegetation experiments (EBF-VD, SAV-VD, and WS-VD) indicate higher ET compared to their counterparts. The relative difference displayed in Fig. S5 indicates that 50 to 75% of ET is added across the forested SBG domain with EBF-VC. SAV-VC and WS-VC increase ET respectively by ~25% and less than 50% from the galley forest in riverbeds (~25%). Meanwhile, the experiments decrease ET in the Niger Delta. In Sissili and Oueme basins, a similar spatial pattern of ΔET occurs.

SAV-VC has the strongest negative impact on ΔSM in the top soil layer as it systematically reduces the average soil moisture by 0.05 to 0.1 m^3 m^{-3}(Fig. 4.20). The relative percentage varies around 10% (see Fig. S5), likewise EBF-VC, which has a lower negative impact (~0.05 m^3 m^{-3}). Remarkably, WS-VC increases the average SM with a relative difference of 5 to 10% (Fig. S5) in the Sahelian region. WS-VC experiment provides the best water restoration scheme for the Sahelian and part of the Sudanian region as it has moderate ET, increases SM, and reduces the water table depth.

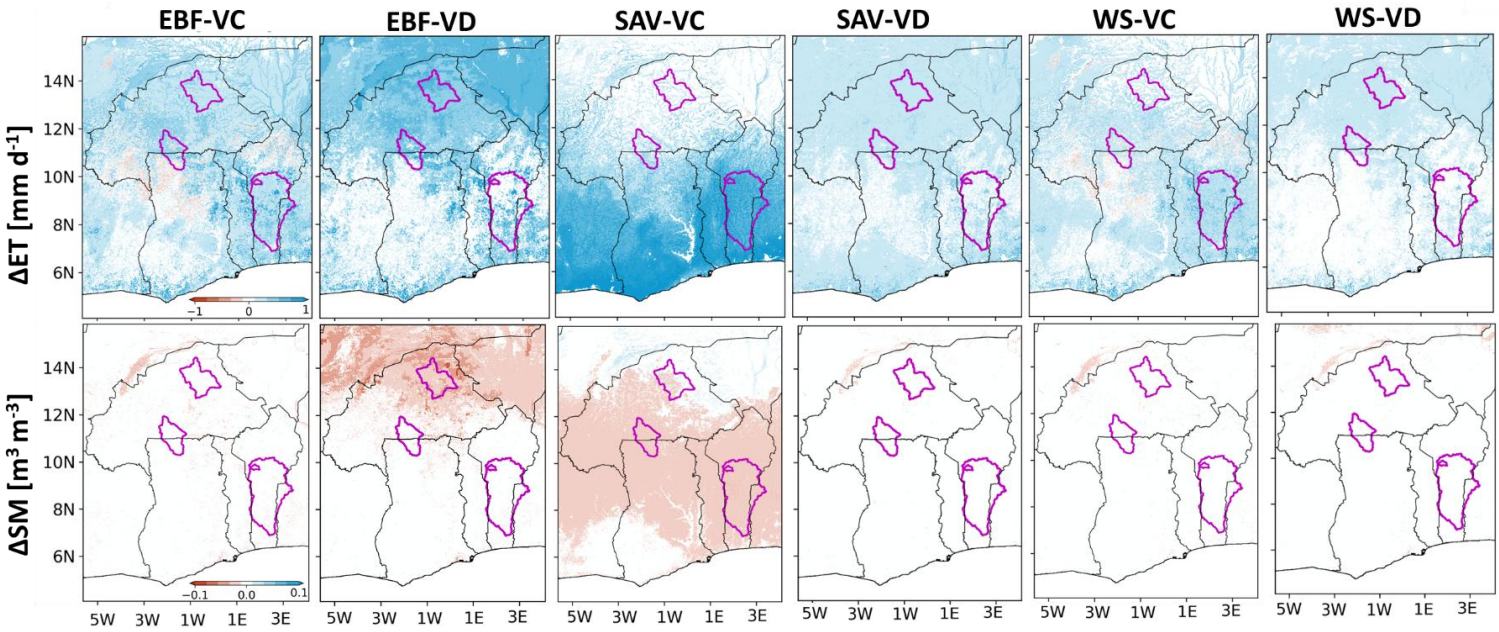

Figure 4.20: Calculated absolute differences of ET between the idealized afforestation experiments and REF (upper) and of ΔSM (lower). The gradient of red and blue patches shows decreasing and increasing ET/ΔSM towards high impact areas. Countries located within the domain are delimited with black line and basins with magenta line. The graph of relative difference is added to the supplementary figures (Fig. S5)

4.2.2.2 Water table and underground runoff responses to different idealized afforestation

The effect of idealized afforestation on underground runoff and water table depth in the region is shown in Figure 4.21. In the supplement figures, similar figures of the relative difference in percentage are displayed for the investigated variables (Fig. S6). The change in temporal mean of UGRF and ZWT (2012-2015) in response to the degraded lands regreening is computed as the difference between the idealized afforestation experiments and the current land use (REF). The range of UGRF responses indicates a positive sign of change for EBF-VC and WS-VC, unlike SAV-VC, which shows a lower effect to negative in regreened areas (SBG). Across the simulated scenarios, ΔUGRF varies from 0 to 10 mm in most of the affected areas. Except for SAV-VC, all the experiments increase the magnitude of UGRF in the riverbeds. As shown in the case of ET, EBF-VD, SAV-VD, and WS-VD experiments increase UGRF compared to their counterpart. Therefore, the rank in the magnitude of the afforestation effect depends mainly on the vegetation density. SAV-VC has the least effect and reduces the average UGRF towards highlands. The experiments with the dynamic vegetation scheme (EBF-VD, SAV-VD, and WS-VD) display a higher increase of UGRF, with the highest potential change achieved with EBF-VD (> 10 mm). This potential change represents 20 to 40% increase (Fig. S6) compared to the current land use scenario. SAV-VC experiment has an opposite effect in Oueme basin as UGRF is increased by ~5 to 10 mm. Furthermore, the idealized afforestation experiments altogether show a lower magnitude of change towards highlands. That is, moving from the riverbed towards higher altitudes, the regreening effect on UGRF decreases gradually. This spatial pattern can be attributed to the characteristics of the groundwater scheme MMF, which is sensitive to the topography. In summary, the aforementioned evidence suggests that the intensity of the afforestation effect is controlled by the vegetation density, while the spatial distribution depends on the subsurface scheme used (MMF scheme in this case).

The potential change in the groundwater depth (ZWT) is shown in Figure 4.21 and S6. Remarkably, SAV-VC increases the water table depth by 0.5 to 1m compared to the reference scenario. In contrast, WS-VC and EBF-VC decrease average ZWT by 0.5 to 1.5m. Altogether, the experiments reduce ZWT in the Oueme basin in higher precipitation conditions. A contrasting spatial effect is recorded with SAV-VC as the experiment increases the water table in the Sahelian region, while it shows the opposite in Oueme (~-0.5). This spatial pattern highlights the interplays between the factors that should define the choice of the afforestation approach. That is, the vegetation density to be achieved in a given area, as described in section 4.2, should take into

account the annual rainfall and the topography. The sensitivity of the groundwater scheme MMF to the topography is reflected in the spatial distribution of ZWT, as a lower magnitude of the afforestation effect is recorded towards the highland, likewise in the case of UGRF. Overall, a higher decrease in water table depth in EBF-VC and EBF-VD experiments is associated with higher water loss through ET and ΔSM decrease. The contrary effects observed between EBF-VC and SAV-VC raise the question of the priorities of the afforestation initiative. That is, the choice of afforestation approach should be based on whether the initiative intends to restore water in the subsurface, the land surface, or both. WS-VC experiment displays a reliable water restoration pattern as it reduces the water table, increases the average SM in most of the Sahelian region, and achieves a moderate water loss through ET. In Sissili, a similar range of ET is achieved with SAV-VC and WS-VC; however, WS-VC increases the average SM, while SAV-VC depletes SM significantly. WS-VC decreases the groundwater table depth in most of the Sahelian region, while SAV-VC shows the opposite effect. These spatial patterns indicate that water restoration in Sissili might be achieved with vegetation density greater than SAV-VC and lower than WS-VC. Although all the idealized afforestation experiments reduce the water table depth in Oueme, SAV-VC decreases significantly SM, with the highest ET. Therefore, the vegetation density close to WS-VC offers a better water restoration in Oueme as it achieves lower ET compared to EBF-VC. EBF-VD, SAV-VD, and WS-VD have similar effects on ZWT as their counterpart but with a high magnitude of potential change.

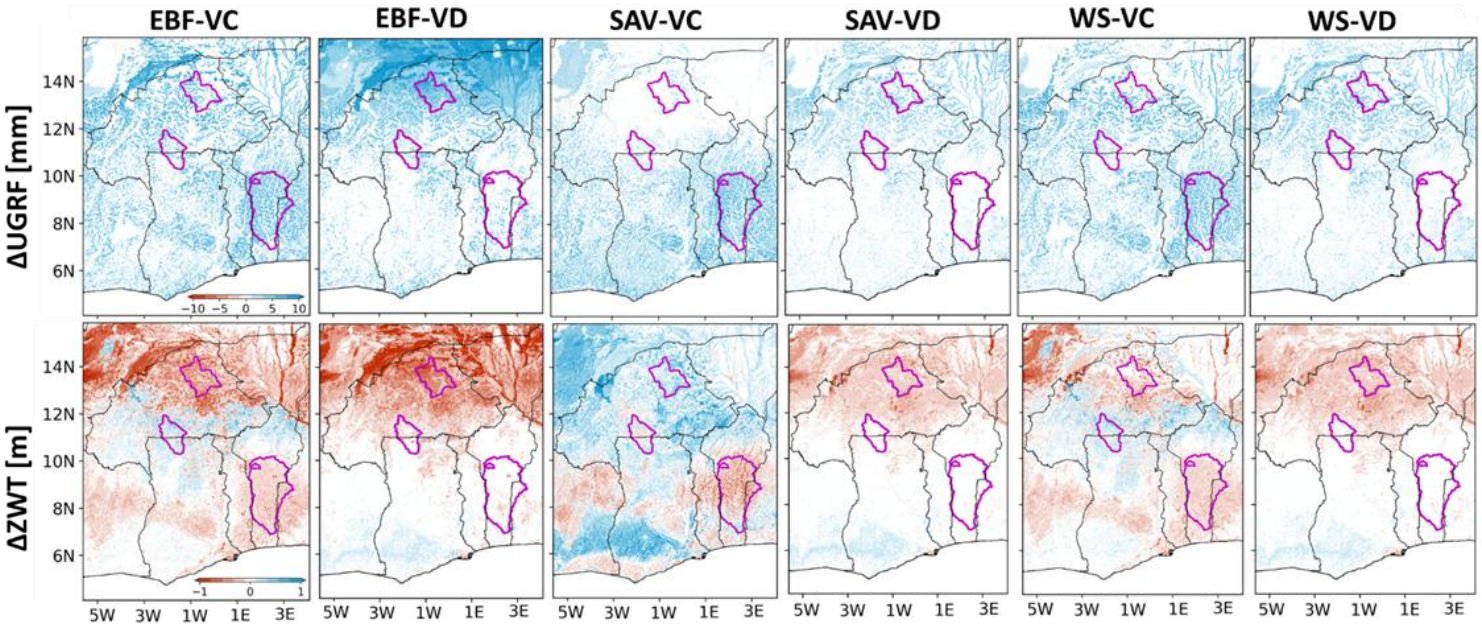

Figure 4.21: Calculated absolute differences of underground runoff (UGRF) between the idealized afforestation experiments and REF (upper) and of water table depth (ΔZWT; lower). The gradient of red and blue patches shows decreasing and increasing UGRF/ΔZWT towards high impact areas. Countries located within the domain are delimited with black line and basins with magenta line. The graph of relative difference is added to the supplementary figures (Fig. S6)

4.2.2.3 Energy fluxes response to different idealized afforestation

In this section, the changes in the latent heat, sensible heat, and ground heat in response to the idealized afforestation experiments are evaluated. Figure 4.22 displays the difference between the simulated fluxes from idealized afforestation and the current land use scenario. It highlights the surface energy input or removal in each of the energy balance component in regreened areas. The spatial pattern of the potential change in latent heat (ΔLH) is similar to what is reported above on ET as higher vegetation density experiments (EBF-VC and WS-VC) show the highest LH increase especially in Central Burkina Faso. Higher density of tree cover in EBF-VC has a cooling effect on the land surface. Towards the Sahelian region in drier conditions, the afforestation experiments (EBF-VC, SAV-VC, and WS-VC) tends to a lower potential change in LH. The range of the potential change across the experiments varies from -10 to 20 W m^{-2}. As in the case of ET, there is a gradient in the magnitude of change in respect to the vegetation density. Remarkably, SAV-VC experiment shows a contrasting effect in the region as it increases average LH towards higher latitude in the Sahelian region (Fig. S7) while decreases LH in North-West of Burkina Faso, South Niger, and in Oueme basin. This spatial heterogeneity of the potential change confirms the mitigated effect of afforestation with low vegetation density as it might result in rather a warming effect. The idealized afforestation experiments with dynamic vegetation scheme (EBF-VD, SAV-VD, and WS-VC) display similar range of ΔLH with the largest impact in Central Burkina Faso. Figure S7 shows the percentage of the potential change. SAV-VC reduces LH by 10 to 15% in Faga, Sissili, and Oueme basins while there is an increase of 10 to 60% with EBF-VC and WS-VC. The sign of the potential change depends on factors like rainfall rate, vegetation density, and topography. Nevertheless, the soil characteristics is another key factor which is not explored in this study. A weaker response of LH to the idealized afforestation experiments is observed towards the Sahelian region suggesting that a minimal annual rainfall is required for their efficiency in storing water. In some parts of south Niger, a negative effect of -30 to -10% is recorded whatever the experiments. The spatial pattern of the potential change in LH is heterogeneous comparatively to ET which suggest the need to evaluate the responses with different levels of model complexity. Remarkably, EBF-VC and WS-VC decreases the sensible heat (SH) across the Sahelian region (above 12^{th} latitude) with values ranging from -50 to 25 W m^{-2}. SAV-VC experiment increases the SH by approximately 10 to 25 W m^{-2}. EBF-VD, SAV-VD, and WS-VD have altogether a higher negative potential change in SH. In Oueme, the afforestation experiments have low to moderate effect on SH (~5 to 10 W m^{-2}). The relative difference of SH

with respect to EBF-VC and WS-VC ranges between -90 to 50%. Remarkably, the spatial pattern of the potential change shows a contrasting effect between the riverbed of Niger river and most of Sahel region. That is, SH is increased by 0 to 20% around the river while most of the region experiences a decrease under WS-VC and EBF-VC experiments. The response of ground heat (GH) to afforestation experiments in the region varies from -25 to 50 W m^{-2}. The lowest vegetation density experiments (SAV-VC) decrease GH by 0 to 25 W m-2 in most the Sahelian region however in higher rainfall conditions (e.g. Oueme), it increases GH by 15 to 30 W m^{-2}. The values of the corresponding relative change are -80 to 5% and 5 to 80%. In drier conditions, WS-VC impact on GH is most significant in riverbed however an overall 25 to 75% increase is recorded in the region. EBF-VD, SAV-VD, and WS-VD indicate the highest GH increase. Higher tree cover in EBF-VC and WS-VD is associated with lower albedo in the Sahelian region which results in a cooling effect while higher albedo with SAV-VC shows a warming effect. Under EBF-VC and WS-VC, GH and LH are increased in Sissili while SH is decreased. The opposite potential change occurs with SAV-VC. GH increase under EBF-VC and WS-VC highlights controversial evidence on the expected cooling effect as it is associated with a trade-off of ground warming. Further, SAV-VC has a negative effect on SH, a moderate positive effect on LH, and achieve GH decrease. Therefore, the suitability of the afforestation experiment should take in the account the rainfall rate, topography, and vegetation density. In Oueme, EBF-VC and WS-VC have a positive effect on energy fluxes.

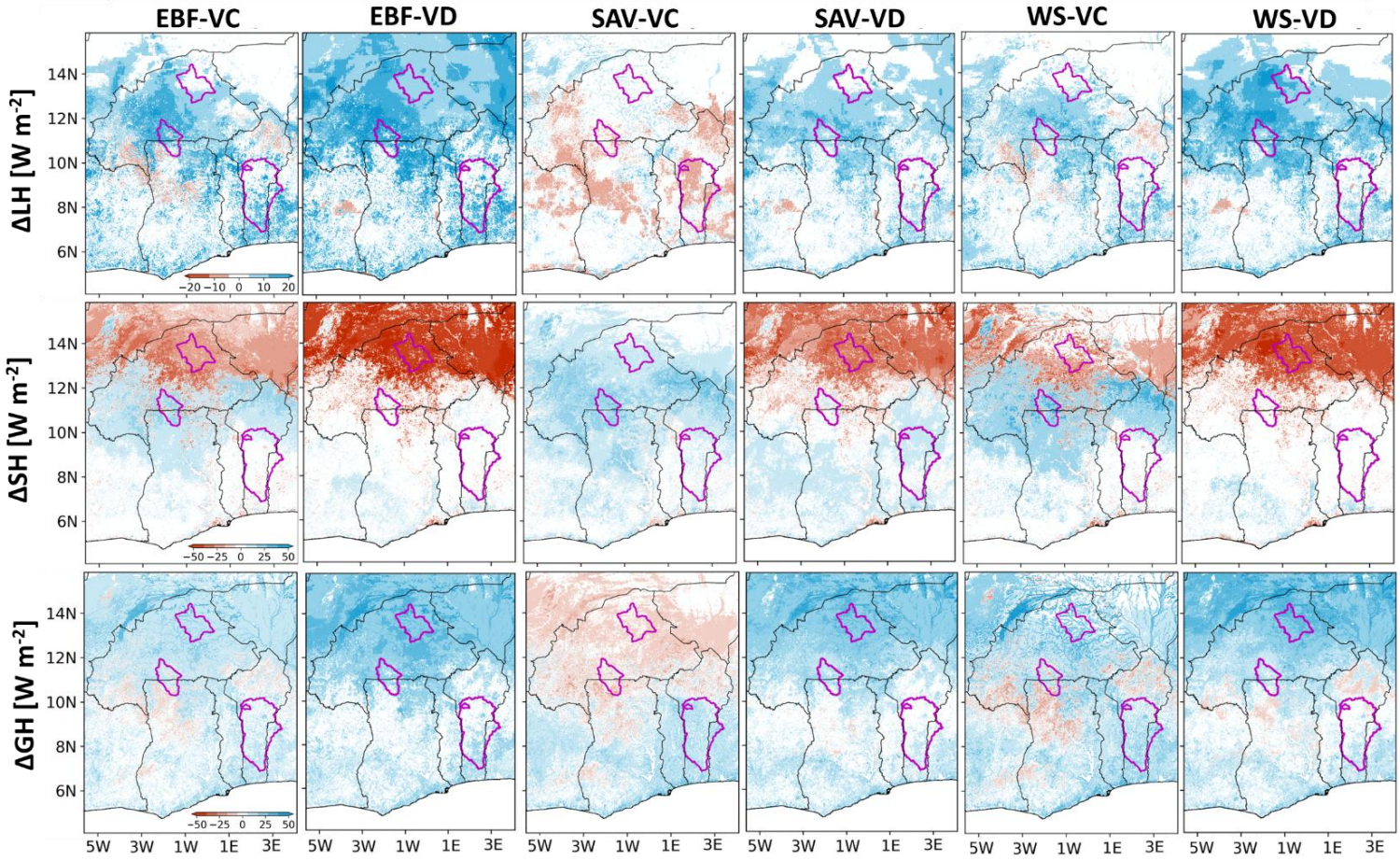

Figure 4.22: Calculated absolute differences of latent heat (ΔLH; upper), sensible heat (ΔSH; middle), ground heat (ΔGH; lower) between the idealized afforestation experiments and REF (upper). The gradient of red and blue patches shows decreasing and increasing LH/SH/GH towards high impact areas. Countries located within the domain are delimited with black line and basins with magenta line. The graph of relative difference is added to the supplementary figures (Fig. S7)

4.2.3. Evaluation of the afforestation impact on the subbasins' water budget

To evaluate the water budget of each basin located in the Sahelian, Sudanian, and Guinea coast climatic zones, this study investigated the water balance components namely evapotranspiration (ET), surface and underground runoff (RF and UGRF), and soil moisture storage (ΔSM). The seasonal cycles of the water budget are shown in Figure 4.23a, Fig. S8, and Fig. S9. EBF-VC, SAV-VC, and WS-VC decrease ET from March to May by 30 to 60 mm in Oueme (Fig. 4.23), March to August in Sissili by 5 to 100 mm, and June to August in Faga by 10 to 120 mm during the study period. The remainder of the year shows an increase of ET in response to the idealized afforestation experiments, with the highest difference occurring in December under WS-VC in Oueme, in October under WS-VC for Sissili and Faga. Further, the depletion of soil moisture storage in the dry season is a critical scientific problem also known as SM dry-downs (Fu et *al.*, 2024). The skill of the idealized afforestation experiments in delaying the dry-down is highlighted in Figs. 4.23, S8, and S9 (lower left). Remarkably, SAV-VC has a positive effect on ΔSM from October to December, sustaining the lowest dry-down with a difference of ~20 mm in Oueme, Sissili, and Faga compared to the REF experiment. The highest ΔSM loss occurs with WS-VD followed by the EBF-VC experiment in November for Oueme (~50 to 60 mm), Sissili (~50 mm), and Faga (~30 mm). In the rainy season, EBF and WS-related experiments achieve the highest increase of ΔSM in April for Oueme (~38 mm), in July for Sissili (~35 mm), and in August for Faga (~25 mm). From May to August, the SAV-VC experiment stores less SM while EBF-VC and WS-VC retain higher SM compared to the current land use (REF) in Faga (Fig. S9). The effect of the idealized afforestation experiments on soil moisture in wetter conditions is rather mitigated in Oueme and Sissili. Somehow, the intermittence between the two rainy seasons and the short dry season breaks down the positive trend of the ΔSM increase. This results in soil moisture loss under the idealized afforestation experiments in June and August in Oueme (Fig. 4.23a) and a lower effect in Sissili in June, August, and September. It is noticeable that this period with a contrasting effect is associated with higher ET. Further, unimodal rainfall climate (e.g., Faga) benefits best in consistently storing SM under the idealized afforestation experiments even with a lower rainfall rate (Fig. S9).

Because the model overestimates the streamflow, it generates runoff (RF) throughout the year, whatever the experiments and climatic conditions. Nevertheless, it turns out that with the experiments, the runoff peak is remarkably delayed by two months in the three basins compared to the REF experiment. EBF-VC, SAV-VC, and WS-VC reduce the RF peak by ~520 to 650 mm

in Oueme, and ~30 to 80 mm in Sissili. SAV-VC increases peak RF by ~5 mm in Faga, while the EBF-VC and WS-VC decrease it by ~35 to 55 mm. EBF-VC has the strongest effect in reducing the RF, but generates higher runoff in the dry season from November to February in Oueme and Sissili. Moreover, the SAV-VC experiment generates higher runoff towards drier areas. Overall, the experiments with LAI and FVEG dynamically computed (e.g., SAV-VD, and WS-VD) generate higher RF from January to December in Oueme compared to SAV-VC and WS-VC. Nevertheless, the same produces lower RF from May-June to November in Sissili and from April-May to November in Faga. EBF-VD shows lower RF compared to EBF-VC from November to July, while the opposite occurs around July-August.

The seasonal cycle of underground runoff highlights the water loss through capillary rise at the basin scale in the water-limited period. It extends from December to June in Oueme, from November to August in Sissili, and from October-November to August in Faga. WS-VC shows the highest UGRF of ~16 mm in Oueme, ~9 mm in Sissili and ~4 mm in Faga. All the idealized afforestation experiments increase significantly water loss through UGRF in water-limited conditions while reduce UGRF in the rainy season. SAV-VC experiment shows the highest UGRF decrease of ~10 mm in Oueme and ~2.5 mm in Sissili. In Faga, UGRF decreases throughout the year under the six experiments.

The seasonal transition associated with the change from water-limited to energy-limited conditions reverses the sources of ET and RF, switching from UGRF and ΔSM to precipitation (and vice versa). ET and RF serve as water loss components, while soil moisture storage, baseflow from UGRF, and precipitation sustain water availability in the basins. In the dry season, ET occupies the highest percentage of the water budget in water-limited conditions as it draws water from the soil and subsurface. The water loss through capillary rise sustains the water cycle in the dry season as UGRF and ΔSM feed both ET and surface RF in Faga (November to April), Sissili (November to March), and Oueme (December to January). Between February and June in Oueme, the water cycle is sustained with both rainfall and subsurface water loss (Fig. 4.23a). A Similar pattern associated with ΔSM increase occurs from May to August in Sissili and Faga.

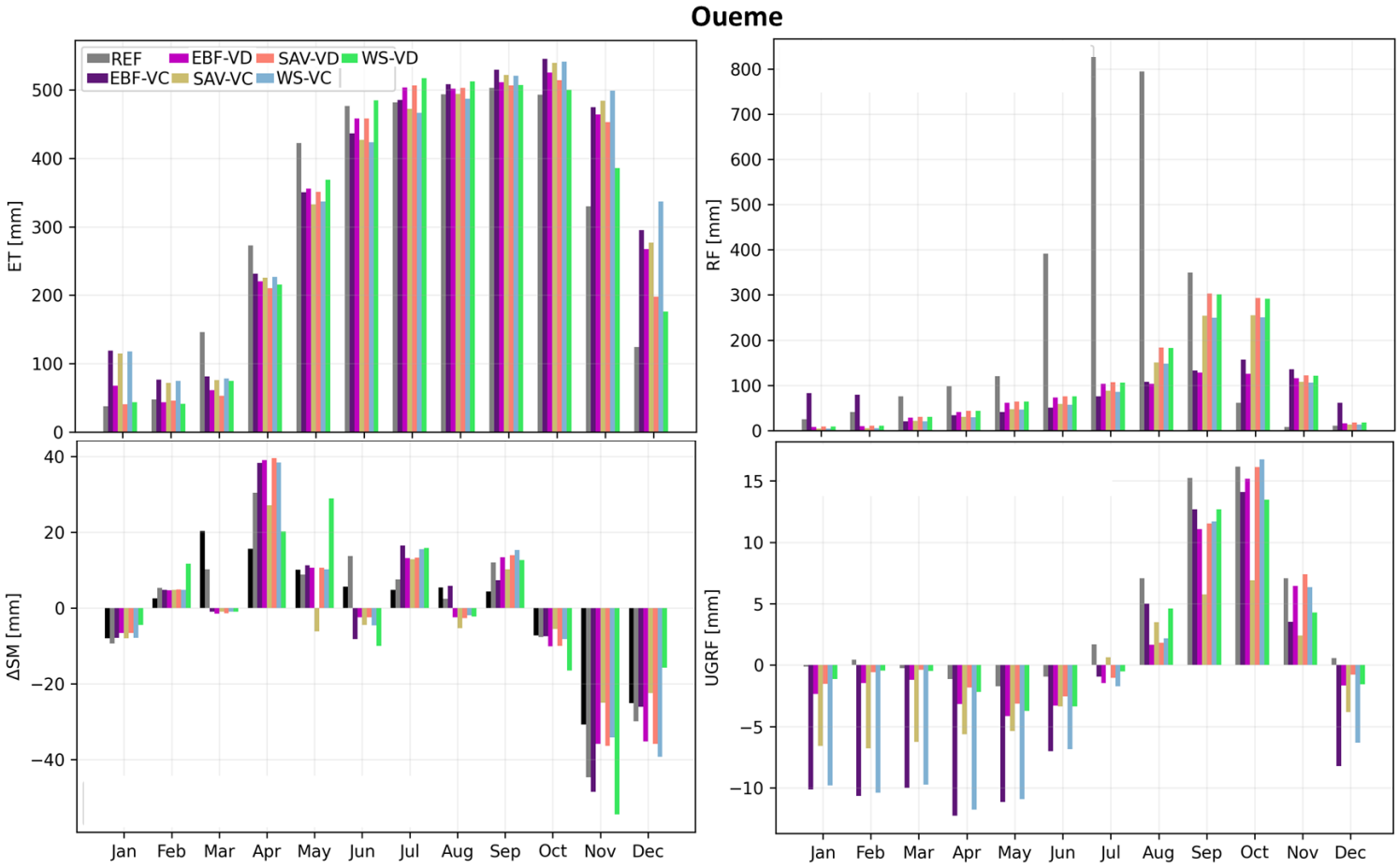

Figure 4.23a: Monthly water budget under the idealized afforestation experiments and current land use in Oueme. Highlight of the seasonal variation of ET (upper left), soil moisture storage (lower left), surface runoff (RF; upper right), and underground runoff (UGRF; lower right) covering the simulation period from 2012 to 2015. All the components are in mm. Similar figure for Sissili and Faga are added to the supplementary documents.

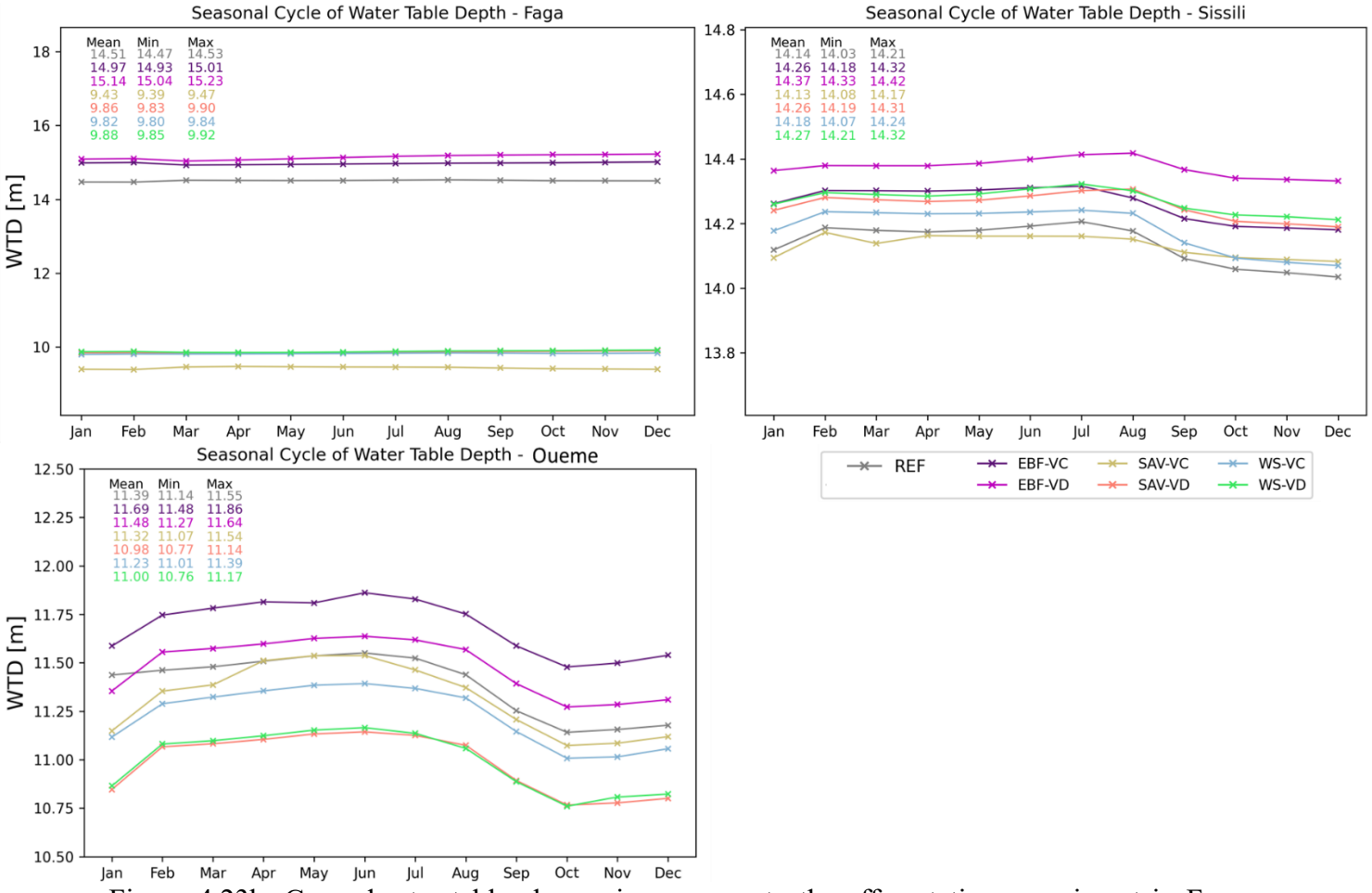

Figure 4.23b: Groundwater table change in response to the afforestation experiment in Faga, Sissili, and Oueme basins.

4.3 Enhancing Depth-to-Bedrock Maps for Groundwater-to-Atmosphere Modeling in Africa

4.3.1 Analysis of Field Depth-to-Bedrock Data and Spatial Statistics

This section evaluates the DTB field measurements from over 4,000 boreholes using descriptive statistical analysis. Boreholes were selected based on their locations within multiple ring buffer zones surrounding three terrain-related features. The buffer distances were divided into nine classes, based on the assumption that significant changes in DTB occur moving from features such as rivers toward more distant points. Notably, the highest percentage of boreholes falls within the 0.5 to 1 km distance class, accounting for 21.3%, 33.1%, and 21.5% for geological lineaments, depression zones, and river networks, respectively. Conversely, the lowest percentages are found in the closest distance classes: 4.8% for lineaments within 10 to 50 m, and 1.2% and 0.8% for depression zones and river networks within 0 to 10 m, respectively (Fig. 4.24). These findings further explain why negative or unproductive borehole siting is common in this bedrock area.

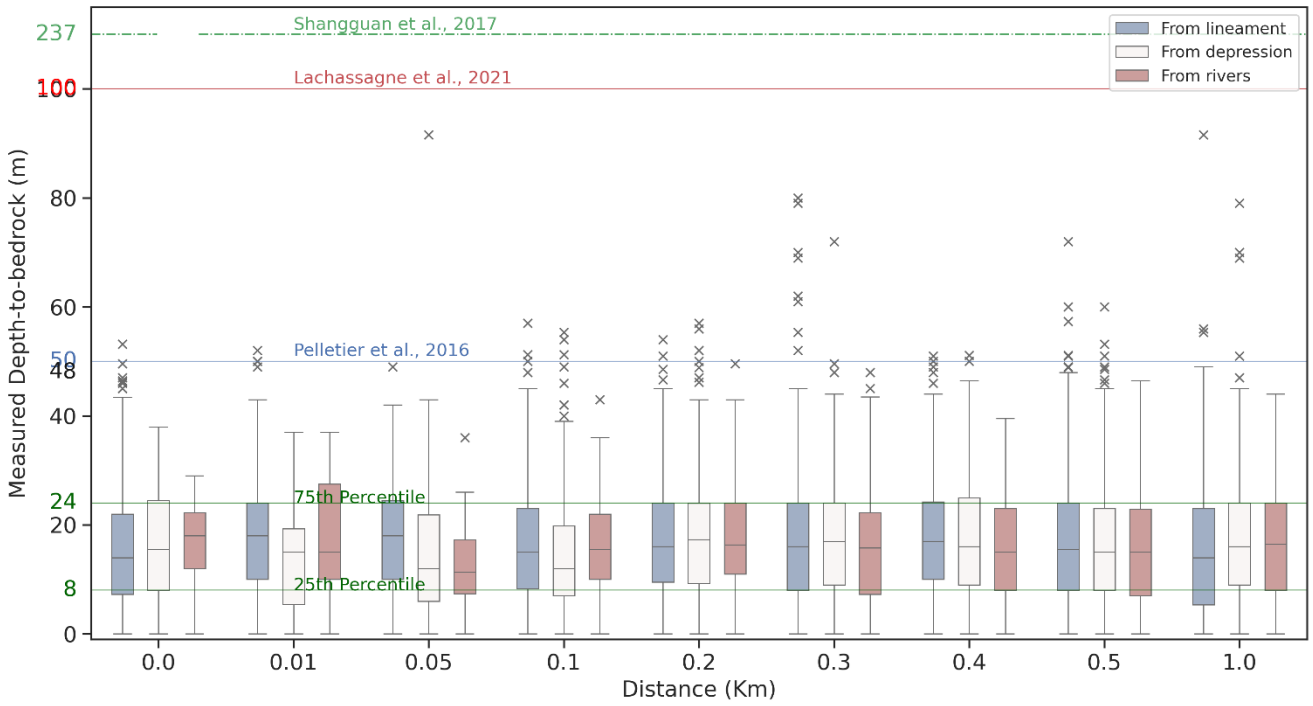

Figure 4.24: Zonal statistic (a) of DTB in relation with geological lineaments, depressions, and Rivers' network

The distribution across distance classes shows that a large percentage of boreholes are located between 100 m and 500 m from terrain-related features, with 51.2%, 41.8%, and 60.6% for geological lineaments, depression zones, and the river network, respectively. Since these DTB measurements were primarily collected during water supply borehole drilling, this suggests that the high rate of unsuccessful boreholes reported by drilling companies in the study area may be due to inaccuracies in identifying these three terrain-related features. However, the low percentage of boreholes found within 100 m of the river network can also be attributed to groundwater quality sometimes being influenced by the river, as the groundwater table is closer to the surface in these areas. This explanation does not apply to the low percentages of boreholes located within 100 m of geological lineaments (4.8% for 10–50 m and 5.8% for 50–100 m distance classes) or depression zones (1.2% for 0–10 m, 1.9% for 10–50 m, and 3.8% for 50–100 m). These low values highlight a lack of precision in mapping geological lineaments and depression zones, indicating a need for more detailed, larger-scale maps as crucial decision-making tools.

Beyond 1 km from these terrain features, the percentages of boreholes are 4.4%, 18.3%, and 5.8% for geological lineaments, depression zones, and the river network, respectively. The low numbers for geological lineaments and rivers confirm that groundwater farther from these features is less explored, even though their average DTB values of 15.8 m and 16.8 m fall within common ranges. Notably, 12.7% of DTB measurements lie within 0 to 10 m of geological lineaments, which could be explained by the high density of these features in the study area. Additionally, 51.4% of DTB measurements are located more than 500 m from depression zones, possibly because large-scale depression maps are rarely used for siting water supply boreholes in this region (Table 4.6). Overall, the average measured DTB across all terrain features and distance classes is 16.5 ± 1.2 m (mean), 15.5 ± 1.8 m (median), and 10.8 ± 1.3 m (standard deviation). This suggests that expected DTB values in hard-rock areas are concentrated within this range, with only limited skewness due to certain geological features (Fig. 4.25a).

Table 4.6: Statistical summary of depth-to-bedrock (DTB) based on geological lineaments, depressions, and river networks

Lineaments / Depressions / Rivers																		
Distance (m)	count			max			mean			median			stddev			Percentage (%)		
0 – 10	520	28	4	53.2	38	29	15.9	17.3	16.3	14	15.5	18	10.6	11.3	10.5	12.7	1.2	0.8
10 – 50	197	43	23	52	37	37	17.1	14.4	17.9	18	15	15	10.6	9.0	10.9	4.8	1.9	4.5
50 – 100	240	87	36	49	91.6	36	17.7	15.2	13	18	12	11.3	10.0	13.1	7.4	5.8	3.8	7.0
100 – 200	554	229	76	57	55.3	43	15.9	14.6	16.1	15	12	15.5	10.4	10.9	8.4	13.5	10.0	14.7
200 – 300	594	242	107	54	57	49.6	17	17.9	18.1	16	17.3	16.4	10.3	11.2	10.2	14.5	10.6	20.7
300 – 400	512	260	72	80	72	48	17	17.5	16.6	16	16.9	15.8	12.1	11.2	11.5	12.5	11.4	14.0
400 – 500	439	224	57	51	51.1	39.5	17.6	17.5	16.1	17	16	15	10.5	10.8	9.6	10.7	9.8	11.1
500 – 1000	875	756	111	72	60	46.4	16.8	16.4	16.1	15.5	15	15	11.2	10.6	10.6	21.3	33.1	21.5
> 1000	181	418	30	91.6	79	44	15.8	16.8	16.8	14	16	16.5	13.9	10.9	11.9	4.4	18.3	5.8
Totals	4112	2287	516													100	100	100

The boxplot in Fig. 4.24 offers a clear view of the spatial distribution of DTB measurements from over 4,000 boreholes around three key terrain-related features—geological lineaments, depression zones, and river networks—which are often considered proxies for successful well siting in hard-rock regions. It is commonly argued that higher groundwater yields are linked to the proximity of these features to a given borehole. To analyze this, Multi-buffer Rings defining nine distance classes ranging from 0 meters to over 1 km, along with Selection by Location algorithms, were applied in a GIS environment to select data and compute descriptive statistics for each class around the three terrain features. The results show no significant decrease in DTB as boreholes are located closer to geological lineaments, depression zones, or rivers. This is reflected in the boxplot patterns (Fig. 4.24), where values from distances above 1 km to near 0 m do not indicate a clear spatial trend. This suggests that while surface erosion from overland flow may affect the regolith near the surface, its impact does not necessarily extend to deeper layers or the furthest points from these features. Nevertheless, the high spatial density of these terrain features marks important infiltration zones essential for productive well siting, especially in fractured hard-rock subsurface systems.

Figure 4.25: Zonal statistics of DTB in relation to (a) geological units and (b) soil units are presented. The dashed green line, along with the red, blue, and purple lines, represent the maximum DTB values estimated or suggested by previous studies. The two dark green lines indicate the 75th and 25th percentiles of the field-measured depth-to-bedrock. This figure complements Figure 4.24. The numbers along the x-axis correspond to the geological units (c) and soil units (b), which are described in detail by Volkoff and Willaime (1976) and OBEMINES (1989), respectively.

Addressing our earlier point about the significant uncertainty related to the basin bottom, the maximum values from the field DTB measurements show a peak of 91.6 m recorded in the distance class over 1000 m from the geological lineaments, 50 to 100 m from the depression zone, with an overall average maximum of 54.6 ± 16.6 m. Minimum values are not listed in Table 4.7 because they are all 0 m. Regarding geological and soil units (Fig. 4.25a-b), Gneiss-related formations exhibit an average DTB of 15.6 ± 2.4 m with a standard deviation of 10.1 ± 1.2 m. Granite with biotite, alkaline granite, and microgranites have average DTB and standard deviations of 16.5 ± 5.6 m and 3.8 ± 6.5 m, respectively. Other formations such as Quartzite feldspathic (Q), Charnockites (ch), Blastomylonite and mylonite of the Kandi Shear (my), Terrigenous Deposits (Daho-Mahou series – dt), and Marbles (M) show mean DTB values of 17.1 ± 10.9 m, 16.1 ± 6.0 m, 22.3 ± 9.1 m, 12.9 ± 6.7 m, and 53.4 ± 23.8 m, respectively. Except for the basic vein (ug), which has a single DTB measurement of 13 m, the remaining geological units belong to a coastal sedimentary basin that is beyond the scope of this study. The 75th and 25th percentiles of DTB based on soil units are 24 m and 8 m, respectively (Fig. 4.25b). Given that there are over 100 soil units, detailed descriptive statistics are omitted for simplicity. However, soil units 42, 85, 86, 88, and 106—which correspond to ferruginous tropical, weakly desaturated ferralitic, and hydromorphic soils of the coastal sedimentary basin—significantly skew the overall DTB range with values of 36.4 ± 23.4 m, 55.1 ± 16.4 m, 64.4 ± 33.2 m, 51.7 ± 22.4 m, and 107.3 ± 45.2 m, respectively (Fig. 4.25b).

Table 4.7: Descriptive statistics of DTB based on rock types.

Geological code	Minimum	Maximum	Mean	STD	Total
gngr	2	50	14.26	9.63	86
gno	3	49	13.02	8.64	44
Q	3	45	17.06	10.86	37
ch ch-g	7	27	16.14	5.94	9
my	2	45	22.28	9.09	48
mgn	2	57	17.72	9.84	540
gnp	2	45	18.55	10.27	60
gnab	2	80	14.22	11.91	73
Y	2	33	13.58	11.40	12
dt	7	30	12.92	6.67	13
M	24	24	24.00	0.00	1
uF	23	23	23.00	0.00	1
TC	6	100	48.95	19.45	60
a	15	15	15.00	0.00	1
M	6	113	53.35	23.83	27
GFD	50	69	62.67	8.96	3
µg	13	13	13.00	0.00	1
PS	60	60	60.00	0.00	1
RAD	112	150	131.00	19.00	2

gngr: Gneiss with biotite granulites and 2 pyroxenes, **gno**: Gneiss ‘’oeillés‘’ with biotite and amphibolite, **Q**: Quartzite – feldspathic with white mica, **ch ch-g**: Charnockites grano-monzodiorite gabbroic, **my**: Blastomylonite and mylonite of the Kandi Shear, **mgn**: Gneiss migmatitic, **gnp**: Gneiss alkaline with pyroxene – granulites acid, **gnab**: Gneiss with amphibole and biotite, **Y**: Granites with biotite finely to averagely grainy, **dt**: Terrigenous deposit (Daho-Mahou Series), **M**: Marbles and marbles with silicates sometimes 184raphitic (Dadjo), **uF**: Granites alkaline, **TC**: Turonien-coniacien, **a**: Basic Filons, **M**: Maestrichtien, **GFD**: Gravel and other fluvial deposits, **µg**: Microgranites ‘’microsyénites‘’, **PS**: Paleocene superior, **RAD**: Recent alluvial deposits.

4.3.2 Evaluation of PF-CLM Model performance

4.3.2.1 Simulated energy fluxes evaluation

Within each grid cell of the 334 by 334 domain, the PF-CLM model solves the variably saturated subsurface equations, providing pressure head and saturation values along with energy fluxes at the land surface at an hourly time resolution. Figures 4.27a-d illustrate the spatial distribution of the mean energy fluxes—sensible heat, latent heat, ground heat, and outgoing longwave radiation—over the simulation period from January to February 2014. The land use map used in the domain setup predominantly controls the spatial distribution of both water and energy fluxes at the land surface, as shown in Figures 4.27a-d and 9a-c. This spatial pattern highlights the importance of using a high spatial resolution and accurately detailed land use map to better capture land surface processes. In this study, the MODIS land cover data resampled to 1 km was used, which, as shown in Figures 4.27a-d and 9a-c, is somewhat limited for the 10 by 10 km domain extent. However, PF-CLM reproduces the observations within the domain quite accurately. The temporal averages of energy fluxes during the simulation period are 105.5 ± 35.9 W m^{-2} for latent heat, -5.2 ± 24.8 W m^{-2} for sensible heat, -9.6 ± 24.8 W m^{-2} for ground heat, and 449.4 ± 5.5 W m^{-2} for outgoing longwave radiation. Shrublands and grasslands along the eastern river boundary show the lowest latent heat but the highest ground heat and sensible heat, indicating that poorly vegetated areas tend to absorb more incoming solar radiation during the dry season's water stress. Conversely, highly vegetated areas, such as Evergreen Needleleaf and Broadleaf Forests, exhibit lower ground heat and higher latent heat, reflecting active plant processes. Outgoing longwave radiation from land use is relatively moderated, though vegetated areas show slightly higher values. Across the catchment, spatially averaged latent heat, sensible heat, ground heat, and outgoing longwave radiation from the simulation are 105.5 ± 89.9 W m^{-2}, -5.2 ± 96.8 W m^{-2}, -9.6 ± 43.6 W m^{-2}, and 449.4 ± 43.5 W m^{-2}, respectively, while observed values for the same period are 75.6 ± 114.4 W m^{-2}, 68.3 ± 121.7 W m^{-2}, 6.8 ± 38.8 W m^{-2}, and 448.5 ± 50.9 W m^{-2} (Fig. 4.26a-d).

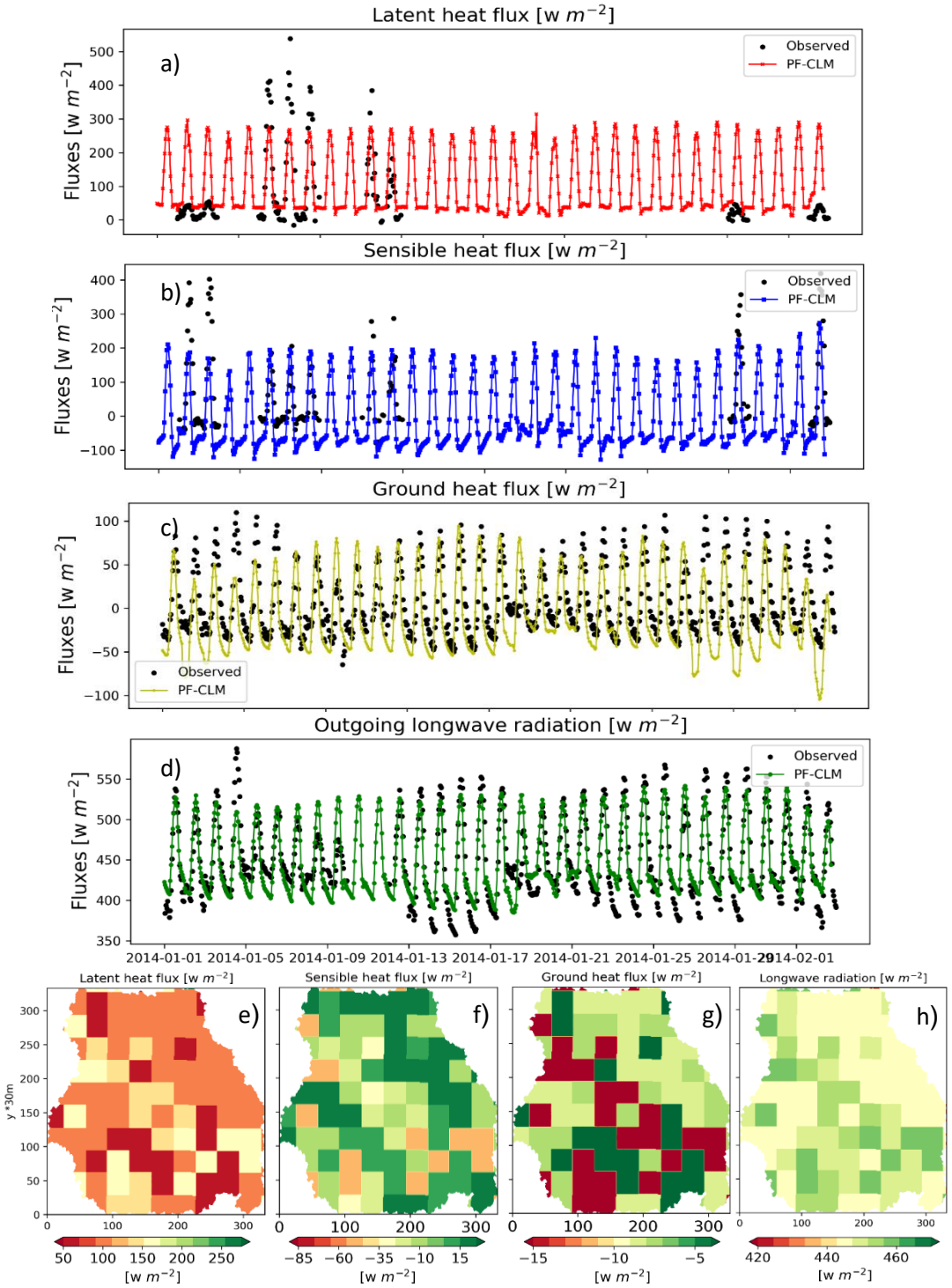

Figure 4.26: Comparison between simulated and observed energy fluxes (a–d), where black dots represent observed values and red, blue, yellow, and green dotted lines indicate PF-CLM simulations. The lower panels show the spatial distribution of temporal averages, using a color gradient from dark red for lower values to dark green for higher values.

The accuracy of the estimated depth-to-bedrock (DTB) in the subsurface configuration of PF-CLM has recently emerged as a growing research concern (Condon et al., 2020). Evaluating model performance in data-scarce regions is therefore essential to improving our understanding of water and energy balances under more realistic groundwater conditions. In this study, PF-CLM simulated energy fluxes are validated against Eddy Covariance measurements from the WASCAL CONCERT project (Bliefernicht et al., 2018). While data collection began in 2012 and is ongoing, this validation focuses on the hourly dataset from January to February 2014. Notably, despite the relatively small size of the simulation domain, the model demonstrates strong performance, achieving a Nash–Sutcliffe Efficiency (NSE) of 0.77 and an R^2 of 0.86 for sensible heat and outgoing longwave radiation, respectively (Table 4.9, Fig. 4.27a–d). For latent heat, the NSE is 0.69, R^2 is 0.60, the percentage bias (PBIAS) is -9.31%, and the root mean square error (RMSE) is 2517.44 W m^{-2}. For ground heat, the corresponding values are 0.34 for NSE, 0.71 for R^2, -162.80% for PBIAS, and 1246.87 W m^{-2} for RMSE. Among the variables, outgoing longwave radiation shows the lowest PBIAS at -0.22%, followed by latent heat at -9.31%, while the relatively poorer performance for sensible heat may be linked to data gaps in the observations. Overall, the PF-CLM setup demonstrates an unexpectedly strong capacity to simulate energy fluxes in the study area, as confirmed by the evaluation metrics.

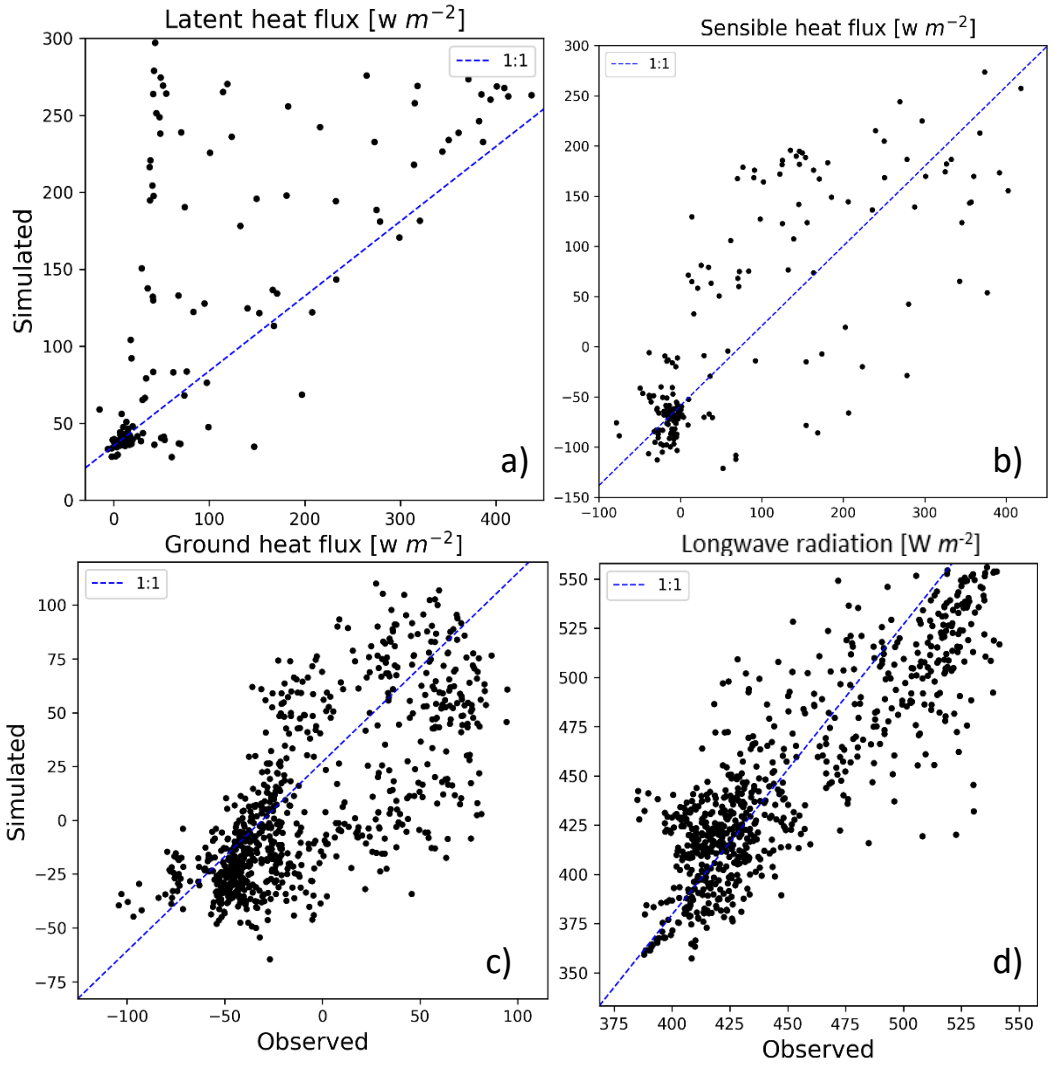

Figure 4.27: Scatter plots display the comparison between simulated energy fluxes and observed values, with the dashed blue line representing the 1:1 line, indicating perfect agreement between simulations and measurements.

4.3.2.2 Simulated evaporation analysis

Figure 4.28a–c presents the three evaporation components simulated by PF-CLM: total evaporation, soil evaporation, and vegetation evaporation. The vegetation evaporation is compared with actual evapotranspiration (ETa) estimated from field measurements (Table 4.8). ETa is calculated by integrating climatic variables—including solar radiation (MJ m^{-2} day^{-1}), air temperature (°C), relative humidity (%), wind speed (m/s), wind measurement height, and shortwave radiation—from the Nazinga Eddy Covariance station, combined with MODIS Normalized Difference Vegetation Index (NDVI), using the approach outlined by Kamble et *al.* (2013). Vremec et *al.* (2023) developed the PyET Python package, which includes several methods for estimating potential evapotranspiration. For this study, only three methods were used: Priestley–Taylor (1972), FAO-56 (Allen et *al.*, 1998), and Penman (1948). Results show that PF-CLM vegetation evaporation tends to overestimate ETa when compared to all three methods, though it aligns most closely with the Penman method (Fig. 4.28c). Importantly, PF-CLM accurately captures the slight upward trend in evaporation observed in the field data, indicating good performance in a data-scarce environment. The spatial average of PF-CLM vegetation evaporation is 2.4±0.1 mm/day, compared to 1.73±0.28 mm/day, 1.68±0.27 mm/day, and 2.06±0.26 mm/day for the Priestley–Taylor, FAO-56, and Penman methods, respectively.

While direct validation of total and soil evaporation is not conducted—due to the need for advanced instrumentation and complex calculations beyond this study's scope—the PF-CLM estimates are shown in Figures 4.28a and 4.28b. The model outputs average values of 3.63±3 mm/day for total evaporation and 1.17±0.5 mm/day for soil evaporation, which fall within reasonable expected ranges.

Table 4.8: PF-CLM Model performance metrics for the energy fluxes

Variables	NSE	R^2	PBIAS	RMSE
LH	0.69	0.60	-9.31	2517.44
SH	0.77	0.77	-254.18	2179.62
GH	0.34	0.71	-162.80	1246.87
LR	0.67	0.86	-0.22	623.08

Additionally, the spatial pattern of PF-CLM evaporation is largely influenced by the MODIS land cover classification, with domain-wide time-averaged values of 3.63±1.2 mm/day for total evaporation, 1.18±0.78 mm/day for soil evaporation, and 2.44±0.7 mm/day for vegetation evaporation (Fig. 4.28d–f). Soil evaporation does not exhibit any clear spatial variation linked to soil type, whereas vegetation evaporation reflects noticeable differences that correspond to vegetation health. Higher vegetation evapotranspiration rates are observed in areas dominated by Evergreen Needleleaf Forest, Evergreen Broadleaf Forest, Savanna, Woody Savanna, and Grassland. In contrast, the lowest rates occur in shrubland regions, particularly in the southern part of the domain.

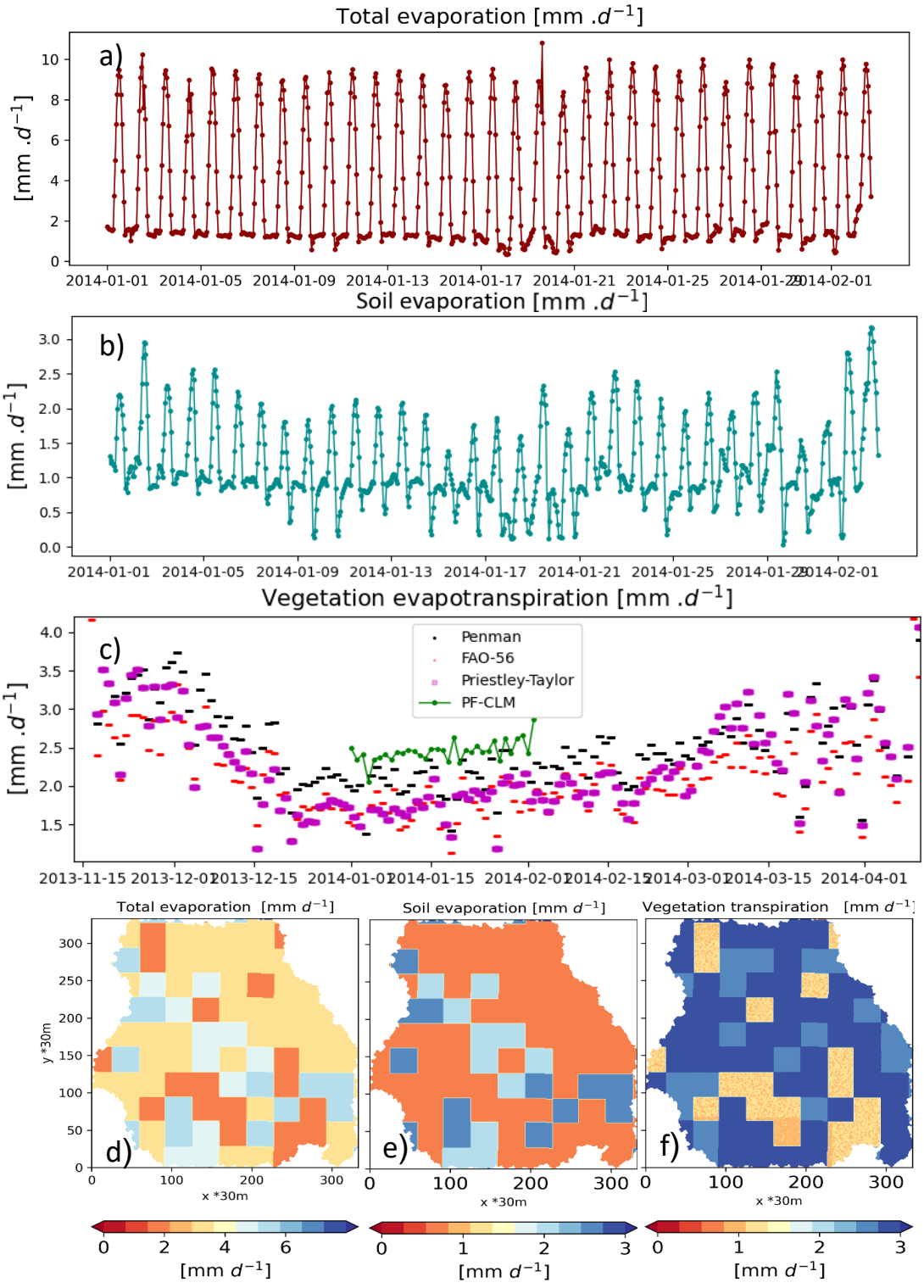

Figure 4.28: Total evapotranspiration (a), soil evapotranspiration (b), and vegetation evapotranspiration (c), shown alongside the estimated actual evapotranspiration derived from the Priestley-Taylor method (magenta squares), Penman equation (black dots), and FAO-56 approach (red dots). Panels (d–f) display the spatial distribution of the respective temporal averages.

4.3.2.3 Computed DTB maps and 2D profiles

The overall patterns across the three computed DTB maps (Eq. 3.36, Eq. 3.46, and Eq. 3.31 – Fig. 4.29) reveal that the highest depth-to-bedrock values are mainly concentrated in coastal areas, along riverbeds, and within major depression zones. To address concerns over reliability in areas with a low probability of high depth-to-bedrock (DTB), certain regions in the maps produced using the best-performing method from this study (Eq. 3.36) and the Lachassagne et al. (2021) approach (Eq. 3.46) have been intentionally left blank. Based on Eq. 3.36, the average DTB values across African subregions are as follows: West Africa – 45.7 ± 3.6 m, North Africa – 43.4 ± 5.8 m, East Africa – 43.5 ± 5.8 m, Central Africa – 41.7 ± 5.9 m, Southern Africa – 44.3 ± 6.3 m, and Madagascar – 46.2 ± 5.2 m. In comparison, Eq. 3.46 (Lachassagne et al., 2021) yields regional averages of 38.9 ± 21.9 m for West Africa, 17.7 ± 39.9 m for North Africa, 33.7 ± 21.9 m for East Africa, 11.9 ± 13.9 m for Central Africa, 43.1 ± 54.1 m for Southern Africa, and 10.8 ± 57.3 m for Madagascar. The depth-to-bedrock estimates derived from Eq. 3.31 (de Graaf et al., 2015) are generally lower, with regional averages of 25.2 ± 6.2 m in West Africa, 20.8 ± 7.9 m in North Africa, 14.17 ± 9.9 m in East Africa, 17.4 ± 6.4 m in Central Africa, 11.4 ± 8.8 m in Southern Africa, and 21.2 ± 11.5 m in Madagascar. It is important to note that these values, particularly in sedimentary basins and desert regions, should be interpreted cautiously, as the underlying geological conditions differ significantly from those in hard rock environments.

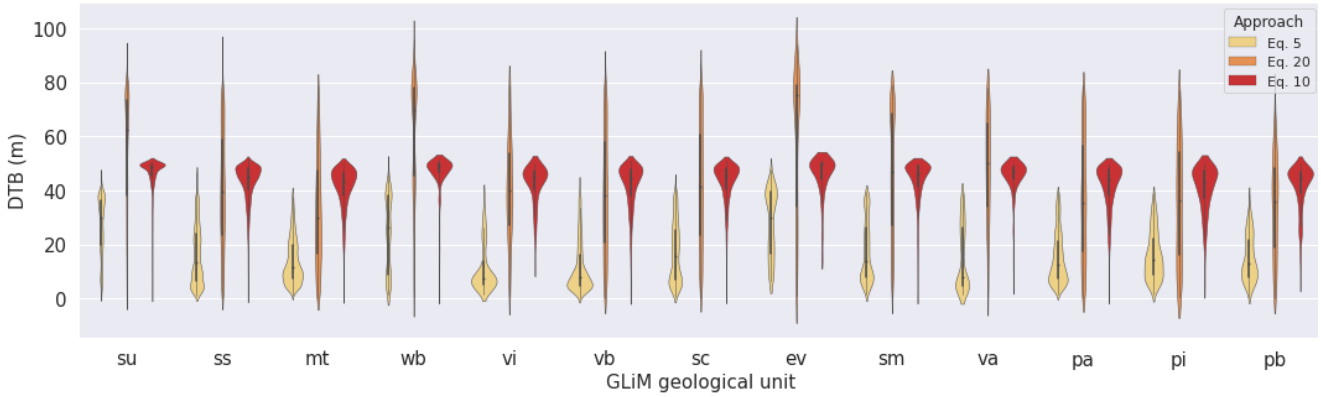

Figure 4.29: Violin plot of DTB based on GliM geological units using the three selected approaches **(ev**: Evaporites, **sm**: Mixed sedimentary rocks, **ss**: Siliciclastic sedimentary rocks, **su**: Unconsolidated sediments, **va**: Acid volcanic rocks, **mt**: Metamorphics, **pa**: Acid plutonic rocks, **pb**: Basic plutonic rocks, **pi**: Intermediate plutonic rocks, **sc**: Carbonate sedimentary rocks, **vb**: Basic volcanic rocks, **vi**: Intermediate volcanic rocks, and **wb**: Water Bodies)

There is a strong and growing need to provide the Earth System Modeling community with reliable subsurface datasets such as depth-to-bedrock (DTB). These datasets are essential for improving model performance, deepening our understanding of the Earth's critical zone, and addressing the frequent oversimplification of groundwater components in many existing models. To support geological zonal analysis, two globally recognized geological maps are employed: the Global Lithological Map (GliM; Hartmann & Moosdorf, 2012) and the Global Unconsolidated Sediments Map (GUM; Börker et al., 2018), which served as the foundation for GLHYMPS 1.0 (Gleeson et al., 2014) and 2.0 (Huscroft et al., 2018). While GUM contains 87 geological units and GliM includes 13, the analysis focuses on GliM due to its more robust representation of hard rock formations. For volcanic units in the GliM dataset, namely va, vb, and vi, the DTB estimates vary across the three equations: Eq. 3.31 yields lower values, with va at 15.1 ± 11.9 m, vb at 11.7 ± 9.4 m, and vi at 11.1 ± 8.8 m; Eq. 3.36 shows higher DTB values with va, vb, and vi estimated at 44.9 ± 7 m, 41.8 ± 8.6 m, and 42.6 ± 7.3 m respectively; while Eq. 3.46 further increases these estimates to 47.7 ± 20 m for va, 39.0 ± 22.4 m for vb, and 40.3 ± 19.1 m for vi. The most dominant consolidated rock type in the GliM dataset is Metamorphic rocks (mt), covering 27.6% of the African continent, for which DTB is estimated at 14.1 ± 8.4 m with Eq. 3.31, 41.0 ± 8.1 m with Eq. 3.36, and 32.6 ± 20.1 m with Eq. 3.46.

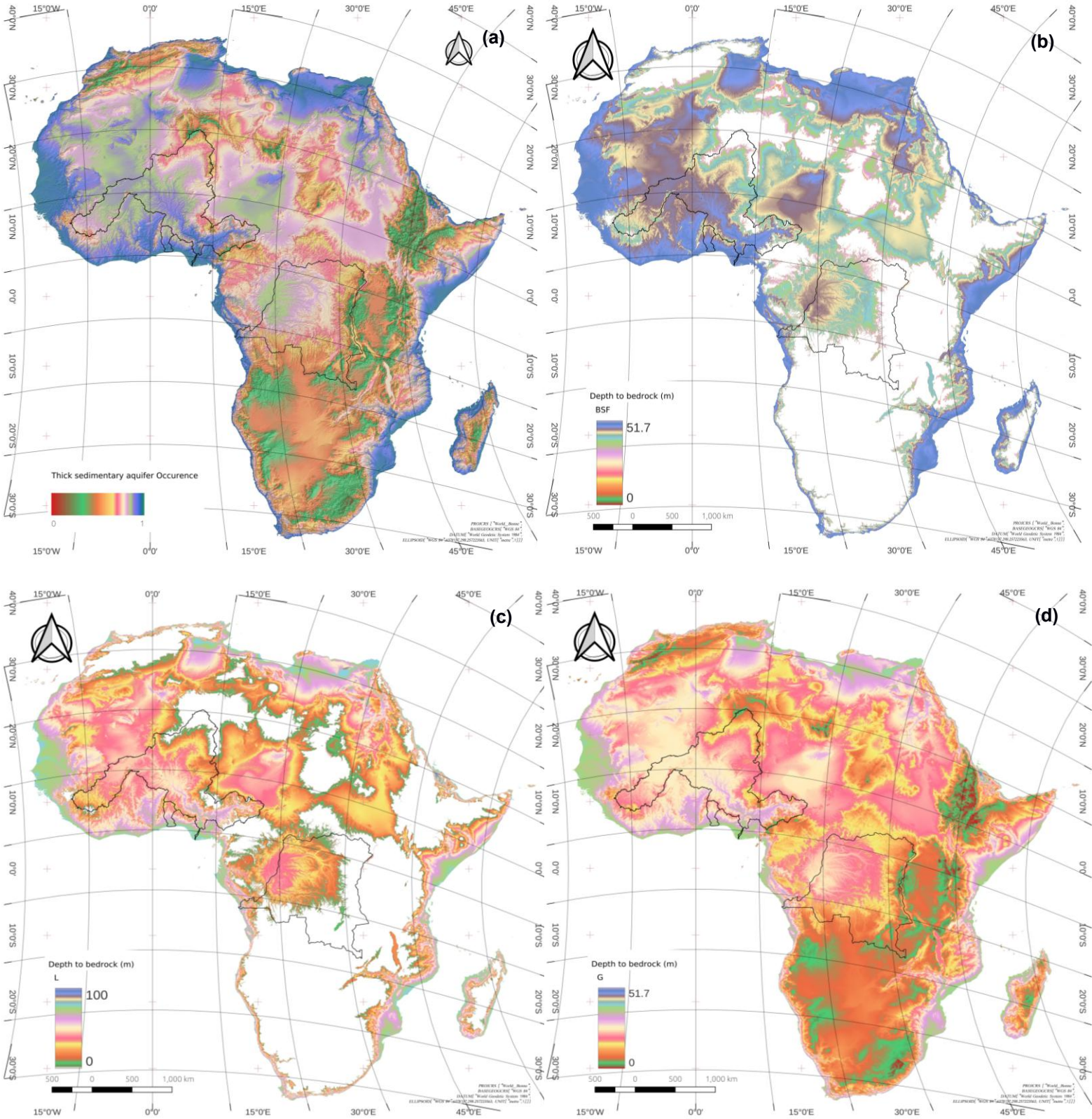

Figure 4.30: Estimated DTB occurrence probability (a), along with DTB maps generated using Eq. 3.31 (d), 3.36 (b), and 3.46 (c); areas left blank represent regions with low to very low likelihood of DTB occurrence.

The evaluation of the computed DTB maps (Eq. 3.36, 3.46, and 3.31) was performed by comparing their estimated values with existing global DTB maps from Pelletier et al. (2016) and Shangguan et al. (2017) across three river catchments: the Congo, Niger, and Oueme basins. In the Congo basin, Figures 4.31a–c show average DTB estimates of 40.9 ± 5.6 m (Eq. 3.36), 12.1 ± 14.01 m (Eq. 3.46), and 15.5 ± 6 m (Eq. 3.31), while the mean DTB values from Pelletier et al. (2016) and Shangguan et al. (2017) are 4.1 ± 8.3 m and 11.5 ± 4.4 m, respectively. A similar pattern is observed in the Niger and Oueme basins. For the Niger basin, the computed estimates are 44.4 ± 4.3 m (Eq. 3.36), 27.4 ± 27.1 m (Eq. 3.46), and 22.2 ± 5.6 m (Eq. 3.31), compared to 3.1 ± 8.4 m (Pelletier et al.) and 56.9 ± 64.5 m (Shangguan et al.). In the Oueme basin, the estimates are 47.2 ± 2 m, 49.7 ± 15.9 m, and 28.4 ± 5.6 m, while Pelletier et al. and Shangguan et al. report 4.9 ± 6.3 m and 4.8 ± 3.8 m, respectively. As previously noted, areas with low to very low DTB occurrence probabilities were excluded from computation, leaving empty pixels in those regions. As a result, the DTB estimates span approximately 60% of the Congo basin and 90% of the Niger basin. The Pearson correlation coefficients (PCC) between the computed DTB maps (Eq. 3.36, 3.46, and 3.31) and the map by Shangguan et al. (2017) are –0.34, 0.29, and 0.30, respectively. Correlations with Pelletier et al. (2016) are even lower, near zero. Across all three computed DTB maps (Fig. 4.31c), the highest DTB values are concentrated in the western part of the Congo basin, particularly along riverbeds, while the eastern regions show the lowest values.

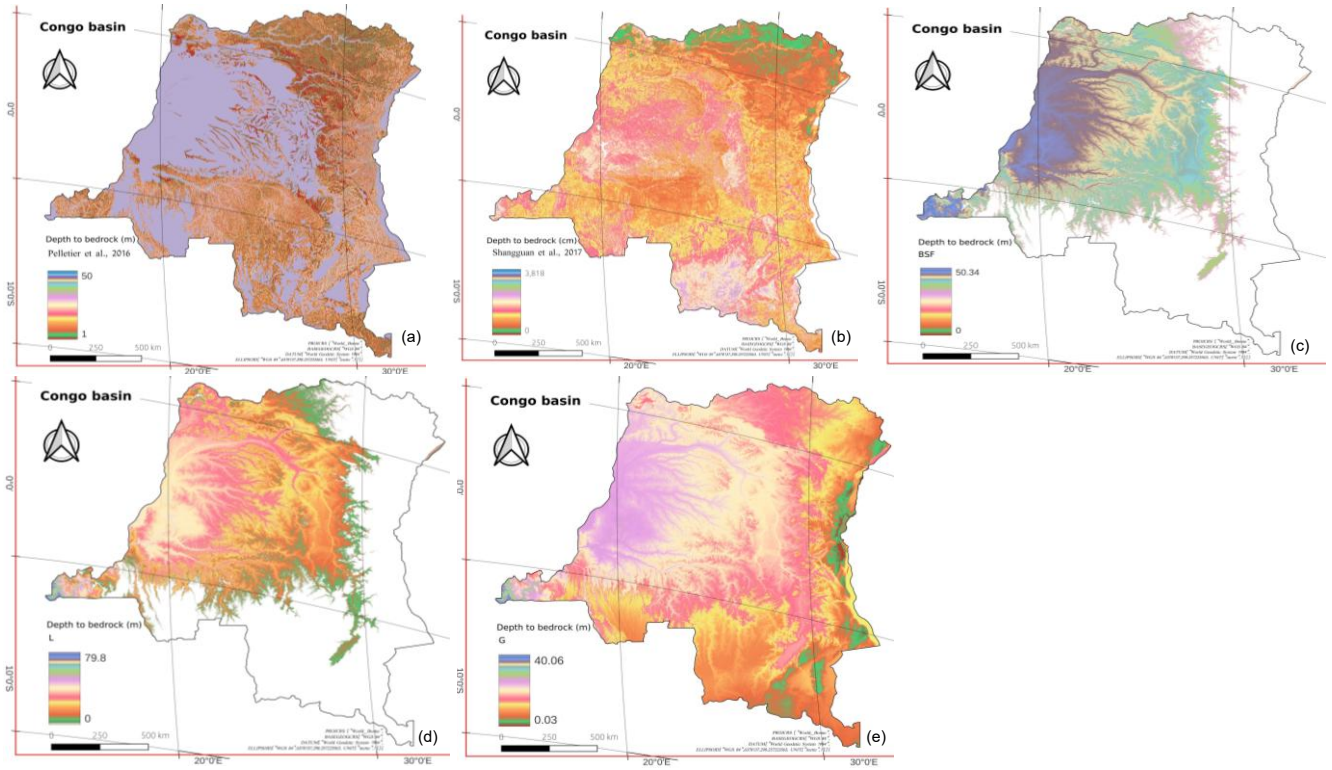

Figure 4.31: DTB maps from previous studies (a–b) alongside the proposed maps from this study for the Congo basin.

In the Niger basin (Figs. 4.32 and 4.33), the Pearson correlation coefficients (PCCs) between the estimated DTB maps and Pelletier et al. (2016) are –0.32, –0.34, and –0.33 for Equations 3.36, 3.46, and 3.31, respectively. When compared with Shangguan et al. (2017), the PCCs are –0.21, –0.37, and –0.37 for the same equations. The minimum and maximum estimated DTB values in the basin are 0/50.4 m (Eq. 3.36), 0/79.9 m (Eq. 3.46), and 0.4/40.1 m (Eq. 3.31). Certain areas particularly desert regions and zones with a near-zero probability of DTB occurrence are left blank in the maps. In the Oueme basin, the PCCs between the estimated DTB maps and Shangguan et al. (2017) are notably higher, with values of 0.47, 0.51, and 0.54 for Eqs. 3.36, 3.46, and 3.31, respectively. In contrast, correlations with Pelletier et al. (2016) remain very low. Despite the relatively weak correlations, the proposed methods have demonstrated utility in predicting field-measured DTB, supporting their reliability for land surface model (LSM) applications. These maps can serve as valuable inputs for critical zone modeling, especially in hard rock regions of the basins. However, caution is advised when applying the estimated values to the sedimentary basin in the southern part of the catchment. The geological conditions in this region—including the seven plateaus (Allada, Sakété, Comè, Aplahoué, Abomey, Zangnanado, and Kétou), the Lama Depression, and surrounding valleys—differ significantly and may not be accurately represented. Nonetheless, the estimates may still hold value in areas with alluvial deposits.For reference, the minimum and maximum DTB values from Pelletier et al. (2016) and Shangguan et al. (2017) are 0–63.48 m and 1–50 m, respectively. The estimated ranges for Eqs. 3.36, 3.46, and 3.31 are 26.11–50.35 m, 1.41–79.93 m, and 15.52–40.12 m.

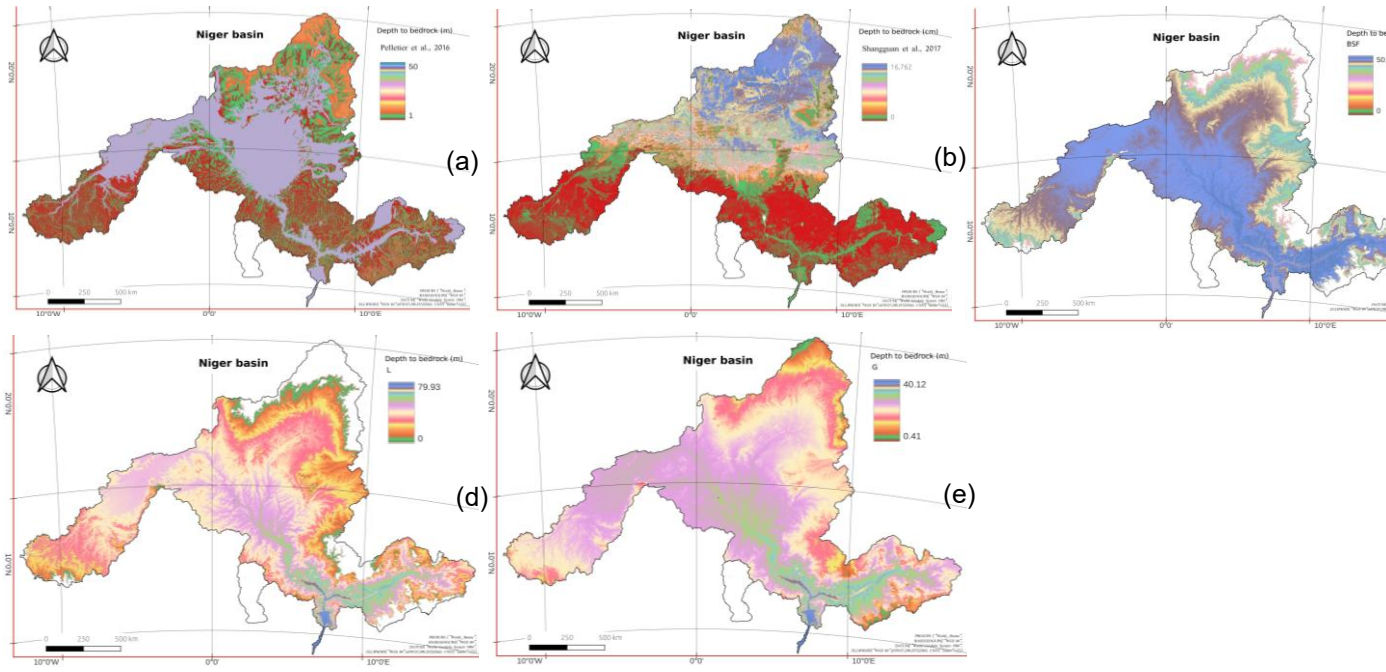

Figure 4.32a: DTB maps from previous studies (a–b) compared with the maps proposed in this study for the Niger basin.

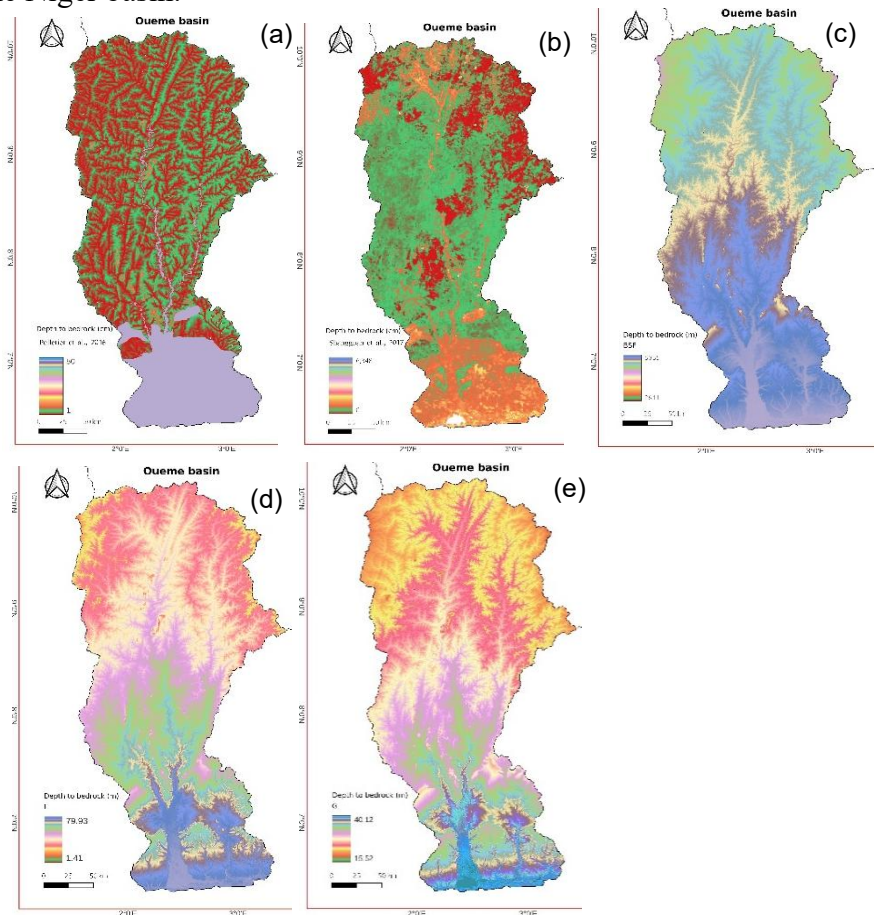

Figure 4.32b: DTB maps from previous studies (a–b) compared with the maps proposed in this study for the Oueme basin.

Figures 4.33a–c display DTB profiles along three transects: from Opala to Masi-Maniba in the Congo basin, Tudun Iya to Lokoja in the Niger basin, and Parakou to Dassa in the Oueme basin. The profile lengths are 348 km, 235 km, and 180.2 km, respectively. For the Opala–Masi-Maniba profile, the average DTB values are 44 ± 1.3 m for Eq. 3.36, 28.2 ± 5.4 m for Eq. 3.46, and 21.5 ± 1.4 m for Eq. 3.31. Along the Tudun Iya–Lokoja profile, the corresponding averages are 40.3 ± 8.4 m, 24.3 ± 22.1 m, and 21.2 ± 6.2 m. For the Parakou–Dassa transect, the average DTB values are 47.3 ± 1.3 m, 49.4 ± 10 m, and 27.9 ± 3.3 m, respectively. The profiles show a strong relationship between DTB and topography, suggesting that surface geomorphology can offer valuable insights into weathering development and the depth to bedrock. Minimum and maximum DTB values along these profiles range from 38.8 to 46.4 m, 11.6 to 41.3 m, and 17.6 to 25.1 m for the Opala–Masi-Maniba section; from 0 to 49.9 m, 0 to 73.9 m, and 14.4 to 37.3 m along Tudun Iya–Lokoja; and from 44.1 to 49 m, 28.2 to 64.3 m, and 21.4 to 33.2 m between Parakou and Dassa, for Eqs. 3.36, 3.46, and 3.31, respectively. Despite the significant elevation changes observed in the third profile (Fig. 4.33c) between Parakou and Dassa, the average DTB remains relatively stable across all three estimation methods.

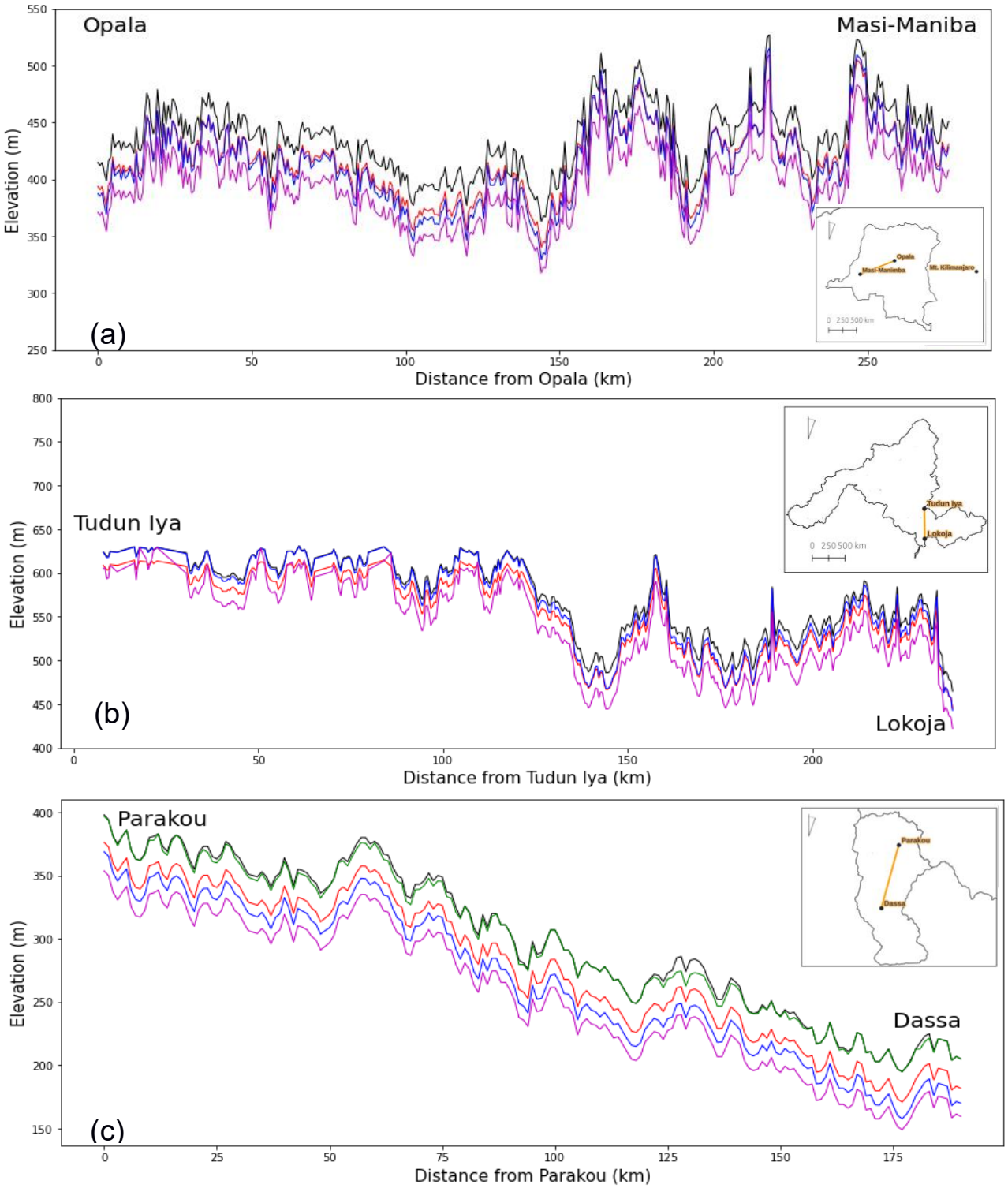

Figure 4.33: Comparison of 2D profiles across the Congo (a), Niger (b), and Oueme (c) basins: red represents DTB estimated using Eq. 3.31, magenta for Eq. 3.36, blue for Eq. 3.46, black for surface elevation (Z), and green for the DTB map from Shangguan et *al.* (2017). The orange profiles correspond to transects from Opala to Masi-Maniba, Tudun Iya to Lokoja, and Parakou to Dassa, respectively.

Accurately mapping depth-to-bedrock (DTB) is essential for effective borehole siting, particularly when integrated with geological lineaments, depression zones, and river networks. However, global DTB maps still suffer from relatively coarse spatial resolution, and the accuracy of existing maps remains questionable. Recent efforts to provide the Earth System Modeling community with this critical yet often overlooked input have not fully addressed these limitations. A recent important discussion titled “Where is the bottom of a watershed?” (Condon et al., 2020) emphasizes the intricate interactions among subsurface, land surface, and atmospheric processes, as explored in studies by Maxwell & Miller (2005), Kollet & Maxwell (2006), Maxwell et al. (2007), Maxwell & Kollet (2008a-b), Sutanudjaja et al. (2014), Rahman et al. (2015), Condon & Maxwell (2015, 2019), Kollet et al. (2018), Furusho-Percot et al. (2019), and Reinecke et al. (2019). One key uncertainty affecting groundwater integration in land surface models (LSMs) is the lack of reliable, ground-truth-based DTB maps. This study presents descriptive statistics derived from over 4,000 field DTB measurements in hard rock regions. Regardless of proximity to terrain features such as geological lineaments, depression zones, and river networks, the average DTB mean, median, and standard deviation are approximately 16.5 ± 1.2 m, 15.5 ± 1.8 m, and 10.8 ± 1.3 m, respectively. This range captures most measured DTB values with relatively few outliers, providing a sound basis for reasonable estimation. To further reduce uncertainty around bedrock depth, the dataset reveals a maximum DTB of 91.6 m, with an average maximum across distance classes of 54.6 ± 16.6 m. These findings align with those of Pelletier et al. (2016), Shangguan et al. (2017), and Lachassagne et al. (2021), who report similar maximum values.

Interestingly, DTB values do not consistently increase closer to geological lineaments, depression zones, or river networks, contrary to the expectation that surface erosion controls regolith thickness over bedrock. Our analysis (Fig. 3) supports this observation and suggests that while overland flow influences DTB, it is not the dominant factor. Nevertheless, the spatial density of terrain-related features remains a valuable indicator for identifying groundwater infiltration zones and optimizing borehole placement (Oussou et al., 2020). Large-scale DTB maps are especially valuable in data-scarce regions for coupling Earth system components in physically based models like PF-CLM, improving monitoring of climate change impacts and water security. Our test case focuses on a 100 km² area around an eddy covariance (EC) flux monitoring tower in Nazinga Park, along the Ghana–Burkina Faso border. Despite the usual constraints of Earth system modeling, this local-scale setup—with 30 m spatial resolution—in a water-stressed natural reserve is the first of its kind to provide both water and energy variables

for monitoring water balance and energy cycles. Though the simulation period was relatively short and the model was not calibrated, results were accurate, with variables falling within expected ranges and temporal and spatial patterns well captured.

To verify DTB map reliability, we used the PF-CLM setup for the domain hosting the EC station established by the WASCAL CONCERT project in 2012. The domain-average DTB (25 ± 1.5 m) served as a key static input for the subsurface model configuration. Simulated energy fluxes closely matched observations despite the domain's limited size. Performance metrics included Nash-Sutcliffe Efficiency (NSE) and R^2 values of 0.67 and 0.86 for outgoing longwave radiation, 0.77 and 0.77 for sensible heat, 0.69 and 0.6 for latent heat, and 0.34 and 0.71 for ground heat. Consistent with other PF-CLM studies in similar climates (Herzog et al., 2020; Cohard et al., 2019; Hector et al., 2017; de Graaf & Stahl, 2022), these results reinforce the model's applicability in West African climate systems. Accordingly, the subsurface setup using computed DTB maps is sufficiently reliable to support fully coupled Earth system modeling.

The DTB map by Shangguan et al. (2017), which incorporates Pelletier et al. (2016) as a covariate, relies on DEM-based data similar to the approach adopted here. However, this study's inclusion of extensive field-measured DTB data enhances estimation reliability and broadens available methodologies. By adapting computation steps from de Graaf et al. (2015), fourteen new approaches are proposed. For basin-specific DTB mapping, it is recommended to use a standardized DTB occurrence likelihood map combined with field measurements from the basin to evaluate and select the most appropriate method.

A comparative analysis of DTB maps generated using Eqs. 3.31, 10, and 20 against those from Pelletier et al. (2016) and Shangguan et al. (2017) reveals relatively low correlations (–0.34 to 0.3) in the Congo and Niger basins, while a notably stronger correlation is observed in the Oueme basin with Shangguan et al. (2017). These results suggest that focusing on basin-specific DTB mapping can enhance estimation accuracy and help reduce uncertainties related to watershed bottom boundaries in Earth system modeling. However, challenges remain with the existing maps. The Shangguan et al. (2017) map tends to overestimate low DTB values and underestimate high ones, while Pelletier et al. (2016) exhibits extreme estimates largely due to landform misclassification. Similar issues appear in the evaluated approaches, whether assessed by regional, geological, or basin-based zonal statistics. For example, Figure 4a shows that most geological units have a high frequency of low DTB values (<20 m) and low frequency of high

values (>30 m) when using Eq. 3.31; conversely, Eq. 3.36 yields low frequencies of low values and high frequencies of high values, almost reaching a ceiling below 60 m. In contrast, Eq. 3.46 produces a nearly uniform distribution from low to high values. These varying patterns present a significant challenge that calls for deeper investigation. Nonetheless, this study provides a ground-truth-based pattern in Figure 4 that can serve as a valuable reference, particularly for hard rock regions. While consensus on the maximum DTB limit across different methods and past maps has yet to be achieved, the field measurements presented here establish a practical threshold for hard rock areas. Leveraging the suggested methods and generated data can improve groundwater-to-atmosphere modeling and alleviate data scarcity issues related to groundwater integration within land surface models (LSMs) across the continent.

4.4 Evaluation of Fractured Groundwater systems' Influence on Water and Energy Fluxes

4.4.1 Model validation

The variation of the lineaments permeability (K) is evaluated with three experiments (High, moderate, and low K) to investigate the sensitivity of the surface fluxes (e.g., LH, SH, GH, RN, ET) and subsurface dynamics (e.g., water table depth). The analysis in this study focuses mainly on the difference in the absolute values of the variables in response to prescribed lineament permeability. In absence of sufficient field measurement to validate the model, only the outgoing longwave radiation is compared to observation at Nalohou site. For the baseline simulation, the model is configured without the representation of geological lineaments. Figure 4.34 shows scatter plots and error metrics (R, KGE, and PBIAS) of simulated versus observed outgoing longwave radiation for four periods of the year (DJF, MAM, JJA, and SON). Results indicate an overall high performance in the dry season with the highest KGE of 0.8 recorded during DJF. A strong linear relationship is recorded with R values of 0.8 to 0.9. Similar strong linear relationship is recorded during SON however KGE criterion is lower ranging between 0.3 and 0.4. In energy-limited conditions (e.g., JJA), the performance of the model in capturing the temporal variability of the outgoing longwave radiation drops significantly (-0.2 to -0.1). However, this performance is associated with a strong linear relationship with R values between 0.7 and 0.8). During the rainfall onset (MAM), KGE criterion varies between 0.3 and 0.4 with high R values. Whatever the experiment, the model shows a higher performance towards drier periods.

The potential change in outgoing longwave radiation in response to lineament permeability in Donga basin is reflected in the PBIAS values. During DJF, the difference of High K experiment compared to the reference simulation (without lineament) is -2% while for Moderate K experiment, outgoing longwave is reduced by -1%. There is no difference between Low K experiment and the reference during the same period. High K and Moderate K experiments show no difference during MAM period however Low K experiment increases outgoing longwave radiation by 1%. During the rainfall (JJA), High K experiment decreases outgoing longwave by 1% while Moderate K and Low K experiments increase the fluxes by 1%. From September to November, there is no difference between Low K experiment and the reference simulation. However, both High K and Moderate K experiments decrease outgoing longwave respectively by -4% and -5%. Overall, the impact of lineament in Donga basin reveals

that higher permeability in the fractures results in a decrease of the outgoing longwave radiation. Nevertheless, lower permeability conditions are associated with an increase of outgoing longwave radiation in energy-limited periods.

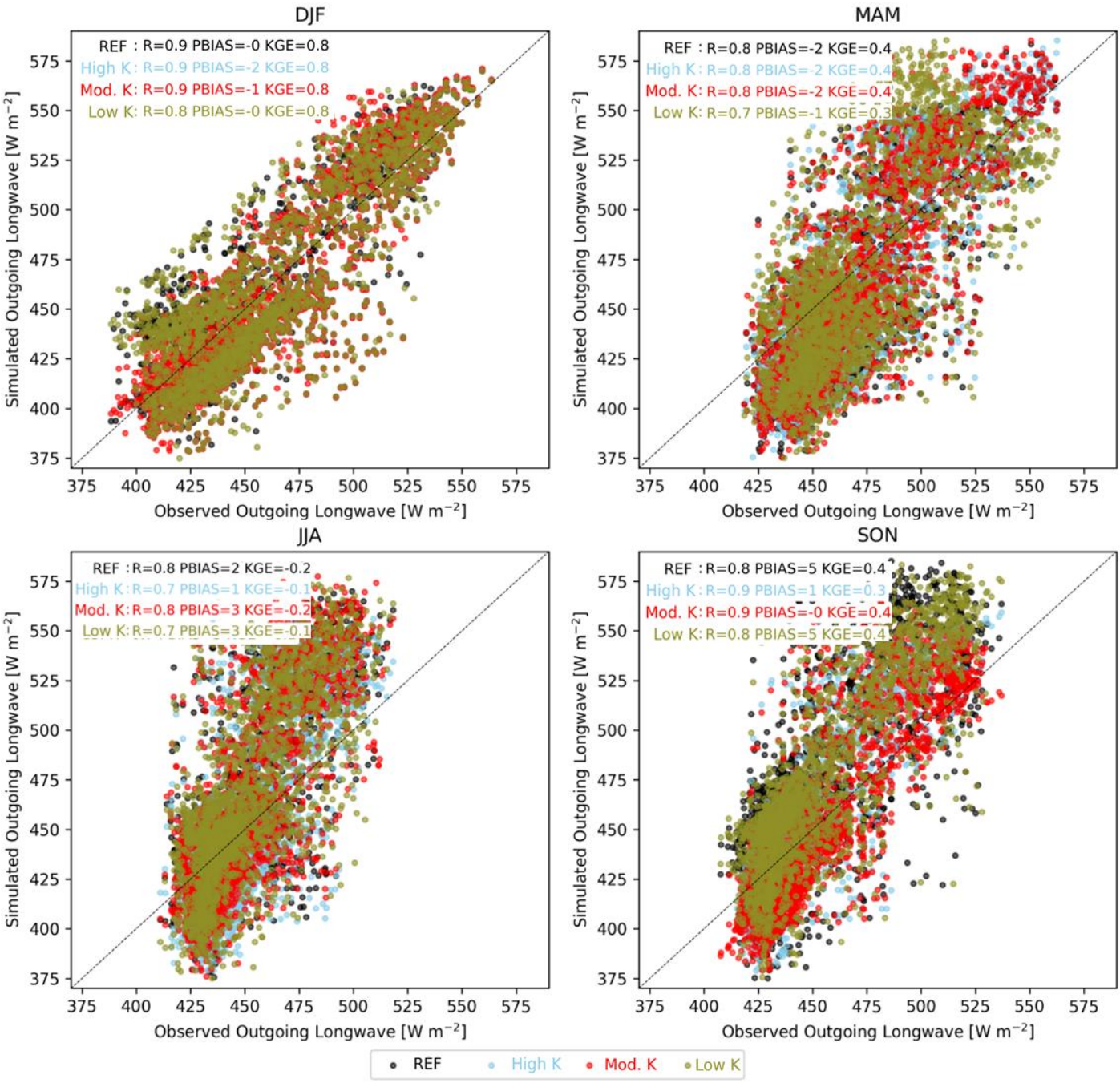

Figure 4.34: Scatter plots of simulated outgoing longwave radiation versus observed for DJF, MAM, JJA, and SON periods under High, moderate and low permeability (High K, Moderate K, and Low K) of geological lineaments in Donga basin.

4.4.2 Sensitivity of energy balance to fractures' permeability

The effects of the geological lineament on the diurnal cycle of the energy fluxes are shown in Figure 4.35. The energy components are listed on the y-axis and the investigated period on the x-axis. Remarkably, the highest difference in the diurnal cycle of the energy fluxes in response to lineament permeability occurs around noon. Compared to the reference scenario, Moderate K and High K experiments decrease latent heat (LH) by 4.3 and 4.9 W m^{-2}, and sensible heat (SH) by 17.9 and 18.1 W m^{-2} during the DJF period. Nevertheless, the Low K experiment increases both LH and SH, respectively, by 0.6 and 4.3 W m^{-2}. The three experiments altogether increase ground heat flux (0.3 to 0.5 W m^{-2}). Within the same period, the net radiation (RN) is increased with the Moderate K and High K experiments by 2.1 and 7.3 W m^{-2}, while a decrease of -0.4 W m^{-2} is recorded with Low K. During MAM, the SH is increased by 1.1 and 1.5 W m^{-2} with Moderate K and Low K experiments, while High K decreases the fluxes by -2.7 W m^{-2}. The three experiments decrease the net radiation during MAM by -18.8, -3.8, and -12.2 W m^{-2}. Except for the SH decrease with the High K experiment in the rainy season (JJA), the experiments increase all the components of the energy balance. Likewise, the observed pattern during DJF, Moderate K and High K experiments decrease LH flux in the morning until 10:00 to 11:00 and late in the evening after 17:00 during SON. The difference between the two experiments compared to the reference is -34 and -39.1 W m^{-2} of SH. The highest difference is recorded around noon and nighttime. In the same period, the Low K experiment decreases both LH and SH. This observed impact on the diurnal cycle of SH, LH, and GH results in an increase of net radiation. Around noon, the two experiments increase LH. During JJA, the Low K experiment increases LH throughout the day, while Moderate K and High K increase the fluxes only between 10:00 AM and 14:00. Similar patterns of the diurnal cycle of LH are observed during MAM for the three experiments.

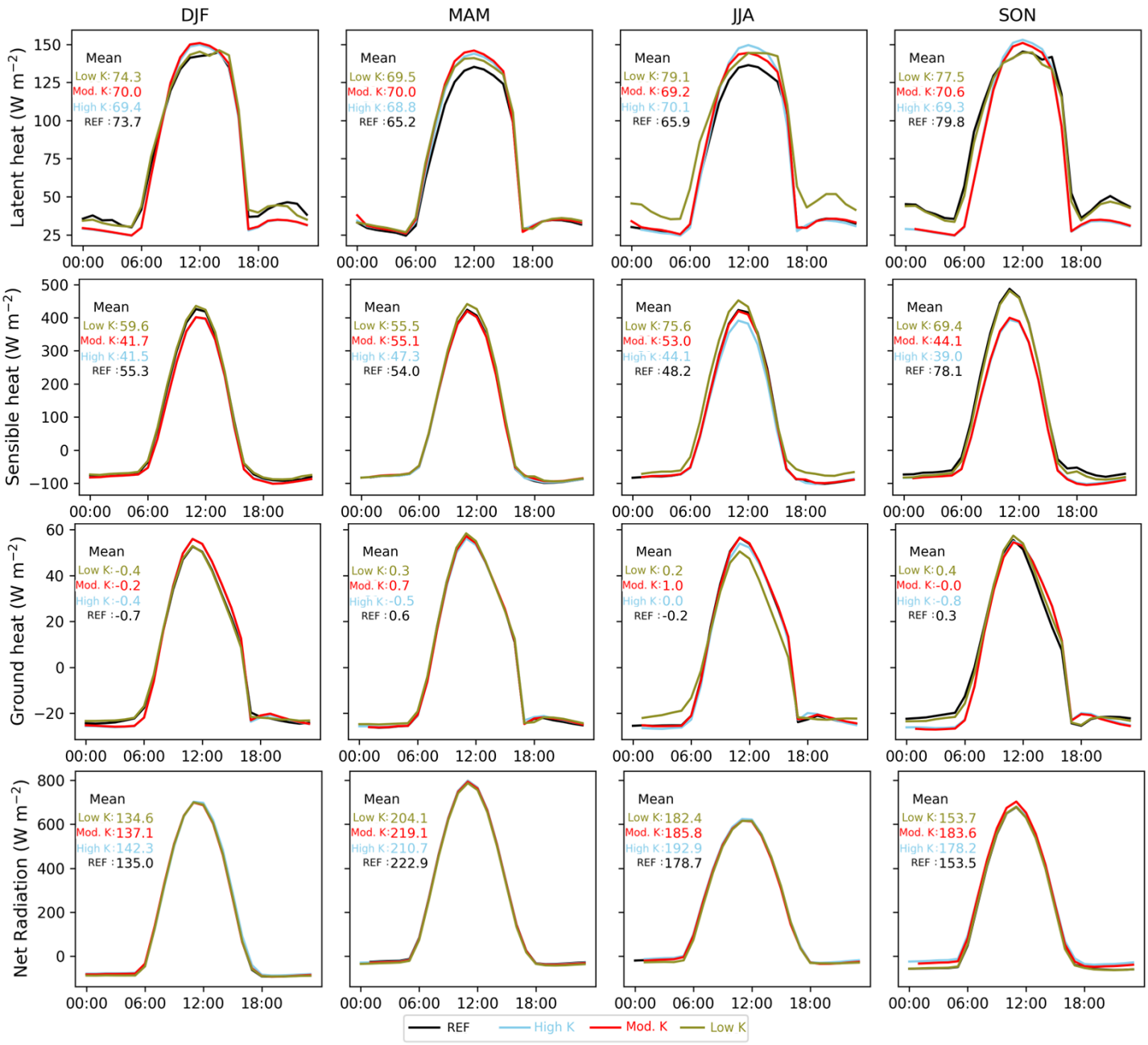

Figure 4.35: Diurnal cycle of the energy balance components under the geological lineament permeability experiments.

For the entire simulation period, the centered Root Mean Squared Deviation (cRMSD), percentage change (PC), and bias are computed and displayed in Table 4.10. The cRMSD values reveal a trend in the magnitude of the effects of the experiments from higher to lower permeability conditions. The values range from 8.99 and 60.49 W m^{-2}. The difference in the pattern of the simulated flux is higher towards lower permeability conditions. The Low K experiment has the highest bias of 4 W m^{-2} compared to the baseline scenario, while High K and Moderate K show 0.77 and -1.55 W m^{-2}. The magnitude of the bias is at its highest with SH. The values are -10.5, -13.19, and 6.06 W m^{-2}, respectively, for High, Moderate, and Low Ks, representing -20.04, -22.91, and 10.53%. The lowest bias is recorded with GH. A positive bias is recorded for the net radiation with High K and Moderate K, while the Low K experiment decreases the average net radiation by -3.39 W m^{-2} for the entire period. High K and Low K experiments increase LH by 1.13 and 5.62%. However, the LH is decreased by -2.18% with the Moderate K experiment. Overall, the impact of the experiments on the diurnal cycle of the energy components is rather mitigated. Though there is a trend in cRMSD in terms of the similarity in the temporal variability of the experiments and the baseline simulation, Moderate K and Low K experiments have opposite effects on the energy components.

Table 4.9: Difference in the energy components between the experiments and the reference simulation

	Variable	High K – REF	Mod. K - REF	Low K – REF
cRMSD	LH	16.09	26.05	34.19
	SH	47.56	53.31	60.49
	GH	8.99	9.34	10.28
	RN	20.02	21.79	23.92
PC %	LH	1.13	-2.18	5.62
	SH	-20.04	-22.91	10.53
	GH	334.5	63.8	-58.38
	RN	3.48	2.6	-1.99
Bias	LH	0.77	-1.55	4
	SH	-10.5	-13.19	6.06
	GH	-0.53	-0.17	0.16
	RN	6.17	4.43	-3.39

Figure 4.36 displays the scatter plots of the energy balance closure (EBC) for DJF, MAM, JJA, and SON. The equation of the linear regression and the EBC of the reference simulation and the lineament permeability experiments are displayed to evaluate the differences. During DJF, the EBC ranges between 18.5 and 18.7%. From December to August, the Low K experiment decreases the EBC by 0.2 to 12.5% compared to the reference, while an increase of 6.5% is recorded during SON. In the same period, the Moderate K experiment slightly decreases the EBC. Though a similar pattern is observed with the High K experiment during DJF and MAM, it increases the energy balance by 5.6% during JJA. The highest difference of energy balance closure is recorded during SON for Moderate K and High K experiments, with an increase of 36.9 and 25.4% respectively. The lowest R value of EBC is recorded during the energy-limited (JJA and SON). Overall, these differences between the lineament permeability and the reference simulation remarkably reveal that the stored or released energy term added to the energy balance closure as a residual is partly influenced by these subsurface features. Moderate K and High K experiments have a significant impact on EBC during SON, as the slope is decreased reaching 0.75.

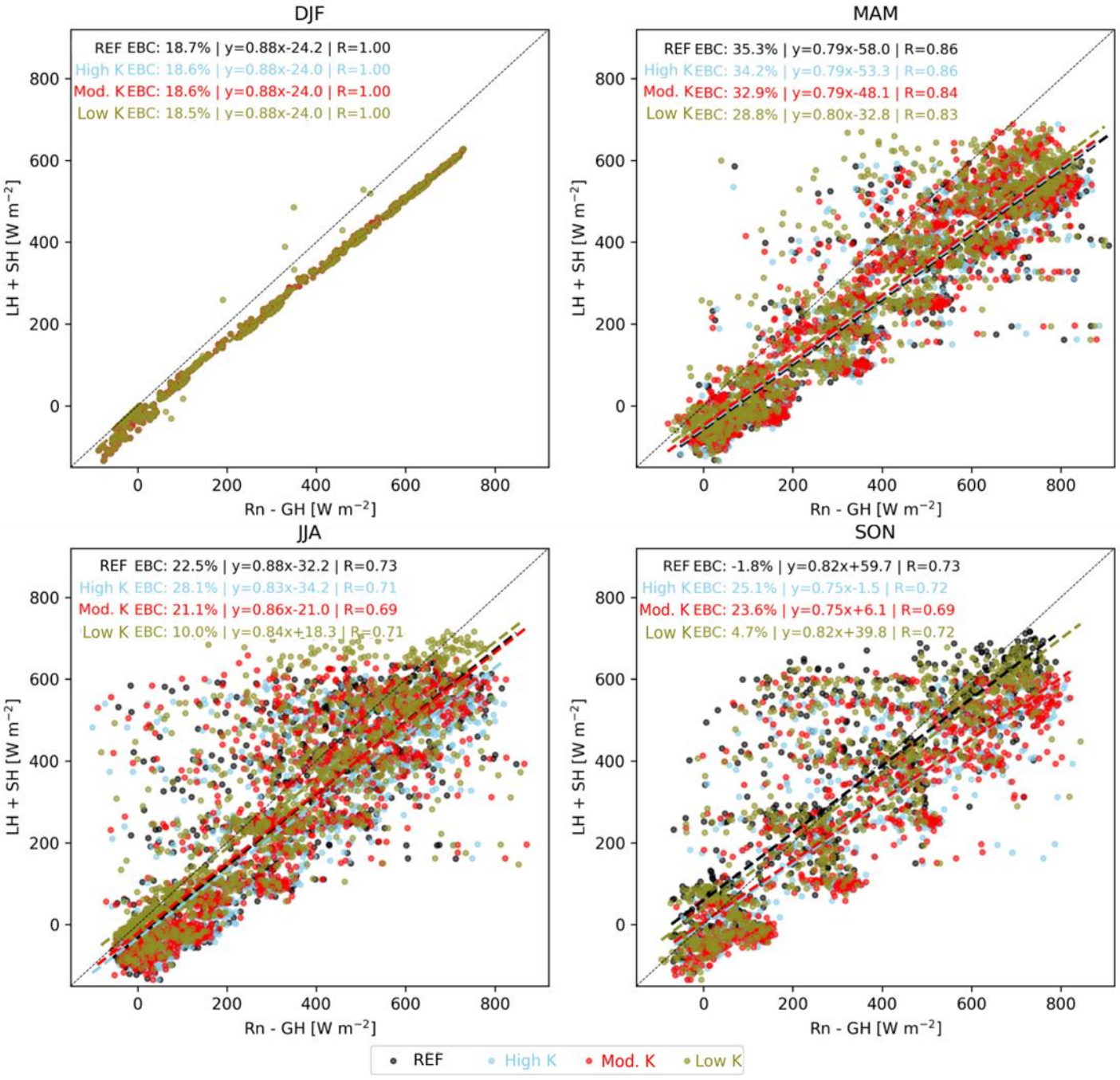

Figure 4.36: Potential change in the energy balance closure under the lineament permeability experiments.

4.4.3 Sensitivity of water fluxes

The variation of total evapotranspiration, transpiration, and infiltration in response to the lineament permeability experiments is displayed in Figure 4.37 and Table 4.10. The low K experiment increases the total evapotranspiration during the four investigated periods. Moderate K and High K experiments decrease total evapotranspiration in the dry season (DJF and SON) by 0.1 to 0.3 mm d^{-1}. Remarkably, the highest difference of the diurnal cycle occurs around noon, whatever the season. Similar patterns are observed for the transpiration. The soil infiltration is decreased by 0.7 mm d-1 with Moderate K and High K experiments, while the Low K experiment increases soil infiltration by 0.1 mm d^{-1}. The effect of the Low K experiment on soil infiltration is at its highest during the JJA period, when the mean soil infiltration reaches 0.6 mm d^{-1}. Likewise, in the case of the energy components, cRMSD indicates a trend in the magnitude of the impact of the lineament permeability on water fluxes. Moderate K experiment decreases total evapotranspiration by -2.18% (-0.05 mm d^{-1}) while High K and Low K increase the average ET, respectively by 1.13% (0.026 mm d^{-1}) and 5.62% (0.137 mm d^{-1}). The same pattern is recorded with the transpiration (Table 4.11). As shown with cRMSD, the highest bias of soil infiltration between the experiments and the baseline scenario is recorded with Low K (0.26 mm). Moderate K has the most significant

negative impact on infiltration (-0.48 mm d^{-1}).

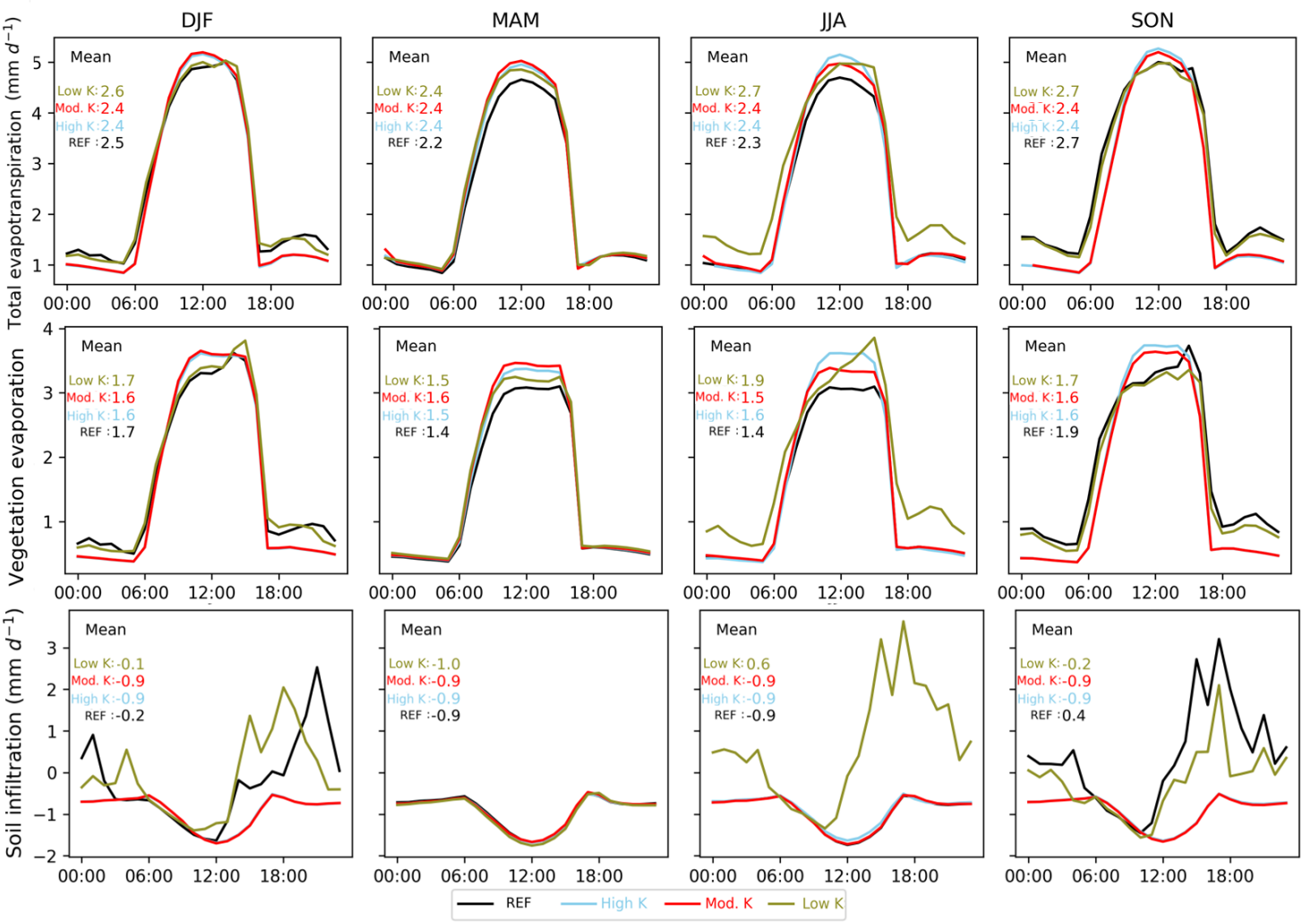

Figure 4.37: Diurnal cycle of the total evapotranspiration, transpiration, and soil infiltration under the geological lineament permeability experiments.

Table 4.10: Difference in the water fluxes between the experiments and the reference simulation

	Variable	High K – REF	Mod. K - REF	Low K – REF
cRMSD	Evap. Tot	0.55	0.89	1.176
	Veg. Evap.	0.42	0.81	1.16
	Infil	2.01	4.98	7.52
PC %	Evap. Tot	1.13	-2.18	5.62
	Veg. Evap.	4.32	-1.87	7.08
	Infil	8.025	110.33	-59.82
Bias	Evap. Tot	0.026	-0.05	0.137
	Veg. Evap.	0.065	-0.03	0.11
	Infil.	-0.068	-0.48	0.26

4.4.4 Sensitivity of water table depth

For the first time in the region, the contribution of lineament permeability to sustaining the water table is assessed in this section. The impact of the lineament permeability experiment on the average water table depth is presented in Figure 4.38. The difference between the simulated scenarios is assessed with cRMSD, PC, and bias. Hence, the High K experiment is associated with the highest cRMSD of 7.4 m of water table depth, followed by the Moderate K experiment (7.12 m). In the basin, water table depth is decreased by -36.29% and -31.73% under High K and Moderate K experiments. The corresponding biases are -7.12 m and -6.23 m. The lowest impact is obtained with the Low K experiment, with a cRMSD of 0.04, a PC of -0.05% and a bias of -0.01 m. The most significant impact is observed near the lineament network, especially in the east around the Nalohou site.

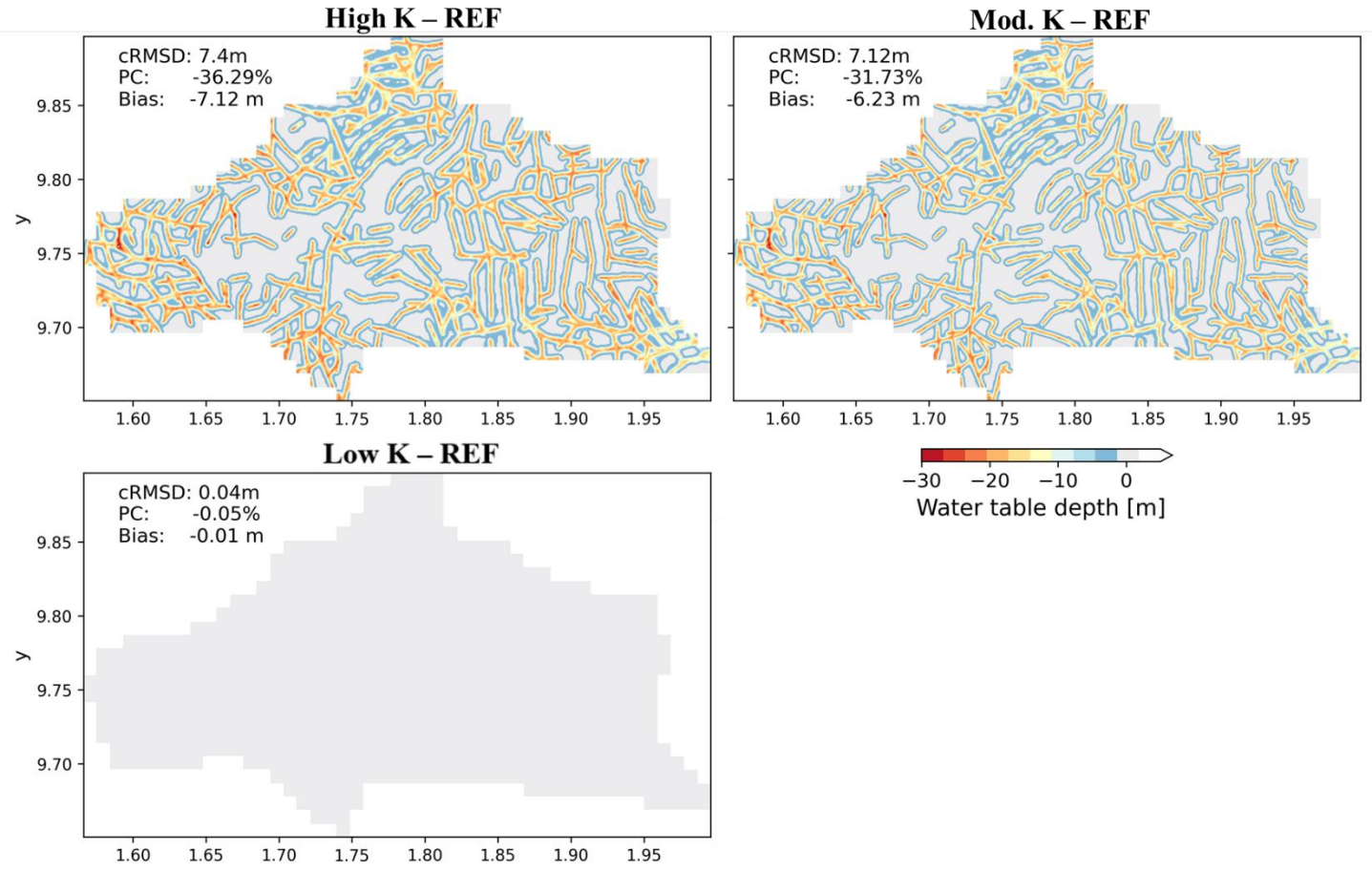

Figure 4.38: Sensitivity of water table depth to the lineament permeability experiments.

4.4.5 Sensitivity of terrestrial water storage

The description of the difference in groundwater storage (GWS) and surface water storage in response to the lineament permeability experiments compared to the reference scenario is displayed in Figure 4.39. The values are shown in million m^3. Remarkably, High K and Moderate K experiments significantly increase the average GWS of the basin. The computed increase is estimated at 355.8 and 326.8 million m^3 respectively for High K and Moderate K experiments. In contrast, the Low K experiment decreases mean GWS by -26.95 million m^3. The corresponding PC values are 7.9, 7.27, and -0.59%. respectively for High, Moderate, and Low K scenarios compared to the baseline. For GWS, the cRMSD values range between 9.13 and 129.33 million m^3.

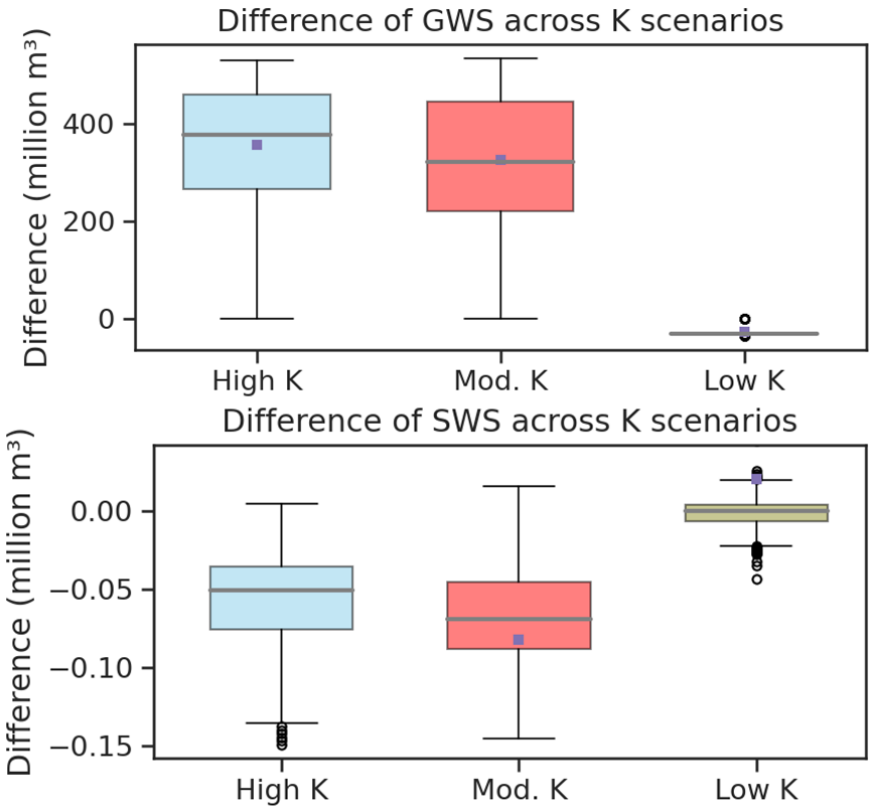

Figure 4.39: Potential change in the groundwater storage and surface water storage under the lineament permeability experiments (High, Moderate, and Low K).

The contrary effect is observed with surface water storage for each of the experiments. The low K experiment has a positive impact on the surface water storage (0.02 million m^3) while Moderate K and High K experiements decrease average SWS by respectively -0.0082 and -0.05 million m^3. The values of cRMSD are 0.016, 0.12, and 0.15 million m^3.

Table 4.11: Difference in the groundwater storage and surface water storage between the experiments and the reference simulation

	Variable	High K – REF	Mod. K - REF	Low K – REF
cRMSD (Million m^3)	GWS	122.26	129.33	9.13
	SWS	0.016	0.12	0.15
PC (%)	GWS	7.9	7.27	-0.59
	SWS	-0.25	-0.0005	0.00014
Bias (Million m^3)	GWS	355.8	326.84	-26.95
	SWS	-0.05	-0.082	0.02

4.5 Impact of Climate projections on groundwater recharge, levels, surface water storge

4.5.1 Climate impact on groundwater recharge

The potential change of mean annual groundwater storage (GWS) under the end of century SSP1-2.6 and SSP5-8.5 scenarios is shown in Figure 4.40. The difference in GWS between the warming levels and the historical scenario (1850-2014) is investigated with the centered Root Mean Squared Deviation (cRMSD), percentage change (PC), bias (Table 4.13). Multiple GCM/SSP combinations are preferred to ascertain the uncertainty in the predictions (Mitchell et *al.*, 2016). The GCM/SSP combinations are 10 out the total model run of 15. With SSP1-2.6 projections for the end of the century, 3 out the 5 GCMs show a groundwater storage increase ranging 0.45 to 30.39 million m^3. However, 2 out the 5 GCMs (IPSL-CM6A-LR and NorESM2-MM) indicate the opposite effect of temperature increase on the average GWS by -3.19 and -4.42 million m^3. The percentage change of the highest increase obtained with GFDL-ESM4 is 0.68% while the lowest increase corresponds to 0.01%. The recorded decrease with IPSL-CM6A-LR and NorESM2-MM represents -0.07 and -0.1% of the historical scenario. The corresponding cRMSD values under climate projection SSP1-2.6 vary from 0.17 and 4.83 million $m^{3,}$ respectively for MIROC6 and GFDL-ESM4.

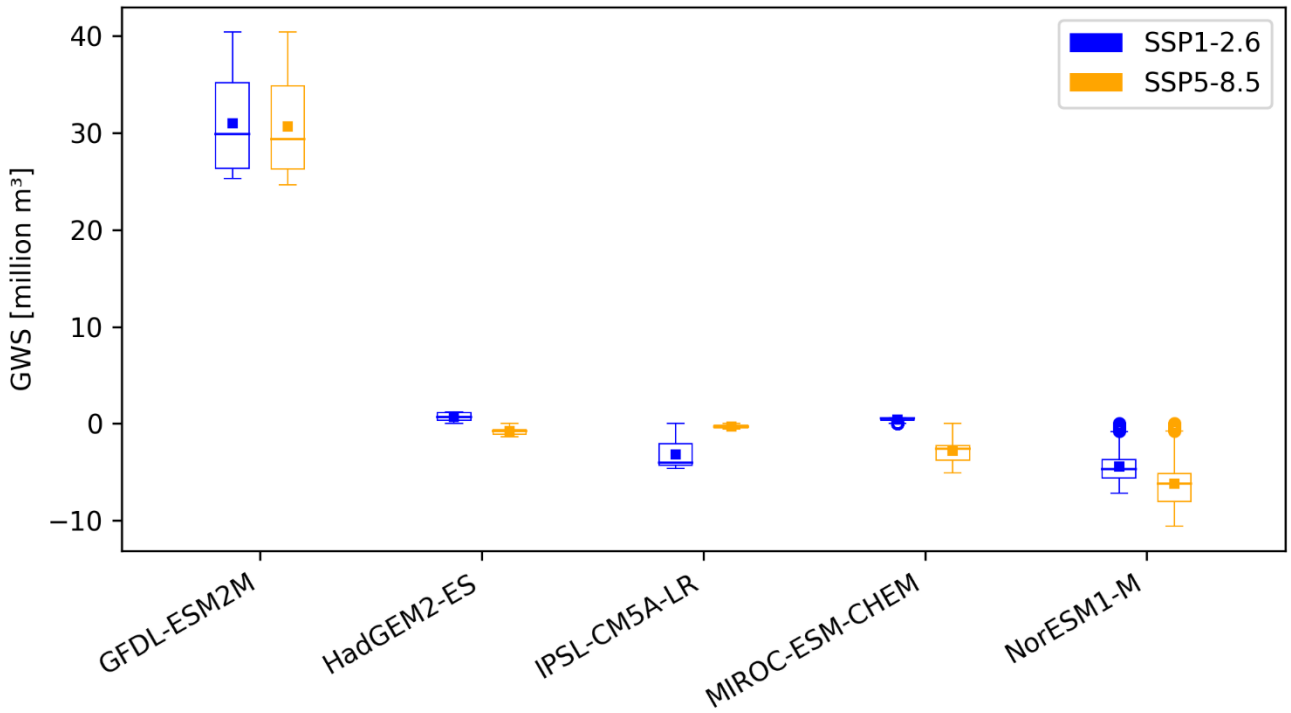

Figure 4.40: Groundwater storage projections under SSP1-2.6 and SSP5.8.5 scenarios for Donga basin.

There is a clear contradiction between the GFDL-ESM4 result and other GCMs as the magnitude of change projected is significantly different. Except for GFDL-ESM4, all the GCMs reveal a decrease of mean GWS under the SSP5-8.5 projection. The projected difference is -6.18, -2.81, -0.79, and -0.30 million m^3, respectively for NorESM2-MM, MIROC6, HadGEM3-GC31-LL, and IPSL-CM6A-LR. The associated PC values are -0.14, -0.06, -0.02, and -0.01%. For this 4 out 5 GCMs, NorESM2-MM has the highest cRMSD of 2.57 million m^3 while the lowest value of 0.17 million m^3 is recorded with IPSL-CM6A-LR. Overall, lower warming levels (SSP1-2.6) reveal the increase of average GWS for 3 out 5 GCMs which confirms past findings by Cook et *al.* (2022) on projected groundwater recharge for the region. However, the opposite effect displayed with 2 out of the 5 GCMs (IPSL-CM6A-LR and NorESM2-MM) shows the disparities in the projection and requires further investigation at the local scale. Across the GCMs under the SSP5-8.5 scenario, the groundwater storage decrease is predominantly projected for the basin. This reveals that though lower warming levels might be associated with groundwater recharge, higher warming levels will result in groundwater depletion.

Table 4.12: Description of the difference in GWS projections compared to the historical period (1850-2014).

	Projections	GFDL-ESM4	HadGEM3-GC31-LL	IPSL-CM6A-LR	MIROC6	NorESM2-MM
cRMSD (million m^3)	SSP1-2.6	4.83	0.40	1.43	0.17	1.76
	SSP5-8.5	4.88	0.35	0.17	1.25	2.57
PC (%)	SSP1-2.6	0.68	0.02	-0.07	0.01	-0.10
	SSP5-8.5	0.68	-0.02	-0.01	-0.06	-0.14
Bias (million m^3)	SSP1-2.6	30.98	0.70	-3.19	0.45	-4.42
	SSP5-8.5	30.67	-0.79	-0.30	-2.81	-6.18

4.5.2 Climate impact on surface water storage

The projected change in the mean annual surface water storage under SSP1-2.6 and SSP5-8.5 warming levels at the end of the century is highlighted in Figure 4.41. The difference is displayed in m^3 for the GCM/SSP combinations. Table 4.14 shows the computed difference between the projected SWS and the historical scenario (1850-2014) with cRMSD, PC, and bias as metrics. Except for GFDL-ESM4, 4 out 5 GCMs show a decrease of average SWS by the end of the century. The differences are -1876.35, -1333.37, -670.82, and -510.19 m^3 for respectively NorESM2-MM, IPSL-CM6A-LR, MIROC6, and HadGEM3-GC31-LL. Under the warming level SSP5-8.5, the 4 GCMs indicate higher decrease of average SWS. The corresponding values are -2146.22, -1258.37, -2053.46, and -3356.64 m^3. GFDL-ESM4 shows the opposite effect under the two warming levels. The highest magnitude of cRMSD is observed with GFDL-ESM4 for both SSP1-2.6 and SSP5-8.5. The percentage change of average SWS is relatively low for all the GCM/SSP combinations.

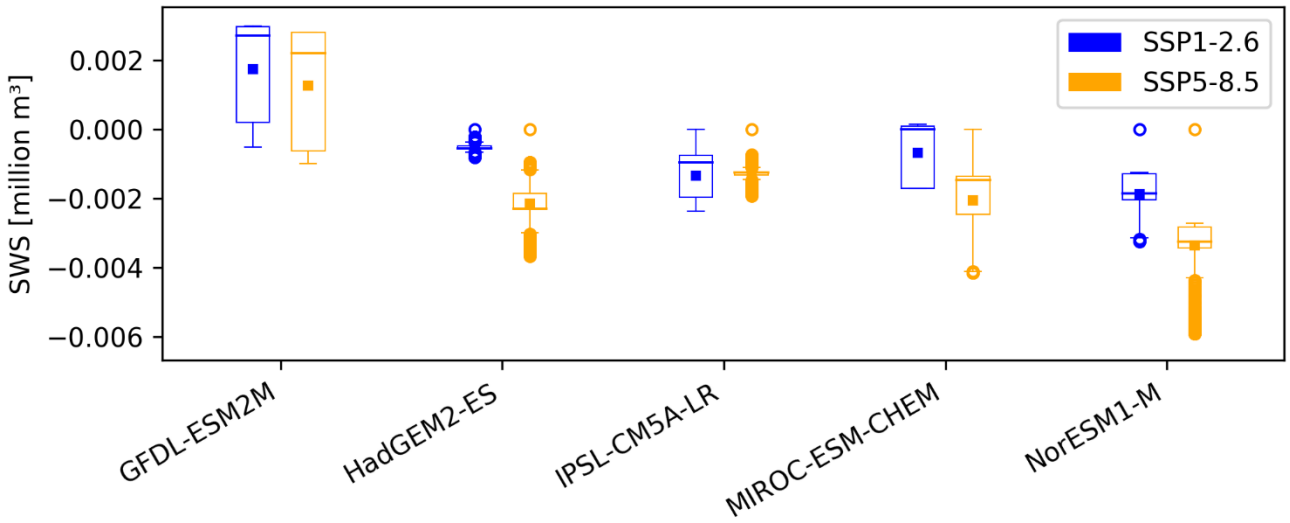

Figure 4.41: Surface water storage projections under SSP1-2.6 and SSP5.8.5 scenarios for Donga basin

Table 4.13: Description of the difference in SWS projections compared to the historical period (1850-2014).

	Projections	GFDL-ESM4	HadGEM3-GC31-LL	IPSL-CM6A-LR	MIROC6	NorESM2-MM
cRMSD (m^3)	SSP1-2.6	1802.61	126.52	639.83	869.98	541.41
	SSP5-8.5	1932.34	640.02	227.39	900.67	842.73
PC (%)	SSP1-2.6	0.00	0.00	0.00	0.00	0.00
	SSP5-8.5	0.00	0.00	0.00	0.00	0.00
Bias (m^3)	SSP1-2.6	1754.10	-510.19	-1333.37	-670.82	-1876.35
	SSP5-8.5	1269.40	-2146.22	-1258.37	-2053.46	-3356.64

4.5.3 Climate impact on groundwater levels

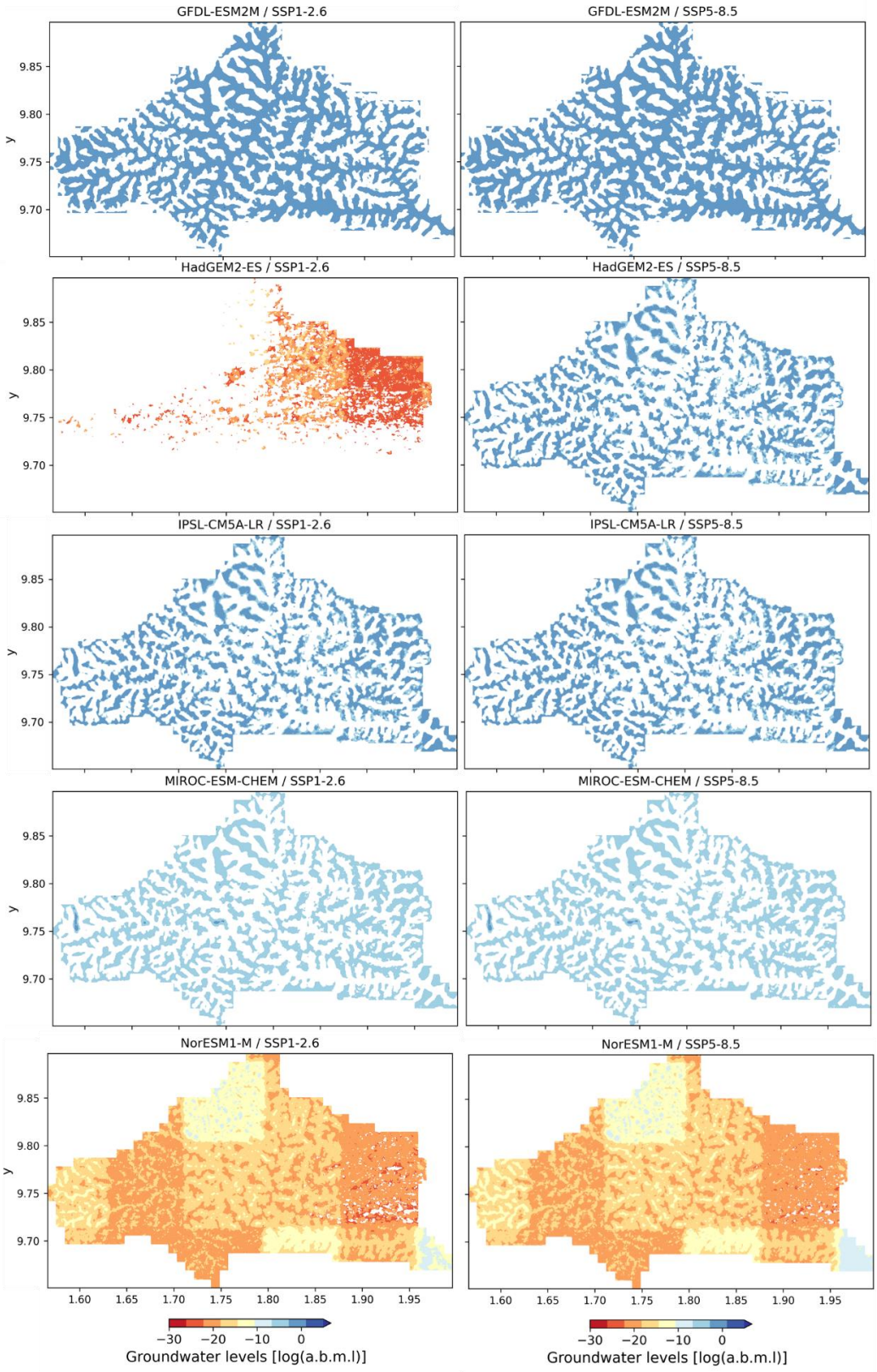

Figure 4.42: Groundwater table projections under SSP1-2.6 and SSP5.8.5 scenarios for Donga basin

4.6 Soil N_2O and CH_4 emissions in contrasting land use of the Sudanian savanna (West Africa)

4.6.1 CH_4 flux

This study assessed for the first time rainfed rice fields methane emissions in the Sudanian savanna using the chamber-based approach. The fluxes oscillate from -33.08 to 13.72 µg C m^{-2} h^{-1} in 2023 and -33.8 to 29.13 µg C m^{-2} h^{-1} in 2024 with seasonal median of -13.86 µg C m^{-2} h^{-1} at Mole Park (Table 3.6). The forests site acts as a CH_4 sink as the averages of the seasonal fluxes are -0.52 and -11.48 µg C m^{-2} h^{-1} for 2023 and 2024. The lowest value was recorded in July 2024 while the strongest flux occurred in September 2024. Throughout the season, the grassland remains predominantly a CH_4 source with fluxes varying from -24.13 to 73.58 µg C m^{-2} h^{-1} in 2023 and -16.15 to 64.25 µg C m^{-2} h^{-1} in 2024. The seasonal average and median are respectively 14.44 and 13.49 µg C m^{-2} h^{-1} for 2023 and 10.13 and 8.04 µg C m^{-2} h^{-1} for 2024. At the cropland site, the perturbed soil resulted in a CH_4 sink with an average of -1.78 and -2.05 for the two years with seasonal medians of -4.79 and -3.45 µg C m^{-2} h^{-1}. The maximum fluxes show a glimpse of the warming potential of the four ecosystems. That is, the Rice fields CH_4 release reaches 8 to 15-folds the forest reserve and cropland maximum fluxes while the grassland shows approximately 2 to 6-folds. Further, the CH_4 sink potential is demonstrated in the minimum fluxes as for the two consecutive years, the forest reserve maintained the highest sink followed by the cropland, the grassland, and the Rice fields (see Table 3.17). However, a CH_4 sink of -40.18 µg C m^{-2} h^{-1} was recorded in the Rice fields on the 28th August 2024 under moderate soil temperature (34.35 °C) and soil moisture of 42.26 %WFPS. The highest seasonal mean of CH_4 emission in 2023 and 2024 occurred in the rice fields (0.69±0.17 kg C ha^{-1} $season^{-1}$ and 0.82±0.22 kg C ha^{-1} $season^{-1}$ - Fig. 4.43).

The paired t-test indicates a significant difference ($p < 0.05$) in methane emissions between the four land use conditions. Except for the forest reserve, there is no significant difference among the years. Compared to other sites, the methane sink in the Forest reserve is significantly higher with the highest value recorded in June 2024 (-25.41 µg C m^{-2} h^{-1}). The second highest emission occurs in the grassland (0.53±0.35 kg C ha^{-1} $season^{-1}$ and 0.37±0.13 kg C ha^{-1} $season^{-1}$) while the most significant methane sink is recorded in the Forest reserve (-0.019±0.2 kg C ha^{-1} $season^{-1}$ and -0.42±0.13 kg C ha^{-1} $season^{-1}$). The emission is low in the cropland (-0.065±0.2 kg C ha^{-1} $season^{-1}$ and -0.074±0.14 kg C ha^{-1} $season^{-1}$) where the soil is

disturbed by agricultural practices at the beginning of the growing season. During the rainfall onset in June, the grassland behaves as a net CH_4 release (4.26±14.3 and 5.33±5.0) for the two years while the forest reserve indicates the highest sink (-25.41±4.8 μg C m^{-2} h^{-1}) in 2024. The soil at the cropland site absorbs 7.18±6.2 μg C m^{-2} h^{-1} and 0.5±7.0 μg C m^{-2} h^{-1} CH_4 in the same period (Table 3.7, Fig. 4.43). The rainfall onset delay at the rice fields in 2024 is revealed in the measurement as the soil indicates a CH_4 sink of -6.19±15.3 μg C m^{-2} h^{-1} while the previous year was a release of 4.96±16.8 μg C m^{-2} h^{-1}.

In July, except for the CH_4 sink at the forest reserve (-19.93±5.9) in 2024, the average CH_4 release was 6.44±11.18 μg C m^{-2} h^{-1} and 3.31±0.9 μg C m^{-2} h^{-1} at the grassland, 0.77±8.7 μg C m^{-2} h^{-1} and 0.70±5.0 μg C m^{-2} h^{-1} at the cropland, and 16.90±15.8 μg C m^{-2} h^{-1} and 1.89±11.3 μg C m^{-2} h^{-1} at the rice fields (see Table S1). The methane sink observed in the previous month continued in August in the forest reserve, with emissions of -3.24 and -16.98 μg C m^{-2} h^{-1} for the two years. In contrast, the methane release is maintained in the grassland and cropland. Though a similar pattern is observed at the rice fields in 2023 (40.89 μg C m^{-2} h^{-1}), lower rainfall recorded in 2024 (380 mm, 31.19% WFPS) during the sampling period is accompanied by methane sink (-8.05 μg C m^{-2} h^{-1}), which is unlikely for the period and site. Toward the end of the growing season, the forest reserve switched to methane release (12.91 and 7.84 μg C m^{-2} h^{-1}) in September. Likewise, the cropland methane release in the previous month changed to sink (-7.34 and -0.64 μg C m^{-2} h^{-1}). The magnitude of the CH_4 flux rate at the grassland site increased significantly by 2 to 3 folds while it decreased at the rice fields. In October, the emissions at the forest reserve changed back to CH_4 sink (-3.48 and -12.75 μg C m^{-2} h^{-1}). The CH_4 release was maintained at the grassland (32.53 and 12.77 μg C m^{-2} h^{-1}) and rice fields (8.03 and 79.16 μg C m^{-2} h^{-1}) while the cropland shows a methane sink (-0.57 and -6.4 μg C m^{-2} h^{-1}). Overall, the temporal pattern indicates a rise in the emission in response to the rainfall at each site. The magnitude of emission is lower at the beginning of the rainy season while the highest release is reached at the peak (July-August). This is followed by a decrease of the emission towards rainfall cessation. There is a remarkable difference between the cropland and rice fields' emissions. The soil disturbance (e.g., ploughing) reduces the ability of the bacteria to take up methane. A stable soil structure is required for increased methane release; the cropland methane flux is mitigated with wetter and drier soil conditions resulting respectively in emission and uptake. The methane flux in the rainfed rice (Janga) is significant compared to other land use however compared to permanently flooded rice fields (0.2 to 99 mg C m^{-2} h^{-1}; IPCC, 1996), the values are quite lower (see Table 3.7). Hence,

this lower methane emission in the rainfed rice is further confirmed in the earlier weeks of the rainy season when the soil behaves as a sink (-6.19±15.3) in 2024 and slight release (4.96±16.8) in 2023.

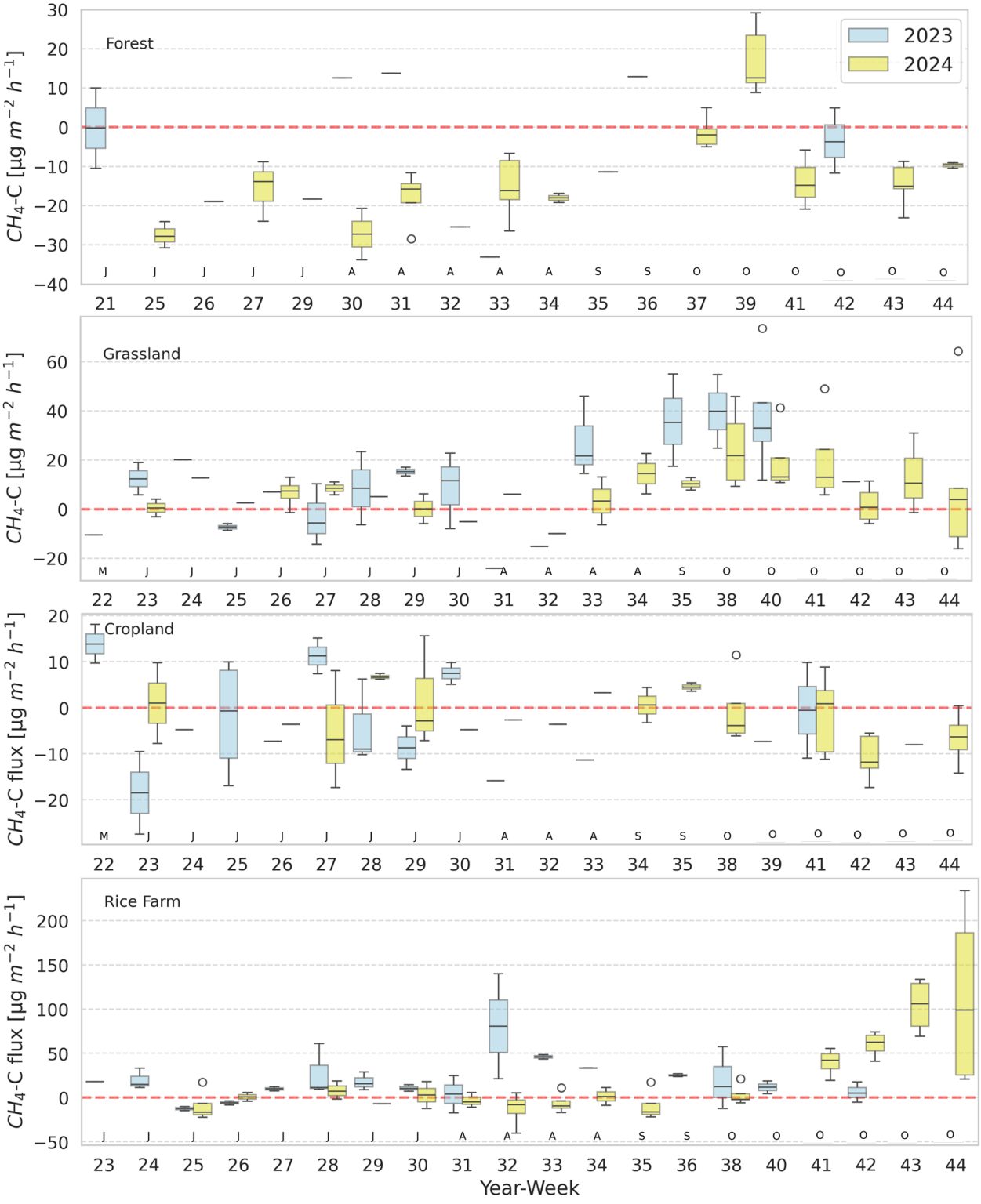

Figure 4.43: Weekly boxplot time series of in situ CH_4 flux for 2023 (light blue) and 2024 (yellow). Each boxplot is made of fluxes from 5 sub-trial points (chambers). From top to bottom are the forest reserve, grassland, cropland, and rice fields. The number of the sampling week is in x-axis.

4.6.2 N_2O flux

In the forest reserve, the N_2O fluxes range from -9.31 to 12.1 μg N m^{-2} h^{-1} in 2023 and -10.56 to 9.27 μg N m^{-2} h^{-1} in 2024 with seasonal medians of 6.32 and -1.37 μg N m^{-2} h^{-1}. Similar range of minimum N_2O sink is recorded in the grassland (-13.21 and -9.65 μg N m^{-2} h^{-1}) however the maximum release is stronger with N_2O fluxes reaching 14.14 and 21 μg N m^{-2} h^{-1}. The seasonal median flux was 3.3 in 2023 and 3.25 μg N m^{-2} h^{-1} in 2024. Further, the cropland displays the strongest N_2O release in September 2023 (16.51 μg N m^{-2} h^{-1}) and June 2024 (29.63 μg N m^{-2} h^{-1}) however, the highest observed N_2O sinks were -12.18 and -15.84 μg N m^{-2} h^{-1} in July and September. Under moderate temperature and high soil moisture, the highest N_2O flux occurred in the rice fields (33.93 μg N m^{-2} h^{-1}) while the highest sink was -11.09 μg N m^{-2} h^{-1} in September. The seasonal medians of the two years are close to the observed fluxes in other land use (3.65 and 4.66 μg N m^{-2} h^{-1}) likewise the minimum N_2O sink (-9.74 and -11.09 μg N m^{-2} h^{-1}).

The paired t-test revealed that there is no significant difference in mean N_2O flux for each land use between the two years. Likewise, the N_2O emissions in both the natural and degraded land cover have no significant difference between the sites. Whatever the observation sites, the investigated land use is a net source of N_2O for each year (Fig. 4.44). The lowest annual mean of N_2O release was recorded at the forest reserve in 2024 (0.011±0.11 kg N ha^{-1} $season^{-1}$) however the rice fields displayed the highest values (0.16±0.31 kg N ha^{-1} $seasonr^{-1}$). There is a slight change in the annual mean of N_2O release at the cropland site (0.12±0.18 and 0.11±0.08 kg N ha^{-1} $season^{-1}$) while it increased by approximately 127 % in the grassland. During the rainfall onset (June), a significant N_2O release is observed for the two years at the cropland (9.52 and 10.48 μg N m^{-2} h^{-1}) and rice fields (9.76 and 10.15 μg N m^{-2} h^{-1}) sites (Table S1). A contrasting land cover effect on N_2O emissions is observed in 2024 as the forest reserve showed N_2O sink (-1.38 μg N m^{-2} h^{-1}) while the grassland displayed a release of 4.42 μg N m^{-2} h^{-1}. Further, the sites altogether released N_2O in July 2024 with the highest value recorded at the rice fields (8.47 μg N m^{-2} h^{-1}). In July 2023, except for the forest reserve, the other three sites behaved as a sink. The rainfall peak in August at the natural forest reserve results in N_2O sink for 2023 (-0.5 μg N m^{-2} h^{-1}) and 2024 (-0.5 μg N m^{-2} h^{-1}). The opposite occurred at the grassland site (4.36 and 3.57 μg N m^{-2} h^{-1}) and even higher flux was observed at the rice fields (6.71 μg N m^{-2} h^{-1}) in 2024. Though there is no significant difference in mean N_2O among the sites, the N_2O release during the rainfall cessation at the forest reserve and grassland is the highest (6.88 and 5.42 μg N m^{-2} h^{-1}) in 2023 (Table S1). The managed systems (cropland and rice fields) showed lower N_2O release compared

to the natural systems (Forest reserve and grassland) for the two years in the same period. Lower nitrogen content in response to plant activities at the end of the growing season might explain the lower emission. The evidence reveals that the land use degradation effects on the nitrous oxide release is complex and less significant in magnitude compared to methane and carbon dioxide.

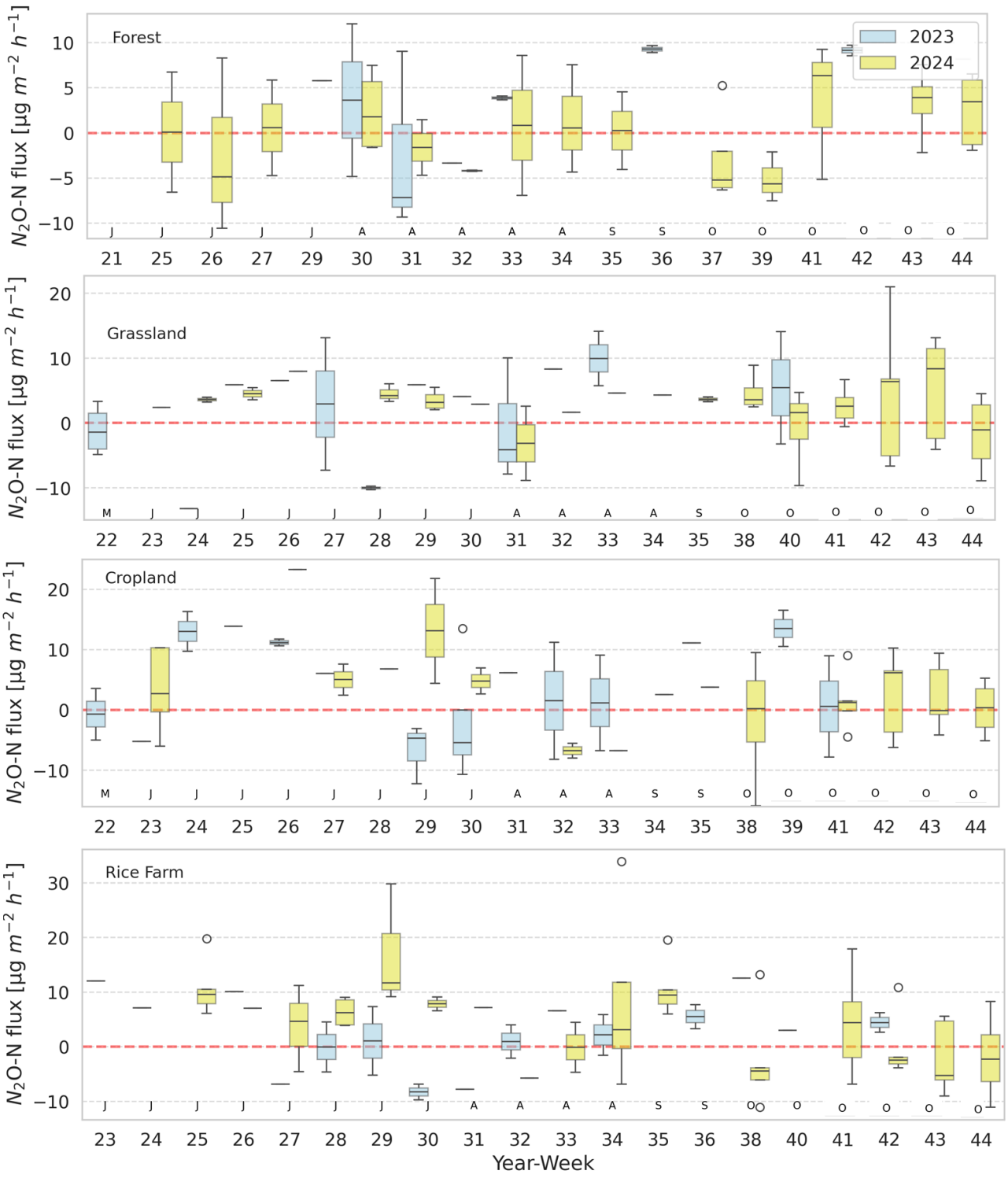

Figure 4.44: Weekly boxplot time series of in situ N_2O flux for 2023 (light blue) and 2024 (yellow). Each boxplot is made of fluxes from 5 sub-trial points (chambers). From top to bottom are the forest reserve, grassland, cropland, and rice fields.

4.6.3 Soil moisture

WFPS values are not calculated for the forest reserve because the bulk density was not measured. The highest annual mean soil moisture is observed at the rice fields (59.99 % WFPS) while the lowest value occurred in the cropland (32.11 % WFPS, Fig. 4.45). In response to the lower precipitation (380 mm) during the sampling period, the annual mean soil moisture dropped by 32% (40.56 % WFPS) in the rice fields while the grassland recorded a higher soil moisture (49.0 % WFPS). For the two years, the soil moisture peak occurred between August and September at the cropland (41.81/43.67 % WFPS) and grassland (73.25/91.02 % WFPS) which is associated with the higher rainfall period. The growing season started with relatively high soil moisture at the grassland site (39.01/27.88 % WFPS) compared to the rice fields where lower values are recorded (16.94/15.69 % WFPS) and this might explain the relatively strong emission observed in the grassland. Although the soil moisture annual mean at the cropland is 32.11 % WFPS in 2023 and 28.33 % WFPS in 2024 which are lower compared to the other sites, the emissions magnitude is even lower because of the soil disturbance by agricultural activities. In fact, similar practices are undertaken at the rice fields, yet higher emissions are observed. The rice fields is in a lowland area where overland flow is delayed after intense rainfall which causes longer soil moisture period. This landscape characteristics is one of the reasons why soil moisture induced emissions is higher at the rice fields even with 56.7% lower rainfall (approximately 380 mm during the 2024 campaign).

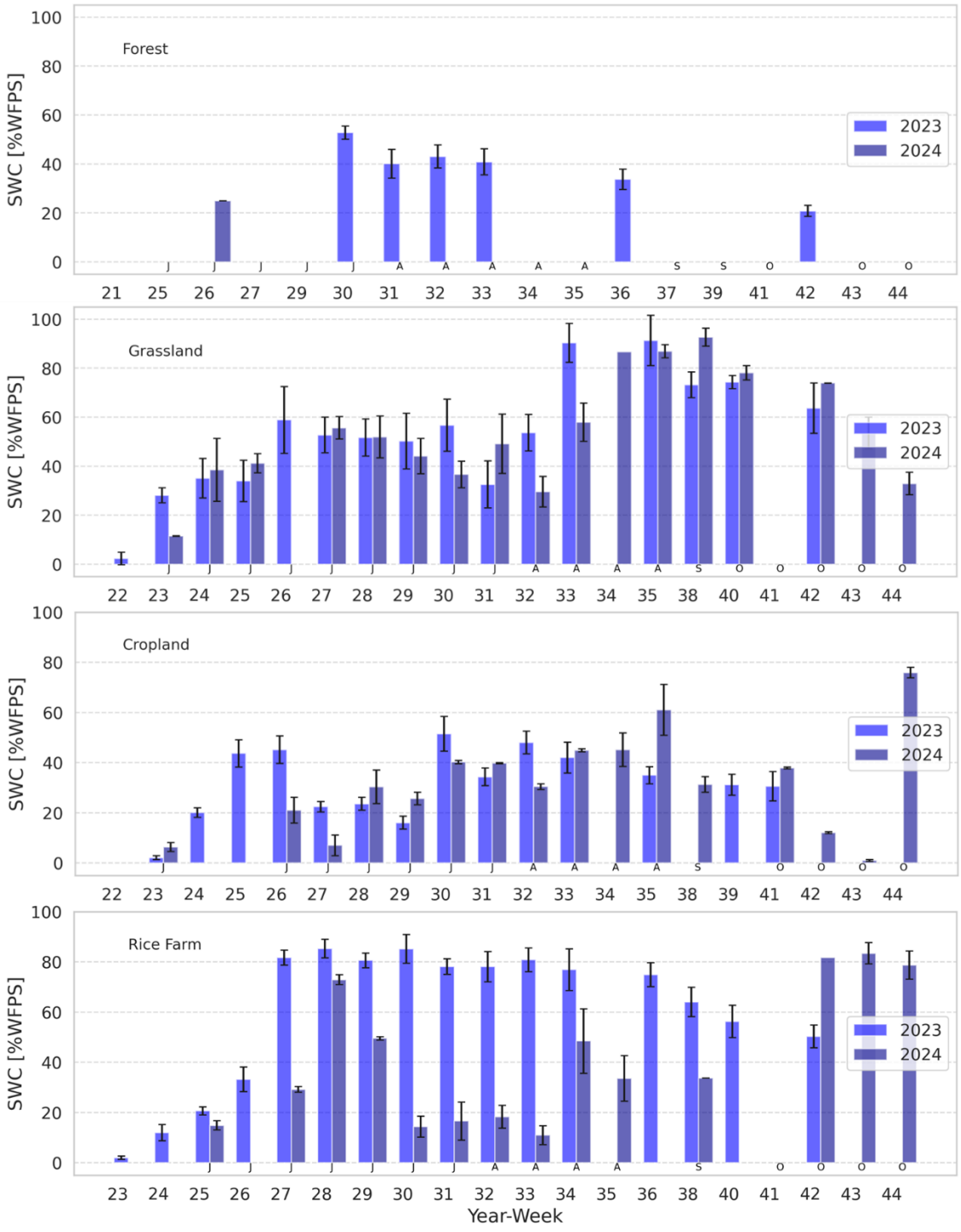

Figure 4.45: Manually measured soil volumetric water content of the four sites for the two years. The soil moisture data were not fully collected noticeably at the forest site.

4.6.4 Evaluation of environmental drivers of the fluxes

The Pearson correlation coefficient of the soil water content and temperature are -0.85, -0.56, -0.59, and -0.38 respectively for the forest, grassland, cropland, and rice fields. The stepwise multi-linear regression indicates an overall performance of 0.58 ($p<0.001$) at the grassland site (see Table 4.15). The soil temperature and water content explain the CH_4 flux by respectively 37% and 13%. Similar CH_4 flux dependence on soil moisture was demonstrated in South Sudanian savanna by Brümmer et *al.*, (2009). The two predictors have opposite effects on the flux, that is a unit increase in the soil water content increases the CH_4 flux by 0.41 μg C m^{-2} h^{-1} while decreases by -0.46 μg C m^{-2} h^{-1} for the soil temperature. The highest methane release occurred around 60% WFPS when the soil temperature ranges between 30 to 40°C. Higher soil temperature (>40°C) with relatively low soil water content leads to low CH_4 uptake or sink. Remarkably, high soil moisture (>60 %WFPS) with low temperature results in predominantly moderate methane release which was confirmed in past studies (Gütlein et *al.*, 2018; Brümmer et *al.*, 2009) at the grassland site. Moderate to low soil carbon content with positive soil moisture effect are major factors controlling the annual average methane release for the two years.

Although the temporal variability displays both CH_4 uptake and sink, the predictors explain overall CH_4 flux by 40% ($p<.005$) and have similar effects as mentioned above at the cropland site. That is, a unit increase of a predictor respectively increases CH_4 flux by 0.26 μg C m^{-2} h^{-1} for soil water content and decreases by -0.35 μg C m^{-2} h^{-1} for the temperature. The methane flux is explained by 0.21 ($p<0.005$) and 0.37 ($p<0.001$) respectively for soil water content and temperature. The predictors influence is less significant compared to the grassland which further confirms that emissions from perturbed soil disrupt the nitrification/denitrification process. Despite the moderate to low soil carbon content, the site displays methane sink for the two years (Table 3.7). Moderate temperature (30 to 40°C) leads to higher CH_4 flux compared to lower soil temperature whatever the range of the soil water content (Fig. 4.46).

At the rice fields site, the highest influence of soil water content occurred as the variability is explained by 42% with a unit increase inducing a CH_4 flux of 0.96 μg C m^{-2} h^{-1}. The soil temperature effect is negative with a decrease of -0.85 μg C m^{-2} h^{-1} and explains 18% ($p<0.005$) of the variability. The overall performance is moderate with a correlation coefficient of 0.5 ($p<0.001$).

Moderate to low soil carbon content combined with the aforementioned factors resulted in annual average CH_4 release of 19.10±4.7 and 22.5±5.9 (μg C m^{-2} h^{-1}) for the two years. Above 30% WFPS, low soil temperature leads to low uptake or release. Predominantly, in moderate temperature conditions, high soil water content leads to significantly high CH_4 release while lower soil moisture shows lower emission magnitude to sink.

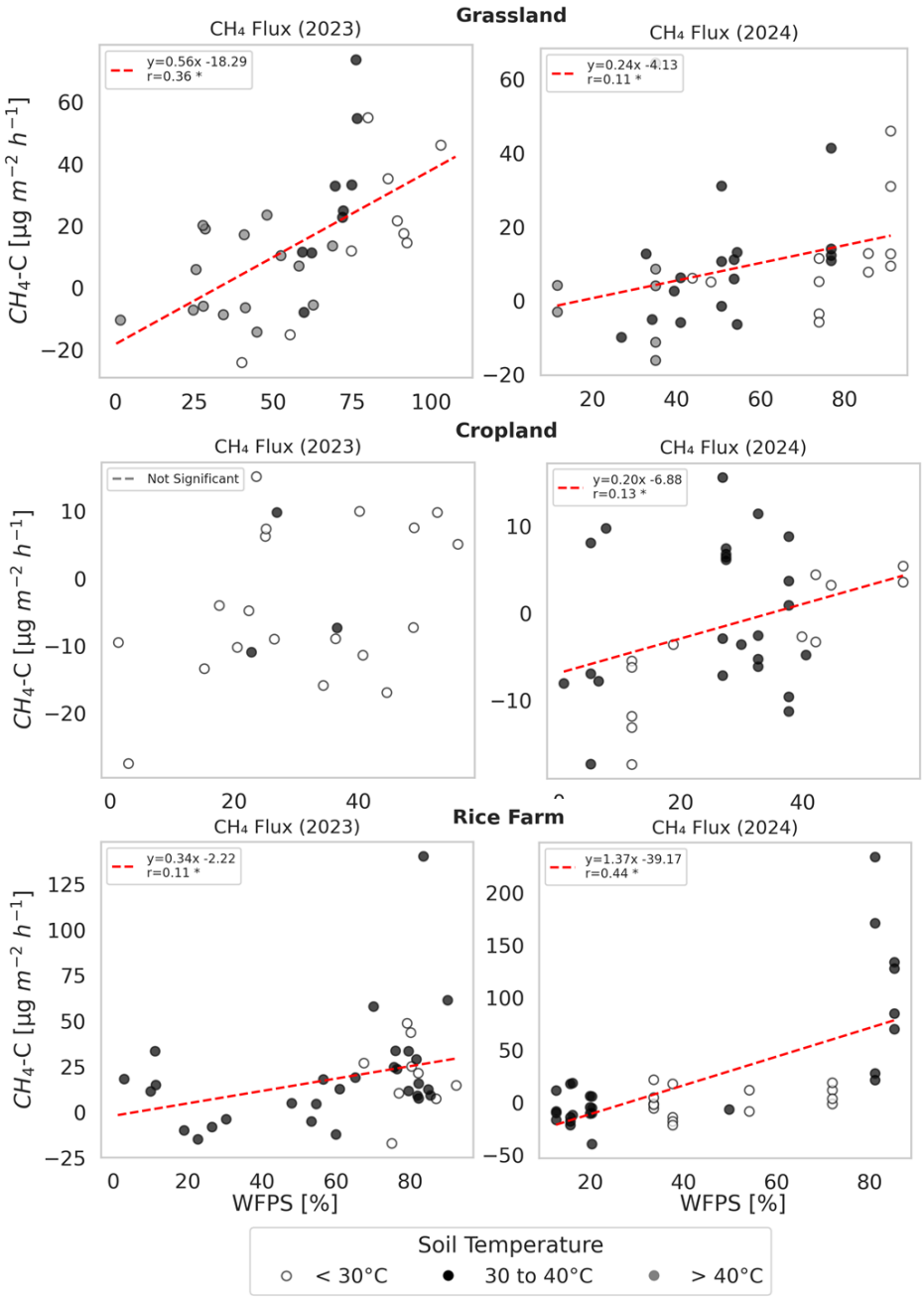

Figure 4.46: CH_4 response to soil moisture change (% WFPS) and temperature classified into three categories for 2023 and 2025. Linear regression is displayed in red if the relationship is significant with corresponding r value.

The performance of the stepwise multi-linear regression multi-linear is relatively low (0.13-0.28) for N_2O flux, whatever the land use. The soil water content and temperature have opposite effects on N_2O emissions. That is a unit increase of each predictor leads to -0.06 and -0.04 μg N m^{-2} h^{-1} decrease in N_2O flux, respectively for the cropland and rice fields. The soil temperature increases N_2O flux respectively by 0.13 and 0.2 μg N m^{-2} h^{-1}. Despite the low soil nitrogen content with less significant soil moisture and temperature effects on N_2O, the investigated sites altogether are N_2O sources (Table 3.7) with no significant difference in mean N_2O flux. There is no significant linear relationship between soil water content and N_2O emissions except at the rice fields site where higher soil water content and moderate soil temperature led to N_2O sink for the two years. Similar conditions associated with lower soil water content (<40% WFPS) result in N_2O release. Below 30°C, the N_2O flux is mitigated as both uptake and sink occur. However, the highest N_2O flux occurs between 40 and 60% WFPS at the rice fields site. Moderate soil temperature with low soil moisture (<30% WFPS) leads predominantly to N_2O release at the cropland site.

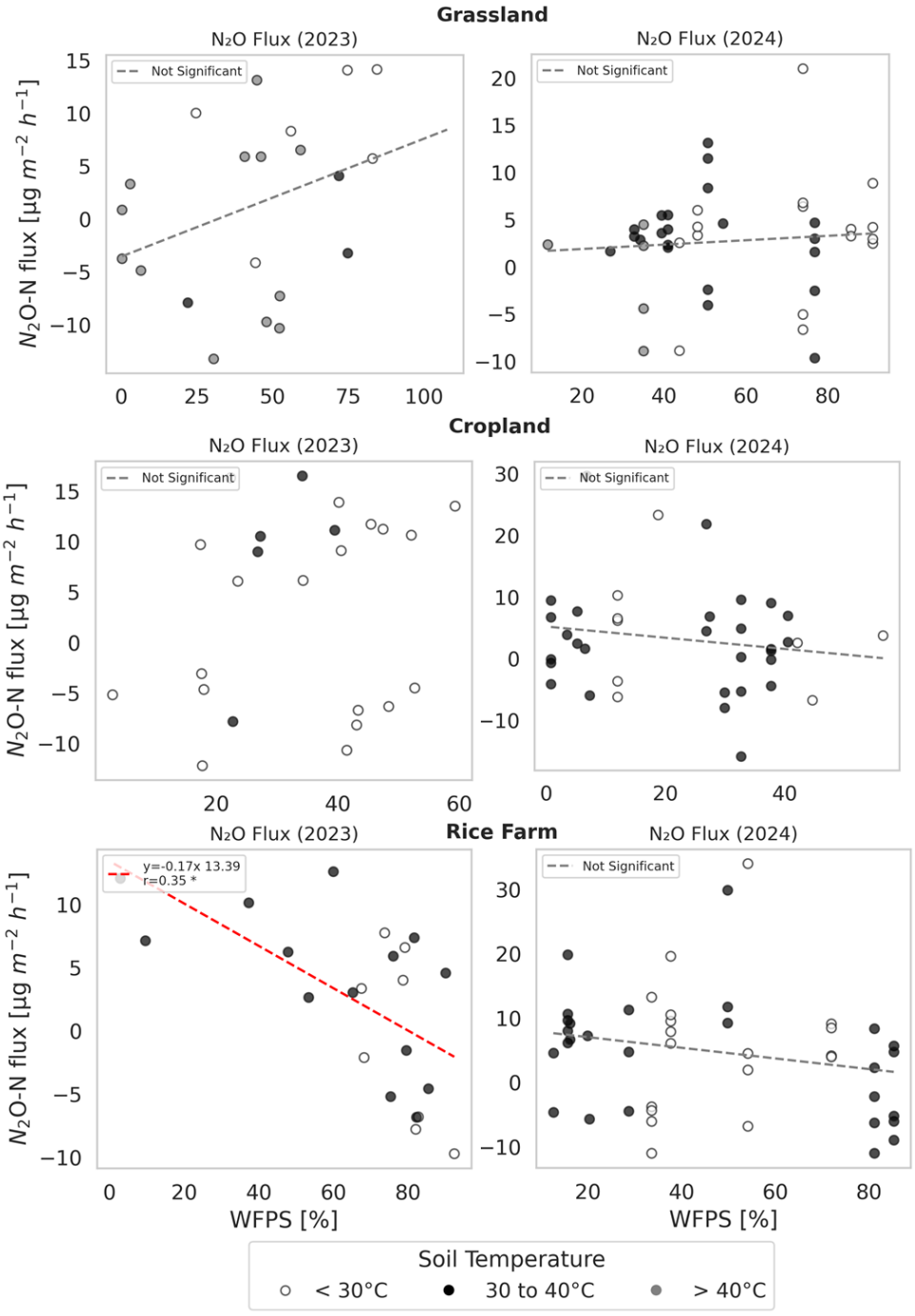

Figure 4.47: N_2O response to soil moisture change (% WFPS) and temperature classified into three categories for 2023 and 2025. Linear regression is displayed in red if the relationship is significant, with the corresponding r value.

This study investigated soil greenhouse gas emissions in the Sudanian savanna over two rainy seasons and updated the evidence about the drivers of the emissions in the region. The soil at the grassland site is a net source of methane whereas the managed cropland site behaves as a sink. Monthly variation of the emissions reveals that both uptake and release occur depending on soil water content in response to rainfall events. In a typical cleared savanna, it was demonstrated that the soil behaves as a net methane source (Zepp et *al.*, 1996; Sanhueza et *al.*, 1994; Poth et *al.*, 1995; Scharffe et *al.*, 1990; Hao et *al.*, 1988) which confirms the observed CH_4 release at the grassland site (14.44±9.6 and 10.13±3.5 µg C m^{-2} h^{-1}). Remarkably, the unperturbed soil of the Sudanian savanna displays significant methane release while the cultivated cropland indicates a net methane sink (-1.78±5.5 and -2.05±3.8 µg C m^{-2} h^{-1}) as reported by Brümmer et *al.*, (2009) in south Sudanian savanna of Burkina Faso. Castaldi et *al.* (2004) confirmed this evidence in an herbaceous savanna (7.2 µg C m^{-2} h^{-1}) and cultivated pasture (-1.5 µg C m^{-2} h^{-1}) of Orinoco (Venezuela) unlike Sanhueza and Donoso (2006) which reported the opposite in a tropical savanna respectively -12.6 and 16.2 µg C m^{-2} h^{-1}. The woodland savanna methane sink (-2.5 µg C m^{-2} h^{-1}) reported by Castaldi et *al.* (2004) corroborates our observation at the forest reserve (-0.52±5.5 and -11.48±3.6 µg C m^{-2} h^{-1}). An average methane sink rate of -40 to -12 µg C m^{-2} h^{-1} was reported in managed and natural savanna systems (Tathy et *al.*, 1992; Keller et *al.*, 1993; MacDonald et *al.*, 1998) which confirms both the observation at the cropland and forest reserve. Castaldi et *al.* (2006) ascertained the uncertainties related to the soil-atmosphere methane exchange in the tropical savanna which confirmed the relatively wide range. Significant methane release occurred at the rainfed rice fields (19.10±4.7 and 22.5±5.9 µg C m^{-2} h^{-1}) compared to the other sites for the two years. However, the CH_4 flux is significantly less than the reported values (0.2 to 99 mg C m^{-2} h^{-1}) for flooded rice fields (IPCC, 1996; Nikolaisen et *al.*, 2023; Lee et *al.*, 2023).

Almost two decades after Brümmer et *al.* (2008), this study investigated the N_2O emissions in the Sudanian savanna of West Africa focusing on four contrasted land use conditions (Forest reserve, Grassland, Cropland, and Rice fields). The need to update this kind of measurement has become crucial due to the increasing effect of climate change in the region. For the four sites the annual mean of N_2O emissions varies between 0.011±0.11 and 0.16±0.31 kg N ha^{-1} $season^{-1}$ which aligns with the range reported for a tropical savanna (0.06 to 1.46 kg N ha^{-1} yr^{-1}) by Dalal and Allen (2008), for Australian savannas (0.06–1.08 kg N ha^{-1} yr^{-1}) by Werner et *al.* (2014), and in near-natural and agricultural land of Burkina Faso (0.18 and 0.7 kg N ha^{-1} yr^{-1})

by Brümmer et *al.* (2008). Notwithstanding, the ongoing debate on the controlling factors, it is reported that either low rainfall or low nitrogen content or the combined effect narrows the N_2O release or sink (Andersson et *al.*, 2003; Castaldi et *al.*, 2006; Donoso et *al.*, 1993; Livesley et *al.*, 2011; Sanhueza et *al.*, 1990 in Werner et *al.* 2014). In high rainfall conditions, the suggestion that low soil nitrogen content limits N_2O emissions (Rosenkranz et *al.*, 2006) corroborates our findings. The nitrogen content at the grassland, cropland, and rice fields sites is low limiting the emissions.

Except for the forest reserve, a strong signal of N_2O emissions is observed during the rainfall onset in June (see Table 2). It was reported that in tropical systems the first rainfall events at the end of the dry season trigger N_2O emission peaks because of accumulated ammonium NH_4^+ and nitrate (NO_3^-) in the soil which was demonstrated by Calvo-Rodriguez et *al.* (2020), Castaldi et *al.* (2006), and Scholes et *al.* (1997) in Brümmer et *al.* (2008). This response to a sudden increase in soil moisture due to intense microbial activities after relatively long water-stress conditions (Ludwig et *al.* 2001) is also reported in the savanna woodlands of Zimbabwe (Rees and *al.* 2006). The soil nitrogen content at the grassland, cropland, and rice fields sites is relatively low (Fig. S2). Therefore, the nitrification and denitrification in the soils are limited by poor substrate availability which narrows the factors' evaluation in this study to the soil moisture and temperature.

The nitrogen isotopic ratio $\delta^{15}N$ of the soil profiles collected at the grassland, cropland, and rice fields indicates that they receive enriched animal manure with losses resulting from nitrification and denitrification processes leading to further enrichments of the soil $\delta^{15}N$ (Fig. S2). The values of the $\delta^{15}N$ ratio vary between 3.0 and 5.6 ‰ with an average of 4.1±0.5‰ at the cropland site, 1.9 and 5.2‰ with an average of 3.8±0.4‰ at the grassland site, and 2.0 and 6.0 ‰ with an average of 3.9±0.4‰ at the rice fields (Fig. S2). The investigations of Gerschlauer et *al.*, (2019) for the soil of the Mount Kilimanjaro range between 0 and 8‰ which corroborate our findings. Similar evidence is reported recently in a heterogeneous landscape of the Schwingbach catchment (Gachibu Wangari et *al.*, 2024). Though the profiles display similar nitrogen $\delta^{15}N$ ratios, the nitrogen content is relatively low for the three sites (Fig. S2). The average nitrogen content values are respectively 0.04±0.01%, 0.04±0.01%, and 0.05±0.01% for the grassland, cropland, and rice fields. This low level of nitrogen substrate availability is a major factor which justifies the consequent limited N_2O emissions.

Table 4.14: Stepwise multiple linear regression between in situ fluxes (CH_4 and N_2O), soil water content (% WFPS), and soil temperature (°C) for each land use.

	LCLU	Parameter	Coef.	Partial r^2	Adj. Partial r^2	p-Value	r^2	Adj. r^2	p-Value
CH_4	Forest	WFPS	-	-	-	-	-	-	-
		T_{soil}	-	-	-	-	-	-	-
	Grassland	WFPS	0.41	0.37	0.56	<.001	0.58	0.54	<.001
		T_{soil}	-0.46	0.13					
	Cropland	WFPS	0.26	0.21	0.37	<.005	0.4	0.34	<.005
		T_{soil}	-0.35	0.37		<.001			
	Rice fields	WFPS	0.96	0.42	0.48	<.001	0.5	0.47	<.001
		T_{soil}	-0.85	0.18		<.005			
N_2O	Forest	WFPS	-	-	-	-	-	-	-
		T_{soil}	-	-	-	-			
	Grassland	WFPS	0.06	0.04	0.24	-	0.28	0.21	<.005
		T_{soil}	0.00	0.00		-			
	Cropland	WFPS	-0.06	0.015	0.08	-	0.13	0.052	
		T_{soil}	0.13	0.07		-			
	Rice fields	WFPS	-0.04	0.023	0.24	-	0.27	0.22	<.005
		T_{soil}	0.2	0.16		<.005			

Chapter Five

5.0 Conclusion and Recommendations

This study assessed the impact of subsurface parameterization, idealized afforestation, subsurface geometry representation, end of century climate projections on water and energy fluxes of the Earth System in West Africa. Furthermore, it explores the greenhouse gas emissions in contrasting land use of the Sudanian savanna and their environmental drivers.

(1) It aimed to reduce uncertainties in simulating water and energy fluxes by employing three subsurface parameterization schemes (FD, TOPMODEL, and MMF) in the data-scarce region of West Africa using the WRF-Hydro model. The results demonstrate a high degree of agreement between simulations and observations, with key water fluxes (e.g., evapotranspiration) well reproduced. The MMF scheme showed clear advantages in capturing spatial heterogeneity, particularly in topographic convergence areas, where it outperformed the other schemes. Correlation coefficients for basin and domain-level evaluations using ESA CCI SM, GLEAM ET, and GLDAS ΔGWS yield relatively strong agreement, confirming the reliability of the models. The MMF scheme's improved representation of water fluxes indicate its potential for better modeling in areas with complex topography. At the domain level, soil moisture validation showed good performance with ESA CCI remote sensing products, with KGE values exceeding 0.8 for all schemes. Similarly, ET comparisons at the basin level revealed that while ET was underestimated in the savanna zone and overestimated in the Sahel zone, the annual seasonality was accurately captured, with an average correlation coefficient of 0.61. Domain-level validation using KGE, NSE, and RMSE metrics highlighted strong model performance in the evergreen forest in the southwest and areas above 9.5° latitude (Savanna and Sahel), but performance declined toward the southeast. Notably, the MMF scheme increased soil moisture and ET by approximately 20%, particularly in topographic convergence areas, while differences between TOPMODEL and FD were negligible. Although streamflow performance was average in this study, the findings suggest that model calibration for specific catchments combined with the MMF scheme could enhance streamflow predictions. These results underscore the value of improved groundwater parameterization in advancing land surface models, particularly in regions with limited data, and contribute to the broader effort to reduce uncertainties in water and energy flux simulations. It requires better hydro-meteorological monitoring networks for reliable early warning systems implementation using WRF-Hydro in the region.

(2) Likewise, the Great Green Wall (GGW) initiative for reducing drought and heatwaves in the Sahel region, this study explored the potential impact of Idealized Afforestation on water cycle and energy fluxes. The experiments setup is undertaken by virtually replacing degraded lands such as shrubland, bare soil, and grassland (SBG) in MODIS-IGBP land cover by the Evergreen Broadleaf Forest (EBF), Savanna (SAV), and Woody Savanna (WS) with the intent to mimic GGW initiative. It turns out that soil water content can be decreased by 0.5, 0.6, and 0.1 mm for EBF-VC, SAV-VC, and WS-VC in higher rainfall areas (Oueme). Meanwhile, except the negative effect in Sissili for SAV-VC, the afforestation experiments increased mean evapotranspiration whatever the climatic conditions. EBF-VC, SAV-VC and WS-VC increased mean LH by 4.9, 2.5, 2.8 W m^{-2} in Faga. The streamflow is decreased respectively by 24%, 18%, and 21% in Donga and 31%, 26%, and 28% in Oueme for EBF-VC, SAV-VC and WS-VC. The mean SH is increased by 20.6, 6.1, and 4.9 W m^{-2} respectively in Faga, Sissili, and Oueme basins.

(3) Accurately representing Earth system components is essential for better understanding water, energy, and greenhouse gas dynamics. This study specifically addresses uncertainties in DTB estimation to support the integration of groundwater into Land Surface Models (LSMs) across Africa. The PF-CLM model setup, based on the estimated DTB in the Nazinga Forest Reserve, demonstrates strong performance, reinforcing the validity of the methods presented. The model reliably captures water and energy fluxes, providing a solid foundation for exploring a wide range of hydrological processes. Notably, this setup implemented at a high spatial resolution is the first of its kind in the area and validates findings from earlier studies conducted at coarser scales. The DTB dataset generated here serves as a current and valuable resource for enhancing simulations of subsurface–land–atmosphere interactions. Furthermore, the study contributes fourteen new DTB mapping approaches, expanding the methodological toolkit available for such work. To further minimize uncertainties at the watershed bottom boundary, basin-scale DTB mapping—combining DTB occurrence likelihood with field-based measurements—is strongly recommended. However, in sedimentary and desert regions, caution is advised when using these computed maps due to geological conditions that differ significantly from those in hard rock environments. Ultimately, the ground-truth-based DTB maps produced in this study offer a reliable reference for future mapping efforts and represent a valuable input for groundwater-to-atmosphere modeling efforts across the African continent.

(4) The lineament permeability influence on water and energy fluxes is assessed by comparing High K, Moderate K and Low K experiments to a reference scenario without lineament

representation in Donga basin. The diurnal cycle of the energy components is most affected around noon. Moderate K and High K experiments increased significantly the energy balance closure (EBC) by 36.9 and 25.4% from September to November (SON). With Moderate K and Low K experiments, SH is increased by 1.1 and 1.5 W m^{-2} during the rainfall onset. The two experiments also increase the groundwater storage of the basin by 355.8 and 326.8 million m^3.

(5) The subsurface dynamics' response to different warming scenarios is evaluated with the projections from five Global Circulation Models (GCMs) namely GFDL-ESM4, HadGEM3-GC31-LL, IPSL-CM6A-LR, MIROC6, and NorESM2-MM under two different Shared Socioeconomic Pathways (SSP1-2.6, SSP5-8.5). In the basin, 3 out the 5 GCMs indicate an increase of groundwater storage (GWS) by 0.45 to 30.39 million m^3 under SSP1-2.6. The magnitude of the change expressed in centered Root Mean Squared Deviation (cRMSD) varies between 0.35 and 4.88 million m^3. Under the SSP5-8.5 projection, all the GCMs show a decrease of mean GWS except GFDL-ESM4. Overall, lower warming levels (SSP1-2.6) results in groundwater recharge increase however higher warming levels lead to subsurface water storage depletion especially in the critical zone. By the end of the century, surface water storage (SWS) decreases by -1876.35, -1333.37, -670.82, and -510.19 m^3 is projected for the basin respectively with NorESM2-MM, IPSL-CM6A-LR, MIROC6, and HadGEM3-GC31-LL.

(6) Investigating the differences in land-atmosphere GHG exchanges under contrasting land use is a major issue in data-scarce areas. This study focused on the greenhouse gas emissions of dominant land use types in the Sudanian savanna during the rainy season of two consecutive years (2023 and 2024). It is an update of the N_2O and CH_4 fluxes assessment in the sub-region after Brümmer et *al.* (2008) in both natural and managed ecosystems. Furthermore, the managed systems are still extensively used, thus differences to natural systems like forests are less pronounced as compared to more intensively used systems as shown recently by Wangari et *al.* (2024) and Guug et *al.* (2025). Key conclusions are:

(a) Methane release was significantly different between the four land use sites with the highest rate recorded in the rainfed rice fields (0.69±0.17 kg C ha^{-1} $season^{-1}$ and 0.82±0.22 kg C ha^{-1} $season^{-1}$). A unit increase in soil water content increased CH_4 flux by 0.96 µg C m^{-2} h^{-1} at the rice fields whereas a temperature increase decreased it by of -0.85 µg C m^{-2} h^{-1}.

(b) The forest reserve behaved as a methane sink (-0.019±0.2 kg C ha^{-1} $season^{-1}$ and -0.42±0.13 kg C ha^{-1} $season^{-1}$) while the grassland was a net source (0.53±0.35 kg C ha^{-1} $season^{-1}$

and 0.37±0.13 kg C ha^{-1} $season^{-1}$). Significant methane release occurred in response to changes of soil water content at the four sites during rainfall onset.

(c) Around 60% WFPS and moderate soil temperature (30 to 40°C), the highest methane release occurred at the grassland site. Notwithstanding, the monthly variability of methane flux is made of uptake and source, depending on soil moisture and temperature.

(d) Cultivated soil of the Sudanian savanna limits CH_4 flux for a net sink (-0.065±0.2 and -0.074±0.14 kg C ha^{-1} $season^{-1}$) unlike the grassland unperturbed soil. Likewise, the methane flux variability is most explained by soil water content (0.21 to 0.42).

(e) Soil water content and temperature have opposite effects on methane flux with the highest impact recorded at the rice fields. (6) Low soil nitrogen content is a major limitation to N_2O flux. Therefore, soil water content and soil temperature have marginal effects on N_2O flux.

(f) No significant difference in N_2O emissions was observed between the different land use types and both years.

Future studies should focus on the evaluation of the sensitivity of the atmospheric boundary layer (ABL) in a fully coupled model over West Africa. The sensitivity of the wetland emissions under water table dynamics should also be assessed.

5.1 Limitations of the study

The validation of the model simulations was limited by spatial disparities in field measurement. Further model spin up is required to improve the results. Data scarcity in West Africa is a general issue that this study suffered from and it finally defined the very structure of the work.

The subsurface representation schemes used in objective 1 despite the improvement compared to the default free drainage scheme need further improvement because of its inability to accurately capture the water table seasonality at local scale. The model calibration strategy using regionalized parameter (e.g., REFKDT) is innovative and should be applied for other hydrological parameters like SLOPE. The idealized afforestation experiments assume a uniform restoration of the degraded lands. However, for ecosystems conservation and habitat preservation, the choice of suitable plant species is vital which is not currently achievable with WRF-Hydro

model. The evaluation of the groundwater-Atmosphere interactions using Parflow-CLM should be achieved for the entire region for reliable findings for instance on the contribution of the subsurface permeability to the energy balance closure. Further the climate projections impact on subsurface dynamics should be achieve at regional level. The chamber-based measurement of greenhouse gas fluxes employed this thesis is rare in the region and should be used for the validation of the existing satellite products and modelling outputs. Land cover degradation by anthropogenic activities is demonstrated to increase the methane emissions but has marginal effect on nitrous oxide in the Sudanian climate. Nevertheless, the remain factors such the soil carbon content should be investigated to ascertain the main drivers of the nitrous oxide fluxes.

5.2 Contribution to knowledge

Some of the key contributions to knowledge from this study are:

- Uncertainties in simulating water and energy fluxes are reduced by evaluating three subsurface parameterization schemes (FD, TOPMODEL, and MMF) in this data-scarce region.
- Likewise, the Great Green Wall (GGW) initiative for reducing drought and heatwaves in the Sahel region, this study explored the potential impact of Idealized Afforestation on the water cycle (e.g., water table) and energy fluxes.
- This study specifically addresses uncertainties in Depth-to-bedrock (DTB) estimation to support the integration of groundwater into Land Surface Models (LSMs) across Africa.
- The subsurface permeability (High K, Moderate K, and Low K experiments) most affects the diurnal cycle of the energy components around noon and increases the energy balance closure (EBC) in the Donga basin.
- The climate projections of five Global Circulation Models (GFDL-ESM4, HadGEM3-GC31-LL, IPSL-CM6A-LR, MIROC6, and NorESM2-MM) under two different Shared Socioeconomic Pathways (SSP1-2.6, SSP5-8.5) are used to assess the subsurface dynamics' sensitivity to extreme warming scenarios.
- This study focused on the greenhouse gas emissions (e.g., CH_4, N_2O) of dominant land use types in the Sudanian savanna during the rainy season of two consecutive years (2023 and 2024).

- Update of the N_2O and CH_4 fluxes assessment in the Sudanian sub-region after Brümmer et *al.* (2008) in both natural and managed ecosystems using chamber-based approach.

REFERENCES

African Union (AU). (2015). Agenda 2063: The Africa We Want. https://au.int/en/agenda2063/overview

African Union Commission. (2020). First continental report on the implementation of Agenda 2063. https://amert.au.int/en/documents/20200208/first-continental-report-implementation-agenda-2063

Allé, I.C., 2019. Évaluation de L'implantation Géophysique des Forages D'eau en Zone de Socle en Milieu Tropical (Bénin, Afrique de l'Ouest): Apport de la Tomographie de Résistivité électrique Pour la Caractérisation de la Cible Hydrogéologique. Thèse 3ème cycle. Université d'Abomey-Calavi, Bénin.

AMMA-ISSC, 2005. The international science plan for AMMA. pp. 103. http://amma-international.org/library/docs/AMMA_ISP_May2005.pdf

Alam, S.; Gebremichael, M.; Li, R.; Dozier, J.; Lettenmaier, D.P. Climate Change Impacts on Groundwater Storage in the Central Valley, California. Clim. Chang. 2019, 157, 387–406. https://doi.org/10.1007/s10584-019-02585-5

Atchley, A. L., & Maxwell, R. M. (2011). Influences of subsurface heterogeneity and vegetation cover on soil moisture, surface temperature and evapotranspiration at hillslope scales. Hydrogeology Journal, 19(2), 289–305. https://doi.org/10.1007/s10040-010-0690-1

Aubinet, M., Vesala, T., Papale, D. (Eds.), 2012. Eddy Covariance: A Practical Guide to Measurement and Data Analysis. Springer, Dordrecht.

Aryee, J. N. A., Afrifa, F. O. T., Agyapong, K.-H., Gyau Frimpong, N. A., Quagraine, K. T., & Davies, P. (2024). Quantifying climatic heavy-precipitation-induced floods in West Africa using multiple precipitation indices. *Scientific African*, *25*, e02309. https://doi.org/10.1016/j.sciaf.2024.e02309

Baldocchi, D., Falge, E., Gu, L., Olson, R., Hollinger, D., Running, S., Anthoni, P., Bernhofer, C., Davis, K., Evans, R., Fuentes, J., Goldstein, A., Katul, G., Law, B., Lee, X., Malhi, Y., Meyers, T., Munger, W., Oechel, W., Paw, K. T., Pilegaard, K., Schmid, H. P., Valentini, R., Verma, S., Vesala, T., Wilson, K., Wofsy, S., 2001. FLUXNET: A New Tool to Study the Temporal and Spatial Variability of Ecosystem–Scale Carbon Dioxide, Water Vapor, and Energy Flux Densities. Bulletin of the American Meteorological Society 11, 2415–2434.

Balogun, A.A., Jegede O.O., Foken T., Olaleye J.O., 2002a. Estimation of sensible and latent heat fluxes over bare soil using bowen ratio energy balance method at a humid tropical site. J African Meteorol Soc 5, 63–71.

Balogun, A.A., Jegede O.O., Foken T., Olaleye J.O., 2002b. Comparison of two Bowen-ratio methods for the estimation of sensible and latent heat fluxes at Ile-Ife. J African Meteorol Soc 5, 63–69.

Benettin, P., Soulsby, C., Birkel, C., Tetzlaff, D., Botter, G., & Rinaldo, A. (2017). Using SAS functions and high-resolution isotope data to unravel travel time distributions in headwater catchments: TRAVEL TIME DISTRIBUTIONS AND SOLUTE DYNAMICS. *Water Resources Research*, *53*(3), 1864–1878. https://doi.org/10.1002/2016WR020117

Berger, S., Bliefernicht, J., Linstädter, A., Canak, K., Guug, S., Heinzeller, D., Hingerl, L., Mauder, M., Neidl, F., Quansah, E., Salack, S., Steinbrecher, R., & Kunstmann, H. (2019). The impact of rain events on CO2 emissions from contrasting land use systems in semi-arid West African savannas. *Science of The Total Environment*, *647*, 1478–1489. https://doi.org/10.1016/j.scitotenv.2018.07.397

Beven, K. J. (1982), Macropores and water flow in soils, Water Resour. Res., 18, 1311 – 1325.

Biancamaria, S., Mballo, M., Le Moigne, P., Sánchez Pérez, J. M., Espitalier-Noël, G., Grusson, Y., Cakir, R., Häfliger, V., Barathieu, F., Trasmonte, M., Boone, A., Martin, E., & Sauvage, S. (2019). Total water storage variability from GRACE mission and hydrological models for a 50,000 km2 temperate watershed: The Garonne River basin (France). *Journal of Hydrology: Regional Studies*, *24*, 100609. https://doi.org/10.1016/j.ejrh.2019.100609

Bijak, J., & Hilton, J. (2022). Uncertainty Quantification, Model Calibration, and Sensitivity. In J. Bijak, Towards Bayesian Model-Based Demography (Vol. 17, pp. 71–92). Springer International Publishing. https://doi.org/10.1007/978-3-030-83039-7_5

Bliefernicht, J., Salack, S., Waongo, M., Annor, T., Laux, P., & Kunstmann, H. (2022). Towards a historical precipitation database for West Africa: Overview, quality control and harmonization. https://doi.org/10.5445/IR/1000141900

Bliefernicht, J., Berger, S., Salack, S., Guug, S., Hingerl, L., Heinzeller, D., Mauder, M., Steinbrecher, R., Steup, G., Bossa, A. Y., Waongo, M., Quansah, E., Balogun, A. A., Yira, Y., Arnault, J., Wagner, S., Klein, C., Gessner, U., Knauer, K., … Kunstmann, H. (2018). The

WASCAL Hydrometeorological Observatory in the Sudan Savanna of Burkina Faso and Ghana. *Vadose Zone Journal*, *17*(1), Article 1. https://doi.org/10.2136/vzj2018.03.0065

Bliefernicht, J., Kunstmann, H., Hingerl, L., & Rummler, T. (2013). *Field and simulation experiments for investigating regional land–atmosphere interactions in West Africa: Experimental set-up and first results*.

Blöschl, G., A.P. Blaschke, M. Broer, C. Bucher, G. Carr, X. Chen, and P. Haas. 2016. The Hydrological Open Air Laboratory (HOAL) in Petzenkirchen: A hypothesis-driven observatory. Hydrol. Earth Syst. Sci. 20:227–255. doi:10.5194/hess-20-227-2016

Bobba, A., Singh, V., Berndtsson, R. & Bengtsson, L. (2000) Numerical simulation of saltwater intrusion into Laccadive Island aquifers due to climate change. J. Geol. Soc. India 55, 589–612

Börker, J., Hartmann, J., Amann, T., & Romero-Mujalli, G. (2018). Terrestrial Sediments of the Earth: Development of a Global Unconsolidated Sediments Map Database (GUM): TERRESTRIAL SEDIMENTS OF THE EARTH. *Geochemistry, Geophysics, Geosystems*, *19*(4), 997–1024. https://doi.org/10.1002/2017GC007273

Bowen, I. S., 1926. The Ratio of Heat Losses by Conduction and by Evaporation from any Water Surface. Physical Review 6, 779–787.

Boysen, L. R., Brovkin, V., Arora, V. K., Cadule, P., de Noblet-Ducoudré, N., Kato, E., Pongratz, J., & Gayler, V. (2014). Global and regional effects of land-use change on climate in 21st century simulations with interactive carbon cycle. *Earth System Dynamics*, *5*(2), 309–319. https://doi.org/10.5194/esd-5-309-2014

Brovkin, V., Boysen, L., Arora, V. K., Boisier, J. P., Cadule, P., Chini, L., Claussen, M., Friedlingstein, P., Gayler, V., van den Hurk, B. J. J. M., Hurtt, G. C., Jones, C. D., Kato, E., de Noblet-Ducoudré, N., Pacifico, F., Pongratz, J., & Weiss, M. (2013). Effect of Anthropogenic Land-Use and Land-Cover Changes on Climate and Land Carbon Storage in CMIP5 Projections for the Twenty-First Century. *Journal of Climate*, *26*(18), 6859–6881. https://doi.org/10.1175/JCLI-D-12-00623.1

Brümmer, C., Papen, H., Wassmann, R., Brüggemann, N., 2009. Fluxes of CH 4 and CO 2 from soil and termite mounds in south Sudanian savanna of Burkina Faso (West Africa). Global Biogeochemical Cycles 1, n/a-n/a.

Burakowski, E., Tawfik, A., Ouimette, A., Lepine, L., Novick, K., Ollinger, S., Zarzycki, C., Bonan, G., 2018. The role of surface roughness, albedo, and Bowen ratio on ecosystem energy balance in the Eastern United States. Agricultural and Forest Meteorology, 367–376.

Barlow, P.M.; Moench, A.F. WTAQ: A Computer Program for Calculating Drawdowns and Estimating Hydraulic Properties for Confined and Water-Table Aquifers; 99-4225; U.S. Geological Survey: Northborough, MA, USA, 1999.

Benbarka, A.M.; Davis, D.R. Aspects of Aquifer Test Error Analysis; Arizona-Nevada Academy of Science: Glendale, AZ, USA, 1981.

Buendia, E., Tanabe, K., Kranjc, A., Baasansuren, J., Fukuda, M., Ngarize, S., Osako, A., Pyrozhenko, Y., Shermanau, P., Federici, S., 2019. Refinement to the 2006 IPCC Guidelines for National Greenhouse Gas Inventories. IPCC, Geneva, Switzerland. https://refhub.elsevier.com/S0167-8809(21)00429-1/sbref4

Brümmer, C., Brüggemann, N., Butterbach-Bahl, K., Falk, U., Szarzynski, J., Vielhauer, K., Wassmann, R., & Papen, H. (2008). Soil-Atmosphere Exchange of N2O and NO in Near-Natural Savanna and Agricultural Land in Burkina Faso (W. Africa). *Ecosystems*, *11*(4), 582–600. https://doi.org/10.1007/s10021-008-9144-1

Butterbach-Bahl, K., Baggs, E. M., Dannenmann, M., Kiese, R., and Zechmeister-Boltenstern, S.: Nitrous oxide emissions from soils: how well do we understand the processes and their controls? Philos. T. R. Soc. B, 368, 20130122, doi:10.1098/rstb.2013.0122, 2013.

Brummer C., H. Papen, R. Wassmann, and N. Bruggemann, “Fluxes of CH4 and CO2 from soil and termite mounds in south Sudanian savanna of Burkina Faso (West Africa),” Global Biogeochemical Cycles, vol.23, no.1, ArticleIDGB1001,2009.

Best, M. J., Pryor, M., Clark, D. B., Rooney, G. G., Essery, R. L. H., Ménard, C. B., et al. (2011). The Joint UK Land Environment Simulator (JULES), model description part 1: Energy and water fluxes. Geoscientific Model Development, 4(3), 677–699. https://doi.org/10.5194/gmd-4-677-2011

Burke, E. J., Chadburn, S. E., & Ekici, A. (2017). A vertical representation of soil carbon in the JULES land surface scheme (vn4. 3_permafrost) with a focus on permafrost regions. Geoscientific Model Development, 10(2), 959–975.

Carlson KM, Gerber JS, Mueller ND, Herrero M, MacDonald GK, Brauman KA, et al. Greenhouse gas emissions intensity of global croplands. Nat Clim Chang. 2016;7(1):63–8. https://doi.org/10.1038/nclimate3158

Ceperley, N. C., Mande, T., van de Giesen, N., Tyler, S., Yacouba, H., Parlange, M. B., 2017. Evaporation from cultivated and semi-wild Sudanian Savanna in west Africa. Hydrology and Earth System Sciences 8, 4149–4167.

Chang, S. W., Memari, S. S., & Clement, T. P. (2021). PyTheis—A Python Tool for Analyzing Pump Test Data. *Water*, *13*(16), 2180. https://doi.org/10.3390/w13162180

Chen, S., Chen, J., Lin, G., Zhang, W., Miao, H., Wei, L., Huang, J., Han, X., 2009. Energy balance and partition in Inner Mongolia steppe ecosystems with different land use types. Agricultural and Forest Meteorology 11, 1800–1809.

Chen, J., and P. Kumar (2001), Topographic influence on the seasonal and inter-annual variation of water and energy balance of basins in North America, J. Clim., 14, 1989 – 2014.

Ciais P, Bombelli A, Williams M, Piao SL, Chave J, Ryan CM, et al. The carbon balance of Africa: synthesis of recent research studies. Phil Trans R Soc. 2011; A369:1–20.

Cohard, J. M., Depeyre, A., Hector, B., Pellarin, T., & Maxwell, R. M. (2019). *Evaluation of global soil products to simulate hydrological water paths in the West-African critical zone. 2019*, H51H-1589.

Camporese, M., Paniconi, C., Putti, M., & Orlandini, S. (2010). Surface-subsurface flow modeling with path-based runoff routing, boundary condition-based coupling, and assimilation of multisource observation data: SURFACE-SUBSURFACE FLOW MODELING. *Water Resources Research*, *46*(2). https://doi.org/10.1029/2008WR007536

Condon, L. E., Kollet, S., Bierkens, M. F. P., Fogg, G. E., Maxwell, R. M., Hill, M. C., Fransen, H. H., Verhoef, A., Van Loon, A. F., Sulis, M., & Abesser, C. (2021). Global Groundwater Modeling and Monitoring: Opportunities and Challenges. *Water Resources Research*, *57*(12). https://doi.org/10.1029/2020WR029500

Condon, L. E., Markovich, K. H., Kelleher, C. A., McDonnell, J. J., Ferguson, G., & McIntosh, J. C. (2020). Where Is the Bottom of a Watershed? Water Resour. Res., 56(3). https://doi.org/10.1029/2019WR026010

Cook, P. A., Black, E. C. L., Verhoef, A., Macdonald, D. M. J., & Sorensen, J. P. R. (2022). Projected increases in potential groundwater recharge and reduced evapotranspiration under

future climate conditions in West Africa. *Journal of Hydrology: Regional Studies*, *41*, 101076. https://doi.org/10.1016/j.ejrh.2022.101076

Cosby, B. J., G. M. Hornberger, R. B. Clapp, and T. R. Ginn (1984), A statistical exploration of the relationships of soil moisture characteristics to the physical properties of soils, Water Resour. Res., 20, 682 – 690.

Cox, P. M., Betts, R. A., Jones, C. D., Spall, S. A., & Totterdell, I. J. (2000). Acceleration of global warming due to carbon-cycle feedbacks in a coupled climate model. *Nature*, *408*(6809), 184–187. https://doi.org/10.1038/35041539

Chen, J., and P. Kumar (2001), Topographic influence on the seasonal and inter-annual variation of water and energy balance of basins in North America, J. Clim., 14, 1989 – 2014.

Cosby, B. J., G. M. Hornberger, R. B. Clapp, and T. R. Ginn (1984), A statistical exploration of the relationships of soil moisture characteristics to the physical properties of soils, Water Resour. Res., 20, 682 – 690.

Cerbelaud, A., Lefèvre, J., Genthon, P., & Menkes, C. (2022). Assessment of the WRF-Hydro uncoupled hydro-meteorological model on flashy watersheds of the Grande Terre tropical island of New Caledonia (South-West Pacific). *Journal of Hydrology: Regional Studies*, *40*, 101003. https://doi.org/10.1016/j.ejrh.2022.101003

Clark, D. B., Mercado, L. M., Sitch, S., Jones, C. D., Gedney, N., Best, M. J., Pryor, M., Rooney, G. G., Essery, R. L. H., Blyth, E., Boucher, O., Harding, R. J., Huntingford, C., & Cox, P. M. (2011). The Joint UK Land Environment Simulator (JULES), model description – Part 2: Carbon fluxes and vegetation dynamics. *Geoscientific Model Development*, *4*(3), 701–722. https://doi.org/10.5194/gmd-4-701-2011

Chadburn, S. E., Aalto, T., Aurela, M., Baldocchi, D., Biasi, C., Boike, J., Burke, E. J., Comyn-Platt, E., Dolman, A. J., Duran-Rojas, C., Fan, Y., Friborg, T., Gao, Y., Gedney, N., Göckede, M., Hayman, G. D., Holl, D., Hugelius, G., Kutzbach, L., … Westermann, S. (2020). Modeled Microbial Dynamics Explain the Apparent Temperature Sensitivity of Wetland Methane Emissions. *Global Biogeochemical Cycles*, *34*(11). https://doi.org/10.1029/2020gb006678

Comyn-Platt, E., Hayman, G., Huntingford, C., Chadburn, S. E., Burke, E. J., Harper, A. B., et al. (2018). Carbon budgets for 1.5 and 2 c targets lowered by natural wetland and permafrost feedbacks. Nature Geoscience, 11(8), 568.

Christy, P. M., Gopinath, L. R., & Divya, D. (2014). A review on anaerobic decomposition and enhancement of biogas production through enzymes and microorganisms. Renewable and Sustainable Energy Reviews, 34, 167–173.

Cui, S., Liu, P., Guo, H., Nielsen, C. K., Pullens, J. W. M., Chen, Q., Pugliese, L., & Wu, S. (2024). Wetland hydrological dynamics and methane emissions. *Communications Earth & Environment*, *5*(1), 470. https://doi.org/10.1038/s43247-024-01635-w

Dragoni, D., Goulden, M. L., Gu, L., Katul, G. G., Pallardy, S. G., Paw U, K. T., Schmid, H. P., Stoy, P. C., Suyker, A. E., Verma, S. B., 2010. Albedo estimates for land surface models and support for a new paradigm based on foliage nitrogen concentration. Global Change Biology 2, 696–710.

de Graaf, I. E. M., Sutanudjaja, E. H., van Beek, L. P. H., & Bierkens, M. F. P. (2015). A high-resolution global-scale groundwater model. *Hydrology and Earth System Sciences*, *19*(2), 823–837. https://doi.org/10.5194/hess-19-823-2015

de Graaf, I. E. M., van Beek, R. L. P. H., Gleeson, T., Moosdorf, N., Schmitz, O., Sutanudjaja, E. H., & Bierkens, M. F. P. (2017). A global-scale two-layer transient groundwater model: Development and application to groundwater depletion. *Advances in Water Resources*, *102*, 53–67. https://doi.org/10.1016/j.advwatres.2017.01.011

de Graaf, I. E. M., Gleeson, T., (Rens) van Beek, L. P. H., Sutanudjaja, E. H., & Bierkens, M. F. P. (2019). Environmental flow limits to global groundwater pumping. *Nature*, *574*(7776), 90–94. https://doi.org/10.1038/s41586-019-1594-4

de Graaf, I., Condon, L., & Maxwell, R. (2020). Hyper-Resolution Continental-Scale 3-D Aquifer Parameterization for Groundwater Modeling. *Water Resources Research*, *56*(5). https://doi.org/10.1029/2019WR026004

de Graaf, I. E. M., & Stahl, K. (2022). A model comparison assessing the importance of lateral groundwater flows at the global scale. *Environ. Res. Lett.*, *17*(4), Article 4. https://doi.org/10.1088/1748-9326/ac50d2

Döll, P., Douville, H., Güntner, A., Müller Schmied, H., & Wada, Y. (2016). Modelling Freshwater Resources at the Global Scale: Challenges and Prospects. *Surveys in Geophysics*, *37*(2), 195–221. https://doi.org/10.1007/s10712-015-9343-1

Dolman, A. J., Gash, J.H.C., Goutorbe, J.-P., Kerr, Y., Lebel, T., Prince, S. D., Stricker, J.N.M., 1997. The role of the land surface in Sahelian climate: HAPEX-Sahel results and future research needs. Journal of Hydrology, 1067–1079.

Dalla Torre, D., Di Marco, N., Menapace, A., Avesani, D., Righetti, M., & Majone, B. (2024). Suitability of ERA5-Land reanalysis dataset for hydrological modelling in the Alpine region. *Journal of Hydrology: Regional Studies*, *52*, 101718. https://doi.org/10.1016/j.ejrh.2024.101718

Draeger, C., Radic, V., White, R. H., & Tessema, M. A. (2023). *Evaluation of ERA5 and Dynamical Downscaling for Surface Energy Balance Modeling at Mountain Glaciers in Western Canada*. https://doi.org/10.21203/rs.3.rs-2663083/v2

Dudhia, J. Numerical study of convection observed during the winter monsoon experiment using a mesoscale two-dimensional model. J. Atmos. Sci. 1989, 46, 3077–3107. [Google Scholar] https://doi.org/10.1175/1520-0469(1989)046%3C3077:NSOCOD%3E2.0.CO;2

Friedl, M.A.; McIver, D.K.; Hodges, J.C.F.; Zhang, X.Y.; Muchoney, D.; Strahler, A.H.; Woodcock, C.E.; Gopal, S.; Schneider, A.; Cooper, A.; et al. Global land cover mapping from MODIS: Algorithms and early results. Remote Sens. Environ. 2002, 83, 287–302. https://doi.org/10.1016/S0034-4257(02)00078-0

Fu, Z., Ciais, P., Wigneron, J.-P., Gentine, P., Feldman, A. F., Makowski, D., Viovy, N., Kemanian, A. R., Goll, D. S., Stoy, P. C., Prentice, I. C., Yakir, D., Liu, L., Ma, H., Li, X., Huang, Y., Yu, K., Zhu, P., Li, X., … Smith, W. K. (2024). Global critical soil moisture thresholds of plant water stress. Nature Communications, 15(1). https://doi.org/10.1038/s41467-024-49244-7

Entekhabi, D., and P. S. Eagleson (1989), Land surface hydrology parameterization for atmospheric general circulation models including subgrid-scale spatial variability, J. Clim., 2, 816 – 831.

Eini, M. R., Massari, C., & Piniewski, M. (2023). Satellite-based soil moisture enhances the reliability of agro-hydrological modeling in large transboundary river basins. *Science of The Total Environment*, *873*, 162396. https://doi.org/10.1016/j.scitotenv.2023.162396

Erler, A. R., Frey, S. K., Khader, O., d'Orgeville, M., Park, Y., Hwang, H., Lapen, D. R., Richard Peltier, W., & Sudicky, E. A. (2019). Simulating Climate Change Impacts on Surface Water Resources Within a Lake-Affected Region Using Regional Climate Projections. Water Resources Research, 55(1), 130-155. https://doi.org/10.1029/2018WR024381

Ezzahar, J., Chehbouni, A., Hoedjes, J., Ramier, D., Boulain, N., Boubkraoui, S., Cappelaere, B., Descroix, L., Mougenot, B., Timouk, F., 2009. Combining scintillometer measurements and an aggregation scheme to estimate area-averaged latent heat flux during the AMMA experiment. Journal of Hydrology 1-2, 217–226.

Fan, Y., Miguez-Macho, G., Weaver, C. P., Walko, R., & Robock, A. (2007). Incorporating water table dynamics in climate modeling : 1. Water table observations and equilibrium water table simulations: WATER TABLE OBSERVATIONS. J. Geophys. Res., 112(D10). https://doi.org/10.1029/2006JD008111

Federal Ministry of Education and Research of Germany (BMBF), 2005. GLOWA – Global Change and the Hydrological Cycle. Editors: Schönlau, J., Alma van der Veen, R.-N., Boon, Berlin.

Fisher, R. A., & Koven, C. D. (2020). Perspectives on the Future of Land Surface Models and the Challenges of Representing Complex Terrestrial Systems. *Journal of Advances in Modeling Earth Systems*, *12*(4). https://doi.org/10.1029/2018MS001453

Finkelstein, P. L., Sims, P. F., 2001. Sampling error in eddy correlation flux measurements. Journal of Geophysical Research: Atmospheres D4, 3503–3509.

Finnigan, J. J., 2004. A Re-Evaluation of Long-Term Flux Measurement Techniques Part II: Coordinate Systems. Boundary-Layer Meteorology 1, 1–41.

Foken, T., 2006. Angewandte Meteorologie – Mikrometeorologische Methoden. Springer, Berlin Heidelberg. Foken, T., Wimmer, F., Mauder, M., Thomas, C., & Liebethal, C. (2006). *Some aspects of the energy balance closure problem*. https://doi.org/10.5194/acpd-6-3381-2006

Foken, T., 2008. The energy balance closure problem: an overview. Ecological Applications 6, 1351–1367.

Foken, T., Aubinet, M., Finnigan, J. J., Leclerc, M. Y., Mauder, M., Paw U, K. T., 2011. Results Of A Panel Discussion About The Energy Balance Closure Correction For Trace Gases. Bulletin of the American Meteorological Society 4, ES13-ES18.

Foken, T., Leuning, R., Oncley, S.P., Mauder, M., Aubinet, M., 2012. In: Aubinet, M., Vesala, T., Papale, D. (Eds.), Eddy Covariance: A Practical Guide to Measurement and Data Analysis. Springer, Dordrecht, pp. 85–132.

Forster, P., T. Storelvmo, K. Armour, W. Collins, J.-L. Dufresne, D. Frame, D.J. Lunt, T. Mauritsen, M.D. Palmer, M. Watanabe, M. Wild, and H. Zhang, 2021: The Earth's Energy Budget, Climate Feedbacks, and Climate Sensitivity. In Climate Change 2021: The Physical

Science Basis. Contribution of Working Group I to the Sixth Assessment Report of the Intergovernmental Panel on Climate Change [Masson-Delmotte, V., P. Zhai, A. Pirani, S.L. Connors, C. Pean, S. Berger, N. Caud, Y. Chen, L. Goldfarb, M.I. Gomis, M. Huang, K. Leitzell, E. Lonnoy, J.B.R. Matthews, T.K. Maycock, T. Waterfield, O. Yelekci, R. Yu, and B. Zhou (eds.)]. Cambridge University Press, Cambridge, United Kingdom and New York, NY, USA, pp. 923–1054, doi:10.1017/9781009157896.009

Friedl, M.A.; McIver, D.K.; Hodges, J.C.F.; Zhang, X.Y.; Muchoney, D.; Strahler, A.H.; Woodcock, C.E.; Gopal, S.; Schneider, A.; Cooper, A.; et al. Global land cover mapping from MODIS: Algorithms and early results. Remote Sens. Environ. 2002, 83, 287–302. https://doi.org/10.1016/S0034-4257(02)00078-0

Friedlingstein P, O'Sullivan M, Jones MW, Andrew RM, Hauck J, Olsen A, et al. Global Carbon Budget 2020. Earth Sys Sci Data. 2020;12(4):3269–340. https://doi.org/10.5194/essd-12-3269-2020

Fu, Z., Ciais, P., Feldman, A. F., Gentine, P., Makowski, D., Prentice, I. C., Stoy, P. C., Bastos, A., & Wigneron, J.-P. (2022). Critical soil moisture thresholds of plant water stress in terrestrial ecosystems. Science Advances, 8(44), eabq7827. https://doi.org/10.1126/sciadv.abq7827

Furusho-Percot, C., Goergen, K., Hartick, C., Kulkarni, K., Keune, J., & Kollet, S. (2019). Pan-European groundwater to atmosphere terrestrial systems climatology from a physically consistent simulation. Scientific Data, 6(1), 320. https://doi.org/10.1038/s41597-019-0328-7

Franssen, H. H., Stöckli, R., Lehner, I., Rotenberg, E., Seneviratne, S. I., 2010. Energy balance closure of eddy-covariance data: A multisite analysis for European FLUXNET stations. Agricultural and Forest Meteorology 12, 1553–1567.

Galle, S., M. Grippa, C. Peugeot, I. B. Moussa, B. Cappelaere, J. Demarty, E. Mougin, G. Panthou, P. Adjomayi, E.K. Agbossou, A. Ba, M. Boucher, J.-M. Cohard, M. Descloitres, L. Descroix, M. Diawara, M. Dossou, G. Favreau, F. Gangneron, M. Gosset, B. Hector, P. Hiernaux, B.A. Issoufou, L. Kergoat, E. Lawin, T. Lebel, A. Legchenko, M. M. Abdou, O. Malam-Issa, O. Mamadou, Y. Nazoumou, T. Pellarin, G. Quantin, B. Sambou, J. Seghieri, L. Séguis, J.-P. Vandervaere, T. Vischel, J.-M. Vouillamoz, A. Zannou, S. Afouda, A. Alhassane, M. Arjounin, H. Barral, R. Biron, F. Cazenave, V. Chaffard, J.-P. Chazarin, H. Guyard, A. Koné, I. Mainassara, A. Mamane, M. Oi, T. Ouani, N. Soumaguel, M. Wubda, E.E. Ago, I.C. Alle, A. Allies, F. Arpin-Pont, B. Awessou, C. Cassé, G. Charvet, C. Dardel, A. Depeyre, F.B. Diallo, T. Do, C. Fatras, F.

Frappart, L. Gal, T. Gascon, F. Gibon, I. Guiro, A. Ingatan, J. Kempf, D.O.V. Kotchoni, F.M.A. Lawson, C. Leauthaud, S. Louvet, E. Mason, C.C. Nguyen, B. Perrimond, C. Pierre, A. Richard, E. Robert, C. Román-Cascón, C. Velluet, Wilcox, C., 2018. AMMA-CATCH, a Critical Zone Observatory in West Africa Monitoring a Region in Transition. Vadose Zone J. 17.

Gasser, T., Crepin, L., Quilcaille, Y., Houghton, R. A., Ciais, P., & Obersteiner, M. (2020). Historical CO2 emissions from land use and land cover change and their uncertainty. *Biogeosciences*, *17*(15), 4075–4101. https://doi.org/10.5194/bg-17-4075-2020

Gbobaniyi I., E. O., Akinlade, G. O., 2005. The Nigerian Micrometeorological Experiment (NIMEX-1): an overview. Ife Journal of Science 2.

Gebler, S., Hendricks Franssen, H.-J., Pütz, T., Post, H., Schmidt, M., & Vereecken, H. (2015). Actual evapotranspiration and precipitation measured by lysimeters: A comparison with eddy covariance and tipping bucket. *Hydrology and Earth System Sciences*, *19*(5), 2145–2161. https://doi.org/10.5194/hess-19-2145-2015

Genereux, D. P., Nagy, L. A., Osburn, C. L., & Oberbauer, S. F. (2013). A connection to deep groundwater alters ecosystem carbon fluxes and budgets: Example from a Costa Rican rainforest: REGIONAL GROUNDWATER AND CARBON FLUXES. Geophysical Research Letters, 40(10), 2066-2070. https://doi.org/10.1002/grl.50423

Gitelson, A. A., & Gamon, J. A. (2015). The need for a common basis for defining light-use efficiency: Implications for productivity estimation. *Remote Sensing of Environment*, *156*, 196–201. https://doi.org/10.1016/j.rse.2014.09.017

Gitelson, A. A., Peng, Y., Arkebauer, T. J., & Suyker, A. E. (2015). Productivity, absorbed photosynthetically active radiation, and light use efficiency in crops: Implications for remote sensing of crop primary production. *Journal of Plant Physiology*, *177*, 100–109. https://doi.org/10.1016/j.jplph.2014.12.015

Gleeson, T., Moosdorf, N., Hartmann, J., & van Beek, L. P. H. (2014). A glimpse beneath earth's surface: GLobal HYdrogeology MaPS (GLHYMPS) of permeability and porosity. *Geophysical Research Letters*, *41*(11), 3891–3898. https://doi.org/10.1002/2014GL059856

Gleeson, T., Smith. L., Jansen, N., Hartmann, J., Dürr, H., Manning, A.H., van Beek, R., and A.M. Jellinek (2011) Mapping permeability over the surface of the earth. Geophysical Research Letters, 38, L02401, doi:10.1029/2010GL045565

Gleeson, T., Wagener, T., Döll, P., Zipper, S. C., West, C., Wada, Y., Taylor, R., Scanlon, B., Rosolem, R., Rahman, S., Oshinlaja, N., Maxwell, R., Lo, M.-H., Kim, H., Hill, M., Hartmann, A., Fogg, G., Famiglietti, J. S., Ducharne, A., … Bierkens, M. F. P. (2021). GMD perspective: The quest to improve the evaluation of groundwater representation in continental- to global-scale models. *Geoscientific Model Development*, *14*(12), 7545–7571. https://doi.org/10.5194/gmd-14-7545-2021

Gleeson, T., Moosdorf, N., Hartmann, J., & van Beek, L. P. H. (2014). A glimpse beneath earth's surface: GLobal HYdrogeology MaPS (GLHYMPS) of permeability and porosity. *Geophysical Research Letters*, *41*(11), 3891–3898. https://doi.org/10.1002/2014GL059856

Gochis, D.J., Yu, W., Yates, D.N., 2013. The WRF-Hydro Model Technical Description and User's Guide, Version 1.0. NCAR Technical Document. 120 pp. https://ral.ucar.edu/sites/default/files/public/projects/wrf_hydro/WRF_Hydro_Technical_Description_and%20User_Guide_v1.0.pdf

Gochis, D.; Mc Creight, J.; Yu, W.; Dugger, A.; Sampson, K.; Yates, D.; Wood, A.; Clark, M.; Rasmussen, R. Multi-Scale Water Cycle Predictions Using the Community WRF-Hydro Modeling System; NCAR: Boulder, CO, USA, 2015; Available online: http://www.ral.ucar.edu/projects/wrf_hydro/ (accessed on 2 October 2024).

Goutorbe, J.P., T. Lebel, A. Tinga, P. Bessemoulin, J. Brouwer, A.J. Dolman, and Y.H. Kerr. 1994. HAPEX-Sahel: A large-scale study of land-atmosphere interactions in the semi-arid tropics. Ann. Geophys. 12:53–64. doi:10.1007/s00585-994-0053-0

Goutorbe, J. P., Lebel, T., Dolman, A. J., Gash, J.H.C., Kabat, P., Kerr, Y. H., Monteny, B., Prince, S. D., Stricker, J.N.M., Tinga, A., Wallace, J. S., 1997. An overview of HAPEX-Sahel: a study in climate and desertification. Journal of Hydrology, 4–17.

Goutorbe, J.-P., Lebel, T., Tinga, A., Bessemoulin, P., Brouwer, J., Dolman, A. J., Engman, E. T., Gash, J. H. C., Hoepffner, M., Kabat, P., Kerr, Y. H., Monteny, B., Prince, S., Said, F., Sellers, P., Wallace, J. S., 1994. HAPEX-Sahel: a large-scale study of land-atmosphere interactions in the semi-arid tropics. Annales Geophysicae 1, 53.

Green, J.K., A.G. Konings, S.H. Alemohammad, J. Berry, D. Entekhabi, J. Kolassa, et al. 2017. Regionally strong feedbacks between the atmosphere and terrestrial biosphere. Nat. Geosci. 10:410–414. doi:10.1038/ngeo2957

Guyot, A., Cohard, J.-M., Anquetin, S., Galle, S., Lloyd, C. R., 2009. Combined analysis of energy and water balances to estimate latent heat flux of a sudanian small catchment. Journal of Hydrology 1-2, 227–240.

Garcia, J.-L., Patel, B. K. C., & Ollivier, B. (2000). Taxonomic, phylogenetic, and ecological diversity of methanogenic archaea. Anaerobe, 6(4), 205–226.

Gedney, N., Huntingford, C., Comyn-Platt, E., & Wiltshire, A. (2019). Significant feedbacks of wetland methane release on climate change and the causes of their uncertainty. Environmental Research Letters, 14(8), 084027

Gedney, N., Cox, P. M., & Huntingford, C. (2004). Climate feedback from wetland methane emissions. Geophysical Research Letters, 31, L20503. https://doi.org/10.1029/2004GL020919

Harbaugh A.W., 2005. MODFLOW-2005, The U.S. Geological Survey Modular Ground-Water Model - the Ground-Water Flow Process. U.S. Geological Survey, Techniques and Methods 6-A16, 253 pp

Hartke, S. H., Wright, D. B., Li, Z., Maggioni, V., Kirschbaum, D. B., & Khan, S. (2022). Ensemble Representation of Satellite Precipitation Uncertainty using a Nonstationary, Anisotropic Autocorrelation Model. Water Resources Research. https://doi.org/10.1029/2021WR031650

Hengl, T., Mendes de Jesus, J., Heuvelink, G. B. M., Ruiperez Gonzalez, M., Kilibarda, M., Blagotić, A., Shangguan, W., Wright, M. N., Geng, X., Bauer-Marschallinger, B., Guevara, M. A., Vargas, R., MacMillan, R. A., Batjes, N. H., Leenaars, J. G. B., Ribeiro, E., Wheeler, I., Mantel, S., & Kempen, B. (2017). SoilGrids250m: Global gridded soil information based on machine learning. *PLOS ONE*, *12*(2), e0169748. https://doi.org/10.1371/journal.pone.0169748

Heusinkveld, B.G., Jacobs, A.F.G., Holtslag, A.A.M., Berkowicz, S.M., 2004. Surface energy balance closure in an arid region: role of soil heat flux. Agricultural and Forest Meteorology 1-2, 21–37.

Hartmann, J., & Moosdorf, N. (2012). The new global lithological map database GLiM: A representation of rock properties at the Earth surface. *Geochemistry, Geophysics, Geosystems*, *13*(12), 2012GC004370. https://doi.org/10.1029/2012GC004370

Hector, B., Cohard, J. M., Séguis, L., Peugeot, C., & Galle, S. (2017). *Hydrological functioning of West-African inland valleys explored with a critical zone model*. *2017*, H51K-1413. *Geosystems*, *13*(12). https://doi.org/10.1029/2012GC004370

He, C., Liu, Z., Wu, J., Pan, X., Fang, Z., Li, J., & Bryan, B. A. (2021). Future global urban water scarcity and potential solutions. *Nature Communications*, *12*(1), 4667. https://doi.org/10.1038/s41467-021-25026-3

Hengl, T., Mendes de Jesus, J., Heuvelink, G. B. M., Ruiperez Gonzalez, M., Kilibarda, M., Blagotić, A., Shangguan, W., Wright, M. N., Geng, X., Bauer-Marschallinger, B., Guevara, M. A., Vargas, R., MacMillan, R. A., Batjes, N. H., Leenaars, J. G. B., Ribeiro, E., Wheeler, I., Mantel, S., & Kempen, B. (2017). SoilGrids250m: Global gridded soil information based on machine learning. *PLOS ONE*, *12*(2), e0169748. https://doi.org/10.1371/journal.pone.0169748

Houghton, R. A., & Nassikas, A. A. (2017). Global and regional fluxes of carbon from land use and land cover change 1850-2015: Carbon Emissions From Land Use. *Global Biogeochemical Cycles*, *31*(3), 456–472. https://doi.org/10.1002/2016GB005546

Herzog, A., Hector, B., Cohard, J.-M., Lawson, F.-M., Vouillamoz, J.-M., & de Graaf, I. (2020). The sensitivity of a critical zone model to the representation of hydraulic conductivity heterogeneity in a deeply weathered hard rock aquifer in West Africa. 17163. https://doi.org/10.5194/egusphere-egu2020-17163

Hollinger, D. Y., Ollinger, S. V., Richardson, A. D., Meyers, T. P., Dail, D. B., Martin, M. E., Scott, N. A., Arkebauer, T. J., Baldocchi, D. D., Clark, K. L., Curits, P. S., Davis, K. J., Desai, A. R., Ingwersen, J., Imukova, K., Högy, P., Streck, T., 2015. On the use of the post-closure methods uncertainty band to evaluate the performance of land surface models against eddy covariance flux data. Biogeosciences 8, 2311–2326

Houéménou, H., Tweed, S., Dobigny, G., Mama, D., Alassane, A., Silmer, R., Babic, M., Ruy, S., Chaigneau, A., Gauthier, P., Socohou, A., Dossou, H.-J., Badou, S., & Leblanc, M. (2020). Degradation of groundwater quality in expanding cities in West Africa. A case study of the unregulated shallow aquifer in Cotonou. *Journal of Hydrology*, *582*, 124438. https://doi.org/10.1016/j.jhydrol.2019.124438

Hosseini, A., Mocko, D. M., Brunsell, N. A., Kumar, S. V., Mahanama, S., Arsenault, K., & Roundy, J. K. (2022). Understanding the impact of vegetation dynamics on the water cycle in the Noah-MP model. *Frontiers in Water*, *4*, 925852. https://doi.org/10.3389/frwa.2022.925852

Huscroft, J., Gleeson, T., Hartmann, J., & Börker, J. (2018). Compiling and Mapping Global Permeability of the Unconsolidated and Consolidated Earth: GLobal HYdrogeology MaPS 2.0 (GLHYMPS 2.0). *Geophysical Research Letters*, *45*(4), 1897–1904. https://doi.org/10.1002/2017GL075860

Hwang, H.-T., Park, Y.-J., Sudicky, E. A., & Forsyth, P. A. (2014). A parallel computational framework to solve flow and transport in integrated surface–subsurface hydrologic systems. *Environmental Modelling & Software*, *61*, 39–58. https://doi.org/10.1016/j.envsoft.2014.06.024

Hantush, M.S. Analysis of data from pumping tests in leaky aquifers. Eos Trans. Am. Geophys. Union 1956, 37, 702–714. https://doi.org/10.1029/TR037i006p00702

Herzog, A., Hector, B., Cohard, J., Vouillamoz, J., Lawson, F. M. A., Peugeot, C., & de Graaf, I. (2021). A parametric sensitivity analysis for prioritizing regolith knowledge needs for modeling water transfers in the West African critical zone. *Vadose Zone Journal*, *20*(6). https://doi.org/10.1002/vzj2.20163

IGRAC (2021) Groundwater In Fast Growing Cities In Western Africa (map)

IPBES, 2018: Summary for policymakers of the regional assessment report on biodiversity and ecosystem services for Africa of the Intergovernmental Science-Policy Platform on Biodiversity and Ecosystem Services. [E. Archer, L. E. D., K. J. Mulongoy, M. A. Maoela, M. Walters, R. Biggs, M-C. Cormier-Salem, F. DeClerck, M. C. Diaw, A. E. Dunham, P. Failler, C. Gordon, K. A. Harhash, R. Kasisi, F. Kizito, W. D. Nyingi, N. Oguge, B. Osman Elasha, L. C. Stringer, L. Tito de Morais, A. Assogbadjo, B. N. Egoh, M. W. Halmy, K. Heubach, A. Mensah, L. Pereira and N. Sitas (ed.)]. IPBES secretariat, Bonn, Germany, 49 pp. Available at: https://ipbes.net/sites/default/files/spm_africa_2018_digital.pdf.

IPCC, 2018c: Summary for Policymakers [Masson-Delmotte, V., P. Zhai, H. O. Pörtner, D. Roberts, J. Skea, P. R. Shukla, A. Pirani, W. Moufouma-Okia, C. Péan, R. Pidcock, S. Connors, J. B. R. Matthews, Y. Chen, X. Zhou, M. I. Gomis, E. Lonnoy, T. Maycock, M. Tignor and T. Waterfield (eds.)]. Global Warming of 1.5°C. An IPCC Special Report on the impacts of global warming of 1.5°C above pre-industrial levels and related global greenhouse gas emission pathways, in the context of strengthening the global response to the threat of climate change, sustainable development, and efforts to eradicate poverty, In press pp. Available at: https://www.ipcc.ch/site/assets/uploads/sites/2/2019/06/SR15_Full_Report_High_Res.pdf.

IPCC (2007b) Summary for Policymakers. In: Climate Change 2007: Impacts, Adaptation and Vulnerability. Contribution of Working Group II to the Fourth Assessment Report of the Intergovernmental Panel on Climate Change (ed. by M. L. Parry, O. F. Canziani, J. P. Palutikof, P. J. van der Linden & C. E. Hanson), 7–22. Cambridge University Press, UK. http://www.ipcc.ch/pdf/assessment-report/ar4/wg1/ar4-wg1-spm.pdf [last accessed 29 July 2025].

Ivanov, V. Y., Vivoni, E. R., Bras, R. L., & Entekhabi, D. (2004). Catchment hydrologic response with a fully distributed triangulated irregular network model: CATCHMENT HYDROLOGIC RESPONSE WITH A TIN. *Water Resources Research*, *40*(11). https://doi.org/10.1029/2004WR003218

IPCC, 2022: Summary for Policymakers [H.-O. Pörtner, D.C. Roberts, E.S. Poloczanska, K. Mintenbeck, M. Tignor, A. Alegría, M. Craig, S. Langsdorf, S. Löschke, V. Möller, A. Okem (eds.)]. In: Climate Change 2022: Impacts, Adaptation and Vulnerability. Contribution of Working Group II to the Sixth Assessment Report of the Intergovernmental Panel on Climate Change [H.-O. Pörtner, D.C. Roberts, M. Tignor, E.S. Poloczanska, K. Mintenbeck, A. Alegría, M. Craig, S. Langsdorf, S. Löschke, V. Möller, A. Okem, B. Rama (eds.)]. Cambridge University Press, Cambridge, UK and New York, NY, USA, pp. 3–33, doi:10.1017/9781009325844.001.

Jaeger, E. B., Stöckli, R., Seneviratne, S. I., 2009. Analysis of planetary boundary layer fluxes and land-atmosphere coupling in the regional climate model CLM. Journal of Geophysical Research: Atmospheres D17, L18405.

Janssens IA, Freibauer A, Ciais P, Smith P, Nabuurs G-J, Folberth G, et al. Europe's terrestrial biosphere absorbs 7 to 12% of European anthropogenic CO2 emissions. Science. 2003;300:1538–42

Jegede, O.O., M. Mauder, E.C. Okogbue, T. Foken, E.E. Balogun, J.A. Adedokun, et al. 2004. The Nigerian Micrometeorological Experiment (NIMEX-1): An overview. Ife J. Sci. 6:191–202. doi:10.4314/ijs.v6i2.32147

Jegede, O. O., Maunder, M., Okogbue, E. C., Foken, T., Balogun, E. E., Adedokun, J. A., Oladiran, E. O., Omotosho, J. A., Balogun, A. A., Oladosu, O. R., La Sunmonu, Ayoola, M. A., Aregbesola, T. O., Ogolo, E. O., Nymphas, E. F., Adeniyi, M. O., Olatona, G. I., Ladipo, K. O., Ohamobi, S.

Jia G, Shevliakova E, Artaxo P, De Noblet-Ducoudré N, Houghton R, House J, Kitajima K, Lennard C, A Popp, Sirin A, Sukumar R, Verchot L. Land–climate interactions. In: Climate Change and Land: an IPCC special report on climate change, desertification, land degradation, sustainable land management, food security, and greenhouse gas fluxes in terrestrial ecosystems [P.R. Shukla, J. Skea, E. Calvo Buendia, V. Masson-Delmotte, H.-O. Pörtner, D.C. Roberts, P. Zhai, R. Slade, S. Connors, R. van Diemen, M. Ferrat, E. Haughey, S. Luz, S. Neogi, M. Pathak, J. Petzold, J. Portugal Pereira, P. Vyas, E. Huntley, K. Kissick, M, Belkacemi, J. Malley, (eds.)]. 2019.

Jing, M., Kumar, R., Heße, F., Thober, S., Rakovec, O., Samaniego, L., & Attinger, S. (2020). Assessing the response of groundwater quantity and travel time distribution to 1.5, 2, and 3 °C global warming in a mesoscale central German basin. *Hydrology and Earth System Sciences*, *24*(3), 1511–1526. https://doi.org/10.5194/hess-24-1511-2020

Jing, M., Heße, F., Kumar, R., Wang, W., Fischer, T., Walther, M., Zink, M., Zech, A., Samaniego, L., Kolditz, O., & Attinger, S. (2018). Improved regional-scale groundwater representation by the coupling of the mesoscale Hydrologic Model (mHM v5.7) to the groundwater model OpenGeoSys (OGS). *Geoscientific Model Development*, *11*(5), 1989–2007. https://doi.org/10.5194/gmd-11-1989-2018

Jung, M., Koirala, S., Weber, U., Ichii, K., Gans, F., Camps-Valls, G., Papale, D., Schwalm, C., Tramontana, G., & Reichstein, M. (2019). The FLUXCOM ensemble of global land-atmosphere energy fluxes. *Scientific Data*, *6*(1), 74. https://doi.org/10.1038/s41597-019-0076-8

Jung, M., Reichstein, M., Margolis, H. A., Cescatti, A., Richardson, A. D., Arain, M. A., Arneth, A., Bernhofer, C., Bonal, D., Chen, J., Gianelle, D., Gobron, N., Kiely, G., Kutsch, W., Lasslop, G., Law, B. E., Lindroth, A., Merbold, L., Montagnani, L., Moors, E. J., Papale, D., Sottocornola, M., Vaccari, F., Williams, C., 2011. Global patterns of land-atmosphere fluxes of carbon dioxide, latent heat, and sensible heat derived from eddy covariance, satellite, and meteorological observations. Journal of Geophysical Research: Atmospheres, G00K02.

Jacob, C.E. On the flow of water in an elastic artesian aquifer. Eos Trans. Am. Geophys. Union 1940, 21, 574–586. https://doi.org/10.1029/TR021i002p00574

Kahan, D.S., Y. Xue, and S.J. Allen. 2006. The impact of vegetation and soil parameters in simulations of surface energy and water balance in the semi-arid Sahel: A case study using SEBEX and HAPEX-Sahel data. J. Hydrol. 320:238–259. doi:10.1016/j.jhydrol.2005.07.011

Klein, C., J. Bliefernicht, D. Heinzeller, U. Gessner, I. Klein, and H. Kunstmann. 2017. Feedback of observed interannual vegetation change: A regional climate model analysis for the West African monsoon. Clim. Dyn. 48:2837–2858. doi:10.1007/s00382-016-3237-x

Kalu I., Ndehedehe, C.E., Okwuashi, O., Eyoh, A.E., and Ferreira, V.G (2021). A new modelling framework to assess changes in groundwater level. J. Hydrol: Reg. Stud. Volume 43, 101185. https://doi.org/10.1016/j.ejrh.2022.101185

Karlsson, C., I. Jamali, R. Earon, B. Olofsson, and U. Mortberg (2014), Comparison of methods for predicting regolith thickness in previously glaciated terrain, Stockholm, Sweden, Geoderma, 226-227, 116–129, doi:10.1016/j.geoderma.2014.03.003.

Kolditz, O., Bauer, S., Bilke, L., Böttcher, N., Delfs, J. O., Fischer, T., Görke, U. J., Kalbacher, T., Kosakowski, G., McDermott, C. I., Park, C. H., Radu, F., Rink, K., Shao, H., Shao, H. B., Sun, F., Sun, Y. Y., Singh, A. K., Taron, J., … Zehner, B. (2012). OpenGeoSys: An open-source initiative for numerical simulation of thermo-hydro-mechanical/chemical (THM/C) processes in porous media. *Environmental Earth Sciences*, *67*(2), 589–599. https://doi.org/10.1007/s12665-012-1546-x

Kollet, S. J., & Maxwell, R. M. (2006). Integrated surface–groundwater flow modeling: A free-surface overland flow boundary condition in a parallel groundwater flow model. *Advances in Water Resources*, *29*(7), 945–958. https://doi.org/10.1016/j.advwatres.2005.08.006

Kollet, S. J., & Maxwell, R. M. (2008). Capturing the influence of groundwater dynamics on land surface processes using an integrated, distributed watershed model: influence of groundwater dynamics on land. *Water Resources Research*, *44*(2). https://doi.org/10.1029/2007WR006004

Kollet, S., Gasper, F., Brdar, S., Goergen, K., Hendricks-Franssen, H.-J., Keune, J., Kurtz, W., Küll, V., Pappenberger, F., Poll, S., Trömel, S., Shrestha, P., Simmer, C., & Sulis, M. (2018). Introduction of an Experimental Terrestrial Forecasting/Monitoring System at Regional to Continental Scales Based on the Terrestrial Systems Modeling Platform (v1.1.0). *Water*, *10*(11), 1697. https://doi.org/10.3390/w10111697

Konikow, L. F. (2011). Contribution of global groundwater depletion since 1900 to sea-level rise: GROUNDWATER DEPLETION. Geophysical Research Letters, 38(17), n/a-n/a. https://doi.org/10.1029/2011GL048604

Koster, R. D., & Walker, G. K. (2015). Interactive Vegetation Phenology, Soil Moisture, and Monthly Temperature Forecasts. Journal of Hydrometeorology, 16(4), 1456-1465. https://doi.org/10.1175/JHM-D-14-0205.1

Krakauer, N. Y., Li, H., & Fan, Y. (2014). Groundwater flow across spatial scales: Importance for climate modeling. *Environmental Research Letters*, *9*(3), 034003. https://doi.org/10.1088/1748-9326/9/3/034003

Kuffour, B. N. O., Engdahl, N. B., Woodward, C. S., Condon, L. E., Kollet, S., and Maxwell, R. M.: Simulating coupled surface–subsurface flows with ParFlow v3.5.0: capabilities,

applications, and ongoing development of an open-source, massively parallel, integrated hydrologic model, Geosci. Model Dev., 13, 1373–1397, https://doi.org/10.5194/gmd-13-1373-2020, 2020.

Kumar, M., Duffy, C. J., & Salvage, K. M. (2009). A Second-Order Accurate, Finite Volume-Based, Integrated Hydrologic Modeling (FIHM) Framework for Simulation of Surface and Subsurface Flow. *Vadose Zone Journal*, *8*(4), 873–890. https://doi.org/10.2136/vzj2009.0014

Kawamiya, M., Hajima, T., Tachiiri, K., Watanabe, S., Yokohata, T.,2020. Two decades of Earth system modeling with an emphasis on Model for Interdisciplinary Research on Climate (MIROC). Prog. Earth Planet Sci.7(1),1 –13.

Kumar, P. (2004), Layer averaged Richard's equation with lateral flow, Adv. Water Resour., 27(5), 522 – 532

Kruseman, G.P.; de Ridder, N.A. Analysis and Evaluation of Pumping Test Data; International Institute for Land Reclamation and Improvement: Wageningen, The Netherlands, 1994.

Kaimal, J.C., Finnigan, J.J., 1994. Atmospheric boundary layer flows: their structure and measurement. Oxford University Press, New York 289p.

Kamble, B., Kilic, A., & Hubbard, K. (2013). Estimating Crop Coefficients Using Remote Sensing-Based Vegetation Inde.g. *Remote Sensing*, *5*(4), 1588–1602. https://doi.org/10.3390/rs5041588

Kling, H., Fuchs, M., & Paulin, M. (2012). Runoff conditions in the upper Danube basin under an ensemble of climate change scenarios. Journal of Hydrology, 424–425, 264–277. https://doi.org/10.1016/j.jhydrol.2012.01.011

Kumar, P. (2004), Layer averaged Richard's equation with lateral flow, Adv. Water Resour., 27(5), 522 – 532.

Labadie, J.W.; Helweg, O.J. Step-drawdown test analysis by computer. Groundwater 1975, 13, 438–444. https://doi.org/10.1111/j.1745-6584.1975.tb03611.x

Lachassagne, P., Dewandel, B., & Wyns, R. (2021). Review: Hydrogeology of weathered crystalline/hard-rock aquifers—guidelines for the operational survey and management of their groundwater resources. Hydrogeology Journal, 29(8), 2561–2594. https://doi.org/10.1007/s10040-021-02339-7

Lachassagne, P., Wyns, R., & Dewandel, B. (2011). The fracture permeability of Hard Rock Aquifers is due neither to tectonics, nor to unloading, but to weathering processes: Weathering

and permeability of Hard Rock Aquifers. *Terra Nova*, *23*(3), 145–161. https://doi.org/10.1111/j.1365-3121.2011.00998.x

Lachassagne, P., Wyns, R., & Dewandel, B. (2011). The fracture permeability of Hard Rock Aquifers is due neither to tectonics, nor to unloading, but to weathering processes: Weathering and permeability of Hard Rock Aquifers. *Terra Nova*, *23*(3), 145–161. https://doi.org/10.1111/j.1365-3121.2011.00998.x

Lawrence, P. J., Chase, T. N., 2010. Investigating the climate impacts of global land cover change in the community climate system model. International Journal of Climatology 13, 2066–2087.

Lebel, T., J.D. Taupin, and N. d'Amato. 1997. Rainfall monitoring during HAPEX-Sahel. 1. General rainfall conditions and climatology. J. Hydrol. 188–189:74–96. doi:10.1016/S0022-1694(96)03155-1

Lebel, T., H. Sauvageot, M. Hoepffner, M. Desbois, B. Guillot, and P. Hubert. 1992. Rainfall estimation in the Sahel: The EPSAT-NIGER experiment. Hydrol. Sci. J. 37:201–215. doi:10.1080/02626669209492582

Lebel, T., Cappelaere, B., Galle, S., Hanan, N., Kergoat, L., Levis, S., Vieux, B., Descroix, L., Gosset, M., Mougin, E., Peugeot, C., Seguis, L., 2009. AMMA-CATCH studies in the Sahelian region of West-Africa: An overview. Journal of Hydrology 1-2, 3–13.

Lee, X., Black, T. A., 1993. Atmospheric turbulence within and above a douglas-fir stand. Part II: Eddy fluxes of sensible heat and water vapour. Boundary-Layer Meteorology 4, 369–389.

Lenschow, D. H., Mann, J., Kristensen, L., 1994. How Long Is Long Enough When Measuring Fluxes and Other Turbulence Statistics? Journal of Atmospheric and Oceanic Technology 3, 661–673.

Li, X., Feng, M., Ran, Y., Su, Y., Liu, F., Huang, C., Shen, H., Xiao, Q., Su, J., Yuan, S., 2023. Big Data in Earth system science and progress towards a digital twin. Nat. Rev. Earth Environ. 1–14. https://refhub.elsevier.com/S0012-8252(24)00314-3/rf0620

Liesch, T.; Wunsch, A. Aquifer Responses to Long-Term Climatic Periodicities. J. Hydrol. 2019, 572, 226–242. https://doi.org/10.1016/j.jhydrol.2019.02.060

Liu, H., Foken, T., 2001. A modified Bowen ratio method to determine sensible and latent heat fluxes. Meteorologische Zeitschrift 1, 71–80.

Lohou, F., Saïd, F., Lothon, M., Durand, P., Serça, D., 2010. Impact of Boundary-Layer Processes on Near-Surface Turbulence Within the West African Monsoon. Boundary-Layer Meteorology 1, 1–23.

Luan, J., Wu, J., Liu, S., Roulet, N., & Wang, M. (2019). Soil nitrogen determines greenhouse gas emissions from northern peatlands under concurrent warming and vegetation shifting. *Communications Biology*, *2*(1), 132. https://doi.org/10.1038/s42003-019-0370-1

Luyssaert, S., Jammet, M., Stoy, P. C., Estel, S., Pongratz, J., Ceschia, E., Churkina, G., Don, A., Erb, K., Ferlicoq, M., Gielen, B., Grünwald, T., Houghton, R. A., Klumpp, K., Knohl, A., Kolb, T., Kuemmerle, T., Laurila, T., Lohila, A., Loustau, D., McGrath, M. J., Meyfroidt, P., Moors, E. J., Naudts, K., Novick, K., Otto, J., Pilegaard, K., Pio, C. A., Rambal, S., Rebmann, C., Ryder, J., Suyker, A. E., Varlagin, A., Wattenbach, M., Dolman, A. J., 2014. Land management and land-cover change have impacts of similar magnitude on surface temperature. Nature Climate Change 5, 389–393.

Ma, S., Zhou, L., Li, F., & Zhu, J. (2020). Evaluation of WRF land surface schemes in land-atmosphere exchange simulations over grassland in Southeast Tibet. Atmospheric Research, 234, 104739. https://doi.org/10.1016/j.atmosres.2019.104739

Mauder, M., O.O. Jegede, E.C. Okogbue, F. Wimmer, and T. Foken. 2007. Surface energy balance measurements at a tropical site in West Africa during the transition from dry to wet season. Theor. Appl. Climatol. 89:171–183. doi:10.1007/s00704-006-0252-

Mauder, M., Cuntz, M., Drüe, C., Graf, A., Rebmann, C., Schmid, H. P., Schmidt, M., Steinbrecher, R., 2013. A strategy for quality and uncertainty assessment of long-term eddy-covariance measurements. Agricultural and Forest Meteorology, 122–135

Mauder, M., Jegede, O. O., Okogbue, E. C., Wimmer, F., Foken, T., 2007b. Surface energy balance measurements at a tropical site in West Africa during the transition from dry to wet season. Theoretical and Applied Climatology 3-4, 171–183.

Maxwell, R. M., & Miller, N. L. (2005). Development of a Coupled Land Surface and Groundwater Model. *Journal of Hydrometeorology*, *6*(3), 233–247. https://doi.org/10.1175/JHM422.1

Maxwell, R. M., & Kollet, S. J. (2008). Interdependence of groundwater dynamics and land-energy feedbacks under climate change. Nature Geosci, 1(10), 665-669. https://doi.org/10.1038/ngeo315

Maxwell, R. M., & Condon, L. E. (2016). Connections between groundwater flow and transpiration partitioning. Science, 353(6297), 377–380.

Maxwell, R. M.: A terrain-following grid transform and preconditioner for parallel, large-scale, integrated hydrologic modeling, Adv. Water Resour., 53, 109–117, 2013

McGloin, R., Šigut, L., Havránková, K., Dušek, J., Pavelka, M., Sedlák, P., 2018. Energy balance closure at a variety of ecosystems in Central Europe with contrasting topographies. Agricultural and Forest Meteorology, 418–431.

McKee, T. B., Doesken, N., & Kleist, J. (1993). The relationship of drought frequency and duration to time scales. Eighth Conference on Applied Climatology, Anaheim CA, 6.

Miguez-Macho, G., & Fan, Y. (2012). The role of groundwater in the Amazon water cycle : 2. Influence on seasonal soil moisture and evapotranspiration: AMAZON GROUNDWATER AND SEASONAL ET. Journal of Geophysical Research: Atmospheres, 117(D15), n/a-n/a. https://doi.org/10.1029/2012JD017540

Miller, D. A., and R. A. White (1998), A conterminous United States multilayer soil characteristics dataset for regional climate and hydrology modeling, Earth Interact., 2, 1–26, doi:10.1175/1087-3562(1998)002h0001:ACUSMSi2.3.CO;2.

Minor, M. A., 2009. Surface energy balance and 24-h evapotranspiration on an agricultural landscape with SRF willow in central New York. Biomass and Bioenergy 12, 1710–1718.

Monteith, J.L. Solar Radiation and Productivity in Tropical Ecosystems. J. Appl. Ecol. 1972, 9, 747–766. https://dx.doi.org/10.2307/2401901

Monteith, J.L.; Moss, C.J.; Cooke, G.W.; Pirie, N.W.; Bell, G.D.H. Climate and the efficiency of crop production in Britain. Philos. Trans. R. Soc. Lond. B Biol. Sci. 1977, 281, 277–294. https://dx.doi.org/10.1098/rstb.1977.0140

Mougin, E., Hiernaux, P., Kergoat, L., Grippa, M., Rosnay, P. de, Timouk, F., Le Dantec, V., Demarez, V., Lavenu, F., Arjounin, M., Lebel, T., Soumaguel, N., Ceschia, E., Mougenot, B., Baup, F., Frappart, F., Frison, P. L., Gardelle, J., Gruhier, C., Jarlan, L., Mangiarotti, S., Sanou, B., Tracol, Y., Guichard, F., Trichon, V., Diarra, L., Soumaré, A., Koité, M., Dembélé, F., Lloyd, C., Hanan, N. P., Damesin, C., Delon, C., Serça, D., Galy-Lacaux, C., Seghieri, J., Becerra, S., Dia, H., Gangneron, F., Mazzega, P., 2009. The AMMA-CATCH Gourma observatory site in

Mali: Relating climatic variations to changes in vegetation, surface hydrology, fluxes and natural resources. Journal of Hydrology 1-2, 14–33.

Müller Schmied, H., Eisner, S., Franz, D., Wattenbach, M., Portmann, F. T., Flörke, M., & Döll, P. (2014). Sensitivity of simulated global-scale freshwater fluxes and storages to input data, hydrological model structure, human water use and calibration. *Hydrology and Earth System Sciences*, *18*(9), 3511–3538. https://doi.org/10.5194/hess-18-3511-2014

Maslia, M.L.; Randolph, R.B. Methods and Computer Program Documentation for Determining Anisotropic Transmissivity Tensor Components of Two-Dimensional Ground-Water Flow; 86-227; U.S.Geological Survey: Reston, VA, USA, 1986.

McElwee, C.D. Theis Parameter Evaluation from Pumping Tests by Sensitivity Analysis. Groundwater 1980, 18, 56–60. https://doi.org/10.1111/j.1745-6584.1980.tb03371.x

Mauder, M., Foken, T., 2015. Documentation and instruction manual of the eddy covariance software package TK3 (update). Arbeitsergebnisse, Univ Bayreuth, Abt. Mikrometeorologie, Nr. 62, Bayreuth, July 2015.

Mauder, M., Cuntz, M., Drüe, C., Graf, A., Rebmann, C., Schmid, H. P., Schmidt, M., Steinbrecher, R., 2013. A strategy for quality and uncertainty assessment of long-term eddy-covariance measurements. Agricultural and Forest Meteorology, 122–135.

McGloin, R., Šigut, L., Havránková, K., Dušek, J., Pavelka, M., Sedlák, P., 2018. Energy balance closure at a variety of ecosystems in Central Europe with contrasting topographies. Agricultural and Forest Meteorology, 418–431.

Munger, J.W., Loescher, H.W., Luo, H., 2012. Measurement, tower and site design considerations. In: Aubinet, M., Vesala, T., Papale, D. (Eds.), Eddy Covariance – A Practical Guide to Measurement and Data Analysis. Springer, Dordrecht, pp. 21–58.

Muñoz-Sabater, J., Dutra, E., Agustí-Panareda, A., Albergel, C., Arduini, G., Balsamo, G., Boussetta, S., Choulga, M., Harrigan, S., Hersbach, H., Martens, B., Miralles, D. G., Piles, M., Rodríguez-Fernández, N. J., Zsoter, E., Buontempo, C., & Thépaut, J.-N. (2021). ERA5-Land: A state-of-the-art global reanalysis dataset for land applications. *Earth System Science Data*, *13*(9), 4349–4383. https://doi.org/10.5194/essd-13-4349-2021

Martens, B., Miralles, D. G., Lievens, H., Van Der Schalie, R., De Jeu, R. A. M., Fernández-Prieto, D., Beck, H. E., Dorigo, W. A., & Verhoest, N. E. C. (2017). GLEAM v3: Satellite-based land evaporation and root-zone soil moisture. *Geoscientific Model Development*, *10*(5), 1903–1925. https://doi.org/10.5194/gmd-10-1903-2017

Miralles, D. G., Holmes, T. R. H., De Jeu, R. A. M., Gash, J. H., Meesters, A. G. C. A., & Dolman, A. J. (2011). Global land-surface evaporation estimated from satellite-based observations. *Hydrology and Earth System Sciences*, *15*(2), 453–469. https://doi.org/10.5194/hess-15-453-2011

Muñoz-Sabater, J., Dutra, E., Agustí-Panareda, A., Albergel, C., Arduini, G., Balsamo, G., Boussetta, S., Choulga, M., Harrigan, S., Hersbach, H., Martens, B., Miralles, D. G., Piles, M., Rodríguez-Fernández, N. J., Zsoter, E., Buontempo, C., & Thépaut, J.-N. (2021). ERA5-Land: A state-of-the-art global reanalysis dataset for land applications. *Earth System Science Data*, *13*(9), 4349–4383. https://doi.org/10.5194/essd-13-4349-2021

Menz, G. (2010). Regional geography of West and Northwest Africa: An introduction. In P. Speth, M. Christoph, & B. Diekkrüger (Eds.), *Impacts of Global Change on the Hydrological Cycle in West and Northwest Africa* (pp. 30–103). Springer Berlin Heidelberg. https://doi.org/10.1007/978-3-642-12957-5_3

Miller, D. A., & White, R. A. (1998). A Conterminous United States Multilayer Soil Characteristics Dataset for Regional Climate and Hydrology Modeling. *Earth Interactions*, *2*(2), 1–26. https://doi.org/10.1175/1087-3562(1998)002<0001:ACUSMS>2.3.CO;2

Mlawer, E.J.; Taubman, S.J.; Brown, P.D.; Iacono, M.J.; Clough, S.A. Radiative transfer for inhomogeneous atmospheres: RRTM, a validated correlated-k model for the longwave. J. Geophys. Res. Atmos. 1997, 102, 16663–16682. https://doi.org/10.1029/97JD00237

Mata-Alvarez, J., Mace, S., & Llabres, P. (2000). Anaerobic digestion of organic solid wastes. an overview of research achievements and perspectives. Bioresource Technology, 74(1), 3–16.

Nash, J. E., & Sutcliffe, J. V. (1970). River flow forecasting through conceptual models part I – A discussion of principles. Journal of Hydrology, 10(3), 282–290. https://doi.org/10.1016/0022-1694(70)90255-6

Naz, B. S., Sharples, W., Ma, Y., Goergen, K., & Kollet, S. (2023). Continental-scale evaluation of a fully distributed coupled land surface and groundwater model, ParFlow-CLM (v3.6.0), over Europe. *Geoscientific Model Development*, *16*(6), Article 6. https://doi.org/10.5194/gmd-16-1617-2023

Ndehedehe, C.E., Ferreira, V.G., Agutu, N.O., Onojeghuo, A.O., Okwuashi, O., Kassahun H.T., Dewan, A., 2021. What if the rains do not come? J. Hydrol. 595, 126040. https://doi.org/10.1016/j.jhydrol.2021.126040.

Ndehedehe, C. E., Awange, J. L., Agutu, N. O., & Okwuashi, O. (2018). Changes in hydro-meteorological conditions over tropical West Africa (1980–2015) and links to global climate. *Global and Planetary Change*, *162*, 321–341. https://doi.org/10.1016/j.gloplacha.2018.01.020

Niu, G.-Y., and Z.-L. Yang (2003), The Versatile Integrator of Surface and Atmosphere processes (VISA) Part II: Evaluation of three topography based runoff schemes, Global Planet. Change, 38, 191 – 208.

Nogueira, M.: Inter-comparison of ERA-5, ERA-interim and GPCP rainfall over the last 40 years: Process-based analysis of systematic and random differences, J. Hydrol., 583, 124632, https://doi.org/10.1016/j.jhydrol.2020.124632, 2020.

OBEMINES, 1989. Carte géologique du Bénin à 1:200 000. Office Béninoise des Mines. Cotonou, Bénin

Oncley, S. P., Foken, T., Vogt, R., Kohsiek, W., DeBruin, H. A. R., Bernhofer, C., Christen, A., van Gorsel, E., Grantz, D., Feigenwinter, C., Lehner, I., Liebethal, C., Liu, H., Mauder, M., Pitacco, A., Ribeiro, L., Weidinger, T., 2007. The Energy Balance Experiment EBEX-2000. Part I: overview and energy balance. Boundary-Layer Meteorology 1, 1–28.

Ohmura, A., 1982. Objective Criteria for Rejecting Data for Bowen Ratio Flux Calculations. Journal of Applied Meteorology 4, 595–598.

O'Neill, M. M. F., Tijerina, D. T., Condon, L. E., and Maxwell, R. M.: Assessment of the ParFlow–CLM CONUS 1.0 integrated hydrologic model: evaluation of hyper-resolution water balance components across the contiguous United States, Geosci. Model Dev., 14, 7223–7254, https://doi.org/10.5194/gmd-147223-2021, 2021.

Oussou, F. E., Ndehedehe, C. E., Oloukoi, J., Yalo, N., Boukari, M., & Diaw, A. T. (2022). Characterization of the hydro-geological regime of fractured aquifers in Benin (West-Africa) using multi-satellites and models. *Journal of Hydrology: Regional Studies*, *39*, 100987. https://doi.org/10.1016/j.ejrh.2021.100987

Oussou FE, Yalo N, Ndehedehe CE, Oloukoi J, Alassane A, Boukari M & Gbewezoun VH, (2020): Fracture aquifers identification in the Zou basin (West Africa) using remote sensing and GIS, Geocarto International, https://doi:10.1080/10106049.2020.1852613

Oussou, F. E., Ndehedehe, C. E., Yalo, N., Asiwaju-Bello, Y. A., Oloukoi, J., Odeloui, D. T. J., Boukari, M., Diaw, A. T., & Kunstmann, H. (2025). Improving the depth-to-bedrock maps for groundwater-to-atmosphere modeling in Africa. *Journal of Hydrology*, *656*, 132964. https://doi.org/10.1016/j.jhydrol.2025.132964

Oussou EF, Oloukoi J, Yalo N, Boukari M. 2019. Analyse Spatiale du potentiel en eau souterraine dans le bassin du Zou au Sud du Benin (Afrique de L'ouest). Eur Sci J. 15(27):1857–7881.

Pan, X., Chen, D., Pan, B., Huang, X., Yang, K., Piao, S., Zhou, T., Dai, Y., Chen, F., & Li, X. (2025). Evolution and prospects of Earth system models: Challenges and opportunities. *Earth-Science Reviews*, *260*, 104986. https://doi.org/10.1016/j.earscirev.2024.104986

Panday, S., & Huyakorn, P. S. (2004). A fully coupled physically-based spatially-distributed model for evaluating surface/subsurface flow. *Advances in Water Resources*, *27*(4), 361–382. https://doi.org/10.1016/j.advwatres.2004.02.016

Paniconi, C., & Putti, M. (2015). Physically based modeling in catchment hydrology at 50: Survey and outlook. *Water Resources Research*, *51*(9), 7090–7129. https://doi.org/10.1002/2015WR017780

Pelletier, J. D., Broxton, P. D., Hazenberg, P., Zeng, X., Troch, P. A., Niu, G., Williams, Z., Brunke, M. A., & Gochis, D. (2016). A gridded global data set of soil, intact regolith, and sedimentary deposit thicknesses for regional and global land surface modeling. *Journal of Advances in Modeling Earth Systems*, *8*(1), 41–65. https://doi.org/10.1002/2015MS000526

Phi, S., Clarke, W., & Li, L. (2013). Laboratory and numerical investigations of hillslope soil saturation development and runoff generation over rainfall events. *Journal of Hydrology*, *493*, 1–15. https://doi.org/10.1016/j.jhydrol.2013.04.009

Pokhrel, Y., Hanasaki, N., Koirala, S., Cho, J., Yeh, P. J.-F., Kim, H., Kanae, S., & Oki, T. (2012). Incorporating Anthropogenic Water Regulation Modules into a Land Surface Model. *Journal of Hydrometeorology*, *13*(1), 255–269. https://doi.org/10.1175/JHM-D-11-013.1

Penman, H. L.: Natural evaporation from open water, bare soil and grass, P. Roy. Soc. Lond. A, 193, 120–145, publisher: The Royal Society London, 1948.

Pongratz, J., Schwingshackl, C., Bultan, S., Obermeier, W., Havermann, F., & Guo, S. (2021). Land Use Effects on Climate: Current State, Recent Progress, and Emerging Topics. Curr Clim Change Rep, 7(4), Article 4. https://doi.org/10.1007/s40641-021-00178-y

Priestley, C. H. B. and Taylor, R. J.: On the assessment of surface heat flux and evaporation using large-scale parameters, Mon. Weather Rev., 100, 81–92, 1972.

Quansah, E., Mauder, M., Balogun, A. A., Amekudzi, L. K., Hingerl, L., Bliefernicht, J., & Kunstmann, H. (2015). Carbon dioxide fluxes from contrasting ecosystems in the Sudanian

Savanna in West Africa. *Carbon Balance and Management*, *10*(1), 1. https://doi.org/10.1186/s13021-014-0011-4

Qu, Y., & Duffy, C. J. (2007). A semidiscrete finite volume formulation for multiprocess watershed simulation: MULTIPROCESS WATERSHED SIMULATION. *Water Resources Research*, *43*(8). https://doi.org/10.1029/2006WR005752

Quinn, P. F., J. Beven, and R. Lamb (1995), The ln(a/tan b) index: How to calculate it and how to use it within the TOPMODEL framework, Hydrol. Processes, 9, 161 – 182.

Quenum, G. M. L. D., Arnault, J., Klutse, N. A. B., Zhang, Z., Kunstmann, H., & Oguntunde, P. G. (2022). Potential of the Coupled WRF/WRF-Hydro Modeling System for Flood Forecasting in the Ouémé River (West Africa). *Water*, *14*(8), 1192. https://doi.org/10.3390/w14081192

Rahman, M., Sulis, M., & Kollet, S. J. (2015). The subsurface–land surface–atmosphere connection under convective conditions. *Advances in Water Resources*, *83*, 240–249. https://doi.org/10.1016/j.advwatres.2015.06.003

Ramier, D., Boulain, N., Cappelaere, B., Timouk, F., Rabanit, M., Lloyd, C. R., Boubkraoui, S., Métayer, F., Descroix, L., Wawrzyniak, V., 2009. Towards an understanding of coupled physical and biological processes in the cultivated Sahel – 1. Energy and water. Journal of Hydrology 1-2, 204–216.

Randow, C. von, Manzi, A. O., Kruijt, B., Oliveira, P. J. de, Zanchi, F. B., Silva, R. L., Hodnett, M. G., Gash, J. H. C., Elbers, J. A., Waterloo, M. J., Cardoso, F. L., Kabat, P., 2004. Comparative measurements and seasonal variations in energy and carbon exchange over forest and pasture in South West Amazonia. Theoretical and Applied Climatology 1-3.

Redelsperger, J.-L., Thorncroft, C. D., Diedhiou, A., Lebel, T., Parker, D. J., Polcher, J., 2006. African Monsoon Multidisciplinary Analysis: An International Research Project and Field Campaign. Bulletin of the American Meteorological Society 12, 1739–1746.

Reinecke, R., Foglia, L., Mehl, S., Herman, J. D., Wachholz, A., Trautmann, T., & Döll, P. (2019). Spatially distributed sensitivity of simulated global groundwater heads and flows to hydraulic conductivity, groundwater recharge, and surface water body parameterization. *Hydrology and Earth System Sciences*, *23*(11), 4561–4582. https://doi.org/10.5194/hess-23-4561-2019

Reitz, O., Graf, A., Schmidt, M., Ketzler, G., & Leuchner, M. (2022). Effects of Measurement Height and Low-Pass-Filtering Corrections on Eddy-Covariance Flux Measurements Over a

Forest Clearing with Complex Vegetation. *Boundary-Layer Meteorology*, *184*(2), 277–299. https://doi.org/10.1007/s10546-022-00700-1

Rigon, R., Bertoldi, G., & Over, T. M. (2006). GEOtop: A Distributed Hydrological Model with Coupled Water and Energy Budgets. *Journal of Hydrometeorology*, *7*(3), 371–388. https://doi.org/10.1175/JHM497.1

Robert J. H. Dunn, Diane M. Stanitski, Nadine Gobron, Kate M. Willett, M. Ades, et al.. Global Climate [in "State of the Climate in 2019"]. Bulletin of the American Meteorological Society, 2020, 101 (8), pp.S9-S127. 10.1175/BAMS-D-20-0104.1. insu-02922292

Rodrigues, T. R., Paulo, S. R. de, Novais, J. W. Z., Curado, L. F. A., Nogueira, J. S., Oliveira, R. G. de, Lobo, F. d. A., Vourlitis, G. L., 2013. Temporal Patterns of Energy Balance for a Brazilian Tropical Savanna under Contrasting Seasonal Conditions. International Journal of Atmospheric Sciences 5, 1–9.

Reed, J.E. Type Curves for Selected Problems of Flow to Wells in Confined Aquifers; 03-B3; U.S. Geological Survey: Washington, DC, USA, 1980.

Rosenzweig, C., Arnell, N. W., Ebi, K. L., Lotze-Campen, H., Raes, F., Rapley, C., et al. (2017). Assessing inter-sectoral climate change risks: the role of ISIMIP. Environmental Research Letters, 12(1), 010301.

Schaller, M. F., & Fan, Y. (2009). River basins as groundwater exporters and importers: Implications for water cycle and climate modeling. *Journal of Geophysical Research*, *114*(D4), D04103. https://doi.org/10.1029/2008JD010636

Schlesinger, W. H., & Jasechko, S. (2014). Transpiration in the global water cycle. *Agricultural and Forest Meteorology*, *189–190*, 115–117. https://doi.org/10.1016/j.agrformet.2014.01.011

Sellar, A. A., Jones, C. G., Mulcahy, J. P., Tang, Y., Yool, A., Wiltshire, A., O'Connor, F. M., Stringer, M., Hill, R., Palmieri, J., Woodward, S., De Mora, L., Kuhlbrodt, T., Rumbold, S. T., Kelley, D. I., Ellis, R., Johnson, C. E., Walton, J., Abraham, N. L., … Zerroukat, M. (2019). UKESM1: Description and Evaluation of the U.K. Earth System Model. *Journal of Advances in Modeling Earth Systems*, *11*(12), 4513–4558. https://doi.org/10.1029/2019ms001739

Seabold, S., & Perktold, J. (2010). statsmodels: Econometric and statistical modeling with python. In *9th Python in Science Conference*.

Sellers, P. J., Fennessy, M. J., & Dickinson, R. E. (2007). A numerical approach to calculating soil wetness and evapotranspiration over large grid areas. *Journal of Geophysical Research*, *112*(D18), D18106. https://doi.org/10.1029/2007JD008781

Seghieri, J., Vescovo, A., Padel, K., Soubie, R., Arjounin, M., Boulain, N., De Rosnay, P., Galle, S., Gosset, M., Mouctar, A. H., Peugeot, C., & Timouk, F. (2009). Relationships between climate, soil moisture and phenology of the woody cover in two sites located along the West African latitudinal gradient. Journal of Hydrology, 375(1–2), 78–89. https://doi.org/10.1016/j.jhydrol.2009.01.023

Shen, C., & Phanikumar, M. S. (2010). A process-based, distributed hydrologic model based on a large-scale method for surface–subsurface coupling. *Advances in Water Resources*, *33*(12), 1524–1541. https://doi.org/10.1016/j.advwatres.2010.09.002

Shangguan, W., Hengl, T., Mendes de Jesus, J., Yuan, H., & Dai, Y. (2017). Mapping the global depth to bedrock for land surface modeling: GLOBAL MAP OF DEPTH TO BEDROCK. *Journal of Advances in Modeling Earth Systems*, *9*(1), 65–88. https://doi.org/10.1002/2016MS000686

Sirota, D., Shragge, J., Krahenbuhl, R., Swidinsky, A., Yalo, N., & Bradford, J. (2022). Development and validation of a low-cost direct current resistivity meter for humanitarian geophysics applications. *GEOPHYSICS*, *87*(1), WA1–WA14. https://doi.org/10.1190/geo2021-0058.1

Shukla, P. R. et al., 2019: Technical Summary [P.R. Shukla, J. S., E. Calvo Buendia, V. Masson-Delmotte, H.-O. Pörtner, D. C. Roberts, P. Zhai, R. Slade,, R. v. D. S. Connors, M. Ferrat, E. Haughey, S. Luz, S. Neogi, M. Pathak, J. Petzold, J. Portugal Pereira, P. Vyas, and K. K. E. Huntley, M, Belkacemi, J. Malley, (eds.)]. Climate Change and Land: an IPCC special report on climate change, desertification, land degradation, sustainable land management, food security, and greenhouse gas fluxes in terrestrial ecosystems, In Press pp. Available at: https://www.ipcc.ch/site/assets/uploads/sites/4/2020/07/03_Technical-Summary-TS_V2.pdf.

Sorensen, J. P. R., Nayebare, J., Carr, A. F., Lyness, R., Campos, L. C., Ciric, L., Goodall, T., Kulabako, R., Curran, C. M. R., MacDonald, A. M., Owor, M., Read, D. S., & Taylor, R. G. (2021). In-situ fluorescence spectroscopy is a more rapid and resilient indicator of faecal contamination risk in drinking water than faecal indicator organisms. *Water Research*, *206*, 117734. https://doi.org/10.1016/j.watres.2021.117734

Spanoudaki, K., Stamou, A. I., & Nanou-Giannarou, A. (2009). Development and verification of a 3-D integrated surface water–groundwater model. *Journal of Hydrology*, *375*(3–4), 410–427. https://doi.org/10.1016/j.jhydrol.2009.06.041

Stahl, K., Tallaksen, L. M., Gudmundsson, L., & Christensen, J. H. (2011). Streamflow Data from Small Basins: A Challenging Test to High-Resolution Regional Climate Modeling. *Journal of Hydrometeorology*, *12*(5), 900–912. https://doi.org/10.1175/2011JHM1356.1

Sutanudjaja, E. H., van Beek, L. P. H., de Jong, S. M., van Geer, F. C., & Bierkens, M. F. P. (2014). Calibrating a large-extent high-resolution coupled groundwater-land surface model using soil moisture and discharge data: CALIBRATING GROUNDWATER-LAND SURFACE MODEL. *Water Resources Research*, *50*(1), 687–705. https://doi.org/10.1002/2013WR013807

Sy, S., Noblet-Ducoudré, N., Quesada, B., Sy, I., Dieye, A., Gaye, A., & Sultan, B. (2017). Land-Surface Characteristics and Climate in West Africa: Models' Biases and Impacts of Historical Anthropogenically-Induced Deforestation. *Sustainability*, *9*(10), 1917. https://doi.org/10.3390/su9101917

Smith, J.W., A.E. Reynolds, A.S. Pratt, S. Salack, B. Klotz, T.L. Battle, et al. 2012. Observations of an 11 September Sahelian squall line and Saharan air layer outbreak during NAMMA-06. Int. J. Geophys. 2012:153256. doi:10.1155/2012/153256

Schedlbauer, J. L., Oberbauer, S. F., Starr, G., Jimenez, K. L., 2011. Controls on sensible heat and latent energy fluxes from a short-hydroperiod Florida Everglades marsh. Journal of Hydrology 3-4, 331–341.

Sjöström, M., Zhao, M., Archibald, S., Arneth, A., Cappelaere, B., Falk, U., Grandcourt, A. de, Hanan, N., Kergoat, L., Kutsch, W., Merbold, L., Mougin, E., Nickless, A., Nouvellon, Y., Scholes, R. J., Veenendaal, E. M., Ardö, J., 2013. Evaluation of MODIS gross primary productivity for Africa using eddy covariance data. Remote Sensing of Environment, 275–286.

Stanislawski LV, Survila K, Wendel J, Liu Y, Buttenfield BP. 2018. An open source high-performance solution to extract surface water drainage networks from diverse terrain conditions. Cartogr Geogr Inf. Sci. 45 (4):319–328.doi.org/

Steffen, W., Richardson, K., Rockstrom, J., Schellnhuber, H.J., Dube, O.P., Dutreuil, S., Lenton, T.M., Lubchenco, J.,2020. The emergence and evolution of Earth System Science. Nat. Rev. Earth Environ. 1(1),54 –63.

Stöckli, R., Lawrence, D. M., Niu, G.-Y., Oleson, K. W., Thornton, P. E., Yang, Z.-L., Bonan, G. B., Denning, A. S., Running, S. W., 2008. Use of FLUXNET in the Community Land Model development. Journal of Geophysical Research: Atmospheres G1, n/a-n/a.

Stoy, P. C., Mauder, M., Foken, T., Marcolla, B., Boegh, E., Ibrom, A., Arain, M. A., Arneth, A., Aurela, M., Bernhofer, C., Cescatti, A., Dellwik, E., Duce, P., Gianelle, D., van Gorsel, E., Kiely, G., Knohl, A., Margolis, H., McCaughey, H., Merbold, L., Montagnani, L., Papale, D., Reichstein, M., Saunders, M., Serrano-Ortiz, P., Sottocornola, M., Spano, D., Vaccari, F., Varlagin, A., 2013. A data-driven analysis of energy balance closure across FLUXNET research sites: The role of landscape scale heterogeneity. Agricultural and Forest Meteorology, 137–152.

Stieglitz, M., D. Rind, J. Famiglietti, and C. Rosenzweig (1997), An efficient approach to modeling the topographic control of surface hydrology for regional and global modeling, J. Clim., 10, 118 – 137.

Sulis, M., Williams, J. L., Shrestha, P., Diederich, M., Simmer, C., Kollet, S. J., & Maxwell, R. M. (2017). Coupling Groundwater, Vegetation, and Atmospheric Processes: A Comparison of Two Integrated Models. *Journal of Hydrometeorology*, *18*(5), Article 5. https://doi.org/10.1175/JHM-D-16-0159.1

Suni, T., Guenther, A., Hansson, H. C., Kulmala, M., Andreae, M. O., Arneth, A., Artaxo, P., Blyth, E., Brus, M., Ganzeveld, L., Kabat, P., De. Noblet-Ducoudré, N., Reichstein, M., Reissell, A., Rosenfeld, D., & Seneviratne, S. (2015). The significance of land-atmosphere interactions in the Earth system—iLEAPS achievements and perspectives. *Anthropocene*, *12*, 69–84. https://doi.org/10.1016/j.ancene.2015.12.001

Sy, S., & Quesada, B. (2020). Anthropogenic land cover change impact on climate extremes during the 21st century. *Environmental Research Letters*, *15*(3), 034002. https://doi.org/10.1088/1748-9326/ab702c

Sy, S., Noblet-Ducoudré, N., Quesada, B., Sy, I., Dieye, A., Gaye, A., & Sultan, B. (2017). Land-Surface Characteristics and Climate in West Africa: Models' Biases and Impacts of Historical Anthropogenically-Induced Deforestation. *Sustainability*, *9*(10), Article 10. https://doi.org/10.3390/su9101917

Soltani, M., Mauder, M., Laux, P., Kunstmann, H., 2018. Turbulent flux variability and energy balance closure in the TERENO prealpine observatory: a hydrometeorological data analysis. Theoretical and Applied Climatology 3-4, 937–956.

Swinbank, W. C., 1951. The measurement of vertical transfer of heat and water vapor by eddies in the lower atmosphere. Journal of Meteorology 3, 135–145.

Sultan, B., and S. Janicot (2003), The West African monsoon dynamics. Part II: The "preonset" and "onset" of the summer monsoon, J. Clim., 16, 3407–3427.

Senatore, A.; Mendicino, G.; Gochis, D.J.; Yu, W.; Yates, D.N.; Kunstmann, H. Fully coupled atmosphere-hydrology simulations for the central Mediterranean: Impact of enhanced hydrological parameterization for short and long time scales. J. Adv. Model. Earth Syst. 2015, 7, 1693–1715. https://doi.org/10.1002/2015MS000510

Seo, E., & Dirmeyer, P. A. (2022). Improving the ESA CCI daily soil moisture time series with physically-based land surface model datasets using a Fourier time-filtering method. *Journal of Hydrometeorology*. https://doi.org/10.1175/JHM-D-21-0120.1

Stieglitz, M., D. Rind, J. Famiglietti, and C. Rosenzweig (1997), An efficient approach to modeling the topographic control of surface hydrology for regional and global modeling, J. Clim., 10, 118 – 137.

Tagesson, T., Fensholt, R., Guiro, I., Rasmussen, M. O., Huber, S., Mbow, C., Garcia, M., Horion, S., Sandholt, I., Holm-Rasmussen, B., Göttsche, F. M., Ridler, M.-E., Olén, N., Lundegard Olsen, J., Ehammer, A., Madsen, M., Olesen, F. S., Ardö, J., 2015. Ecosystem properties of semiarid savanna grassland in West Africa and its relationship with environmental variability. Global change biology 1, 250–264.

Tallaksen, L. M., & Stahl, K. (2014). Spatial and temporal patterns of large-scale droughts in Europe: Model dispersion and performance. *Geophysical Research Letters*, *41*(2), 429–434. https://doi.org/10.1002/2013GL058573

Tanguy, M., Baille, A., González-Real, M. M., Lloyd, C., Cappelaere, B., Kergoat, L., Cohard, J.-M., 2012. A new parameterisation scheme of ground heat flux for land surface flux retrieval from remote sensing information. Journal of Hydrology, 113–122.

Taylor, R. G., Koussis, A. D., & Tindimugaya, C. (2009). Groundwater and climate in Africa—A review. *Hydrological Sciences Journal*, *54*(4), 655–664. https://doi.org/10.1623/hysj.54.4.655

Tesfa, T. K., D. G. Tarboton, D. G. Chandler, and J. P. McNamara (2009), Modeling soildepth from topographic and land cover attributes, Water Resour. Res., 45, W10438, doi:10.1029/2008WR007474.

Thibault Hallouin. (2021). hydroeval: an evaluator for streamflow time series in Python (v0.1.0). Zenodo. https://doi.org/10.5281/zenodo.4709652

Tian, H., Xu, R., Canadell, J. G., Thompson, R. L., Winiwarter, W., Suntharalingam, P., Davidson, E. A., Ciais, P., Jackson, R. B., Janssens-Maenhout, G., Prather, M. J., Regnier, P., Pan, N., Pan, S., Peters, G. P., Shi, H., Tubiello, F. N., Zaehle, S., Zhou, F., … Yao, Y. (2020). A comprehensive quantification of global nitrous oxide sources and sinks. *Nature*, *586*(7828), 248–256. https://doi.org/10.1038/s41586-020-2780-0

Timouk, F., Kergoat, L., Mougin, E., Lloyd, C. R., Ceschia, E., Cohard, J.-M., Rosnay, P. d., Hiernaux, P., Demarez, V., Taylor, C. M., 2009. Response of surface energy balance to water regime and vegetation development in a Sahelian landscape. Journal of Hydrology 1-2, 178–189.

Theis, C.V. The relation between the lowering of the piezometric surface and the rate and duration of discharge of a well using ground water storage: Transaction of American Geophysical Union. Trans. Am. Geophys. Union 1935, 16, 519–524. https://doi.org/10.1029/TR016i002p00519

Troeger, U., & Chambel, A. (2021). Topical Collection: Progress in fractured-rock hydrogeology. *Hydrogeology Journal*, *29*(8), 2557–2560. https://doi.org/10.1007/s10040-021-02414-z

United Nations (UN). (2015). Transforming our world: The 2030 Agenda for Sustainable Development. United Nations. https://www.un.org/en/our-work/support-sustainable-development-and-climate-action

United Nations Economic Commission for Africa (UNECA). (2023). Salvaging the 2030 Agenda for Sustainable Development and Agenda 2063: The Africa we want, of the African Union. https://repository.uneca.org/handle/10855/49986

United Nations Framework Convention on Climate Change (UNFCCC). (2015). Paris Agreement. United Nations. https://unfccc.int/process-and-meetings/the-paris-agreement/the-paris-agreement

United Nations Framework Convention on Climate Change (UNFCCC). (2024). Opportunities and options for integrating climate change adaptation with the Sustainable Development Goals and the Sendai Framework for Disaster Risk Reduction 2015–2030 – Technical paper. https://unfccc.int/documents/641716

United Nations Office for Disaster Risk Reduction (UNDRR). (2015). Sendai Framework for Disaster Risk Reduction 2015–2030. https://www.undrr.org/publication/sendai-framework-disaster-risk-reduction-2015-2030

United Nations Office for Disaster Risk Reduction (UNDRR). (2015). Disaster risk reduction and resilience in the 2030 agenda for sustainable development. https://www.undrr.org/publication/disaster-risk-reduction-and-resilience-2030-agenda-sustainable-development

USGS. (2020a). Bioclimatic regions map. USGS. https://eros.usgs.gov/westafrica/node/147

USGS. (2020b). Landscapes of West Africa: A window on a changing world. USGS. https://eros.usgs.gov/westafrica/

Van Meter, K. J., Basu, N. B., & Van Cappellen, P. (2017). Two centuries of nitrogen dynamics: Legacy sources and sinks in the Mississippi and Susquehanna River Basins: Two centuries of nitrogen dynamics. *Global Biogeochemical Cycles*, *31*(1), 2–23. https://doi.org/10.1002/2016GB005498

VanderKwaak, J. E., & Loague, K. (2001). Hydrologic-Response simulations for the R-5 catchment with a comprehensive physics-based model. *Water Resources Research*, *37*(4), 999–1013. https://doi.org/10.1029/2000WR900272

Virtanen, P., Gommers, R., Oliphant, T. E., Haberland, M., Reddy, T., Cournapeau, D., … SciPy 1.0 Contributors. (2020). SciPy 1.0: Fundamental Algorithms for Scientific Computing in Python. *Nature Methods*, *17*, 261–272. https://doi.org/10.1038/s41592-019-0686-2

Volkoff, B. and Willaime, P. (1976) Notice Explicative No. 66. Carte pédologique de reconnaissance de la République Populaire du Bénin à 1/200.000. Feuille de Porto-Novo. ORSTOM.

von Schuckmann, K. et al., 2016: An imperative to monitor Earth’s energy imbalance. Nature Climate Change, **6(2)**, 138‐144, doi:10.1038/nclimate2876.

Vremec, M., Collenteur, R. A., & Birk, S. (2024). *PyEt* v1.3.1: A Python package for the estimation of potential evapotranspiration. *Geoscientific Model Development*, *17*(18), 7083–7103. https://doi.org/10.5194/gmd-17-7083-2024

Vremec, M., Collenteur, R. A., & Birk, S. (2023). *Technical note: Improved handling of potential evapotranspiration in hydrological studies with PyEt* [Preprint]. Catchment hydrology/Modelling approaches. https://doi.org/10.5194/hess-2022-417

Wada, Y., & Bierkens, M. F. P. (2014). Sustainability of global water use: Past reconstruction and future projections. *Environmental Research Letters*, *9*(10), 104003. https://doi.org/10.1088/1748-9326/9/10/104003

Wada, Y., Wisser, D., & Bierkens, M. F. P. (2014). Global modeling of withdrawal, allocation and consumptive use of surface water and groundwater resources. *Earth System Dynamics*, *5*(1), 15–40. https://doi.org/10.5194/esd-5-15-2014

Wada, Y. (2016). Modeling Groundwater Depletion at Regional and Global Scales: Present State and Future Prospects. Surveys in Geophysics, 37(2), 419–451. https://doi.org/10.1007/s10712-015-9347-x

Wallace, J. S., Wright, I. R., Stewart, J. B., Holwill, C. J., 1991. The Sahelian Energy Balance Experiment (SEBEX): Ground based measurements and their potential for spatial extrapolation using satellite data. Advances in Space Research 3, 131–141.

Weill, S., Mouche, E., & Patin, J. (2009). A generalized Richards equation for surface/subsurface flow modelling. *Journal of Hydrology*, *366*(1–4), 9–20. https://doi.org/10.1016/j.jhydrol.2008.12.007

Wellington, M. J., Kuhnert, P., Renzullo, L. J., & Lawes, R. (2022). Modelling Within-Season Variation in Light Use Efficiency Enhances Productivity Estimates for Cropland. *Remote Sensing*, *14*(6), 1495. https://doi.org/10.3390/rs14061495

Weller, S., Kraus, D., Butterbach-Bahl, K., Wassmann, R., Tirol-Padre, A., & Kiese, R. (2015). Diurnal patterns of methane emissions from paddy rice fields in the Philippines. *Journal of Plant Nutrition and Soil Science*, *178*(5), 755–767. https://doi.org/10.1002/jpln.201500092

Werner, C., Kiese, R., and Butterbach-Bahl, K.: Soil–atmosphere exchange of N2O, CH4, and CO2 and controlling environmental factors for tropical rain forest sites in western Kenya, J. Geophys. Res., 112, D03308, doi:10.1029/2006JD007388, 2007b.

Werner, C., Reiser, K., Dannenmann, M., Hutley, L. B., Jacobeit, J., & Butterbach-Bahl, K. (2014). N_2O, NO, N_2, and CO_2 emissions from tropical savanna and grassland of northern Australia: An incubation experiment with intact soil cores. *Biogeosciences*, *11*(21), 6047–6065. https://doi.org/10.5194/bg-11-6047-2014

Wenzel, L.K.; Fishel, V.C. Methods for Determining Permeability of Water-Bearing Materials with Special Reference to Discharging Well Methods, Water-Supply Paper 887; United States Government Printing Office: Washington, DC, USA, 1942.

Wild, M. et al., 2015: The energy balance over land and oceans: an assessment based on direct observations and CMIP5 climate models. Climate Dynamics, 44(11–12), 3393 – 3429, doi:10.1007/s00382-014-2430-z.

Wild, M. et al., 2019: The cloud-free global energy balance and inferred cloud radiative effects: an assessment based on direct observations and climate models. Climate Dynamics, 52(7–8), 4787 – 4812, doi:10.1007/s00382-018-4413-y.

Wiltshire, A. J., Burke, E. J., Chadburn, S. E., Jones, C. D., Cox, P. M., Davies-Barnard, T., et al. (2020). JULES-CN: A coupled terrestrial carbon-nitrogen scheme (jules vn5.1). Geoscientific Model Development Discussions, 2020,1–40. https://doi.org/10.5194/gmd-2020-205

Wolock, D. M., and G. J. McCabe (1995), Comparison of single and multiple flow direction algorithms for computing topographic parameters in TOPMODEL, Water Resour. Res., 31, 1315 – 1324.

Wood, E. F., Roundy, J. K., Troy, T. J., van Beek, L. P. H., Bierkens, M. F. P., Blyth, E., de Roo, A., Döll, P., Ek, M., Famiglietti, J., Gochis, D., van de Giesen, N., Houser, P., Jaffé, P. R., Kollet, S., Lehner, B., Lettenmaier, D. P., Peters-Lidard, C., Sivapalan, M., … Whitehead, P. (2011). Hyper-resolution global land surface modeling: Meeting a grand challenge for monitoring Earth's terrestrial water: OPINION. *Water Resources Research*, *47*(5). https://doi.org/10.1029/2010WR010090

Wood, W. W., & Hyndman, D. W. (2017). Groundwater Depletion: A Significant Unreported Source of Atmospheric Carbon Dioxide: GROUNDWATER DEPLETION. Earth's Future, 5(11), 1133–1135. https://doi.org/10.1002/2017EF000586

Wolock, D. M., and G. J. McCabe (2000), Differences in topographic characteristics computed from 100- and 1000-m resolution digital elevation model data, Hydrol. Processes, 14, 987 – 1002.

Wolock, D. M. (1993), Simulating the variable-source-area concept of watershed hydrology with TOPMODEL, U.S. Geol. Surv. Water Resour. Invest. Rep. 93-4124, 33 pp.

Wouters, B., Bonin, J. A., Chambers, D. P., Riva, R. E. M., Sasgen, I., & Wahr, J. (2014). GRACE, time-varying gravity, Earth system dynamics and climate change. *Reports on Progress in Physics*, *77*(11), 116801. https://doi.org/10.1088/0034-4885/77/11/116801

Wunsch, A., Liesch, T., & Broda, S. (2022). Deep learning shows declining groundwater levels in Germany until 2100 due to climate change. *Nat Commun*, *13*(1), Article 1. https://doi.org/10.1038/s41467-022-28770-2

Xu, X., Yuan, F., Hanson, P.J., Wullschleger, S.D., Thornton, P.E., Riley, W.J., Song, X., Graham, D.E., Song, C., Tian, H., 2016. Reviews and syntheses: four decades of modeling methane cycling in terrestrial ecosystems. Biogeosciences 13, 3735–3755. https://doi.org/10.5194/bg-13-3735-2016.

Yahaya Seydou, A. N., Sy, S., Quesada, B., Bliefernicht, J., Manevski, K., Amekudzi, L. K., Appiah-Adjei, E. K., Ogunjobi, K. O., Traore, B., Gyamfi, C., & Kunstmann, H. (2025). Biophysical effects of land cover changes in West Africa: A systematic review. *Environmental Research Letters*. https://doi.org/10.1088/1748-9326/addbf4

Yan, F., Shangguan, W., Zhang, J., & Hu, B. (2020). Depth-to-bedrock map of China at a spatial resolution of 100 meters. Sci Data, 7(1), Article 1. https://doi.org/10.1038/s41597-019-0345-6

Yao, Y., Liang, S., Li, X., Liu, S., Chen, J., Zhang, X., Jia, K., Jiang, B., Xie, X., Munier, S., Liu, M., Yu, J., Lindroth, A., Varlagin, A., Raschi, A., Noormets, A., Pio, C., Wohlfahrt, G., Sun, G., Domec, J.-C., Montagnani, L., Lund, M., Eddy, M., Blanken, P. D., Grünwald, T., Wolf, S., Magliulo, V., 2016. Assessment and simulation of global terrestrial latent heat flux by synthesis of CMIP5 climate models and surface eddy covariance observations. Agricultural and Forest Meteorology, 151–167.

Younaise Sounkanmi Olouwachéyi Adeotan, Jean-Michel Vouillamoz, Fabrice Messan Amen Lawson, Mahamadou Koita, Malicki Zorom, Yacouba Saly Traore, Richard Sanou, Basile Hector, Massaoudou Balima (2025). Beyond lineaments: Exploring the influence of weathered layers on borehole productivity in basement rocks of Burkina Faso, West Africa. Hydrogeology Journal. https://doi.org/10.1007/s10040-025-02876-5

Zamrsky, D., Oude Essink, G. H. P., & Bierkens, M. F. P. (2018). Estimating the thickness of unconsolidated coastal aquifers along the global coastline. Earth Syst. Sci. Data, 10(3), 1591-1603. https://doi.org/10.5194/essd-10-1591-2018

Zhang, L.-X., Zhou, D.-C., Fan, J.-W., & Hu, Z.-M. (2015). Comparison of four light use efficiency models for estimating terrestrial gross primary production. *Ecological Modelling*, *300*, 30–39. https://doi.org/10.1016/j.ecolmodel.2015.01.001

Zhou, T., Zhang, W., Chen, D., Zhang, X., Li, C., Zuo, M., Chen, X., 2022. Understanding and building upon pioneering work of Nobel Prize in Physics 2021 laureates Syukuro Manabe and Klaus Hasselmann: from greenhouse effect to Earth system science and beyond. Sci. China Earth Sci.65(4),589 –600.